THESE

PRESENTEE PAR

JOSE EMILIO LORENZO DIAZ

POUR OBTENIR LE TITRE DE
DOCTEUR DE L'UNIVERSITE JOSEPH FOURIER - GRENOBLE I
(ARRETES MINISTERIELS DU 5 JUILLET 1984 ET DU 23 NOVEMBRE 1988)
SPECIALITE: PHYSIQUE

TITRE

ETUDE PAR DIFFUSION DE NEUTRONS DES TRANSITIONS DE PHASE DANS LES COMPOSES QUASI-UNIDIMENSIONNELS $(TaSe_4)_2I$ ET $(NbSe_4)_3I$

SOUTENUE LE 12 NOVEMBRE 1992 DEVANT LA COMMISSION D'EXAMEN

COMPOSITION DU JURY:

M. M. VALLADE	PRESIDENT	Prof. UJF
Mme. F. MOUSSA	RAPPORTEUR	Prof. Paris Sud, LLB, Saclay
M. S. BRAZOVSKII	RAPPORTEUR	Institut Landau, Moscou
M. R. CURRAT	EXAMINATEUR	Institut Laue-Langevin
M. P. MONCEAU	EXAMINATEUR	Directeur de Recherche, CNRS
M. F. LEVY	INVITE	Prof. EPF Lausanne, Suisse

THESE PREPAREE A L'INSTITUT LAUE-LANGEVIN

à mes parents

Le travail présenté dans ce mémoire a été effectué à l'Institut Laue-Langevin à Grenoble. Je tiens à remercier les directeurs qui se sont succédés depuis mon arrivée en 1988: W. Gläser, P. Day et J. Charvolin, pour m'y avoir accuelli.

L'origine de cette thèse remonte à l'année 1986, lorsque l'Espagne a décidé de prendre part aux activités de l'Institut Laue-Langevin. La communauté scientifique espagnole a alors proposé d'envoyer des étudiants pour se former directement sur place. C'est pour cette raison que j'ai pu faire un stage de deux mois à l'Institut Laue-Langevin (Octobre-Novembre 1987) avec M. R. Currat et commencer ultérieurement une thèse (Septembre 1988) financée par le gouvernement espagnol (C.A.Y.C.I.T.).

Je tiens à remercier

M. M. Vallade, professeur à l'Université Joseph Fourier (Grenoble), de présider le jury de cette thèse.

Mme. F. Moussa, M. S. Brazovskii et M. F. Levy d'accepter de juger cette thèse

Je veux remercier M. R. Currat d'avoir accepté de diriger cette thèse, et ainsi de m'avoir fait bénéficier de sa compétence et de sa rigueur scientifique, en matière de diffusion de neutrons ainsi qu'en d'autres domaines de la physique. Il a su toujours diriger avec diligence et patience ce travail. Pendant ces quatre années, j'ai également été encadré par M. P. Monceau, du Centre de Recherche sur les Très Basses Températures (CNRS-Grenoble), grand spécialiste des systèmes à onde de densité de charge. Son ouverture d'esprit, son dynamisme et son courage m'ont beaucoup aidé pendant ces années.

Je témoigne ma gratitude à:

(ILL): M. Alba, B. Aubert, P. Bassas, J. Bossy, A. Brochier, J. Dianoux, B. Dorner, G. Eisele, B. Fåk, M.T. Fernandez, P. Flores, E. Garcia-Martres, J.L. Garcia-Muñoz, S. Hayden, J. Kulda, J.L. Martinez, L. Neetham, J. Rodriguez, S. Pouget, J. Sandonis, B. Schmid, H. Schober, X. Torrelles, J. Trampenau, C. Vettier, I. Volino.

(LLB-Saclay) S. Aubry, P. Boutrouille, G. Coddens, B. Hennion, M. Hennion, A. Moudden, M. Quilichini

(CRTBT-CNRS) L. Bernard, K. Hasselbach, J.C. Lasjaunias, J.C. Martinez, M. Saint-Paul.

(Lab. Cristall-CNRS) M. Artigas, J.L. Hodeau, J.P. Levy, S. Obbade, M. Perroux.

(Autres lab.) J. Bermejo, K. Biljakovic, J. Blanco, J.M. Pérez-Mato, A. Smontara.

Michèle pour ses encouragements et son enthousiasme.

Sommaire

CHAPITRE I: INTRODUCTION

1. Les ondes de densités de charge: concepts de base

2. Distorsion de réseau et couplage électron-phonon.

3. Les excitations dans les composes à ODC.

4. Le spectre électromagnétique du condensat d'ODC.

APPENDICES

CHAPITRE I

1. LES ONDES DE DENSITES DE CHARGE: CONCEPTS DE BASE

1.1. L'idée de Peierls (1955).

En 1955, Peierls montra que l'hypothétique métal unidimensionnel ne présenterait certainement jamais un comportement métallique, car au zéro absolu, il serait énergétiquement plus favorable au réseau de développer une distorsion périodique de vecteur d'onde $\mathbf{q}_0$, $\mathbf{q}_0$ étant égal au double du vecteur d'onde de Fermi k_F des électrons de conduction. Une telle distorsion conduirait à un état isolant à T=0K.

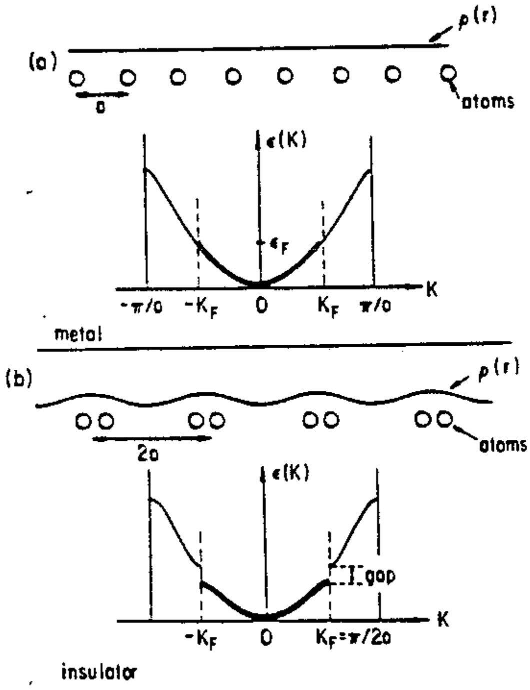

Figure 1.1 La distorsion de Peierls dans un métal unidimensionnel avec bande demi-plaine. (a) métal normal; (b) isolant de Peierls.

Son argumentation était relativement simple. Dans une chaîne linéaire uniforme à T=0K, tous les états électroniques de conduction, dont les vecteurs d'onde $k<k_F$, sont occupés, alors que ceux dont $k>k_F$ sont vides. La densité d'états au niveau de Fermi est donc finie. Supposons que la chaîne uniforme soit soumise à une distorsion périodique dans laquelle le j^{eme} atome ou la j^{eme} molécule est déplacée de sa position d'équilibre, $\mathbf{R}_j$, d'une quantité $\mathbf{u}_j$ telle que $\mathbf{u}_j = \mathbf{u} \cos(\mathbf{q}_0\mathbf{R}_j)$. Du fait de l'interaction électron-ion, les électrons de conduction sont soumis à un nouveau potentiel périodique de vecteur de modulation $2k_F$. Un tel potentiel périodique ouvre un gap dans le spectre électronique d'amplitude 2Δ, au niveau de Fermi, d'où une densité d'états nulle au niveau de Fermi. L'énergie des états électroniques en-dessous de k_F diminue ce qui implique que l'énergie électronique de la chaîne distordue est inférieure à celle de la chaîne uniforme. Si cette perte d'énergie électronique δE_{el} est supérieure au gain d'énergie élastique δE_L, la structure distordue est stable. Dans le cas d'une chaîne linéaire à T=0K, ceci est toujours vérifié: δE_L varie comme le carré de l'amplitude de la distorsion périodique du réseau (DPR), tandis que δE_{el} est de la forme $\delta E_{el} = b\,|\mathbf{u}|^2 \log(1/|\mathbf{u}|)$, où b est une constante, le terme logarithmique caractérisant l'unidimensionalité.

1.2. Le modèle de Fröhlich (1954).

Parallèlement, Fröhlich a mené des études sur les métaux 1D. Il a souligné l'importance de la réponse électronique à une distorsion périodique du réseau ainsi que les conséquences qui en découlent. Les principaux points de son raisonnement sont les suivants:

(a) la distorsion périodique du réseau est contrebalancée par une modulation périodique dans la densité n des électrons de conduction. n est de la forme $n(\mathbf{x}) = n_0 + \delta n(\mathbf{x})$, n_0 représente le densité uniforme des états métalliques et $\delta n(\mathbf{x}) = n_0 A \cos(\mathbf{q}_0\mathbf{x})$, $\delta n(\mathbf{x})$ décrit une onde de densité de charge (ODC) de vecteur de modulation $\mathbf{q}_0$ et d'amplitude A qui peut être reliée à l'amplitude $\mathbf{u}$ de la distorsion périodique de réseau. Ainsi, l'ODC et la DPR sont intimement liées et forment le condensat.

(b) la phase ϕ du condensat spécifie la position relative du condensat par rapport à un référentiel fixe du laboratoire; ainsi, l'ODC et la DPR peuvent être décrites par les équations suivantes:

$$\mathbf{u}_j = \mathbf{u}\,\cos(\mathbf{q}_0\mathbf{x} + \phi) \tag{1.1a}$$

$$\delta n(\mathbf{x}) = n_0 A \cos(\mathbf{q}_0\mathbf{x} + \phi) \tag{1.1b}$$

{Dans le cas d'une distorsion de caractère acoustique, la densité électronique est couplée au gradient des déplacements ioniques et un déphasage de $\pi/2$ apparait entre $\mathbf{u}_j$ et $\delta n(\mathbf{x})$.}

Une variation de la phase $\delta\phi$ entraîne un déplacement de tout le condensat, c'est à dire le déplacement de n_0 électrons par unité de longueur, d'une distance $\delta|\mathbf{x}| = \delta\phi/\mathbf{q}_0$.

(c) Pour un système homogène élastique (jelium), tel celui considéré par Fröhlich, l'énergie du condensat E_C est indépendante de la phase ϕ et par conséquent, le condensat peut se déplacer avec une vitesse uniforme v: $\phi(t) = \phi(0) + vt$. Le mouvement du condensat est à l'origine d'un courant collectif:

$$i = n_0 e \frac{\dot{\phi}}{q_0} \tag{1.2}$$

En présence d'un champ électrique, l'équation du mouvement du condensat s'exprime par:

$$M^* \frac{\ddot{\phi}}{q_0} = e^* E \tag{1.3}$$

où M* représente la masse d'inertie du condensat. D'après Fröhlich, l'invariance par translation de l'énergie de l'ODC dans un métal unidimensionnel aurait pû être à l'origine du phénomène, alors inexpliqué, de la supraconductivité.

1.3. Le modèle de Lee, Rice et Anderson (1974).

La synthèse du premier métal unidimensionnel (KCP, cf 2.2) a permis de démontrer l'existence de systèmes présentant un état fondamental ODC de vecteur d'onde $2k_F$, le long des chaînes. Lee, Rice et Anderson (LRA) considèrent la question du piégeage de la phase de l'ODC par le potentiel du réseau atomique. Ile distinguent les mécanismes suivants:

(a) la commensurabilité du réseau
(b) l'interaction entre les chaînes (présence d'ODC sur des chaînes voisines)
(c) les défauts du réseau (principalement, les impuretés chargées)

L'énergie du condensat dépend, dans ce cas, de la phase ϕ et de l'amplitude A de l'ODC. Ainsi, le condensat est soumis à une force de rappel finie:

$$F_R = -\frac{\partial E_C}{\partial x} = -q_0 \frac{\partial E_C}{\partial \phi} \tag{1.4}$$

autour d'une position préférentielle ϕ_0 qui correspond à la solution de l'équation précédente avec $F_R=0$. On dit que le condensat est piégé. Supposons une force de rappel harmonique de la forme $F_R= K\delta\phi$ et une constante de ressort $K = M^*\omega_0^2$,

ω_0 étant homogène à une fréquence, l'équation du mouvement, lors de petits déplacements $\delta\phi$ par rapport à ϕ_0, du condensat piégé, s'écrit:

$$M^* \frac{\ddot{\delta\phi}}{q_0} = e^*E - \left(\frac{\omega_0^2 M^*}{q_0}\right)\delta\phi \tag{1.5}$$

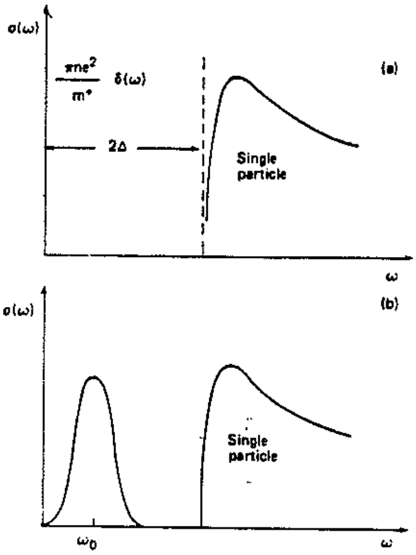

Figure 1.2 La réponse du mode collectif (a) sans piégeage, et (b) avec piègeage et amortissement. La réponse à haute fréquence correspond aux excitations à une particule à travers le gap 2Δ.

Cette équation décrit le mouvement harmonique simple de la phase avec une fréquence ω_0, et implique une conductivité en fonction de la fréquence de la forme:

$$\sigma(\omega) = \frac{1}{L}\frac{e^{*2}}{i\omega M^*}\frac{\omega^2}{\omega_0^2 - \omega^2} \tag{1.6}$$

et une constante diélectrique statique ε_S égale à:

$$\varepsilon_S \approx \frac{4\pi e^{*2}}{LM^*}\frac{1}{\omega_0^2} \tag{1.7}$$

qui diverge lorsque ω_0 ---> 0. L est la longueur du système. Il apparait donc qu'un faible piégeage, c'est à dire ω_0 petit, donne lieu à une absorption à faible fréquence et à une grande constante diélectrique statique.

Les trois origines du potentiel de piégeage sont les suivantes:

(a) le potentiel commensurable apparaît lorsque le rapport entre le vecteur du réseau réciproque **G** et le vecteur de modulation $\mathbf{q}_0$ est un entier M. Il s'exprime par:

$$V(\phi) \approx \left(\frac{\Delta}{W}\right)^M \left(1 - \cos\left(M\phi\right)\right) \tag{1.8}$$

W étant la largeur de bande électronique. L'ODC se déplace dans un potentiel de phase de période 2π/M.

(b) l'interaction coulombienne entre les ODC de chaînes voisines est une fonction qui dépend de la différence de phases de ces ODC $\phi_1 - \phi_2$:

$$V_{12} \approx \Delta_1\Delta_2 \cos\left(\phi_1 - \phi_2\right) \tag{1.9}$$

Cette interaction est à l'origine de la mise en ordre des chaînes à basse température. Elle donne lieu à un potentiel de piégeage périodique pour la phase de chaque chaîne $V(\phi) \approx \cos \phi$, avec une périodicité 2π.

(c) Le piégeage dû à des défauts est plus compliqué et conduit en général à un potentiel de piégeage qui n'est pas une fonction périodique de la phase. Pour une distribution aléatoire d'impuretés chargées, le potentiel de piégeage prend la forme:

$$V(\phi) = \sum_i V_i \cos\left(\mathbf{q}_0\mathbf{x}_i + \phi(\mathbf{x}_i)\right) \tag{1.10}$$

$\mathbf{x}_i$ et V_i décrivent respectivement la position et l'amplitude du potentiel des impuretés. D'après Fukuyama et Lee, ceci conduit à une phase d'ODC piégée localement et à un état fondamental d'ODC de phase inhomogène.

1.4. Le modèle d'Aubry (1981).

L'approche faite dans ce modèle de la transition de phase à ODC diffère des précédentes. Le concept sous-jacent principal est la transition par brisure de l'analyticité: au-delà d'une valeur critique de l'interaction électron-phonon, k_C, l'état fondamental de la modulation ne peut être calculé simplement à partir de l'état fondamental du système non perturbé comme le font LRA (formules 1.1a et 1.1b). L'état fondamental du régime non analytique est composé par des paires d'électrons fortement piégées sur le réseau (bipolarons). Ce régime est caractérisé par l'existence d'états métastables de basse énergie avec des temps caractéristiques de relaxation longs sur l'échelles de temps des phonons. Ils jouent un rôle fondamental dans le comportement thermodynamique du système. Un régime analytique peut également exister si le couplage électron-phonon est suffisamment petit mais il sera instable par rapport aux fluctuations quantiques du réseau. Dans ce cas, les bipolarons se délocalisent sous l'action des fluctuations quantiques de réseau (paires de Cooper). L'état d'ODC disparaît et est remplacé, à 0K, par un état supraconducteur. Cet effet n'ayant pas été observé dans un composé ODC, Aubry affirme que tous les composés incommensurables à ODC ont un état fondamental non analytique.

La function d'onde électronique du bipolaron centré sur un site à x=0, est donné par l'expression:

$$\Psi(x) = \frac{k}{2\sqrt{2}} \frac{1}{\cosh\left(\frac{k^2 x}{4}\right)} \tag{1.11}$$

où k est défini par:

$$k = \lambda \sqrt{\frac{2}{t M \omega_0^2}} \tag{1.12}$$

ω_0 est une fréquence caractéristique de phonon et M la masse associée à chaque site; t est l'énergie de couplage électronique entre deux sites voisins et λ est la constante de couplage électron-phonon.

Dans la limite des grands k, les paires d'électrons sont fortement localisées sur les sites du réseau et la distorsion incommensurable disparaît pour céder place à des liaisons chimiques entre atomes. Les deux échelles d'énergie importantes sont l'énergie de formation d'un bipolaron, U_{bip}, et l'énergie d'interaction (répulsive) entre deux bipolarons, J_m. Dans la limite des grands k, ces deux énergies sont définies par:

$$U_{bip} \cong -\frac{k^2}{2} - \frac{4}{k^2} + \dots$$

$$J_m \cong -t\,\frac{3m+1}{k^{4m-2}} \tag{1.13}$$

où m représente la distance entre deux bipolarons exprimée en nombre de mailles.

Aubry a prouvé que l'état fondamental d'un système incommensurable non analytique, avec k suffisamment grand, peut être représenté exactement par l'état fondamental d'un Hamiltonien de pseudo-spin Ising. Le facteur de structure dynamique du système ne présente pas un mode de phase sous-amorti mais un pic central dû au mouvement diffusif des bipolarons. Toutefois la dynamique du modèle d'Ising associé n'est pas traitée de façon quantitative dans le travail d'Aubry.

A l'approche de k_C, la taille des bipolarons augmente et les états électroniques associés se transforment en ondes de Bloch. Le croisement entre le régime ordre-désordre et le régime displacif se produit lorsque l'énergie caractéristique de l'interaction entre bipolarons devient comparable ou supérieure à l'énergie de liaison des bipolarons.

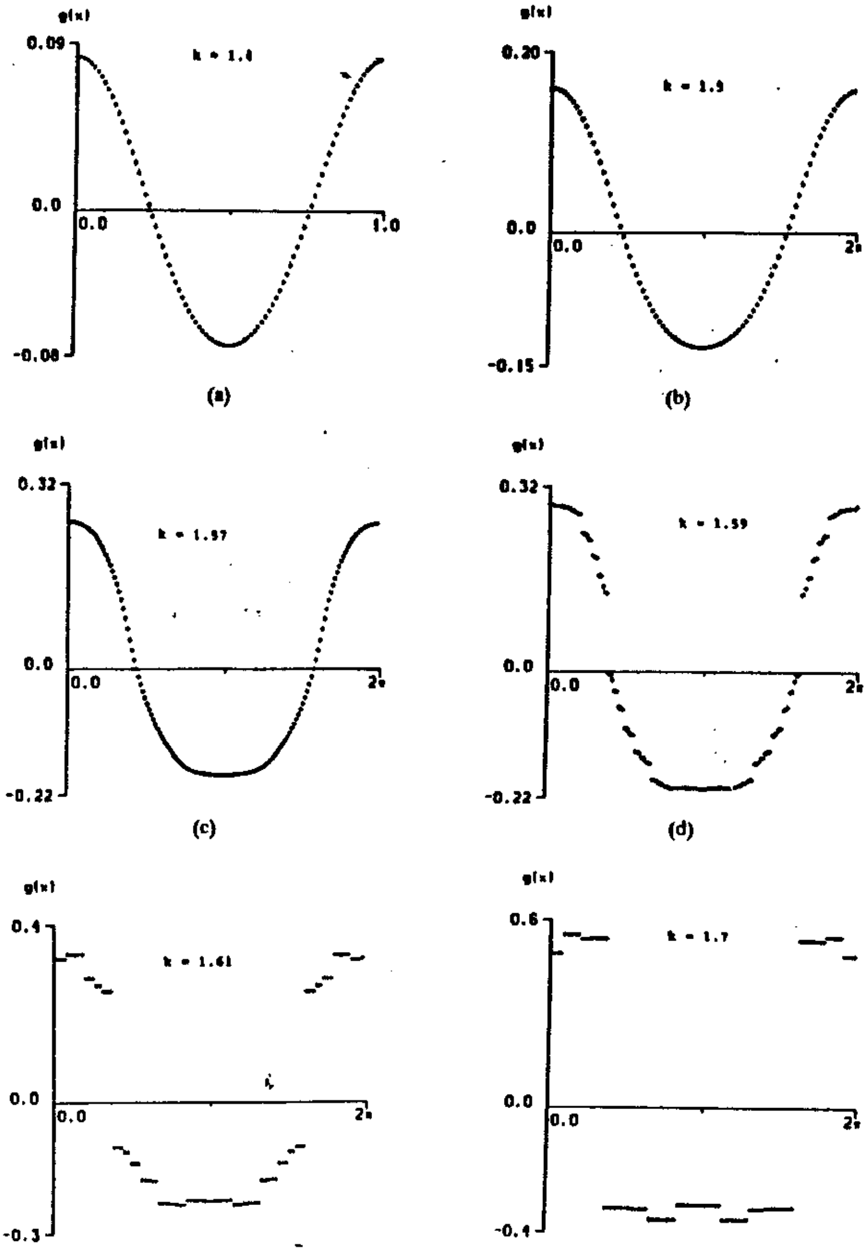

Figure 1.3 La distorsion périodique de réseau (DPR) dans la théorie d'Aubry pour le modèle de Holstein et pour différent valeurs de la constante de couplage k défini dans la équation (1.12). La valeur critique pour ce modèle vaut $k_C = 1.575$

2. DISTORSION DE RESEAU ET COUPLAGE ELECTRON-PHONON.

2.1. Dans le cadre du modèle LRA, la transition de Peierls appartient à la classe des transitions de phase possédant un mode mou. En première approximation, la fréquence d'un phonon située à $2k_F$, tend vers zéro près de la température de transition T_P. Cet amortissement a son parallèle dans les métaux tridimensionnels, comme l'a signalé Kohn, et se nomme " l'anomalie géante de Kohn". L'effet de Kohn 3D est très faible en comparaison de l'effet 1D et n'est pas associé à une instabilité du réseau.

Pour comprendre la position du vecteur d'onde et la nature des déplacements atomiques associés à la DPR, en-dessous de T_P, il est nécessaire de connaître la structure de bande électronique au niveau de Fermi et près de k_F. Dans le paragraphe suivant, nous passons en revue un certain nombre de composés quasi-unidimensionnels présentant une distorsion périodique de réseau.

2.2. D'un point de vue électronique, la structure de bande du composé KCP (abréviation de $K_2Pt(CN)_4Br_{0.3}\ xH_2O$) est très simple (Whangbo et Hoffmann 1978): une seule bande de conduction provenant des orbitales d_{z^2} de la molécule plane $Pt(CN)_4$. Le brome retire 0.3 électron par formule $Pt(CN)_4$, alors que sans atome de brome, la bande de conduction serait complètement pleine.

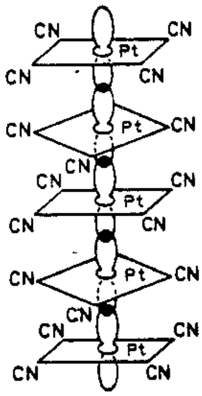

Figure 2.1.a Recouvrement des orbitales d_{z^2} entre les empilements $Pt(CN)_4$ le long de la direction des chaînes. La périodicité est deux fois la distance entre deux molécules $Pt(CN)_4$.

Comme le motif cristallographique dans la direction c (direction de la chaîne) comprend deux formules $Pt(CN)_4$, il manque 0.6 électron à la bande de conduction, d'où $2k_F = 0.3\ c^*$, ce que corrobore l'expérience. La façon la plus aisée d'ouvrir un gap au niveau de Fermi par couplage électron-phonon consiste à moduler la distance entre les molécules $Pt(CN)_4$ par un déplacement de type acoustique le long de la direction des chaînes, en accord avec l'observation de l'anomalie de Kohn sur la branche longitudinale acoustique le long de la direction c* (Renker et al. 1974).

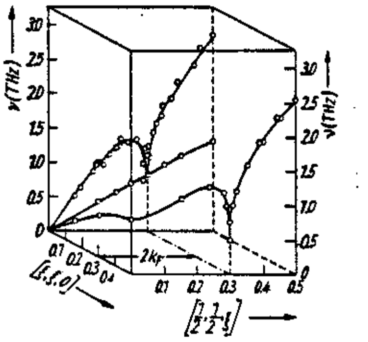

Figure 2.1.b Courbes de dispersion des phonon à température ambiante. L'anomalie de Kohn géant est localisée sur la branche longitudinale acoustique (Renker et al. 1974).

2.3. Les composés organiques à transfert de charges constituent une autre catégorie de matériaux quasi-unidimensionnel; ils sont composés d'empilements de molécules donneuses (**D**) ou accepteuses (**A**).

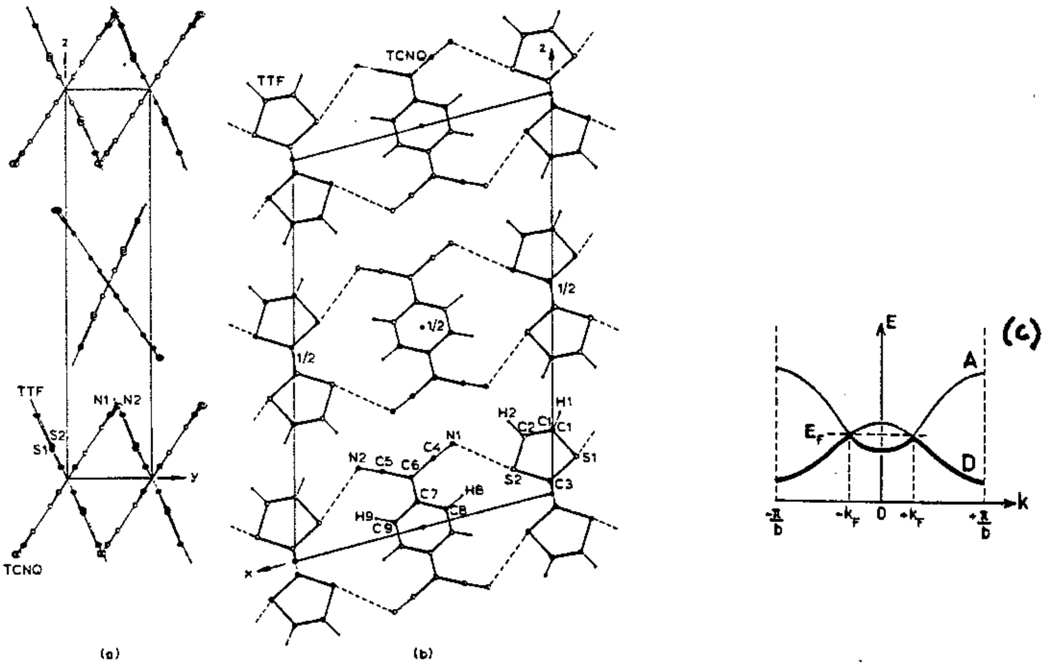

Figure 2.3 Structure de TTF-TCNQ projetée sur l'axe a (a) et b (b).(c) Représentation schématique de la structure de bandes avec D représentant la bande des orbitales correspondant aux molécules donneuses et A celles des accepteuses. Leur croisement détermine le niveau de Fermi.

Le composé le plus étudié est TTF-TCNQ (abréviation de tetrathiafulvalene-tetracyanoquinodimethane), TTF jouant le rôle de donneur et TCNQ celui d'accepteur. Les deux bandes électroniques provenant des deux empilements se recouvrent, un transfert partiel de charges entre les deux bandes permet d'obtenir un niveau de Fermi commun. k_F est commun aux deux bandes car la mise en commun concerne deux électrons. Une situation plus complexe résulte de la substitution de TTF par NMP: un seul électron est mis en commun et k_F diffère pour les empilements donneurs et accepteurs. Ces considérations ne permettent pas, à priori, de connaître le vecteur d'onde de la DPR avec précision ni les déplacements atomiques, différents modes de phonon pouvant se coupler avec l'ODC. Ces effets se manifestent par la complexité des transitions de phases observées dans ces divers composés. En première approximation, il est possible de dire que la DPR provient du glissement des molécules dans des plans inclinés par rapport à la direction d'empilement. C'est pourquoi, des mesures de diffusion inélastique de neutrons ont pu situer l'anomalie de Kohn à la fois sur les branches acoustiques longitudinale et transverse (Shirane et al 1976).

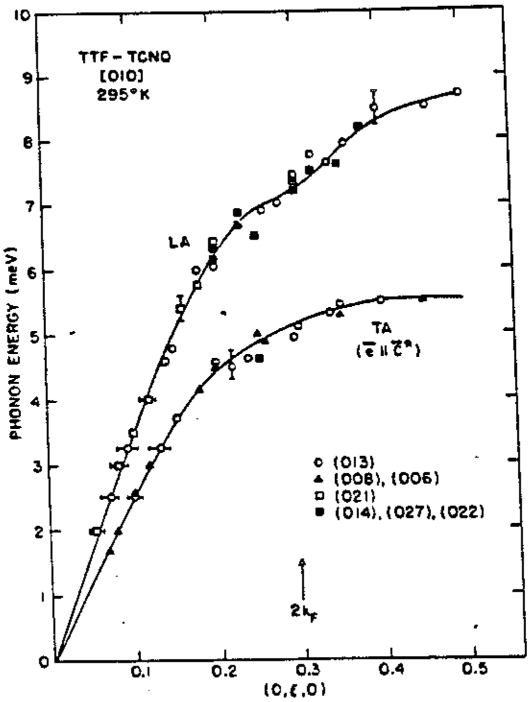

Figure 2.4 Branches acoustiques à 295 K dans TTF-TCNQ. Le phonon TA situé a $2k_F$ qui vaut 5 meV, se ramolli légèrement et près de T_P (54K) vaut 4.4 meV (Shirane et al 1976).

2.4. La structure de bandes des trichalcogénures des métaux de transition MX_3 ($NbSe_3$, TaS_3) est plus complexe (Wilson 1979, Whangbo et Gressier 1984). La structure de ces composés est constituée de chaînes prismatiques trigonales dans lesquelles chaque atome métallique est situé entre deux triangles X_3.

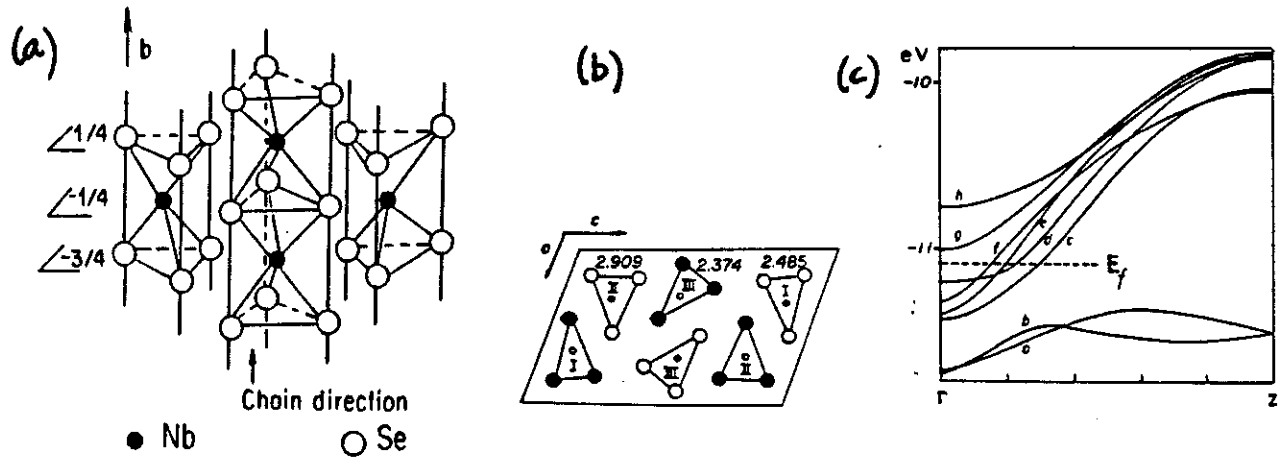

Figure 2.5 (a) Structure de $NbSe_3$. (b) Projection le long de l'axe de chaînes avec les trois types de chaînes. (c) Structure électronique de bandes au voisinage du niveau de Fermi. Quatre bandes croisent E_F.

Dans la variété monoclinique, le motif est constitué de 6 chaînes le long de la direction b. Trois types de chaînes se différencient par la longueur de la distance X-X la plus courte: cette distance est la plus longue dans la chaîne II (dite rouge) et la plus courte dans la chaîne III (jaune). Le nombre d'électrons libres qui remplissent la bande de conduction, est déterminé par l'état d'oxydation du triangle X_3: $X^{2-}(X_2)^{2-}$ pour les chaînes de type I (orange) et de type III et $(X^{2-})_3$ pour les chaînes de type II (l'état d'oxydation de l'atome métallique est M^{5+}). Un simple calcul montre que seuls deux électrons remplissent les bandes de conduction. Des calculs plus complexes de structure de bande montrent que quatre bandes croisent le niveau de Fermi, deux bandes provenant de chaînes de type III (bandes d et e) et les deux autres de chaînes de type I (bandes c et f). Les combinaisons 2 à 2 des vecteurs de Fermi correspondant à chaqu'une des 4 bandes devraient conduire à 10 vecteurs de "nesting" différents. Cependant, des expériences de RMN (Devreux 1982, Ross Jr et al. 1986) soulignent que seules des chaînes de type III sont impliquées dans la transition de phase supérieure (T_{P1}) tandis que seules des chaînes de type I sont impliquées dans la transition de phase inférieure (T_{P2}). Ceci réduit le nombre de vecteurs de nesting à 2: $2k_{F1} = k_{Fd} + k_{Fe}$ à T_{P1} et $2k_{F2} = k_{Fc} + k_{Ff}$ à T_{P2}. La comptabilisation du nombre d'électrons impose la relation suivante entre les deux vecteurs d'onde: $4(2k_{F1} + 2k_{F2}) = 2$. Expérimentalement, on vérifie que la somme des deux vecteurs $2k_{F1}$ et $2k_{F2}$ est très voisine de 0.50 b*. Des résultats de diffraction X montrent que la composante longitudinale de la distorsion de vecteur d'onde $2k_{F1}$ dans le composé $NbSe_3$ est dominée par le déplacement des atomes de niobium dans la chaîne jaune (Moudden et al., unpub.). La diffusion inélastique des neutrons ne permet pas de conclure quant à la présence d'un mode mou dans la branche longitudinale acoustique selon la direction b* (Monceau et al. 1986).

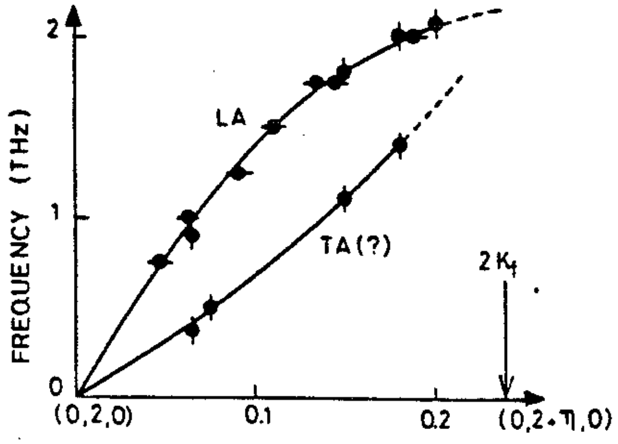

Figure 2.6 Courbes de dispersion des phonones de $NbSe_3$ dans le direction des chaînes à T=200K (Monceau et al. 1986).

2.5. Le bronze bleu $A_{0.3}MoO_3$ (A = K, Rb, Tl) est l'un des composés inorganiques unidimensionnels les plus étudiés. Des groupements (cluster) de dix octaèdres distordus MoO_6, ayant des sommets communs le long des directions b (direction 1D) et [102], constituent la structure de ces composés. Dans la direction perpendiculaire à [010] et [102], les plans d'octaèdres sont séparés par des atomes monovalents.

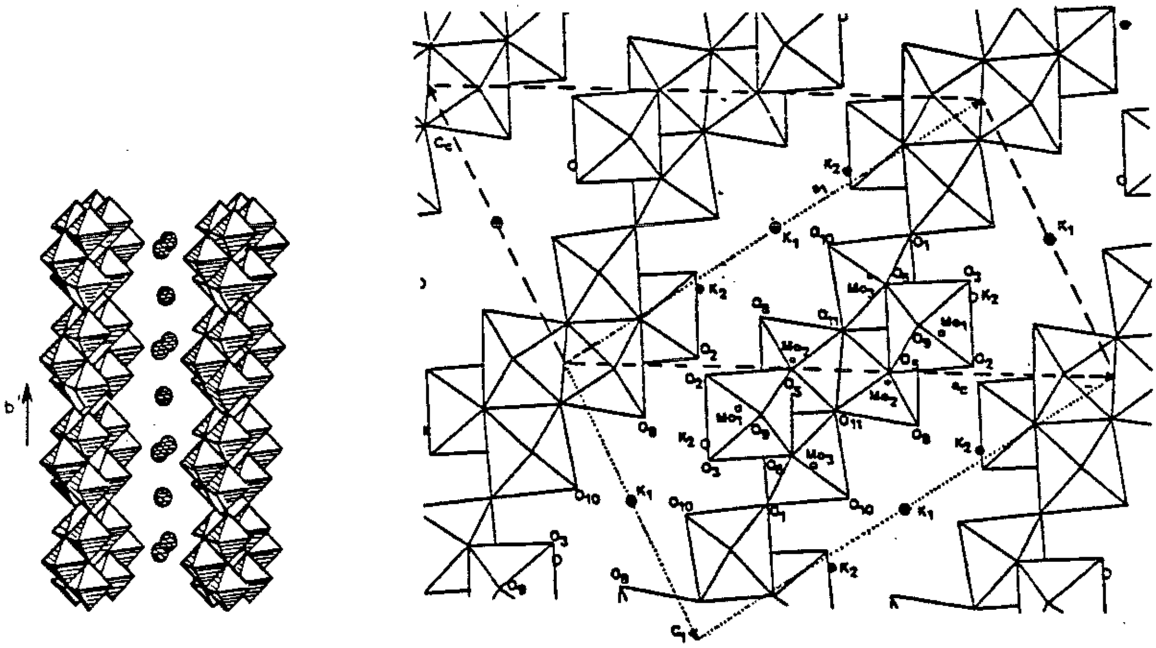

Figure 2.7 Structure cristalline du bronze bleu $A_{0.3}MoO_3$. (a) Chaînes infinis d'octaèdres MoO_6 le long de la direction b. (b) Projection sur le plane (010)

Des calculs de structure de bande (Whangbo et Schneemeyer 1986) indiquent la présence de deux bandes de conduction provenant des orbitales moléculaires de chaque cluster. Ces bandes sont respectivement de type liant et anti-liant; elles sont remplies par trois électrons provenant d'atomes métalliques monovalents. Deux bandes croisent le niveau de Fermi et donnent lieu a deux vecteurs d'onde de Fermi. Parmi les différentes possibilités de nesting, l'examen de la structure basse température montre que c'est le nesting d'une bande sur l'autre qui est réalisé: $2k_F = k_{F1} + k_{F2}$.

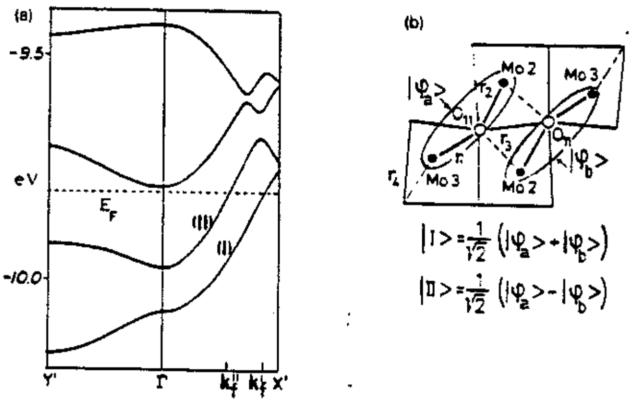

Figure 2.8. (a) Structure de bande au voisinage du niveau de Fermi pour des vecteurs d'onde le-long de la direction de chaîne (ΓX') et sur une direction transverse (ΓY'). I et II correspondent, respectivement, aux états liant et anti-liant. (b) Amplification de la figure 2.7(c). Les combinaisons symétrique et anti-symétrique des orbitales moléculaires φ_a et φ_b appartenant aux même ruban donnent lieu aux deux bandes de conduction montrées en (a).

En effet les symétries des déplacements nécessaires au couplage entre orbitales liantes (ou anti-liantes) d'une part, et entre orbitales liante / anti-liante d'autre part, sont différentes. La détermination de la structure incommensurable (Schutte at de Boer) montre que la distorsion dans le composé $K_{0.3}MoO_3$ est due à un déplacement transverse des atomes Mo(2) et Mo(3), qui forment les chaînes d'octaèdres, vers l'atome d'oxygène commun O(11). Cette distorsion est à l'origine d'une modulation de la distance Mo-O qui modifie, au premier ordre, l'énergie du site et les intégrales de "tunnel" dans les rubans. Ceci est confirmé également par la présence de l'anomalie de Kohn sur les phonons acoustiques transverses (Pouget et al. 1991).

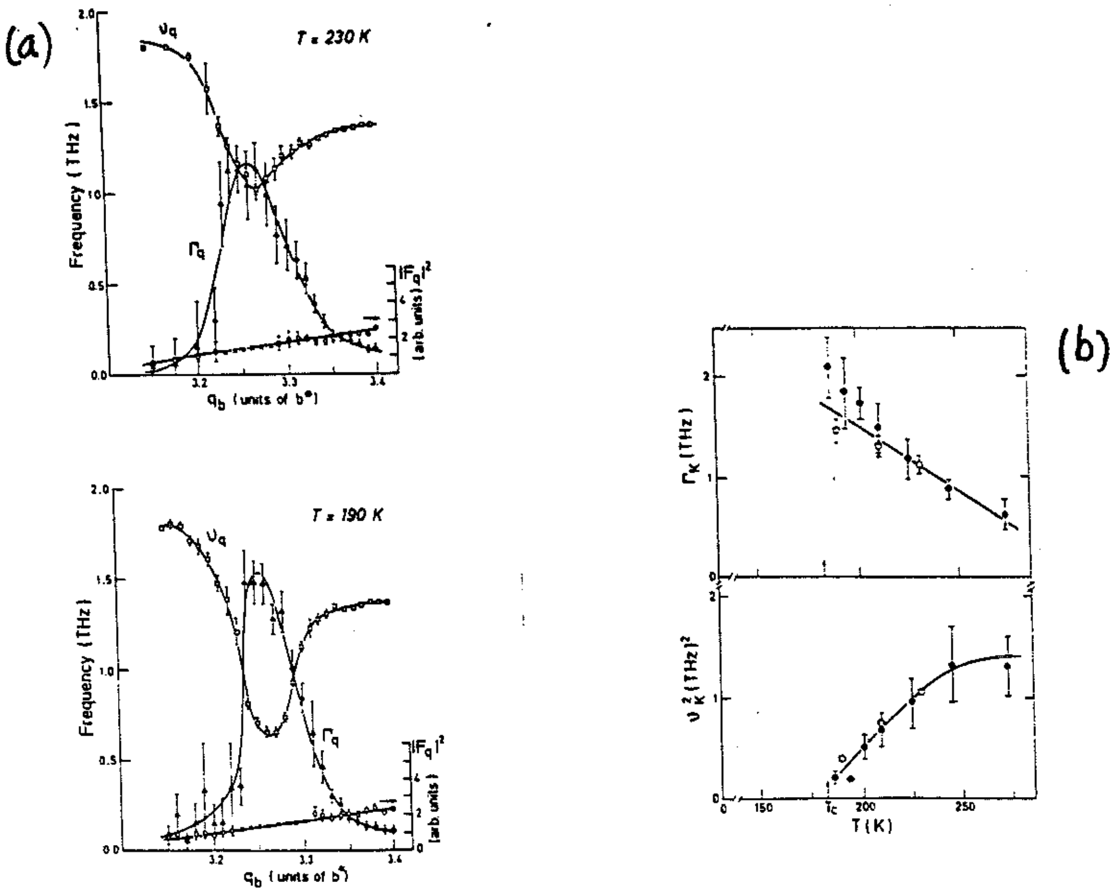

Figure 2.9 (a) Fréquence (υ_q), amortissement (Γ_q) et carré du facteur de structure dynamique ($|F_q|^2$) pour la anomalie de Kohn dans $K_{0.3}MoO_3$ à deux températures. (b) Dépendance en température du carré de la fréquence et de l'amortissement du mode mou (Pouget et al. 1991).

3. LES EXCITATIONS DANS LES COMPOSES A ODC

3.1 La limite displacive.

Par analogie avec les transitions de phase displacives dans les composés incommensurables isolants, il est permis de supposer qu'il existe des transitions de Peierls pilotées par une branche de phonons mous, dont la fréquence s'annulerait à T_P pour $q=2k_F$.

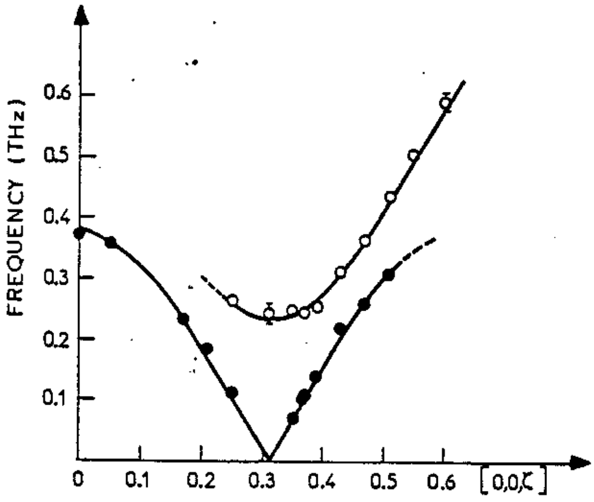

Figure 3.1 Courbes de dispersion pour le phason et l'amplitudon dans le composé incommensurable isolant $ThBr_4$ (Bernard et al. 1983).

En-dessous de T_P, dans la phase ordonnée à ODC, ce mode se scinde en deux modes: le phason qui a une fréquence nulle à $2k_F$ et l'amplitudon. Une telle limite est prise en considération dans le modèle LRA qui propose une loi de dispersion pour l'amplitudon et le phason du type:

$$\omega_A^2(q) = \omega_A^2(2k_F) + \frac{1}{3}\frac{m}{M^*}[v_F(q - 2k_F)]^2 \qquad (3.1.a)$$

$$\omega_\phi(q) = \sqrt{\frac{m}{M^*}}\, v_F(q - 2k_F) \qquad (3.1b)$$

$\omega_A(2k_F) = \sqrt{\lambda}\,\omega_0(2k_F)$, λ est la constante de couplage électron-phonon, sans dimension, et $\omega_0(2k_F)$ est la fréquence du mode de phonon en l'absence de couplage electron-phonon. Le rapport entre la masse effective des électrons (m) et la masse effective de l'ODC (M*) est relié à la valeur du gap électronique par l'expression:

$$\frac{M^*}{m} = 1 + \frac{4}{\lambda}\left[\frac{\Delta}{\omega_0(2k_F)}\right]^2 \qquad (3.2)$$

Dans les systèmes réels la limite displacive théorique n'est pas observée. Le ramollissement de la branche de phonons est incomplet. Au voisinage du vecteur d'onde et de la température critiques, le facteur de structure dynamique associé au mode mou est suramorti avec apparition d'une composante élastique critique ("pic central").

La plupart des auteurs s'accordent sur l'origine extrinsèque de la composante centrale, au moins dans les systèmes où des études détaillées ont pu être effectuées. La présence de défauts ou d'impuretés couplés aux oscillations du phonon mou et dotés d'une dynamique propre (lente), introduit une échelle de temps supplémentaire. Ceci permet de rendre compte à la fois, de l'apparition de la composante centrale et de la saturation de la fréquence du phonon mou à l'approche de la température critique.

Les défauts éloignent les systèmes réels de la limite displacive. Dans le cas des systèmes incommensurables ce comportement se prolonge dans la phase condensée par l'apparition d'un gap de phason. L'extension du modèle de LRA proposée par Fukuyama et Lee, qui constitue le modèle de base pour l'interprétation des propriétés de transport des systèmes à ODC, est fondé sur l'hypothèse que le piégeage de l'ODC est lié à la présence de défauts.

3.2. La limite ordre-désordre.

Cette limite correspond au cas du couplage électron-phonon fort (formule 1.12). D'après Aubry, elle implique la localisation dans l'espace réel de paires d'électrons (bipolarons) (chapitre 1.4). Le facteur de structure dynamique présente alors un pic quasi-élastique qui n'est pas associé aux défauts, mais à la diffusion des bipolarons. Le temps caractéristique correspondant, $\tau(q)$, diverge au voisinage du vecteur d'onde et de la température critiques. Ce temps caractéristique est relié au temps de relaxation microscopique, t_0, observable en l'absence de corrélations ($T>>T_P$), et qui correspond au temps de résidence d'un bipolaron sur un site donné. En principe, on s'attend à ce que t_0 suive une loi d'activation:

$$t_0 \propto \exp(-T_{PN}/T) \qquad (3.3)$$

où l'energie d'activation, k_BT_{PN}, est donnée par le potentiel de Peierls-Nabarro du bipolaron

Toutefois, Aubry n'aborde pas la description détaillée de la dynamique critique associée à la transition de Peierls. Il souligne seulement que dans la limite ordre-désordre, on ne s'attend pas à observer de ramollissement critique sur les branches de phonons. On notera que l'existence d'un régime ordre-désordre suppose $T_P << T_{PN}$, ou encore que l'énergie d'interaction entre les bipolarons (de l'ordre de k_BT_P) est bien inférieure à l'energie de liaison des bipolarons (de l'ordre de k_BT_{PN}).

Dans les cas intermédiaires, on observera une dynamique mixte phonon-pseudospins avec un ramollissement partiel et une composante quasi-élastique critique. Dans la phase condensée, on prévoit un gap de phason plus important que dans la limite displacive en présence de défauts (Aubry et al. 1992).

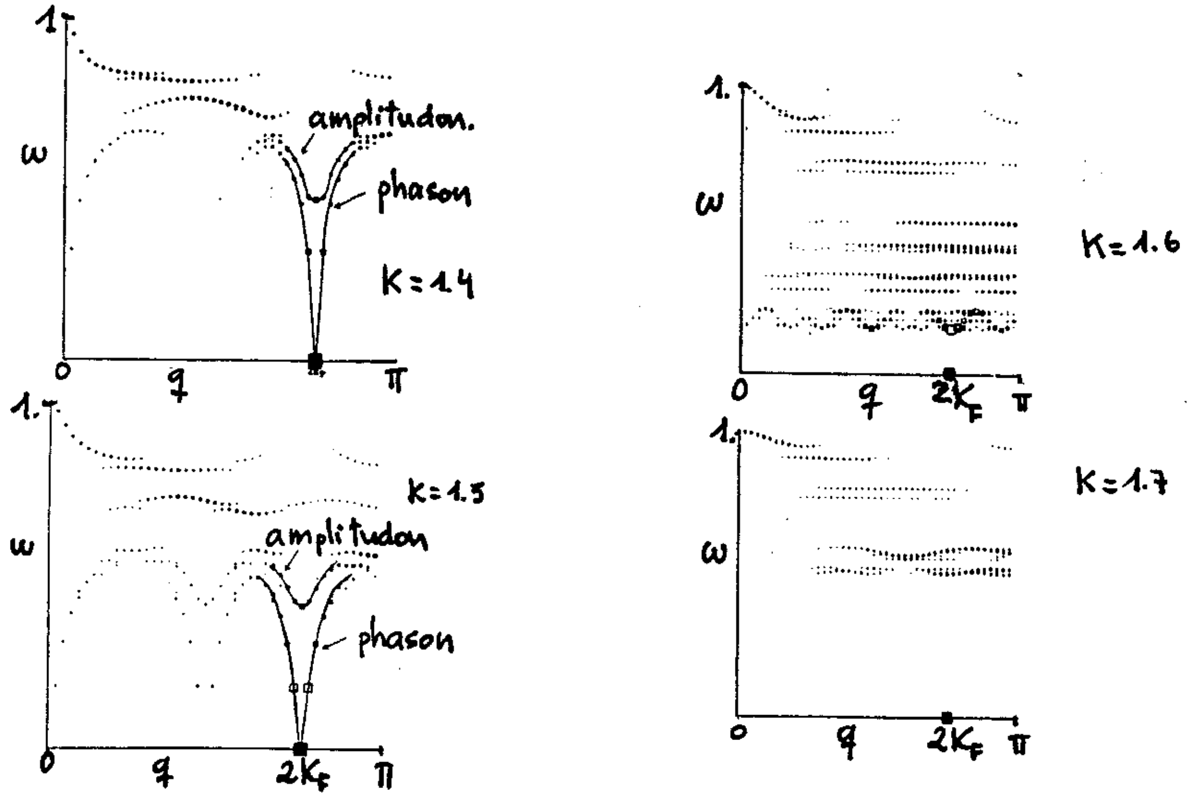

Figure 3.2 Distribution d'intensité du facteur de structure dynamique pour le modèle de Holstein en-sous et au-dessus de la valeur critique k_C. En-desous de k_C l'amplitudon et le phason (sans gap) sont les excitations du l'ODC tandis que au-dessus le pic central domine le spectre (Aubry et al. 1992).

3.3. Les excitations d'ODC dans le composé KCP.

Les propriétés dynamiques du KCP ont été étudiées par diffusion inélastique des neutrons (Renker et al. 1974, Lynn et al. 1975, Carneiro et al 1976, et Comès et al. 1975), diffusion Raman (Steigmeier et al. 1975 et 1976) et réflectivité infra-rouge (Brüesch et al. 1975, et Guilliani et Tosatti 1978). Pour des températures très élevées par rapport à la température de transition de phase (de l'ordre de 100 K dans le composé KCP), la fréquence du mode mou se situe autour de 2THz (8 meV). Le mode mou est présent à toutes températures sur la branche des phonons longitudinales acoustiques le long de la direction c*, mais l'anomalie de Kohn est tellement étroite en q que la fréquence du mode mou, $\omega_0(2k_F)$, n'est déterminée que par interpolation. L'energie de l'amplitudon, mesurée par diffusion Raman, vaut 5.5 meV dans le composé KCP et 4.7 meV dans ce même composé dans lequel H est substitué par D. L'energie de l'amplitudon mesurée par diffusion inélastique des neutrons vaut 6 meV pour KCP. La largeur de raie de l'amplitudon est anormalement grande à haute température et décroît lorsque la température baisse. Kurihara a proposé un modèle qui explique ce phénomène en faisant intervenir un couplage non linéaire entre l'amplitudon et le phason.

L'energie du phason piégé, mesuré par réflectivité infra-rouge, vaut 2 meV. Cette valeur est confirmée par des mesures de diffusion inélastique de neutrons. L'origine de cette valeur unique n'est pas comprise. D'une part, la délocalisation des atomes de brome est à l'origine d'une énergie potentielle suffisante pour piéger l'ODC. D'autre part, $2k_F$, proche d'une valeur commensurable, peut être une source supplémentaire de piégeage (chapitre 1.3.). Une étude plus approfondie de la localisation des atomes de brome et de leur facteur d'occupation révèle que leur énergie potentielle a une composante commensurable avec le paramètre de maille c et une composante commensurable avec le vecteur d'onde $2k_F$. Il est donc probable que la configuration particulière du brome induise un potentiel commensurable et un désordre incommensurable d'ou le gap du phason.

3.4. Les excitations d'ODC dans le composé $K_{0.3}MoO_3$.

Des expériences de diffusion inélastique de neutrons mettent en évidence le ramollissement de l'anomalie de Kohn et la croissance d'un pic central à l'approche, par valeur supérieure, de la température critique (Pouget et al. 1991). Le mode mou, qui se condense à T_P=183K, donne lieu à un amplitudon d'énergie 4.3 meV et un phason piégé d'énergie 0.4 meV. Ces résultats sont en accord avec les résultats de diffusion Raman (pour l'amplitudon) (Pouget et al. 1987) et avec des résultats de réflectivité infra-rouge (pour l'énergie de piégeage des phasons) (Kim et al. 1989). L'évolution en température de la fréquence de l'amplitudon est représentée figure 3.3 (b). La fréquence de piégeage du phason ne varie pas beaucoup. Les vitesses de propagation du phason, le long des directions principales, ont été mesurée récemment (Hennion et al. 1992); les résultats obtenus à $T=T_P$-8K sont les suivants:

$$v_{b*} = 23.2\ 10^3\ \mathrm{m\ s^{-1}}$$
$$v_{2a*+c*} = 10\ 10^3\ \mathrm{m\ s^{-1}}$$
$$v_{2a*-c*} = 2.2\ 10^3\ \mathrm{m\ s^{-1}}$$

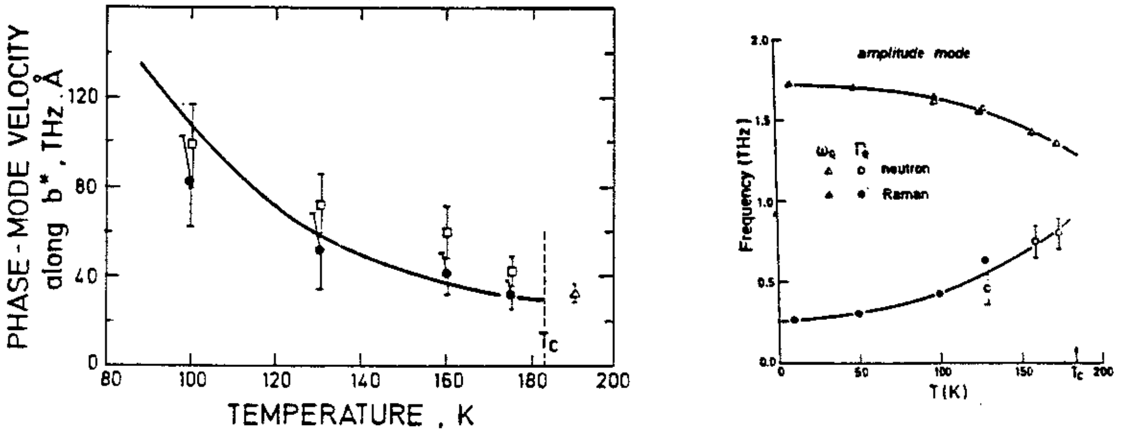

Figure 3.3 Variation de la vitesse du phason (a) et de la fréquence de l'amplitudon (b) avec la température.

L'anisotropie des vitesses de propagation selon les trois directions principales est conforme à l'anisotropie d'autres propriétés physiques du bronze bleu, telles que la conductivité électrique, la longueur de corrélation des fluctuations au-dessus de T_P, la taille des domaines de Lee-Rice mesurée sur des échantillons désordonnés. A 100K, la vitesse de propagation du phason dans la direction des chaînes passe à v_{b*}=51.5 10^3 m s^{-1}, alors que dans les deux autres directions ces vitesses restent constantes (Figure 3.3 (a)). Cette augmentation de la vitesse longitudinale s'explique par la réduction du nombre de porteurs libres; en effet, la réduction du nombre d'électrons atténue l'écrantage de la force de Coulomb impliquée dans la déformation de la phase, dans la direction b. Notons, de plus, que la variation de la vitesse en fonction de la température n'est pas observée dans des composés diélectriques incommensurables tel que $ThBr_4$ (Bernard et al. 1983).

3.5. L'influence du pseudo-gap sur la dynamique de la transition de phase.

Les effets des fluctuations sur la transition de Peierls 1D ont été traités par LRA. Leurs calculs ont mis en évidence que la température de transition passe de T_P^{MF} au quart de cette valeur, pour l'effet des fluctuations. Les fluctuations apparaissent sur le spectre électronique comme un pseudo-gap qui se transforme en un gap ordinaire, en-dessous de la température de transition de Peierls: gap de

Peierls. La diminution de la susceptibilité magnétique à l'approche de T_P a été interprétée de cette façon. Des mesures récentes de réflectivité montrent l'ouverture du pseudo-gap et la contribution des excitations des modes collectifs à la conductivité dans les composés.$(TaSe_4)_2I$ et $K_{0.3}MoO_3$ (Geserich et al. 1986 et Degiorgi et Grüner 1992).

Ces remarques conduisent naturellement à envisager la possibilité d'une séparation entre phason et amplitudon en-dessous de T_P comme une conséquence du régime des fluctuations. Ce travail, entrepris par Tutis et Barisic (1991), montre que dans un système strictement unidimensionnel, le mode mou est sur-amorti ente $0.4T_P^{MF}$ et $0.3T_P^{MF}$, et que la séparation entre phason et amplitudon ne commence qu'en-dessous de $0.3\ T_P^{MF}$ (figure 3.4).

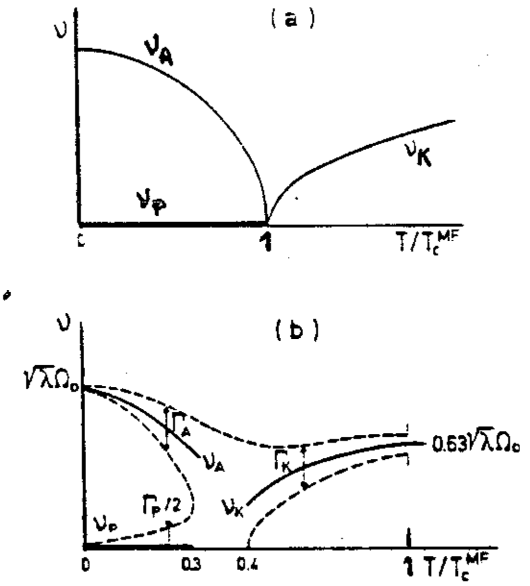

Figure 3.4 (a) Champ moyen résultats pour la variation des fréquences de mode mou (υ_K), amplitudon (υ_A) et phason avec la temperature (υ_P). (b) Résultats du calcul de Tutis et Barisic.avec Γ_i les hauteur à mi-largeur de la fonction réponse $S(2k_F,\upsilon)$.

Dans des systèmes réels, les résultats 1D peuvent être perturbés par des couplages 3D entre chaînes

(a) les faibles couplages entre chaînes conduisent à une transition de phase avec peu de changement dans la dynamique de la transition.

(b) un couplage 3D plus fort diminue l'amplitude des fluctuations (augmentation de la fréquence caractéristique du mode mou) d'où découplage plus important entre les fluctuations du phason et de l'amplitudon de l'ODC. Dans ce cas, la description unidimensionnelle reste qualitativement vraie mais, les températures caractéristiques sont plus élevées que celles obtenues par le modèle strictement 1D.

Le résultat figure 3.5 montre que le découplage entre phason et amplitudon se produit entre 190 et 230K (ce qui correspond à 0.5 T_P^{MF}) pour le composé $K_{0.3}MoO_3$. Ce résultat est consistant avec la mesure de la longueur de corrélation des fluctuations qui met en évidence la présence d'un grand régime de fluctuation quasi-bidimensionnel (Girault, Moudden et Pouget 1989).

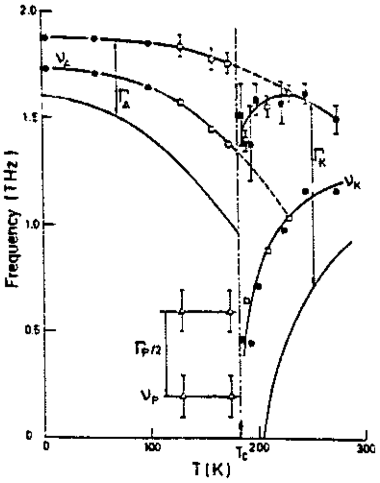

Figure 3.5 Découplage mode mou et, amplitudon et phason (Girault et al. 1991).

4. LE SPECTRE ELECTRO-MAGNETIQUE DU CONDENSAT D'ODC.

De nombreux aspects de l'électrodynamique de l'état condensé à ODC ont été explorés récemment par mesures de transport en fonction de la fréquence sur plusieurs composés types (Grüner 1988). Contrairement aux supraconducteurs dont la réponse est limitée aux fréquences optiques supérieures au gap, pour les systèmes à ODC il existe des excitations collectives dont le spectre s'étend sur l'ensemble des fréquences électromagnétiques. Des expériences sur ces composés ont été menées sur une bande spectrale très large de 10^{-2} Hz à 10^{14} Hz (Donovan et al. 1990 and Degiorgi et al. 1991). La combinaison des résultats expérimentaux obtenus dans les diverses gammes de fréquence est nécessaire à la caractérisation correcte des paramètres associés à chaque type d'excitation. Par souci de simplicité, dans ce qui suit, nous ne discutons que la réponse linéaire du système qui correspond, à basses fréquences, à la conductivité ohmique. A plus hautes fréquences, la réponse électromagnétique linéaire peut être comparée aux spectres obtenus par diffusion inélastique de la lumière et des neutrons. Toutefois, il convient de souligner que l'existence d'une conductivité non-linéaire, liée au dépiégeage de l'ODC (Monceau et al. 1976) au-dessus d'un champ seuil, constitue la véritable signature des systèmes à ODC.

Le spectre électromagnétique est divisé en quatre domaines:

4.1. La conductivité dans le domaine optique: transitions de particules libres et niveau de Fermi.

4.1.1. Le gap électronique de l'ODC.

Le gap électronique de l'ODC peut être estimé à partir des résultats de diverses expériences: conductivité DC, effet Hall, susceptibilité magnétique, absorption infrarouge. Cependant, les divers résultats demeurent ambigus. Le présent chapitre donne quelques détails sur des résultats d'absorption infrarouge dans des composés types : TaS_3 (Herr et al. 1986), $(TaSe_4)_2I$ (Geserich et al. 1986, et Minton et Brill 1987) et $K_{0.3}MoO_3$ (Travaglini et al. 1980).

Les mesures de la fréquence de plasma ($\omega_p^2 = 4\pi e^2 N/m_b$, où N est la concentration de porteurs et m_b leur masse effective) dans les spectres correspondant à la lumière polarisée parallèlement ($e_{\parallel}$) et perpendiculairement ($e_{\perp}$) aux chaînes confirment la forte anisotropie électrique (de 10^4 à 10^5 pour le composé

$K_{0.3}MoO_3$ et de 200 pour $(TaSe_4)_2I$). Ainsi, pour des polarisations parallèles aux chaînes, le matériau se comporte comme un métal, alors que pour des polarisations perpendiculaires aux chaînes, il se comporte comme un semiconducteur.

Au-dessous de la température de transition, et dans la gamme de fréquences allant de l'infrarouge au visible, une large résonance domine la conductivité optique. La fréquence de cette résonance correspond à celle du gap mesuré par conductivité DC.

La figure 4.1 représente les spectres de conductance pour les composés TaS_3 et $(TaSe_4)_2I$. Dans le composé $(TaSe_4)_2I$, le bord d'absorption (qui définit l'énergie du gap) est plus élevé pour le spectre $\mathbf{e}_\perp$ que pour celui de $\mathbf{e}_\parallel$, ce qui est probablement dû au couplage entre les chaînes. Cependant la valeur du gap ainsi obtenue est plus petite que celle obtenue par mesure de resistivité. Les positions des deux seuils et les amplitudes d'absorption sont presque égales pour le deux polarisations dans le composé TaS_3. Cette quasi-isotropie implique que la bande de conduction a un grand moment dipolaire transverse (forte hybridation entre les orbitales d du tantale et les orbitales p du soufre). Ce résultat s'oppose aux résultats des mesures de resistivité.

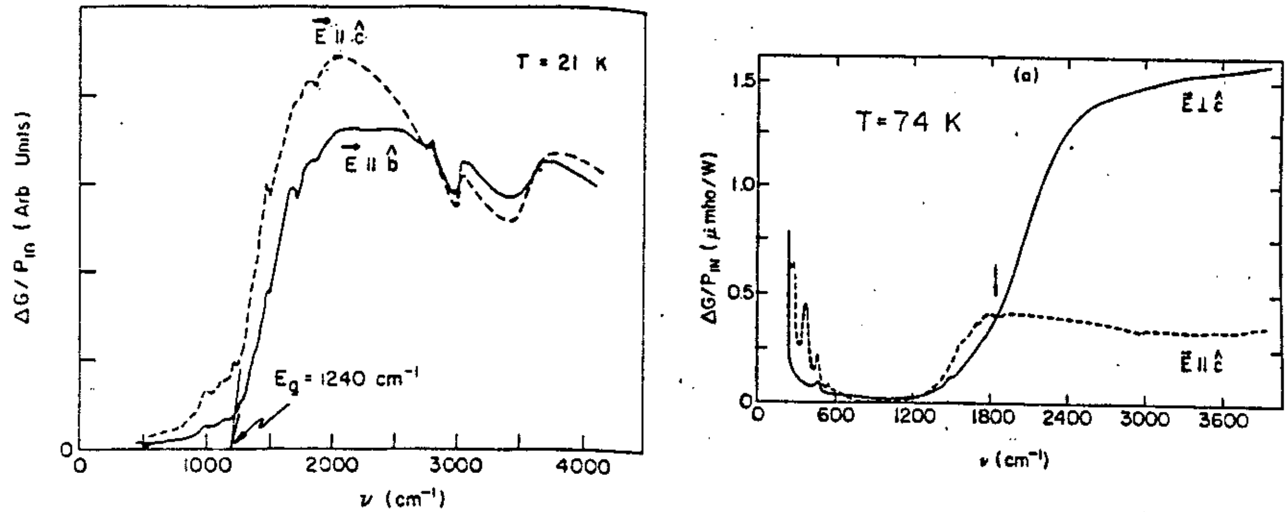

Figure 4.1 Spectres infrarouges de TaS_3 (gauche) et $(TaSe_4)_2I$ (droite). Les flèches indiquent la valeur du gap obtenu par mesures de résistivité (Herr et al. 1986, et Minton et Brill 1987).

4.1.2. Absence de niveau de Fermi dans le spectre de photoémission (Dardel et al. 1991).

Des expérience récentes de photoémission à haute résolution ont montré l'absence du niveau de Fermi, même au-delà de la température critique, dans un domaine où le système est supposé se comporter comme un métal quasi-unidimensionnel (Dardel et al. 1991). Ces résultats s'opposent aux comportements des composés métalliques 2D ($TaSe_2$) et 3D (rhodium, par exemple) d'après la figure 4.2. L'élargissement du spectre au niveau de Fermi provient des effets de température.

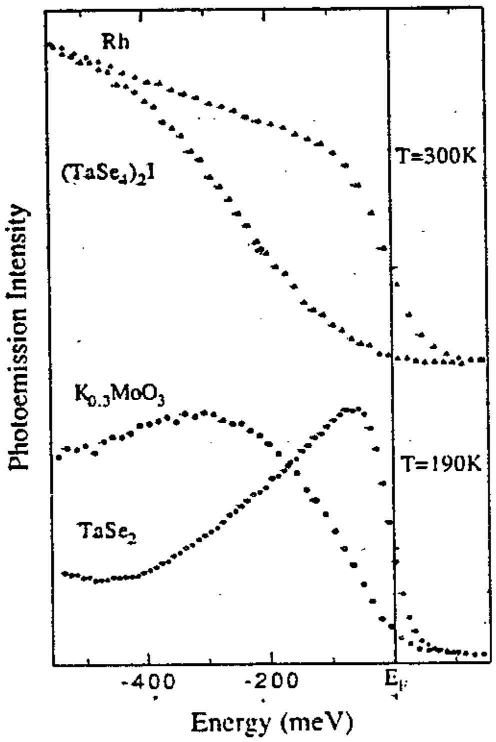

Figure 4.2 Spectres de photoémission dans l'ultraviolet pour les composés $(TaSe_4)_2I$ et $K_{0.3}MoO_3$, pour de températures au-dessus de T_P. Les spectres d'un métal 2D ($TaSe_2$) et 3D (Rh) (mesures aux mêmes températures) sont inclus pour comparaison (Dardel et al. 1991).

Une explication possible de la faible intensité à E_F est la présence d'un pseudo-gap (Lee et al. 1973) dans la phase haute température. Ce pseudo-gap a été observé dans les composés quasi 1D $(TaSe_4)_2I$ et $K_{0.3}MoO_3$ par des mesures de susceptibilité magnétique (Johnston et al. 1984 et 1985) et d'absorption optique dans l'infrarouge (Geserich et al. 1986, et Degiorgi et Grüner 1992). La présence d'un pseudo-gap implique aussi une dépendance en temperature du spectre de photoémission. Cependant, les spectres de photoémission dans le composé $K_{0.3}MoO_3$ à température ambiante (proche de T_P^{MF} pour ce composé) et près de la temperature de transition, ne montrent aucune différence.

Une autre explication consiste à considérer les électrons des systèmes à ODC comme un liquide de Fermi marginal présentant un comportement spéctroscopique particulier. Une telle approche n'a pas encore été envisagée dans le cas d'un système d'électrons unidimensionnels corrélés. La fonction spectrale, $\rho(E_F)$, et la densite d'états au niveau de Fermi, $N(E_F)$ sont reliées par une facteur de renormalisation Z

($\rho(E_F) = Z\,N(E_F)$). Dans les systèmes 3D, les corrélations électroniques modifient la fonction spectrale à l'approche de E_F (cas des fermions lourds, par exemple [Patthey et al. 1990]). Cettes modifications sont plus importantes ($Z \rightarrow 0$) et peuvent induire une forte réduction dans le spectre de photoémission à l'approche du niveau de Fermi.

4.2 Les phonons de phase

Une série d'absorptions dans le spectre obtenu par polarisation du rayonnement infrarouge dans la direction des chaînes, a été observée dans des composés organiques: TTF-TCNQ, TEA$(TCNQ)_2$ (Rice et al. 1975, Rice 1976, et Rice et al., 1977). Ces absorptions correspondent aux vibrations intra-moléculaires des empilements TCNQ. De façon surprenante, les données expérimentales impliquent que ces modes vibrationnels intra-moléculaires, polarisés dans le plan de la molécule, c'est à dire, avec une forte composante perpendiculaire à la direction des chaînes, ont acquis une polarisation parallèle à la direction des chaînes avec une force d'oscillateur anormalement grande. Une explication de ce phénomène a été avancée par Rice. L'ODC est stabilisée dans la maille par l'intermédiaire du couplage entre les électrons de conduction et certaines bandes de phonons. Ce modèle ne spécifie pas la nature précise de ces bandes mais certaines d'entre elles sont associées aux vibrations intra-moléculaires qui induisent une modulation dans la densité locale des électrons de conduction. En plus de la conduction des électrons libres, l'observation de la contribution collective associée aux oscillations de la phase autour de sa position d'équilibre constitue le point clé du modèle. De telles oscillations impliquent un déplacement collectif d'une composante appropriée de la charge condensée d'où l'activité optique des oscillations le long des chaînes. Le modèle de Rice a récemment été appliqué au spectre optique du bronze bleu (Degiorgi et al. 1991) et les résultats concordent avec le spectre observé (Figure 4.3). Néanmoins, ce résultat est à considérer avec précaution: la distinction entre vrais modes polarisés le long des chaînes et phonons de phase n'a pas été faite.

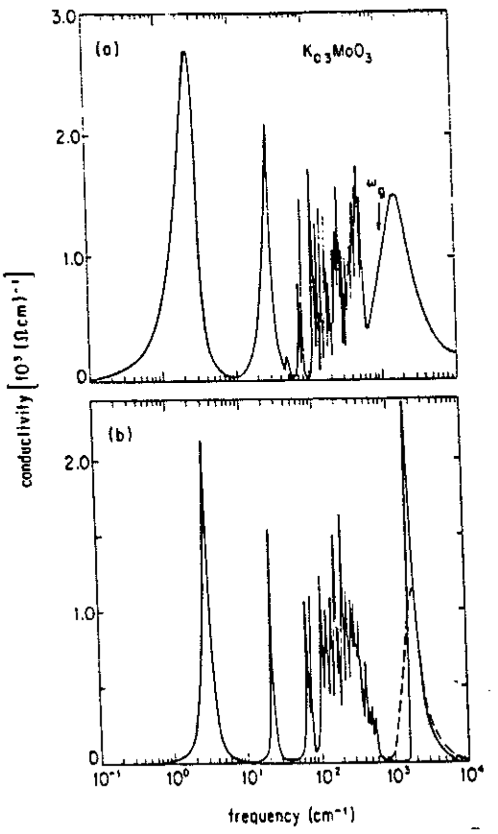

Figure 4.3 Spectre de conductivité optique mesuré (haut) et calculé (bas) par le modèle des phonons de phase de Rice pour le composé $K_{0.3}MoO_3$ (Degiorgi et al.1991). Les deux premiers pics correspondent aux résonances de mode piégé et de mode d'état lié, décrits dans le chapitre 4.3.

4.3. Les résonances dans les gammes de fréquence millimétrique et infrarouge: les résonances de mode piégé et de mode de l'état lié.

Dans cette fenêtre spectrale, deux résonances sont associées au condensat de l'ODC (Degiorgi et Grüner 1991 a et b).

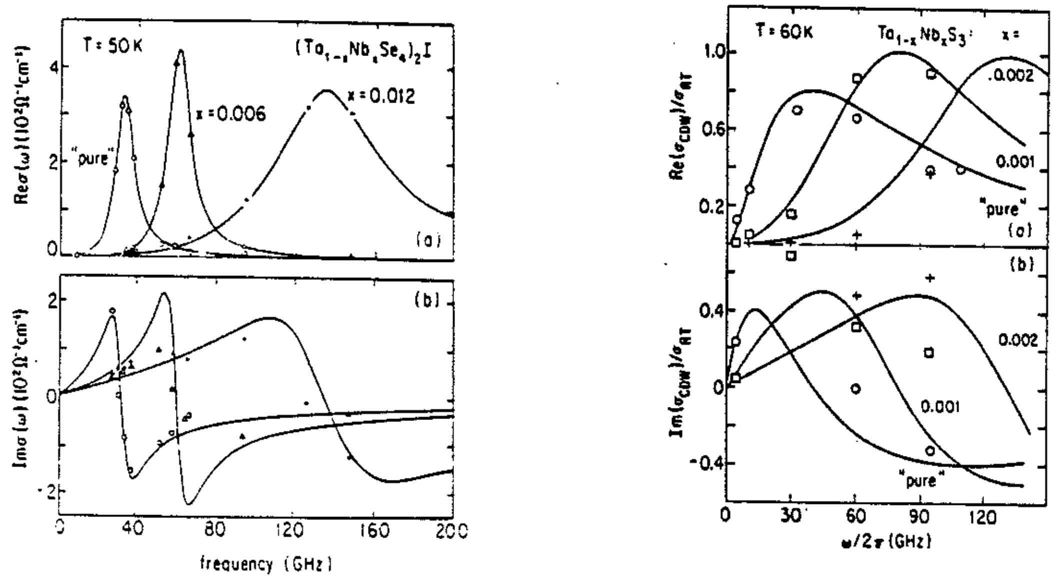

Figure 4.4 A gauche, la dépendance avec la fréquence de Reσ et Imσ pour l'alliage $(Ta_{1-x}Nb_xSe_4)_2I$. La ligne continu répresente le résultat de l'affinement avec un oscillateur harmonique amorti. A droite, le même pour $Ta_{1-x}Nb_xS_3$. (d'après Reagor et Grüner 1989, et Kim et al. 1991)

(a) la fréquence dite de piégeage, déjà mentionnée au chapitre 1.3., apparaît à 1.5 cm^{-1} (45GHz) dans les composés TaS_3 et $(TaSe_4)_2I$ (Figure 4.4) et à 3.33 cm^{-1} (100GHz) dans le bronze bleu. La masse effective associée à cette résonance peut être évaluée à partir de la force de l'oscillateur.

$$\int \sigma_1(\omega)\, d\omega = \frac{\pi}{2}\frac{n e^2}{m^*} \tag{4.1}$$

La masse effective est $m^*/m=300$ pour le bronze bleu et 10^4 pour $(TaSe_4)_2I$, en bon accord avec le résultat de la théorie du champ moyen obtenu à partir de l'équation 3.2. La fréquence caractéristique de cette résonance ne varie que peu avec la température et le temps de de vie de l'excitation augmente lorsque la température décroît. Cependant elle augmente d'un facteur trois lorsque on dope avec 1.2% d'impureté, comme il est montré sur la figure 4.4. L'origine de cette résonance est liée, dans le bronze bleu, à la réponse oscillatoire du mode collectif, tandis que la situation est moins claire dans $(TaSe_4)_2I$: la fréquence correspond à un phonon acoustique de basse énergie (c.f. cette these et Kim et al. 1989).

(b) la seconde résonance est située à une fréquence de 40cm^{-1} dans le bronze bleu, 38 cm^{-1} dans $(TaSe_4)_2I$ et 10 cm^{-1} dans TaS_3. Cette résonance apparaît comme une résonance géante dans le spectre infra-rouge des deux premiers composés, elle est moins visible dans le troisième composé (Fig. 4.5).

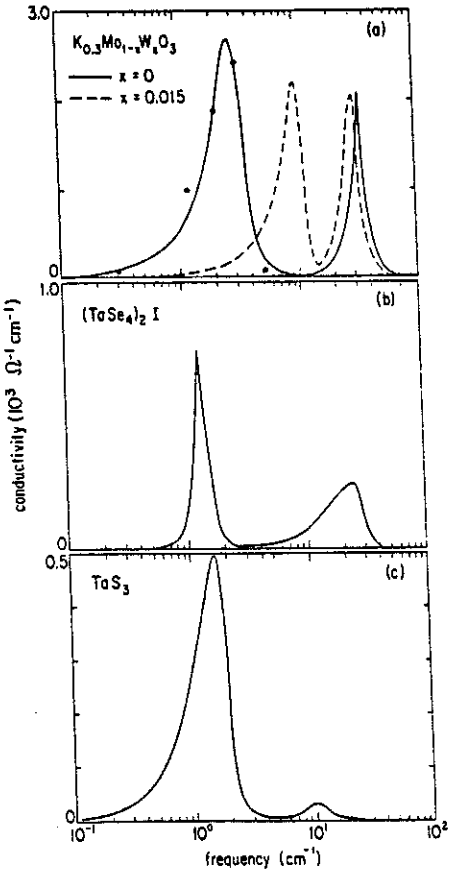

Figure 4.5 Conductivité optique dans la fenêtre spectrale de micro-ondes à infrarouge lointain obtenu à partir de l'analyse de Kramers Kronig. Le premier pic correspond au mode de phase piégé, le deuxième au mode d'état lie.(d'après Degiorgi et Grüner 1991)

L'origine de cette résonance est loin d'être comprise en dépit des travaux expérimentaux et théoriques récents. Par la suite, différentes interprétations sont proposées même si aucune d'entre elles n'explique clairement la résonance.

(1) Une explication possible est de considérer cette résonance comme celle d'un amplitudon. L'amplitudon est actif en diffusion Raman (voi par example Poulet et Pick, 1981) et inactif en réflectivité infra-rouge (Lee et al., 1973). Ceci n'est que partiellement vérifié: dans un système incommensurable à vecteur de modulation multiple, comme le quartz (Vallade et al., 1987), l'amplitudon peut être actif en IR également. Cette affirmation est valable pour $(TaSe_4)_2I$ mais probablement fausse pour le bronze bleu. Les impuretés peuvent conduire à une polarisation finie de la fluctuation de l'amplitudon et activer l'amplitudon dans l'infra-rouge. L'amplitudon a été mesuré à 60 cm^{-1} , fréquence supérieure à celle de

la résonance optique. Des mesures de diffusion Raman montrent que le composé $(TaSe_4)_2I$ a une résonance à 90 cm^{-1} qui pourrait correspondre à l'amplitudon. Cependant, les mesures de diffusion neutronique n'ont pu confirmer ce résultat.

(2) A basse température, l'écrantage par porteurs libres étant inexistant, les effets coulombiens sont importants et la relation de dispersion des phasons présente un gap (Wong et Takada, 1987), analogue au splitting LO-TO dans les systèmes isolants

$$\omega_{LO} = \frac{\sqrt{6}\Delta}{\hbar}\sqrt{\frac{m_b}{m^*}} = \sqrt{\frac{3}{2}}\omega_A \tag{4.2}$$

On obtient ω_{LO}=400 cm^{-1} et 500 cm^{-1} pour le bronze bleu et $(TaSe_4)_2I$, respectivement. Ces valeurs sont approximativement supérieure d'un ordre de grandeur à la fréquence de la résonance observée. Cette différence ne peut s'expliquer par la différence entre m_b et m_e, bien que m_b soit légèrement supérieur à m_e.

(3) Il a été récemment proposé une description de type Clausius Mossotti (Barker, 1973 et Degiorgi et Grüner 1991) de la constante diélectrique qui caractérise la réponse électrodynamique du condensat à ODC. Dans le cadre de cette description, le système est caractérisé par une fonction diélectrique moyenne, ε_m, cette fonction correspond précisément à celle du mode de phase piégé, et des impuretés ou défauts (supposés sphériques de rayon r_s et de concentration N_s) de constante diélectrique ε_s(figure 4.6). La fonction diélectrique effective du système est donnée par:

$$\varepsilon_{eff} = \varepsilon_m + \frac{3\varepsilon_m(\varepsilon_s - \varepsilon_m)f}{\varepsilon_s + 2\varepsilon_m - (\varepsilon_s - \varepsilon_m)f} \tag{4.3}$$

$f = N_s(4\pi/3)r_s^3$ facteur de remplissage sans dimension. Pour f fini, ε_{eff} a deux pôles, l'un correspondant au pôles de ε_m, l'autre étant proche de la fréquence pour laquelle $\varepsilon_s = -2\varepsilon_m$. Ce dernier mode définit une résonance localisée et centrée sur les impuretés.

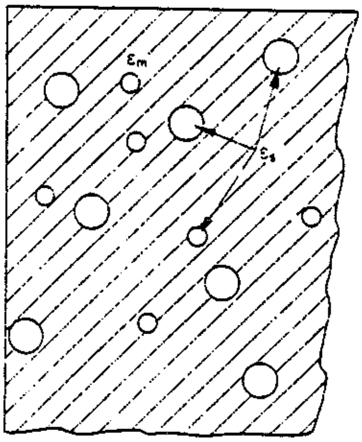

Figure 4.6 Modèle d'un solide de constante diélectrique ε_m et sphères de constante diélectrique ε_s.(Barker 1973)

Comme vu au chapitre 1.3, la fonction diélectrique du mode collectif de l'ODC s'exprime comme un oscillateur harmonique, donné par:

$$\varepsilon_m(\omega) = \varepsilon_\infty + \frac{\omega_{p0}^2}{\omega_0^2 - \omega^2 - i\omega\gamma} \tag{4.4}$$

ω_0: fréquence de résonance, γ: amortissement et ω_{PO}: fréquence de plasma des électrons condensés. Cette équation est similaire à celle de 1.6. à l'exception du terme lié à l'amortissement omis dans l'équation 1.5. par souci de simplicité. Autour de chaque impureté, la fonction diélectrique s'exprime par

$$\varepsilon_s(\omega) = \varepsilon_m(\omega) + \varepsilon_i \tag{4.5}$$

ε_i: constante diélectrique caractéristique du volume entourant l'impureté. La constante diélectrique est supérieure à la constante diélectrique ε_Δ (de l'ordre de grandeur de 100), liée aux transitions de particules libres au travers du gap de Peierls. Les paramètres utilisés dans ce calcul, pour les trois composés, sont indiqués ci-dessous, et la figure 4.7 représente les résultats du calcul.

	ω_0	γ	ω_{p0}	ϵ_∞	ϵ_0	f	$m^*\omega_0^2$
$K_{0.3}MoO_3$	3.33	1.34	600	100	1000	0.2	7 984
$K_{0.3}Mo_{0.985}W_{0.015}O_3$	10.0	1.34	600	300	1000	0.8	72 000
$(TaSe_4)_2I$	2.0	2.0	300	50	190	0.2	12 000
TaS_3	2.0	0.66	189	100	1000	0.05	2 000

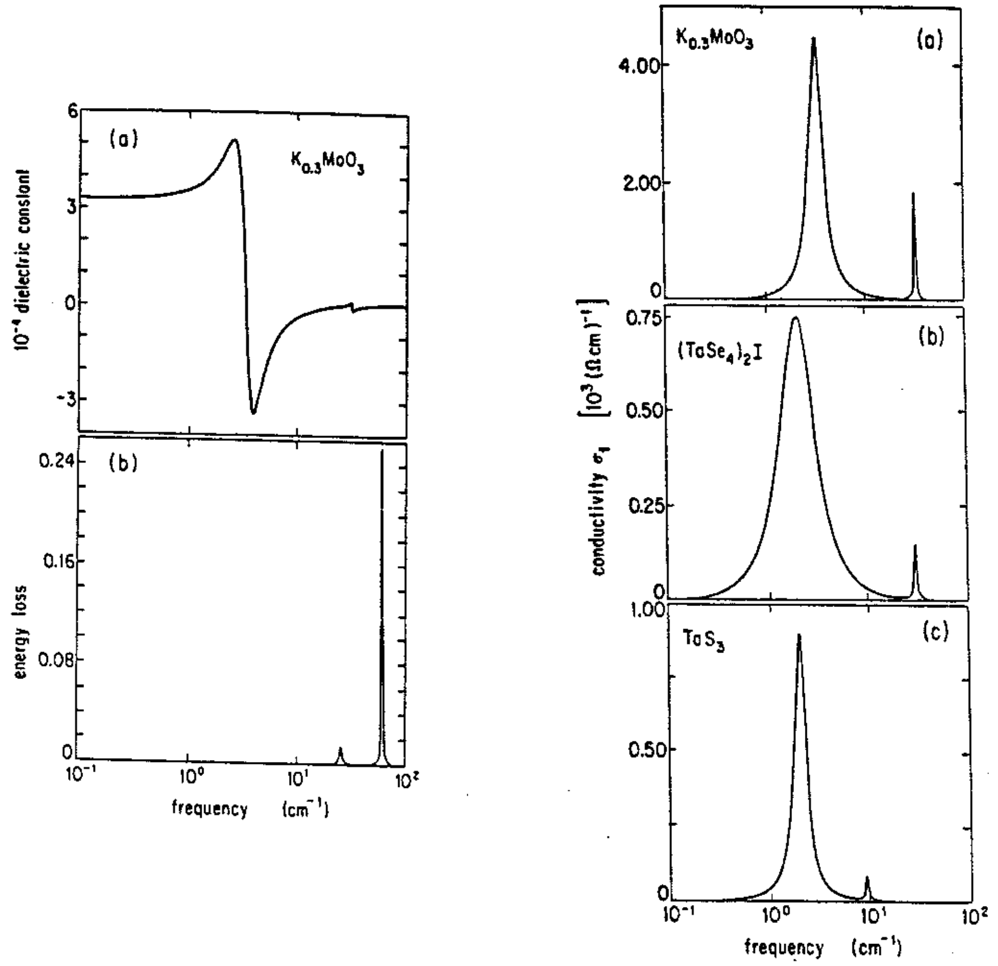

Figure 4.7 Les résultats du calcul du spectre optique à partir des équations (4.3) et (4.4). Gauche, la fonction diélectrique effective (haut), et le spectre de perte d'énergie ($Im(-1/\varepsilon_{eff})$) (bas). Le deux pics correspondent aux zéros de la équation (4.3) (ω_{LO}). A droite, les spectres de conductivité. Les pics correspondent aux pôles de la même équation (ω_{TO}). Ces résultats doivent être comparés aux celles de la figure 4.5 (Degiorgi et Grüner 1991).

Ce modèle simple, purement électrostatique, semble être en bon accord avec la position de la résonance, du moins à basse température où la densité de porteurs libres est très faible. D'àpres la figure 4.7 l'origine de cette resonance 'geante' est le 'splitting' LO-TO du mode de phase piégé. L'évolution en fonction de la température de cette résonance n'est pas claire. Ainsi, les auteurs affirment que la température ne fait qu'élargir la résonance. Cette résonance peut éventuellement disparaître à l'approche, par valeur inférieure, de T_P dû au disparition progressive du 'splitting' LO-TO du mode de phase piégé par l'écrantage des électrons de conduction.

Des résultats de diffusion inélastique de neutrons obtenus sur le composé $(TaSe_4)_2I$ (voir cette thèse) montrent la présence d'un mode à la même fréquence que celle obtenue par infra-rouge. Ce mode est présent à température ambiante et est indépendant de la température dans l'intervalle de 150 à 293K. Ces résultats sont en désaccord avec l'interprétation fournie précédemment et posent la question de l'existence systématique de ce mode dans les systèmes quasi-unidimensionnels (Degiorgi et al. 1991).

4.4. Le régime relaxationnel basse fréquence.

Les mesures à basses températures montrent que la conductivité DC suit une loi d'activation: $\sigma_{DC}(T) = A \exp(-\Delta_0/k_BT)$ où $2\Delta_0$ correspond au gap de Peierls.

Des mesures de conductivité alternative ($\sigma(\omega) = \sigma_1(\omega) + i\sigma_2(\omega)$) montrent une réponse très étalée en fréquence [10^{-2}, 10^9 Hz] (voir Grüner 1988 et references ci-incluses) (figure 4.8, pour le bronze bleu).

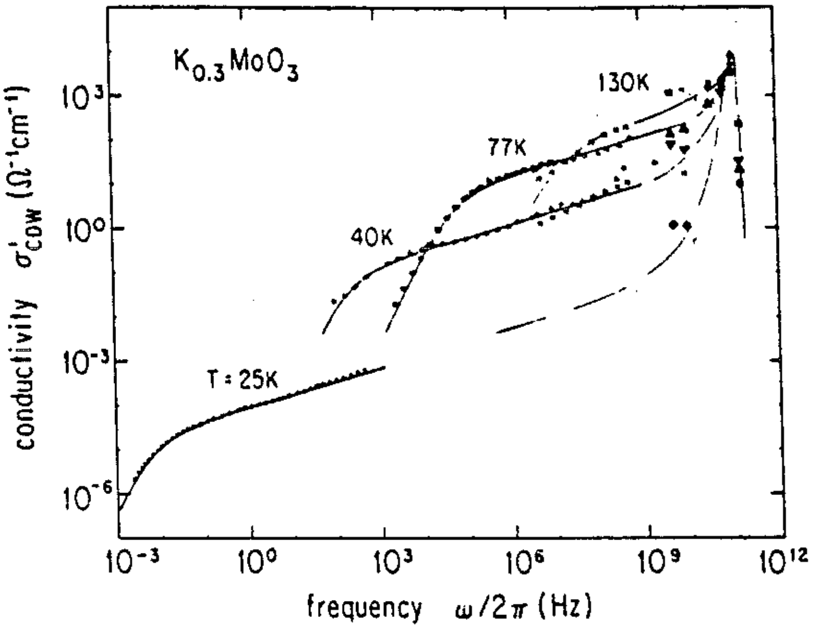

Figure 4.8 La dépendance de la conductivité avec la fréquence pour plusieurs températures dans le composé $K_{0.3}MoO_3$ (Degiorgi et al. 1991). La ligne continue correspond au résultat de l'analyse avec l'équation (4.7).

La relation entre partie réelle de la conductivité, $\sigma_1(\omega)$, et partie imaginaire de la constante diélectrique, $\varepsilon_2(\omega)$, ($\varepsilon_2(\omega)=4\pi\sigma_1(\omega)/\omega$) permet d'utiliser les relations de Kramers-Kronig pour obtenir la constante diélectrique statique:

$$\varepsilon_1(\omega=0) = \frac{2}{\pi}\int \frac{\varepsilon_2(\omega)}{\omega}\,d\omega \tag{4.6}$$

La constante diélectrique statique des composés à ODC est très élevée, typiquement 10^6-10^8. Son comportement en température varie fortement d'un composé à l'autre. Ainsi dans le cas du bronze bleu ε_0 augmente continûment lorsque la température diminue et n'atteint pas de limite aux basses températures. Un comportement opposé est observé dans les composés $(TaSe_4)_2I$ (Cava et al. 1986) et TaS_3 (Cava et al. 1985) où ε_0 augmente lorsque la température augmente.

Les processus relaxationnels qui contribuent à $\varepsilon(\omega)$ aux basses fréquences sont liés à la présence d'un continuum d'états métastables associé aux distributions spatiales de la phase de l'ODC. La plupart des auteurs admettent que le désordre de phase est directement lié au piégeage par les défauts. La description phénoménologique des résultats expérimentaux, basée sur la formule généralisée de Havriliak et Negami, a été proposée par de nombreux auteurs:

$$\varepsilon(\omega) = \varepsilon_\infty + (\varepsilon_0 - \varepsilon_\infty)\frac{1}{\left[1 + (i\omega\tau_0)^{1-\alpha}\right]^\beta} \qquad (4.7)$$

Cette formule représente une distribution formelle du temps de relaxation au voisinage de la valeur moyenne τ_0. α at β caractérisent respectivement la largeur et l'assymétrie de la distribution et ne dépendent que légèrement de la température. Le paramètre α du bronze bleu augmente lorsque la température baisse tandis que la quantité β $(1-\alpha)$ reste constante. La fréquence de relaxation moyenne τ_0 présente également un comportement activé et son énergie d'activation est similaire à celle de la conductivité DC. Dans le cas de $(TaSe_4)_2I$, les deux énergies d'activation sont identiques et dans le composé TaS_3 la loi d'activation n'est suivi que dans une fenêtre de températures très petit (100 à 130K). Le comportement du temps de relaxation en fonction de la température est lié aux effets d'écrantage dus aux électrons excités thermiquement. A très basse température, le processus de relaxation s'allonge et le temps caractéristique de relaxation est obtenu à partir de la variation de la polarisation en fonction du temps, qui suit une loi exponentielle étirée.(Cava et al. 1984, et Kriza et Mihály 1986):

$$P(T) = P_0 \exp\left[-\left[\frac{t}{\tau_n}\right]^{1-n}\right] \qquad (4.8)$$

Une transformée de Fourier appropriée de la dérivée de la polarisation en fonction du temps permet l'obtention de une expression de la constante diélectrique analogue a celle de la formule (4.7) avec l'identification de $\tau_n = \tau_0$, et $1\text{-}n = \beta(1-\alpha)$.

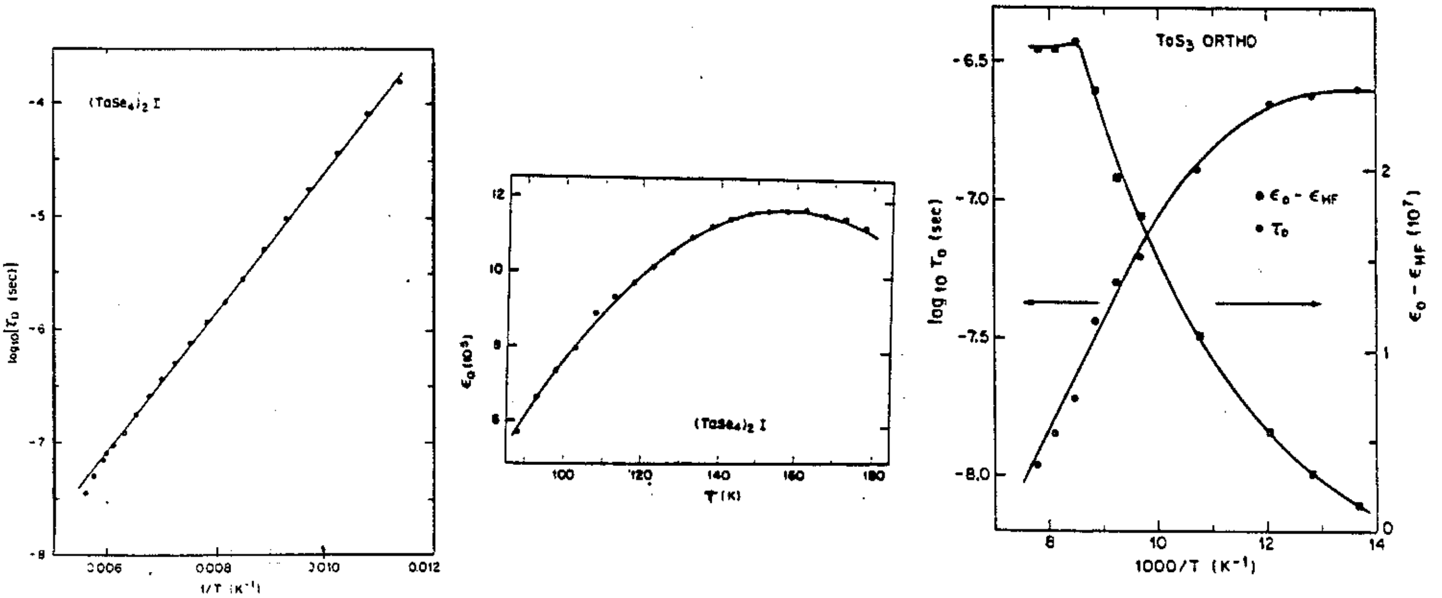

Figure 4.9 De gauche à droite, la dépendance en température du temps de relaxation (τ_0) et de la constante diélectrique statique (ε_0), pour $(TaSe_4)_2I$; les mêmes pour TaS_3 (Cava et al. 1985).

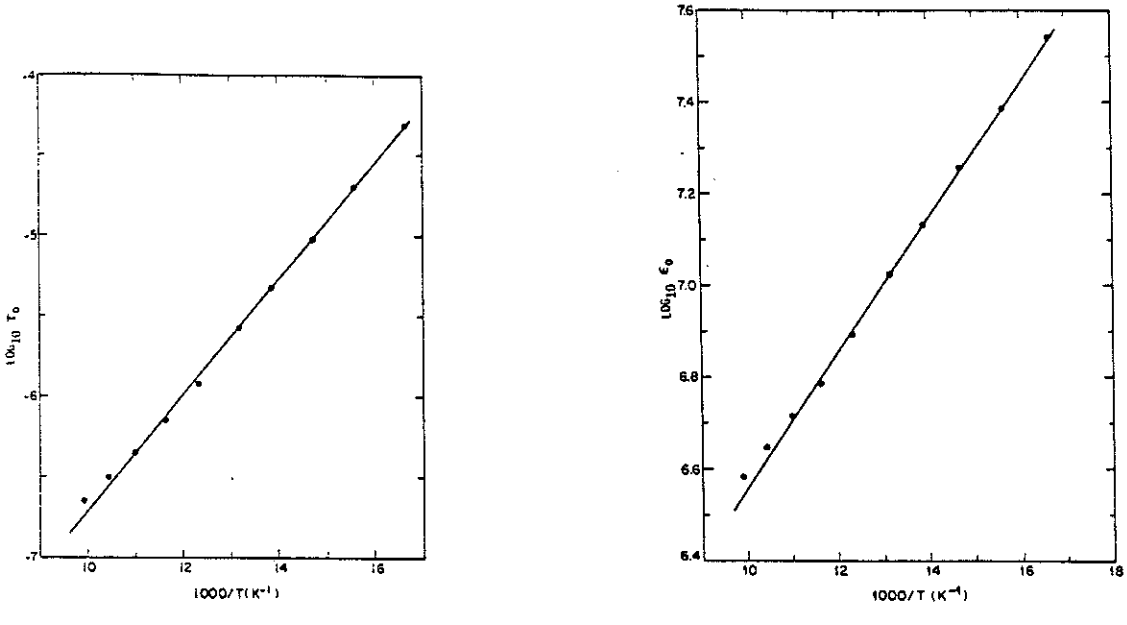

Figure 4.10 De gauche à droite, la dépendance en température du temps de relaxation (τ_0) et de la constante diélectrique statique (ε_0), pour $K_{0.3}MoO_3$ (Cava et al PRB 1984).

4.4.1. Le rôle des impuretés dans le régime basse fréquence.

Dans le cadre de la théorie LRA, le piégeage de l'ODC détermine les différentes propriétés de transport de l'ODC et les distributions des temps de relaxation sont données par la densité d'état de l'ODC piégée. Deux types de piégeage sont distingués:

- dans le cas d'un **piégeage fort**, la phase de l'ODC locale est fonction de la force de piégeage d'une seule impureté.

- dans le cas d'un **piégeage faible**, la phase de l'ODC locale est un compromis entre les phases piégées sur différents sites.

Fort et faible couplages sont présents dans le bronze bleu; ils dépendent du type de dopant (Cava et al. 1984):

(a) La substitution de K par Rb est considérée comme un piégeage faible: la substitution de 50% de K diminue ε_0 (= $\varepsilon_1(\omega=0,T)$) de 1 ordre de grandeur et augmente $1/\tau_0$ de 3 ordres de grandeur. τ_0 suit une loi d'activation; son énergie d'activation est inférieure à celle du composé non dopé. Le produit $\beta(1-\alpha)$ varie avec la température, le maximum étant obtenu à 45K.

(b) La substitution de Mo par W perturbe fortement le système: la substitution de 1% de Mo diminue ε_0 de 3.5 ordres de grandeur et augmente $1/\tau_0$ de 5 ordres de grandeur. De plus, τ_0 ne suit pas une loi d'activation et le produit $\beta(1-\alpha)$ est indépendant de la température.

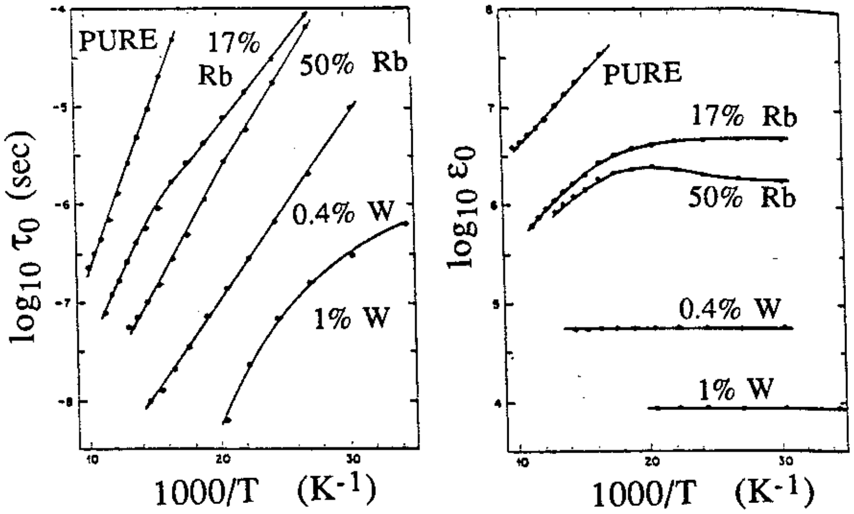

Figure 4.11 De gauche à droite, la dépendance en température du temps de relaxation (τ_0) et de la constante diélectrique statique (ε_0), pour le composés $K_{0.3}MoO_3$ pure et dopé. Les substitutions sont: K pour Rb, et Mo pour W.

4.4.2. La transition de phase vitreuse à basse température ?

La réponse électrique d'un système à ODC peut être comparée à la réponse magnétique d'un système type verre de spin. La partie réelle de la susceptibilité diélectrique en fonction de la température, et pour plusieurs fréquences comprises entre 10^2 et 10^5 Hz, est représentée en figure 4.12 (gauche). Les données près du maximum sont affinées par une fonction gaussienne, la variation du maximum (qui definit une certaine T_F) en fonction de la fréquence est représentée en figure 4.12 (droite). D'après cette figure, il est possible de localiser une changement de regime au voisinage de 55K. Dans le chapitre suivant on poursuivra cette discussion, et les resultats sur la mesure du temps de relaxation de la chaleur specifique semble montrer que un crossover doit exister entre 1K et 55K. D'autres mesures à plus basses températures et fréquences sont nécessaires pour confirmer cette observation.

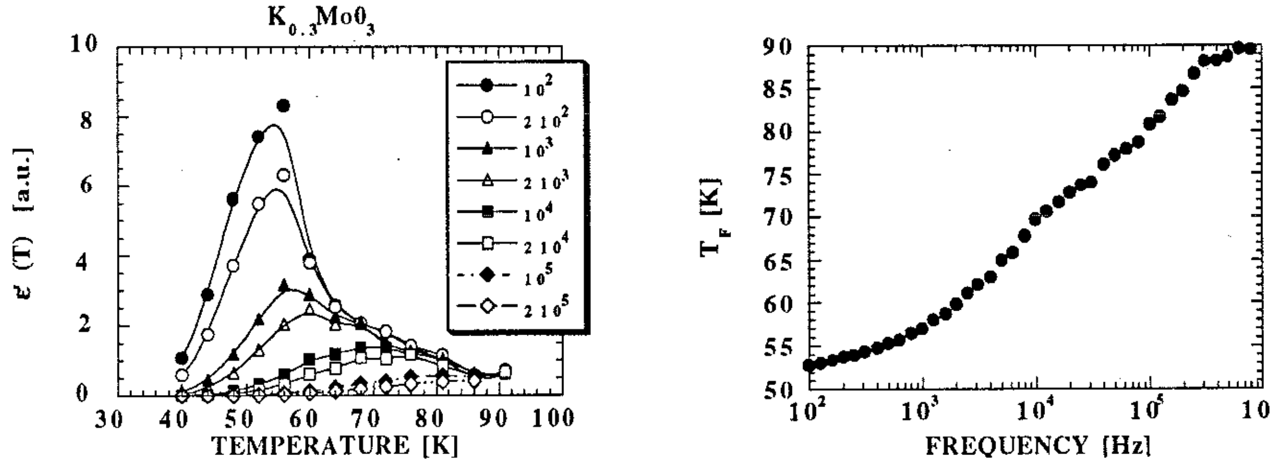

Figure 4.12 A gauche, parti réelle de la constante diélectrique en fonction de la température à plusieurs fréquences. A droite, la variation avec la température du maximum de ε'(T) en fonction de la fréquence (adaptée par J.E. Lorenzo à partir de donnés de Cava et al. 1985).

Des expériences sur des composés dopés à ODC semblent apporter la preuve du rôle joué par les impuretés dans la dynamique de l'ODC à basse fréquence. Cependant, une analyse détaillée des données, et gardant à l'esprit les idées de Ngai (1984), montre que les paramètres principaux qui caractérisent le phénomène de relaxation diffèrent selon que le composé soit dopé ou non. Ngai a établi une classification des verres selon la variation en fonction de la température des deux paramètres suivants: n et τ_0.

(a) Type A: à l'approche de la température de transition vitreuse, n augmente et τ_0 s'écarte de la loi d'activation pour augmenter plus rapidement.

(b) Type B: n est constant et τ_0 suit une loi d'Arrhénius.

(c) Type C: n est pratiquement indépendant de la température et τ_0 ne suit pas une loi d'activation.

A partir de cette classification, il est possible de déduire que le bronze bleu pur appartient au type B, le bronze bleu dopé par W au type C; le bronze bleu dopé par Rb a un comportement opposé aux tendances du type A. Comme chacun de ces composés appartient à un type différent d'état vitreux, il est difficile de conclure que les états métastables dans des systèmes à ODC ne soient liés qu'au piégeage de l'ODC par des impuretés (cf composé non dopé).

La possibilité de ce que les états métastables soient des propriétés intrinsèques de l'ODC des composés non dopés n'est pas exclue. Le piégeage de l'ODC par le réseau permet l'existence de domaines de phase qui sont métastables. Dans chaque domaine, l'ODC a une phase constante mais différente de celle des domaines voisines. Dans le cadre de cette description la situation est très semblable a celle des ferroélectriques. Cependant, et lié à l'incommensurabilité de l'ODC, la différence de phase entre deux domaines adjacents peut prendre un continiuum de valeurs entre $[0,2\pi]$.

4.4.3 Les relaxations à basse temperature dans les expériences de chaleur specifique

Des mesures de chaleur spécifique, au-dessous de 2K, ont montré que les composés quasi unidimensionnels présentent un excès de capacité calorifique qui suit une loi en T^α, l'amplitude de cette capacité calorifique étant comparable à celle des matériaux désordonnés (Figure 4.13). L'exposant α, étant inférieur à 1, varie d'un composé à l'autre. Des expériences menées sur des échantillons $(TaSe_4)_2I$ ont montré que l'amplitude de ces excitations de basse énergie dépend de l'échantillon considéré, et aucun lien avec la pureté des échantillons n'a pu être établi.

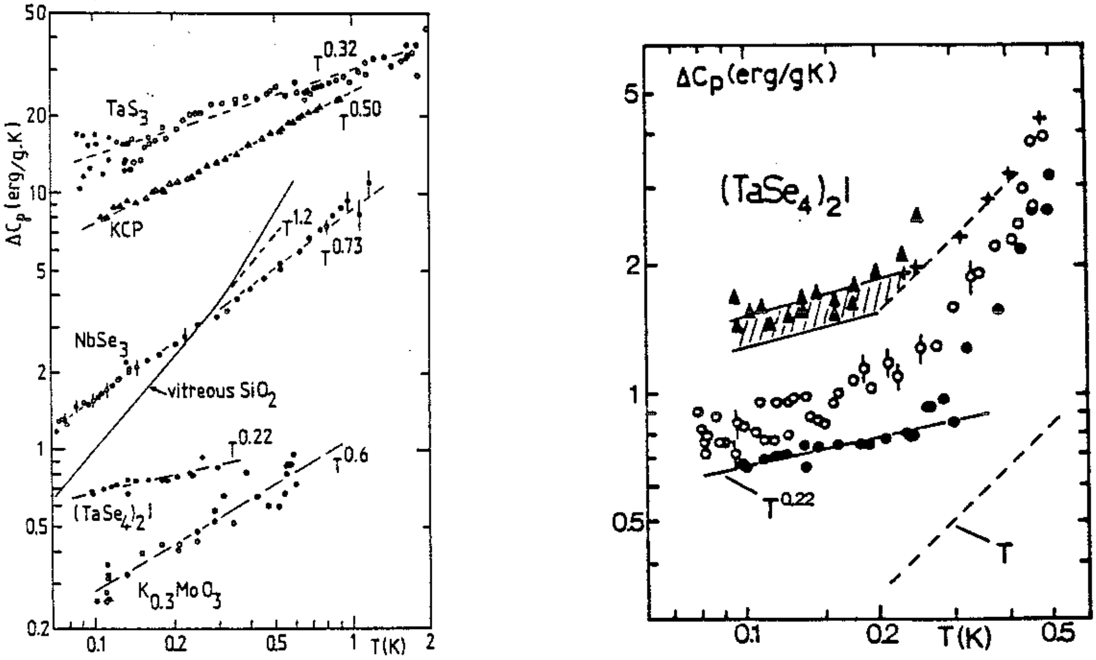

Figure 4.13 A gauche, contribution résiduelle à la chaleur spécifique après la soustraction de la contribution dû aux phonons (Lasjaunias et al. 1990). A droite, la même contribution résiduelle pour $(TaSe_4)_2I$ pour différents échantillons (Biljakovic et al. 1989).

Malgré les similitudes de ces excitations avec celles des verres classiques, comme la silice, ces excitations de basse énergie sont caractérisées par des relaxations non-exponentielles, semblables à celles des verres de spin et des polymères. Pour ces derniers systèmes, les théories prédisent une divergence du temps de relaxation à l'approche de la température de transition par valeur supérieure; cette divergence suit une loi identique à celle d'une certaine longueur de corrélation ξ

$$\tau/\tau_0 \approx (1 - T_C/T)^{-z\nu} = \xi^\nu$$

où ν est l'exposant critique pour la longueur de corrélation et z l'exposant critique dynamique. Les données expérimentales peuvent être affinées par cette expression, T_C étant de l'ordre de 10mK et zν de l'ordre de 30, selon le composé considéré. De même, une loi d'Arrhenius permet d'obtenir des affinements valables, avec une énergie d'activation proche de 1K (c.f. figure 4.14). Castaing et Souletie (1991) ont montré récemment que la loi d'Arrhenius correspond à la limite pour laquelle la température critique tend vers zéro, soulignant ainsi la validité des deux descriptions précédentes. Expérimentalement, il a été montré que certains verres de spin 2D présentent une température critique proche de 0K.

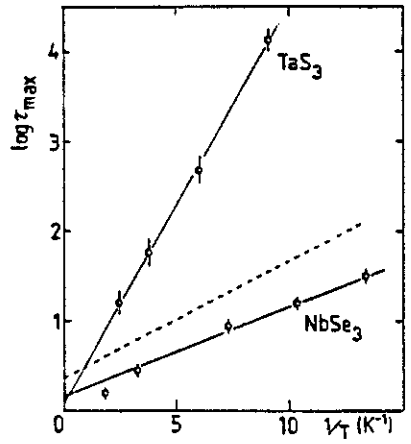

Figure 4.14 La variation du logarithme du temps de relaxation en fonction de l'inverse de la température dans TaS_3 et $NbSe_3$.(d'après Biljakovic et al. 1991)

Biljakovic et al. (1991) ont proposé une explication quant à l'origine de ces relaxations. Au chapitre 4.4, il a été établi que la constante diélectrique statique augmente lorsque la température diminue, le système devenant de plus en plus polarisable. La neutralité électrique est preservée par la conversion de porteurs libres en charges liées, ce qui explique que le temps caractéristique de relaxation de la contante diélectrique suit une loi d'activation en température semblable à celle de la résistivité. Cependant, lorsque ce mécanisme est épuisé à basse température, la neutralité de charge doit être assurée par une autre moyen. D'après Biljakovic et al.(1991), les défauts, les glissements de la phase de l'ODC unidimensionnelle, les dislocations sont à l'origine de ces relaxations à très basse température.

Un excès de chaleur spécifique, analogue à celui observé dans des composés à ODC, fut observé dans les composés ferroélectriques (Lawless 1976). Les systèmes ferroélectriques sont caractérisés par une forte polarisabilité. Contrairement aux systèmes à ODC, dans lesquels l'absence de limite supérieure de la phase implique la présence d'un continuum des polarisations, la polarisation dans un ferroélectrique ne peut prendre que deux valeurs discrètes. Plusieurs explications ont été proposées pour rendre compte de ces effets dans ces composés ferroélectriques: oscillations quantiques des parois de domaines (Lawless 1976 et 1978), présence d'ondes dipolaires (Gonzalo 1978) ou défauts chargés (Kirkpatrick et Varma 1978). Des mesures récentes sur des échantillons très purs n'ont indiqué aucune contribution anormale à la chaleur spécifique (Villar et. al. 1986). Ce résultat permet de conclure que les défauts jouent un rôle important dans la dynamique à basse température. En effet, d'après les calculs de Kirkpatrick et Varma, une concentration de 1 ppm d'impuretés chargées suffit à expliquer l'anomalie de la chaleur spécifique dans les ferroélectriques à basse température. Il est donc très probable que cette interprétation, issue des ferroélectriques, puisse être étendue de façon naturelle aux systèmes à ODC, en accord avec celle proposée par Biljakovic et al.

REFERENCES

S. Aubry et P. Quemerais, in "Low Dimensional Electronic Properties of the Molybdenum Bronzes and Oxides", pag. 295-405, Ed. C. Schlenker, Kluwer Academic Press (1989), et références ci-incluses.

S. Aubry, G. Abramovici et J.L. Raimbault, J. Stat. Phys 67, 675 (1992), et références ci-incluses.

J. Bardeen, L.N. Cooper et J.R. Schrieffer, Phys. Rev. 108, 1175 (1957).

A.S. Barker, Jr., Phys. Rev. B7, 2507 (1973).

L. Bernard, R. Currat, P. Delamoye, C.M.E. Zeyen, S. Hubert et R. de Kouchkovsky, J. Phys. C 16, 433 (1983).

K. Biljakovic, J.C. Lasjaunias et P. Monceau, Synt. Metals 29 (1989) F289-286.

K. Biljakovic, J.C. Lasjaunias, P. Monceau et F. Levy, Phys. Rev. Lett. 67, 1902 (1991).

P. Brüesch, S. Strässler et H.R. Zeller, Phys. Rev. B 12, 219 (1975)

K. Carneiro, G. Shirane, S.A. Werner et S. Kaiser, Phys. Rev. B13, 4258 (1976).

K. Carneiro, in "Electronic Properties of Inorganic Quasi-One-Dimensional Materials", pag. 1-68, Ed. P. Monceau, D. Reidel Publishing Company (1985), et références ci-incluses.

B. Castaing et J. Souletie, J. Phys. I 1, 403 (1991).

R.J. Cava, R.M. Fleming, E.A. Rietman, R.G. Dunn et L.F. Schneemeyer, Phys. Rev. Lett. 53, 1677 (1984).

R.J. Cava, R.M. Fleming, E.A. Rietman, L.F. Schneemeyer et R.G. Dunn, Phys. Rev. B 30, 3228 (1984).

R.J. Cava, R.M. Fleming, R.G. Dunn et E.A. Rietman, Phys. Rev. B 31, 8325 (1985).

R.J. Cava, L.F. Schneemeyer, R.M. Fleming, E.A. Rietman, et R.G. Dunn, Phys. Rev. B 32, 4088 (1985).

R.J. Cava, P. Littlewood, R.M. Fleming, P.B. Littlewood et E.A. Rietman, Phys. Rev. B 33, 2439 (1986).

R. Comès, B. Renker, L. Pintschovius, R. Currat, W. Gläser et G. Scheiber, Phys. Stat. Sol. (b) 71, 171 (1975).

R. Currat et T. Janssen, Solid Sate Phys. 41, 201 (1988).

B. Dardel, D. Malterre, M. Grioni, P. Weibel, Y. Baer et F. Levy, Phys. Rev. Lett. 67, 3144 (1991).

L. Degiorgi, B. Alavi, G. Mihály et G. Grüner, Phys. Rev. B 44, 7808 (1991).

L. Degiorgi et G. Grüner, Phys. Rev. B 44, 7820 (1991).

L. Degiorgi et G. Grüner, J. Phys. I France 2, 523 (1992).

F. Devreux, J. Phys. (France) 43, 1489 (1982).

H. Fröhlich, Proc. R. Soc. A 223, 296 (1954).

H. Kukuyama et P.A. Lee, Phys. Rev. B17, 535 (1978).

H.P. Geserich, G. Scheiber, M. Dürrler, F. Lévy et P. Monceau, Physica B143, 198 (1986).

S. Girault, A.H. Moudden et J.P. Pouget, Phys. Rev. B39, 4430 (1989).

J.A. Gonzalo, Ferroelectrics 20, 159 (1978).

G. Grüner, Rev. Mod. Phys. 60, 1129 (1988).

G. Guilliani et E. Tosatti, Il Nuovo Cimento 47B, 135 (1978).

S. Havriliak et S. Negami, J. Polym. Sci. C 14, 99 (1966).

B. Hennion, J.P. Pouget et M. Sato, Phys. Rev. Lett. 68, 2374 (1992).

S.L. Herr, G. Minton et J.W. Brill, Phys. Rev. B33, 8851 (1986).

D.C. Johnston, Phys. Rev Lett. 52, 2049 (1984).

D.C. Johnston, M. Maky et G. Grüner, Solid State Commun. 53, 5 (1985)

T.W. Kim, D. Reagor, G. Grüner, K. Maki et A. Virosztek, Phys. Rev. B 40, 5372 (1989).

T.W. Kim, S. Donovan, G. Grüner et A. Philipp, Phys. Rev. B43, 6315 (1991).

S. Kirkpatrick et C.M. Varma, Solid State Commun. 25, 821 (1978).

W. Kohn, Phys. Rev. Lett. 2, 393 (1959).

G. Kriza et G. Mihály, Phys. Rev. Lett. 56, 2529 (1986).

S. Kurihara, J. Phys. Soc. Japan 48, 1821 (1980).

J.C. Lasjaunias, K. Biljakovic et P. Monceau, Physica B165&166 (1990) 893.

W.N. Lawless, Phys. Rev. B14, 134 (1976).

W.N. Lawless, Phys. Rev. Lett. 36, 478 (1976).

W.N. Lawless, Phys. Rev. B17, 1458 (1978).

P.A. Lee, T.M. Rice et P.W. Anderson, Phys. Rev. Lett. 31, 462 (1973).

P.A. Lee, T.M. Rice et P.W. Anderson, Solid State Commun. 14, 703 (1974).
J.W. Lynn, M. Iizumi, G. Shirane, S.A. Werner et R.B. Saillant, Phys. Rev. B12, 1154 (1975)
P. Monceau, L. Bernard, R. Currat, F.Levy et J. Rouxel, Physica 136B, 352 (1986).
A.H. Moudden, S. Girault, J.P. Pouget, P. Monceau et F. Levy, (to be published).
G. Minton et J.W. Brill, Phys. Rev. B36, 4254 (1987).
K.L. Ngai, A.K. Rajagopal et C.Y. Huang, J. Appl. Phys. 55, 1714 (1984).
F. Patthey, J.M. Imer, W.D. Schneider, H. Beck, Y. Baer et B. Delley, Phys. Rev. B42, 8864 (1990).
R.E. Peierls, Quantum Theory of Solids, p. 108, Oxford Univer. Press (1955).
J.P. Pouget, S. Kagoshima, C. Schlenker et J. Marcus, J. Phys. (Paris) Lett 44, L113 (1983).
J.P. Pouget, B. Hennion, C. Escribe-Filippini et M. Sato, Phys. Rev. B43, 8421 (1991).
H. Poulet et R.M. Pick, J. Phys. C 11, 4827 (1978).
D. Reagor and G. Grüner, Phys. Rev B39, 7626 (1989).
B. Renker, L. Pintschovious, W. Glaiser, H. Rietschel, R. Comès, L. Liebert et W. Drexel, Phys. Rev. Lett. 32, 836 (1974).
M.J. Rice, C.B. Duke et N.O. Lipari, Solid State Commun. 17, 1089 (1975).
M.J. Rice, Phys. Rev. Lett. 37, 36 (1976).
M.J. Rice, L. Pietronero et P. Brüesch, Solid State Commun. 21, 757 (1977).
J.H. Ross Jr, Z. Wang et C.P. Slichter, Phys. Rev. Lett. 56, 663 (1986).
G. Shirane, S.M. Shapiro, R. Comès, A.F. Garito et A.J. Heeger, Phys. Rev. B14, 2325 (1976).
E.F. Steigmeyer, R. Loudon, G. Harbeke, H. Auderset et G. Scheiber, Solid State Commun. 17, 1447 (1975).
E.F. Steigmeyer, D. Baeriswyl, G. Harbeke, H. Auderset et G. Scheiber, Solid State Commun. 20, 661 (1976).
G. Travaglini, P. Wachter, J. Marcus et C. Schlenker, J. Phys. Soc. Japan 49 (1980) Suppl. A 869.
E. Tutis et S. Barisic, Phys. Rev. B43, 8431 (1991).
M. Vallade, V. Dvorak et J. Lajzerowicz, J. Phys. (Paris) 48, 1171 (1987).
R. Villar, E. Gmelin et H. Grimm, Ferroelectrics 69, 165 (1986).
M.H. Whangbo et R. Hoffmann, J. Amer. Cem. Soc., 6093 (1978).
M.H. Whangbo et P. Gressier, Inorg. Chem. 23, 1305 (1984).
M.H. Whangbo et L.F. Schneemeyer, Inorg. Chem. 25, 2424 (1986).

CHAPITRE II

Neutron investigation of optic phonon branches in the quasi-one dimensional compound $(TaSe_4)_2I$

J.E. Lorenzo and R. Currat
Institut Laue-Langevin, 38042 Grenoble-Cedex, France.

P. Monceau
Centre de Recherches sur les Très Basses Températures. CNRS,
38042 Grenoble-Cedex, France.

B. Hennion
Laboratoire Léon Brillouin, Centre d'Etudes de Saclay,
91191 Gif-sur-Yvette-Cedex, France

F. Levy
Institut de Physique Appliquée, Ecole Polytechnique Fédérale de
Lausanne, CH-1015, Lausanne, Switzerland.

Abstract

Inelastic neutron scattering measurements on the quasi-one dimensional compound $(TaSe_4)_2I$ show evidence of an optic branch with a zone-center frequency of 1.1 THz (36 cm^{-1}). Its relationship to the 'giant' resonance observed in infrared reflectivity spectra is discussed. In the present work, the mode is seen at room temperature, i.e. above the Peierls transition, as well as in the CDW-state. This finding does not seem consistent with the suggested assignment of the infrared peak as a bound CDW collective mode. In the context of the coupled-mode phase-transition mechanism proposed by Sugai et al. we have searched for optic modes with same polarisation as the unstable TA-branch. The lowest such frequency is found at 1.45 THz (48 cm^{-1}) at the Γ-point, in contrast to previous theoretical estimates (90-170 cm^{-1}).

I. INTRODUCTION

The excitation spectrum of quasi-one dimensional charge-density-wave (CDW) systems is the object of intensive studies[1-4]. Its experimental characterization is an essential step toward understanding the CDW dynamics such as the pinning effects[5], Coulomb screening of the CDW deformation[6,7], the nature of the dynamical effects associated with the Peierls transition[8,9].

Three classes of inorganic compounds have been recently investigated: the molybdenum bronzes ($K_{0.3}MoO_3$, $Rb_{0.3}MoO_3$ and tungsten-doped alloys), the transition-metal trichalcogenide TaS_3 and two tetrachalcogenides $(TaSe_4)_2I$ and $(NbSe_4)_2I$. Information on the dynamics of these compounds is available from Raman scattering[10,11], inelastic neutron scattering[7,8,12-14], optical reflectivity[15-19] and micro- and millimeter wave[20-24] conductivity measurements.

In spite of their very different crystal structures, the three classes of compounds appear to show similarities with respect to optical conductivity. In particular, at low temperature, the response $\sigma(\omega)$ includes two sharp oscillator-type resonances. In view of current interpretations of these resonances as "generic" CDW-condensate excitations[1-3], it is of considerable interest to correlate the $\sigma(\omega)$ results with those obtained by other techniques.

We shall attempt to do so here for the compound $(TaSe_4)_2I$. In Sect. IV below, we present a set of inelastic neutron scattering results on a low-lying optic branch. In Sect.V we discuss the significance of our result in the context of the available $\sigma(\omega)$ data. In Sect. VI we present additional optic mode measurements and we comment on the applicability to the case of $(TaSe_4)_2I$, of "zone-folding" schemes[25], sometimes used in the interpretation of optical spectra[11,17].

II. OPTICAL CONDUCTIVITY: SUMMARY OF RESULTS

For the three classes of compounds mentioned above, the analysis of optical reflectivity data together with conductivity measurements over a broad frequency range, reveal the following common spectral features:

(1) a relaxational contribution with a broad temperature-dependent frequency distribution in the MHz range. This component is ascribed to the spontaneous relaxation of metastable CDW-configurations, as produced, for instance, by domain-wall motions, in a Fukuyama-Lee-Rice-type approach[21,26,27].

(2) an oscillator contribution in the 10-100 GHz range associated with the pinned collective oscillation of the CDW-condensate. The resonance frequency, ω_0 , is found to increase sharply with dopant concentration in Nb-doped $(TaSe_4)_2I$ (ref. 5) and W-doped $K_{0.3}MoO_3$ (ref. 2), as expected for a pinning frequency.

(3) contributions from infrared-active lattice modes in the 1-10 THz range. In both $K_{0.3}MoO_3$ (ref. 2) and $(TaSe_4)_2I$ (ref.17), the lowest such frequency, ω_1 , has an unusually large oscillator strength, comparable to that of the pinned phason. For this reason the authors in refs. 1-3 have interpreted the ω_1-mode as a new "generic" CDW-excitation. By analogy with the theory of lattice modes in doped semiconductors, they refer to the ω_1-mode as a "bound" collective mode arising from the presence of polarizable impurities. This interpretation is questioned by Creager et al.[19], who point out that in TaS_3 all lattice modes, apart from the pinned phason, have normal oscillator strengths.

(4) a high frequency peak corresponding to single-particle excitations across the Peierls gap[2,19].

III. $(TaSe_4)_2I$: STRUCTURAL ASPECTS

In the metallic state ($T > T_P = 263$ K), the structure of $(TaSe_4)_2I$ consists of an array of identical $(TaSe_4)_n$-chains parallel to the fourfold c-axis and separated by iodine strands[27]. The crystallographic unit cell is body-centered tetragonal (a = 9.531 Å, c = 12.824 Å; space group I422) and includes two chains with four tantalum ions on each chain. The long repeat unit along c is due to the rotating pattern of Se_4 arrangements along the chains. Note that although consecutive Ta-sites are not symmetry-related the nearest-neighbour Ta-Ta distance d is uniform (c = 4d), above T_P.

Below T_P, satellite reflections are observed at positions $\mathbf{G}_{hkl} + \{\mathbf{q}_s\}$[28,29], which are very near the main Bragg spots at $\mathbf{G}_{hkl}$:

$$\mathbf{G}_{hkl} = h\mathbf{a}^* + k\mathbf{b}^* + l\mathbf{c}^* \qquad ; (h + k + l = \text{even}) \tag{1a}$$

$$\{\mathbf{q}_s\} = \pm 0.05\mathbf{a}^* \pm 0.05\mathbf{b}^* \pm 0.085\mathbf{c}^* \tag{1b}$$

The satellite extinction rules[30] indicate that the ionic displacements associated with the phase transition are predominantly transverse to the CDW-wavevector and restricted to the basal plane.

Some care must be exercised in working out the relationship between the observed CDW-wavevector and the Fermi wavevector of the conduction electrons. The band involved in the Peierls instability originates from the metallic d_{z^2}-orbitals[25]. With $1/2e^-$ per Ta, the band is approximately 1/4-filled and thus $k_F \approx \pi/4d$ and $2k_F \approx 2\pi/4d = c^*$. In practice, this would correspond to the appearance of satellite peaks near forbidden Bragg positions (h + k + l = odd), *contrary to experiment.*

The point which must be recognized is that the phase relationship between CDW's on adjacent chains cannot be obtained from "one-dimensional" band structure arguments as above. One should therefore write the expression for the CDW-wavevector in the following general form:

$$\mathbf{q}_s = \lambda\mathbf{a}^* + \mu\mathbf{b}^* + \mathbf{c}^* \tag{2}$$

The values of the parameters λ and μ can be determined if we make the additional assumption that CDW's on nearest-neighbour chains have opposite signs (anti-phase arrangement):

$$\mathbf{q_s} \cdot 1/2(\mathbf{a} \pm \mathbf{b}) = \pi \tag{3}$$

which implies: $(\lambda, \mu) = (\pm 1, 0)$ or $(0, \pm 1)$, i.e.:

$$\mathbf{q_s} = \pm\mathbf{a}^* + \mathbf{c}^* \quad \text{or} \quad \mathbf{q_s} = \pm\mathbf{b}^* + \mathbf{c}^* \tag{4}$$

These values are equivalent to a Brillouin zone Γ-point ($\mathbf{q_s} = \mathbf{0}$), in agreement with experiment. The small deviation of the actual $\mathbf{q_s}$-value from the Γ-point, may arise from a number of possible effects, some related to the electronic band structure, as discussed by Whangbo et al.[25], others related to lattice-mode interactions, as outlined in Sect. VI below.

IV. INELASTIC NEUTRON SCATTERING RESULTS

Previous neutron studies[12-14] have concentrated on the low-frequency region (ω_0-mode). Constant-Q spectra at and near the strong (2 2 4) and (1 1 0) satellite positions have mapped out the dispersion of a low-lying transverse acoustic (TA) branch, predominantly polarized in the basal plane. The branch is a good 'soft-mode' candidate in the sense that its polarization corresponds to that of the static ionic displacements associated with the phase transition. Its spectral response, however, shows only limited temperature variation between 400K and 10K. The transition region is marked by a slight increase of the TA-mode damping and by the development of a critical elastic (or unresolved quasi-elastic) 'central peak'. A detailed account of this work, together with a complementary study of a Nb-doped sample will be published separately[14].

Even though the transition at $T_P = 263$K in $(TaSe_4)_2I$ does not fit into a simple displacive model, it still makes sense to consider the decoupling of the phase and amplitude degrees of freedom associated with the TA-mode, below T_P. Within a completely general description of modulated crystals, one expects 'hard' phonon branches to develop gaps in the vicinity of the modulation wavevector. The selection rules for infrared and Raman activity of the corresponding gap modes have been worked out by several authors[31-33] in the case of modulated insulators. In the present case one expects that the TA-mode at $\mathbf{q}=\mathbf{q}_s$, or some unresolved 'phason-like' component of it, becomes infrared active below T_P, and gives rise to the observed ω_0-resonance at 35 GHz.

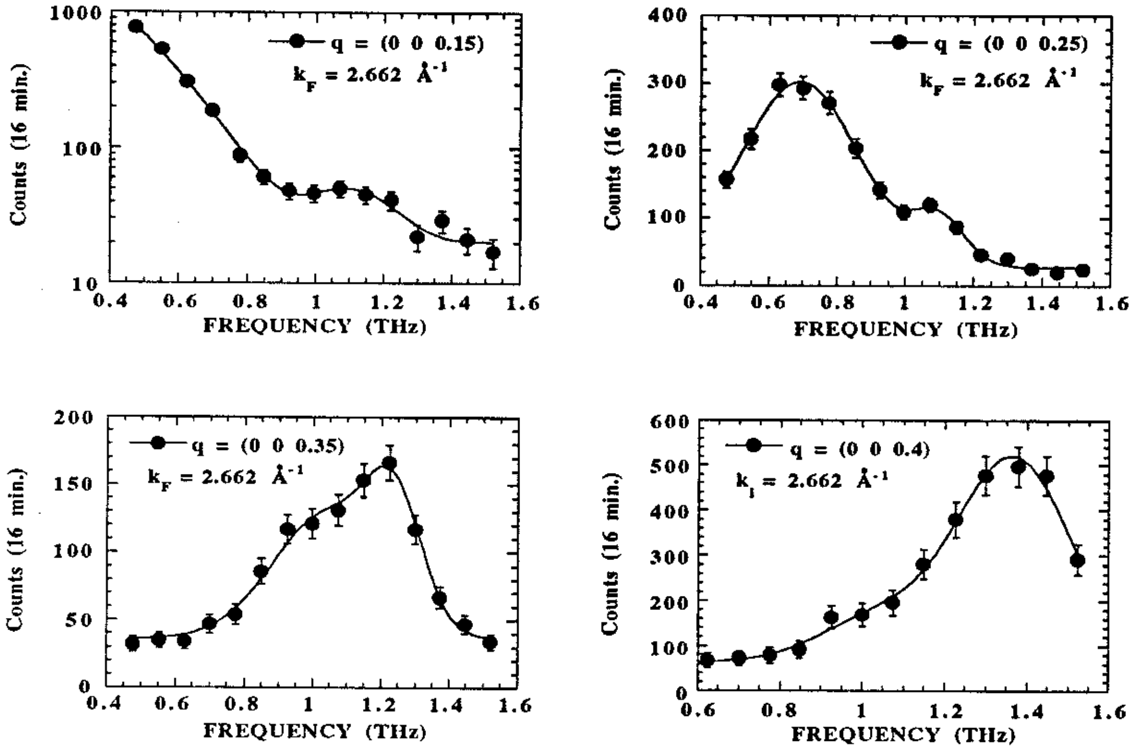

Figure 1a. Inelastic scans at different q-positions along the **c*** direction.

Here we wish to report on measurements in the 1 THz range in search of the analog of the infrared ω_1-resonance. Experiments were carried out on a 0.2 cm^3 $(TaSe_4)_2I$ single crystal, using three-axis spectrometers 1T at Laboratoire Léon-Brillouin, Saclay (France) and IN3 and IN14 at ILL, Grenoble (France). The incident (or outcoming) neutron wavevector was held fixed at 2.662 Å^{-1} (E= 14.7 meV or 3.53 THz), and a graphite filter was used to remove higher-order neutrons from the incident (outcoming) neutron beam.

Constant-Q scans were performed at 150 K and room temperature near several Γ-points. The only conclusive results were obtained near the (0 0 8) Bragg reflection, i.e. in a scattering geometry optimized for the observation of phonons with **c**-polarisation. This is consistent with the **E** ‖ **c** infrared activity of the ω_1-resonance.

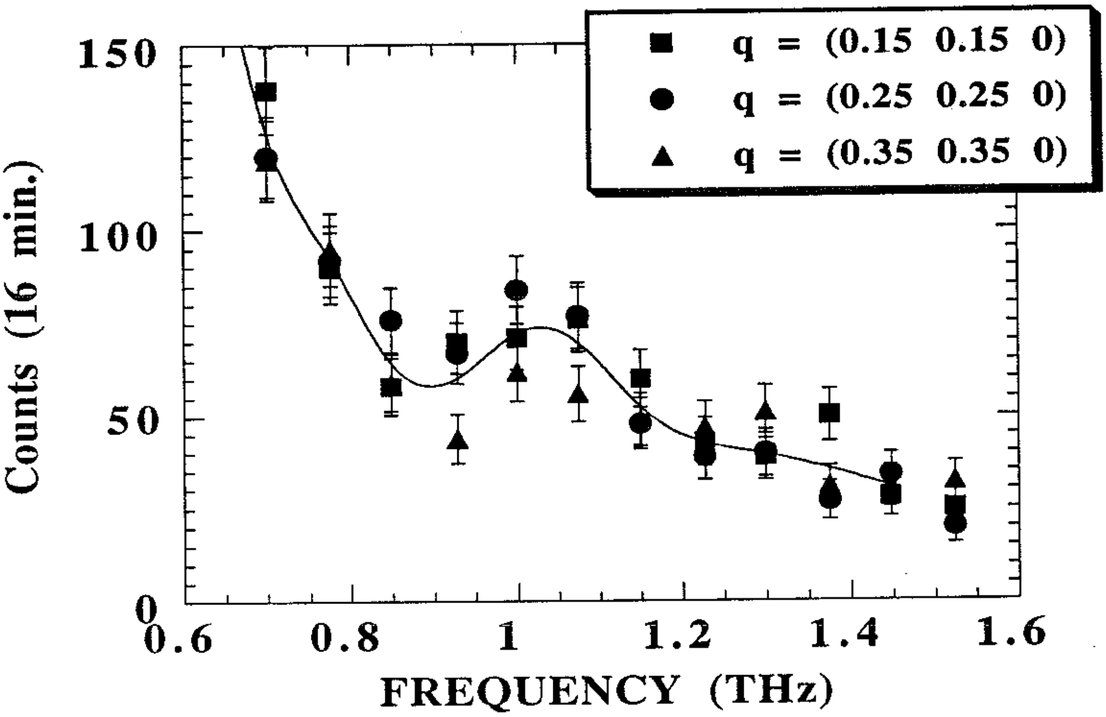

Figure 1b. Inelastic scans at three q-positions along the **a*+b*** direction. The straight line is the average of the three scans.

Fig. 1a and 1b show scans performed at **Q** = 8**c*** + **q**, with **q** ‖ **c*** and **q** ‖ **a***+**b***, respectively. At **q** = (0, 0, 0.15) and (0, 0, 0.25) a weak mode is visible at 1.1 THz, in addition to the strong longitudinal acoustic (LA-) mode at lower frequency. Between **q** = 0.25 **c*** and 0.35 **c***, the two branches exchange characters in a standard anti-crossing pattern. At 0.40 **c***, the 1.1 THz mode is still visible as a bump on the low-frequency wing of the LA-mode. It vanishes at larger **q**-values.

For **q** along **a***+**b***, the 1.1 THz mode is observed up to the zone-boundary. The sloping background in Fig 1b is due to the tail of the response from a flat low-frequency TA-branch polarized along **c**. The other two acoustic branches are predominantly polarized in the basal plane and are not visible in the present geometry.

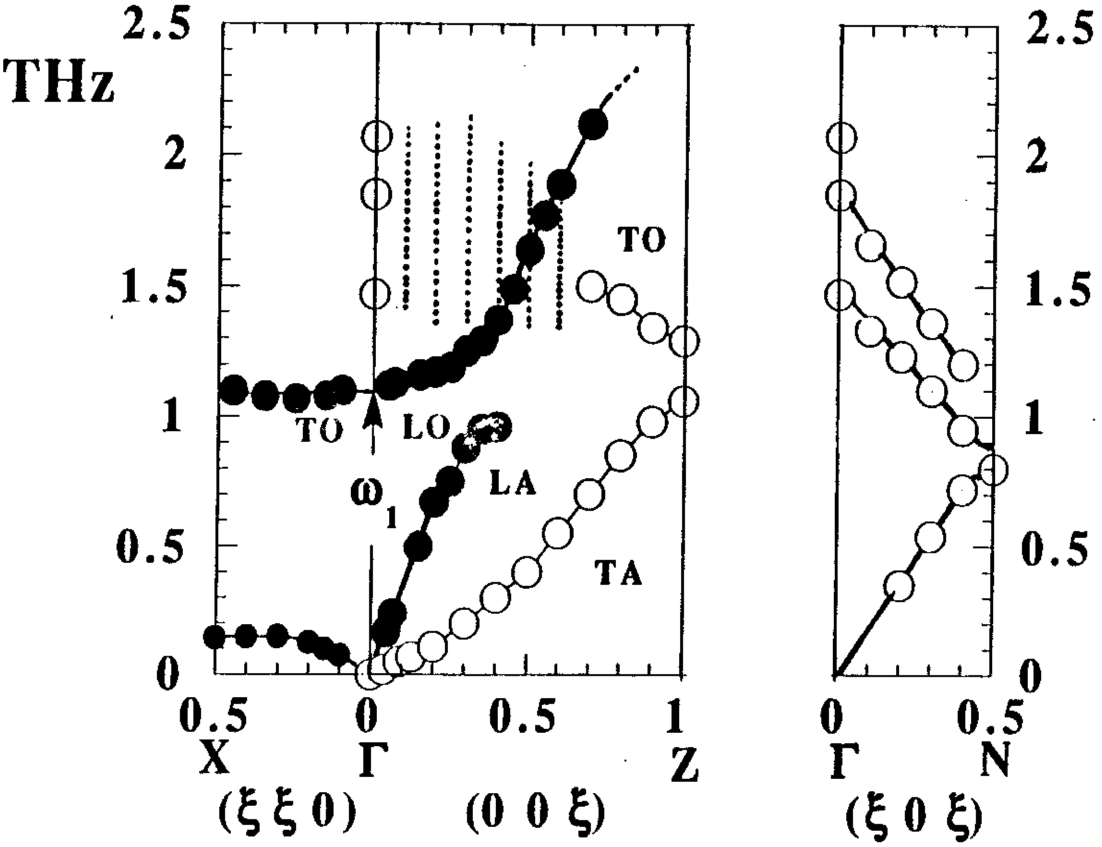

Figure 2. (a) Phonon dipersion curves along selected high symmetry directions at T=295 K. Modes polarized mainly along c (in the basal plane) are shown as full (open) dots. (b) Phonon dispersion curves for modes propagating along the (1 0 1) direction and polarized mainly along the (0 1 0)-direction.

The mode-frequencies are shown as closed circles in Fig. 2a, after deconvolution for finite instrumental resolution. The data points refer to room temperature measurements. A few scans were repeated at 150 K, under identical experimental conditions: no change in mode-frequencies could be detected and intensity variations could be explained solely on account of thermal population factors.

V. INTERPRETATION OF THE 1.1 THz MODE

We now address the question of whether the Γ-point mode at 1.1 THz should be identified as the ω_1-resonance seen in the infrared spectra.

The anti-crossing with the LA-mode shows that the two branches belong to the same irreducible representation for **q** along **c***. This implies that the Γ-point symmetry of the 1.1 THz mode is either A_1 (i.e. totally-symmetric and Raman active) or A_2 (odd with respect to both 2-fold axes perpendicular to the c-axis and infrared active with **E** ‖ **c**).

No indication of a 1.1 THz (36 cm^{-1}) mode can be found in the A_1-symmetry Raman spectra[11], which would seem to rule out the first hypothesis.

The second hypothesis is interesting because it implies that the two techniques see the same or closely related excitations. It is not possible to be more specific in the present case as one should bear in mind that the two probes (neutrons and infrared photons) couple to excitations in the modulated state in quite different ways[34]. What has to be clarified first, in the infrared case, is whether the mode corresponds to a Γ-point phonon of the high-temperature structure which becomes unscreened below T_P due to the progressive disappearance of free carriers, or whether it corresponds to a "new" mode in the same sense as the ω_0-phason.

In a neutron scattering experiment, on the other hand, one can in principle distinguish between the two situations, as the excitation is *primarily* visible near $\mathbf{q} = \mathbf{0}$ and $\mathbf{q} = \mathbf{q}_s$, respectively. Of course here $\mathbf{q}_s$ is so small that a neutron experiment with relaxed resolution, as required by the low intensities, can barely distinguish between $\mathbf{q} = \mathbf{0}$ and $\mathbf{q} = \mathbf{q}_s$ and a more detailed discussion, therefore, would not be meaningful.

To summarize, a mode has been found by inelastic neutron scattering, at the same frequency as the infrared ω_1-peak. The two modes appear to have related symmetry and polarization characteristics. The neutron mode has very *low* inelastic structure factor and is observed largely through mixing with the c-polarized acoustic branches which have a *large* structure factor near the strong (008) Bragg reflection.

The low structure factor of the neutron mode is indeed consistent with the current interpretation of the infrared peak as due to the presence of impurities. On the other hand, our observation of the 1.1 THz mode at room temperature, i.e. above the Peierls transition, does not seem compatible with the interpretation of the ω_1-mode as a bound CDW collective mode. Indeed, in the model proposed in refs. 2-3, the frequency ω_1 is closely related to the longitudinal phason frequency ω_{LO}. As T_P is approached from below, ω_{LO} is expected to renormalize rapidly towards $\omega_{TO} = \omega_0 = 35$ GHz, due to the effect of free-carrier screening. At room temperature, the free-carrier concentration is higher by 3 or 4 orders of magnitude than at 150 K and the distinction between ω_{TO}, ω_{LO} and ω_1, is probably no longer relevant. Hence, if the two techniques do see the same excitation, the current interpretation of the ω_1-peak as a bound CDW collective mode must be reconsidered.

VI. THE SEARCH FOR E-TYPE Γ-POINT OPTIC MODES

Several authors have proposed to view the Peierls instability in $(TaSe_4)_2I$ as produced by a TA-TO mode interaction[11]. In such a model, a moderate anharmonic softening of a TO branch, in the vicinity of the Γ-point, may induce a strong renormalization of the TA branch through normal (harmonic) level repulsion, and eventually lead to a displacive instability at finite wavevector via the complete softening of the TA mode. Models of this kind have been discussed in the context of modulated insulators such as quartz[35] and thiourea[36]. An order-disorder version of the same has also been developed and applied to the case of sodium nitrite[36] and to various minerals[37].

Since the long-wavelength TA branch is expected to interact more strongly with low-lying TO modes of same polarization, one is lead to look for low-lying E-type (X,Y) modes at the Γ-point.

One way to proceed is to follow the dispersion of the doubly-degenerate TA-branch in the (0 0 1) direction from one Brillouin zone into the next, i.e. along a Γ - Z - Γ path in Fig. 3. This was done at room temperature, starting from the strong (4 4 0) Bragg peak and going toward (4 4 2). The results are shown in Fig. 2a as open circles. A small

TA-TO gap is observed at the (4 4 1) Z-point, but the TO-mode response is lost before reaching (4 4 2). The extrapolated Γ-point TO-frequency can nevertheless be estimated to lie in the range from 1.5 to 2.0 THz.

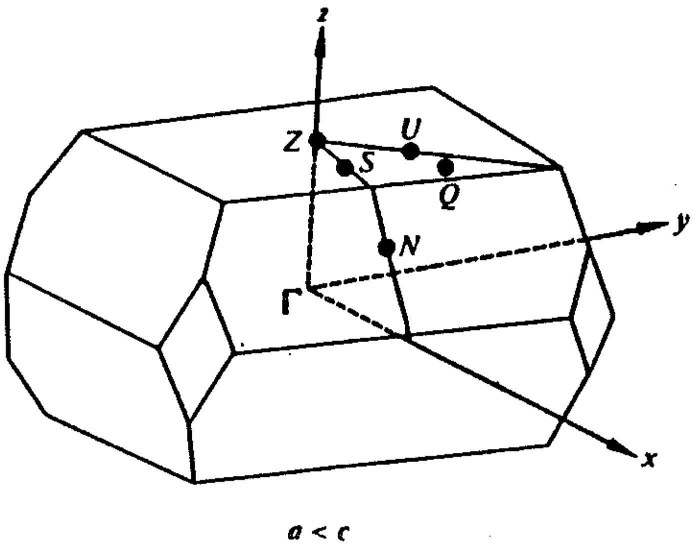

Figure 3. Brillouin zone of the body centered tetragonal lattice in the case a < c.

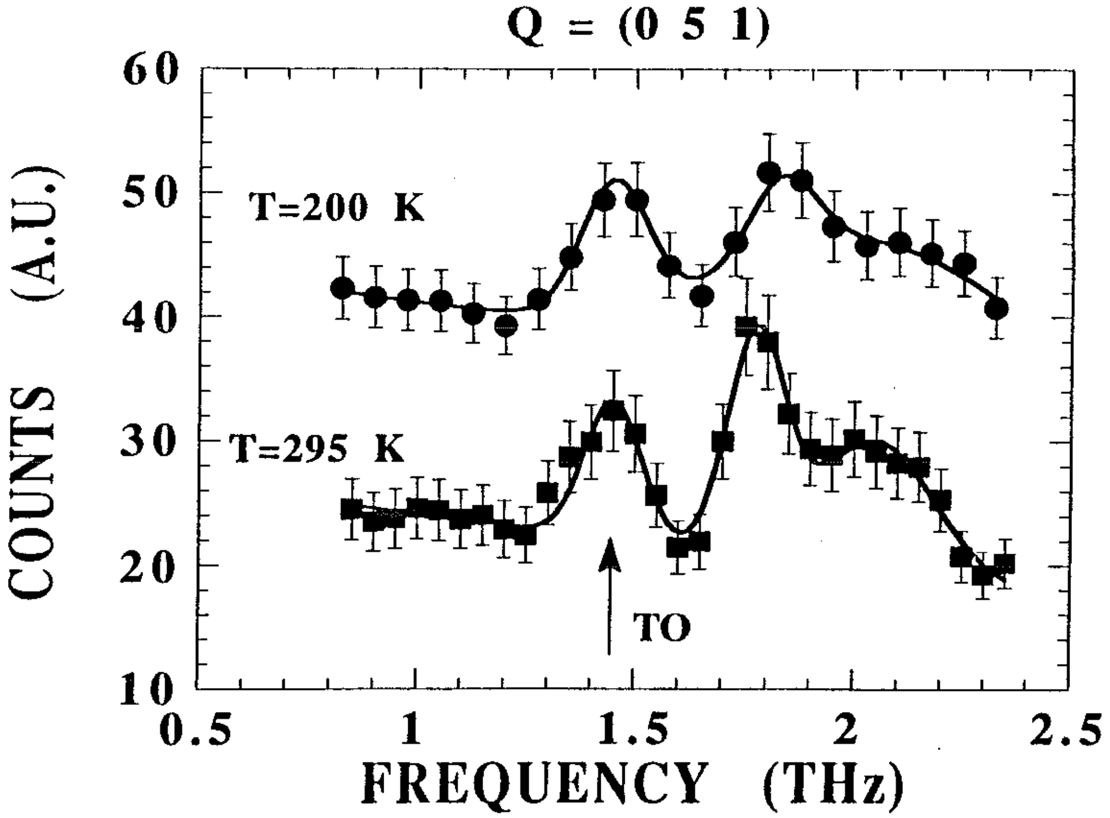

Figure 4. Inelastic scans at the zone center corresponding to Q=(0 5 1) at two temperatures, above and below Tp.

Another method, which is suggested by the topology of the body-centered Brillouin zone and by the discussion in Sect. III, is to proceed along a (1 0 1)-type direction (Γ - N - Γ path in Fig. 3): this is indeed the shortest path between adjacent zone centers. Along (1 0 1) the two transverse TA branches are non-degenerate and in order to end up with an E-type Γ-point optic mode one selects the branch which is predominantly polarized along (0 1 0). Experimentally this selection is done by working in a Brillouin zone G_{hkl} with a large value of k. In Fig 2a (right hand side), we show the results from a series of constant-Q scans between (1 5 0) and (0 5 1). The original TA branch is followed unambiguously across the zone boundary N-point at (1/2 5 1/2), up to a frequency of 1.45 THz (48.5 cm^{-1}) at the (0 5 1) Γ-point. Near (0 5 1) several new branches are detected. None show any measurable frequency shift between room temperature and 200 K (see Fig. 4).

VII. DISCUSSION AND CONCLUSION

In this paper we have performed inelastic neutron scattering experiments in the 1-2 THz frequency range on the quasi one dimensional compound $(TaSe_4)_2I$. At 1.1 THz (36 cm^{-1}) and in the vicinity of the Brillouin zone center (Γ-point) we have found a mode with a weak structure factor and polarization along the c-axis. This mode becomes clearly visible for propagation vectors along the c* direction, in the region where it anticrosses the LA mode, whereas in the a*+b* direction it remains dispersionless and weak. The measurements were performed at 150 K and room temperature and no change in mode-frequencies is observed. The frequency of this mode and its polarization are compatible with the infrared resonance observed in the semiconducting state, i.e. below T_P = 263 K, and currently denoted in the literature as the ω_1-mode[2,3,17]. However our observation of the 1.1 THz mode at room temperature does not seem compatible with its assignment as a bound CDW collective mode.

The next point we address concerns the mechanism of the phase transition proposed by Sugai et al.[11]. On the basis of Kurihara's[11,38] TA-TO mode-interaction model, Sugai and coworkers postulate the existence of a 'soft' TO mode with a frequency varying from 170 cm^{-1} at high temperature to 93 cm^{-1} at T_P. Raman data by the same authors only show the appearence of a new mode below Tp, at a temperature-independent frequency of 93 cm^{-1}. The present work shows that the lowest TO-mode having the same polarization as the TA-mode has a frequency of 1.45 THz (48.3 cm^{-1}) at room temperature and remains unchanged in the incommensurate phase. Two other temperature-independent optic modes are found between 1.5 and 2 THz. Measurements beyond 2 THz are not possible at present because of limited sample size. In the light of the present results the TA-TO mode-interaction model proposed in ref. 11 appears, at best, oversimplified.

We are very pleased to thank P. Boutrouille, A. Brochier, G. Eisele, and H. Schober for their kind assistance in the experiments and S. Brazovskii for several fruitful discussions. One of us, J.E.L., also acknoledges financial support from the Spanish Ministry of Education and Science.

References

1. S. Donovan, Y. Kim, B. Alavi, L. Degiorgi and G. Grüner, Sol. State Comm. 75, 721 (1990).

2. L. Degiorgi, B. Alavi, G. Mihály and G. Grüner, Phys. Rev B44 7808 (1991).

3. L. Degiorgi and G. Grüner, Phys. Rev B44, 7820 (1991).

4. For a recent review on CDW systems see for instance, Charge Density Waves in Solids, edited by L.P. Gorkov and G. Grüner, Modern Problems in Condensed Matter Sciences vol. 25 (North-Holland, Amsterdam, 1989).

5. T.W. Kim, S. Donovan, G. Grüner and A. Philipp, Phys. Rev. B43, 6315 (1991), and references therein.

6. Y. Nakane and S. Takada, J. Phys. Soc. Jpn.54, 977 (1985); K.Y.M. Wong and S. Takada, Phys. Rev. B36, 5476 (1987).

7. B. Hennion, J.P. Pouget and M. Sato, Phys. Rev. Lett. 68, 2374 (1992).

8. J.P. Pouget, B. Hennion, C. Escribe-Filippini and M. Sato, Phys. Rev. B43, 8421 (1991).

9. E. Tutis and S. Barisic, Phys. Rev. B43, 8431 (1991).

10. G. Travaglini, I. Mörke and P. Wachter, Solid State Comm. 45, 289 (1983).

11. S. Sugai, M. Sato and S. Kurihara, Phys. Rev. B32, 6809 (1985).

12. P. Monceau, L. Bernard, R. Currat, F. Levy and J. Rouxel, Physica 136B, 352 (1986).

13. H. Fujishita, S.M. Shapiro, M. Sato and S. Hoshino, J. Phys. C 19, 3049 (1986)

14. J.E. Lorenzo, R. Currat, P. Monceau and F. Levy, to be published.

15. G. Travaglini and P. Watcher, Phys. Rev. B30, 1921 (1984).

16. H.K. Ng, G.A. Thomas and L.F. Schneemeyer, Phys. Rev. B33, 8755 (1986).

17. M.S. Sherwin, A. Zettl and P.L. Richards, Phys. Rev. B 36, 708 (1987).

18. H.P. Geserich, G. Scheiber, M. Dürrler, F. Levy and P. Monceau, Physica 143B, 198 (1986)

19. W.N. Creager, P.L. Richards and A. Zettl, Phys. Rev. B44, 3505 (1991)

20. R.J. Cava, P. Littlewood, R.M. Fleming, R.G. Dunn and E.A. Rietman, Phys. Rev. B33, 2439 (1986), and references therein.

21. S. Sridhar, D. Reagor and G. Grüner, Phys. Rev. B34, 2223 (1986).

22. G. Mihaly, T. Chen, T.W. Kim and G. Grüner, Phys. Rev. B38, 3602 (1988).

23. A. Philipp, W. Mayr, T.W. Kim, B. Alavi, M. Maki and G. Grüner, Phys. Rev. B39, 7536 (1989).

24. D. Reagor and G. Grüner, Phys. Rev. B39, 7626 (1989).

25. P. Gressier, M.H. Whangbo, A. Meerschaut and J. Rouxel, Inorg. Chem. 23, 1221 (1984).

26. P. Littlewood, Phys. Rev. B36, 3108 (1987).

27. P.A. Lee, T.M. Rice and P.W. Anderson, Solid State Commun. 14, 703 (1974); H. Fukuyama and P.A. Lee, Phys. Rev. B17, 535 (1977); P.A. Lee and T.M. Rice, Phys. Rev. B19, 3970 (1979).

27. P. Gressier, L. Guemas and A. Meerschaut, Acta Cryst. B38, 2877 (1982).

28. C. Roucau, R. Ayroles, P. Gressier and A. Meerschaut, J. Phys. C 17, 2993 (1984).

29. H. Fuhishita, M. Sato, S. Sato and S. Hoshino, J. Phys. C 18, 1105 (1985).

30. K.B. Lee, D. Davidov and A.J. Heeger, Solid State Comm. 54, 673 (1985).

31. V. Dvorák and J. Petzelt, J. Phys. C 11, 4827 (1978).

32. H. Poulet and R.M. Pick, J. Phys. C 14, 2675 (1981).

33. M. Vallade, V. Dvorak and J. Lajzerowicz, J. Phys. (Paris) 48, 1171 (1987).

34. R. Currat and T. Janssen, Solid State Phys. 41, 201 (1988).

35. T.A. Aslanyan and A.P. Levanyuk, Solid State Comm. 31, 547 (1979); T.A. Aslanyan, A.P. Levanyuk, M. Vallade and J. Lajzerowicz, J. Phys. C 16, 6705 (1983).

36. A.P. Levanyuk and D.G. Sannikov, Sov. Phys.: Solid State 18, 1122 (1976).

37. J.D.C. McConnell, Z. Kristall. 147, 45 (1978).

38. S. Kurihara, J. Phys. Soc. Jpn. 48, 1821 (1980).

CHAPITRE III

Neutron studies of the quasi-one dimensional conductor $(TaSe_4)_2I$: I. Elastic scattering from pure and Nb-doped samples.

J.E. Lorenzo and R. Currat
Institut Laue-Langevin, 38042 Grenoble-Cedex, France.

P. Monceau
Centre de Recherches sur les Très Basses Températures, CNRS,
38042 Grenoble-Cedex, France.

B. Hennion
Laboratoire Léon Brillouin, Centre d'Etudes de Saclay,
91191 Gif-sur-Yvette-Cedex, France

F. Levy
Institut de Physique Appliquée, Ecole Polytechnique Fédérale de
Lausanne, CH-1015, Lausanne, Switzerland.

Abstract

We study the temperature dependence of satellite reflections in $(TaSe_4)_2I$ by means of elastic neutron scattering. Values for the Peierls transition temperature T_P,, are found to be strongly sample-dependent. The intensity distribution among symmetry-related satellite reflections indicates a domain structure with slowly fluctuating domain populations. Correlation lengths associated with the diverging "central peak" are determined and are found to be nearly isotropic in agreement with previous x-ray work on the related compound $(NbSe_4)_2I$. We discuss the significance of this result in the context of weak electron-phonon coupling theory. The effect of doping by 0.4% of Nb has a severe effect on the modulated state. The low-temperature satellites are replaced by a diffuse scattering distribution elongated along **c***. The temperature dependence of the integrated diffuse intensity indicates a smeared out transition around 200 K, in agreement with resistivity measurements.

1. Introduction

Quasi-one dimensional conductors(1) are unstable under electronic fluctuations which open gaps on the conduction-electron Fermi surface. The result of the electron-lattice interaction is the formation of a charge-density wave (CDW) coupled to a periodic lattice modulation of wavevector $\mathbf{q}_S=2\mathbf{k}_F$, where k_F is the conduction-band Fermi wavevector.

The quantum description of the CDW instability involves the Bose condensation of electron-hole pairs with total momentum $\pm 2\mathbf{k}_F$. The CDW itself can be viewed as resulting from the interference between the right-going ($+2k_F$) and left-going ($-2k_F$) condensates(2). In a weak electron-phonon coupling description, the electronic gap $2\Delta(T)$ and the mean-field transition temperature T_P^{MF} are related through:

$$2\Delta(0)=3.5\ k_B T_P^{MF}$$

Experimentally, the ratio between the low-temperature electronic gap and the actual 3D transition temperature T_P is often found to be much larger than predicted by the above BCS-type relation. This discrepancy is ascribed to the renormalisation of the transition temperature ($T_P<T_P^{MF}$) arising from the weak interchain interactions and the large-amplitude 1D-fluctuations above T_P.

An alternate strong-coupling description has been proposed by Aubry et al.(3,4). For sufficiently large electron-phonon interaction strengths, the electrons become pairwise localised in real space (bipolarons). In this latter picture T_P corresponds to the ordering temperature of the bipolaron gas, while the gap energy 2Δ corresponds to the binding energy of a single bipolaron. T_P being of the order of magnitude of the residual (repulsive) interaction energy between bipolarons, one naturally expects to find $T_P \ll 2\Delta/k_B$.

Hence, the validity of the weak-coupling model rests heavily on the assumption of a large ratio between intrachain and interchain interaction energies. The relevant interactions are elastic as much as electronic, as the Peierls instability involves a lattice distorsion, as well as electronic charge ordering. The anisotropy of the electrical resistivity in the metallic state, only reflects the anisotropy of the electronic mean-free path and does not provide a proper estimate for the anisotropy of the pretransitional fluctuations.

Direct information on the q-dependent order-parameter susceptibility and correlation lengths above T_P, can be deduced from diffuse x-ray scattering data. Such measurements have been performed on a few of the model CDW compounds, such as $NbSe_3$ and $K_{0.3}MoO_3$ (for a review of recent work, see Pouget and Comes(5)).

The case of $K_{0.3}MoO_3$ is probably the best documented. Gap measurements, analysed in the weak coupling framework, suggest a ratio T_P^{MF}/T_P of the order of 2 to 3, depending upon sources(6,7). On the other hand, x-ray measurements(8,9) between T_P=180 K and room temperature indicate that the ratio of the in-chain to largest transverse correlation length is only a factor 4. In fact the largest transverse correlation length is always found to be larger than the relevant interchain distance, so that the 1D-fluctuation regime is not observed in that case.

In other quasi-1D CDW systems the situation is less clear due to uncertainties on the value of the gap or absence of direct correlation length measurements. In 2D CDW systems such as 2H-$TaSe_2$, with $2\Delta/k_BT_P = 28$, it seems clear that weak coupling is no longer applicable(10).

The present work deals with the compound $(TaSe_4)_2I$, which undergoes a Peierls transition near 260 K and for which low-temperature resistivity data(11) indicate a gap energy of $2\Delta \approx 3000$ K = $11.5\ k_BT_P$. X-ray results by Fujishita et al.(12) on $(TaSe_4)_2I$ and on the related compound $(NbSe_4)_2I$, indicate a low anisotropy ratio ($\xi_{\parallel}/\xi_{\perp} < 2$). However, the accuracy of the x-ray measurements in Ref.(12) suffers from resolution limitations and from contamination by non-critical scattering.

In this paper and in a following publication(13), we show how inelastic neutron scattering can be used to explore the energy scale of the critical fluctuations and to discriminate against non-critical scattering. Over a large temperature range above T_P , the energy scale of the critical fluctuations is narrow enough ("central peak") for the correlation lengths to be measurable by elastic 3-axis spectrometry. We present neutron results which confirm the low anisotropy of the critical fluctuations. We suggest that strong interchain interactions arise in this compound due to the long-wavelength acoustic character of the atomic displacements involved in the Peierls distorsion.

We also present preliminary results on the Nb-doped compound which illustrate how a small amount of isoelectronic impurities drastically change the nature of the low-temperature state. Finally, the implication of the present results for the interpretation of microwave and infrared absorption spectra(14) is considered

2. Structure and dynamics of $(TaSe_4)_2I$

$(TaSe_4)_2I$ belongs to the family of transition metal tetraselenides $(MSe_4)_nI$ with M=Ta, Nb and n=2,3,10/3. The crystal structure of these compounds consists in an arrangement(15) of strongly bonded $(MSe_4)_\infty$ chains parallel to the tetragonal c-axis, separated by strands of iodine ions (cf. Fig. 1). In each chain, M atoms and Se_4 rectangles alternate, the latter following a nearly regular screw arrangement along c with an angle of approximately 45° between consecutive rectangles. Within the rectangles the shortest Se-Se distance corresponds to that of a Se_2^{2-} dimer. The crystallographic space group in the undistorted metallic state is I422 with lattice parameters a=9.531 Å and c=12.824 Å. The unit cell contains two adjacent chains with four $(TaSe_4)$ units in each chain.

The Peierls transition temperature, as obtained from diffraction and resistivity data(11), varies between 235 K and 265 K, depending on samples. The low temperature electrical response shows non-linear effects characteristic of a CDW-groundstate(11). X-ray(12) and electron(16) diffraction experiments reveal the formation of an incommensurate distorsion below T_P with a modulation wave vector

$q_S=(\pm\eta, \pm\eta, \pm\delta)$ with $\eta = 0.045$ and $\delta = 0.085$ for $(TaSe_4)_2I$ and $\eta = 0.065$ and $\delta = 0.159$ for isomorphous $(NbSe_4)_2I$ (T_P=210 K).

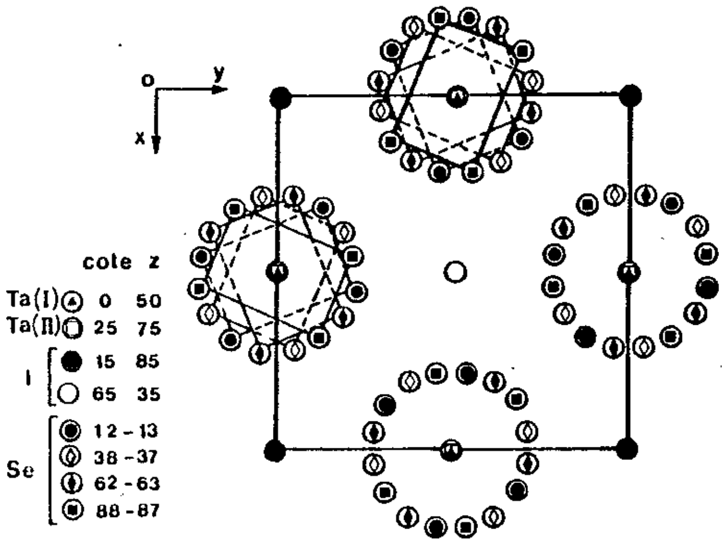

Figure 1: Structure of $(TaSe_4)_2I$ projected along the tetragonal c-axis.

These two compounds are the only ones in the $(MSe_4)_nI$ family to exhibit a unique metal-metal distance (d=3.206 Å). Consecutive Ta atoms along a chain occupy two alternating non-equivalent sites. XPS measurements(17) distinguish between the two Ta lattice sites while UPS(18) experiments do not. From ionicity considerations, assuming a I^- state for the iodine ions, the two Ta sites formally correspond to Ta^{4+} and Ta^{5+} valence states, with one conduction electron per formula unit. This picture is confirmed by Hall effect(19) and thermopower measurements(20) and by band structure calculations(21) which suggest a single quarter-filled d_{z^2} electronic band at the Fermi level and electron conduction. Optical data give account of the strong anisotropy in the conductivity ($\sigma_{\parallel}/\sigma_{\perp} \approx 500$), between directions parallel and perpendicular to the chain axis.

The star of the modulation wavevector $\{q_S\}$ spans eight vectors(12,13,22). The detailed analysis of the modulated structure is a difficult task because of the large high temperature unit cell and because of the domain structure present below T_P. It has not been attempted so far. The satellite extinction rules observed by Fujishita et al.(12,13) imply that the atomic displacements are transverse acoustic-like and predominantly polarised in the basal plane (i.e. along $[1\,\bar{1}\,0]$ for

$\mathbf{q}_S=(\eta, \eta, \delta)$). A rough fit of selected high intensity satellites at low temperature (Lee et al.(22)) shows that the average transverse (in-plane) displacements are four times larger than in the chain direction and among the largest observed for a CDW system (≈ 0.087 Å).

Previous inelastic neutron scattering measurements(23,24) found a spoon-like anomaly on the dispersion curve of the TA branch propagating along $\mathbf{q}_S$ and predominantly polarised along $[1\,\bar{1}\,0]$ Note that, since $\mathbf{q}_S$ lies along a general direction in reciprocal space, the mode-polarisations are not fixed by symmetry.

The small value of the modulation wavevector can be understood on the basis of band structure arguments. The 1/4-filled conduction band leads to a Fermi wavevector of $(1/4)(2\pi/d)=c^*$, where $d=c/4$ is the Ta-Ta distance along the chain. Assuming in addition an antiphase arrangement of the CDW's on adjacent chains, one arrives at possible $\mathbf{q}_S$ values of $\pm\mathbf{a}^*\pm\mathbf{c}^*$ or $\pm\mathbf{b}^*\pm\mathbf{c}^*$, which are equivalent to $\mathbf{q}_S=0$, modulo a body-centered-tetragonal reciprocal-lattice vector. The observed departure of $\mathbf{q}_S$ from the Brillouin zone center may arise from band structure effects(21) or from a wavevector-dependent coupling between phonon branches. Indeed, it is difficult to understand why electron-phonon interactions should affect directly a long-wavelength transverse acoustic mode. Therefore Sugai et al.(25) have developed a phenomenological model in which the phase transition is brought about by the interaction between the acoustic branch and a transverse optic mode coupled to the electronic variables.

We comment elsewhere(26) on the applicability of Sugai's model to the case of $(TaSe_4)_2I$. Inelastic measurements have failed to yield evidence for an unstable optic branch below 2 THz. Thus, even if the driving "soft mode" has optic character its spectral weight can be safely neglected and correlation lengths may be evaluated by consideration of the TA mode response alone.

The TA mode response itself shows a rather limited softening as $T\rightarrow T_P$. Its dispersion *does not* show a local minimum at $\mathbf{q}=\mathbf{q}_S$, at any temperature. The main temperature-dependent effect is the growth of a central component whose energy width is resolution limited (<10 GHz).

The intensity of the central component is found to be maximum at **q**=**q**s, whereas the integrated intensity from the TA phonon increases continuously as **q**→0. The sum of the two contributions may or may not go through a maximum at finite wavevector depending upon the relative weight of the two contributions. It will, in the limit T→T_P because the central component dominates.

In such a situation it is not clear which experimental procedure yields the most relevant correlation lengths. In the following, we chose to use the central component alone. This choice affects our results more severely at high temperatures than in the limit T→T_P. We are therefore satisfied that the anisotropy of the correlations which we deduce from the present measurements is found to be approximately temperature independent, as expected on theoretical grounds.

2.Experimental results

(a) $(TaSe_4)_2I$

Experiments were carried out on the 4F1, 4F2 and IN12 cold-source three-axis spectrometers installed, respectively, at the Laboratoire Léon-Brillouin, Saclay (France) and at the Institut Laue-Langevin, Grenoble (France). For most measurements we used a 5 meV incident neutron energy (k_i=1.55 Å^{-1}; λ=4.05 Å) and tight collimations (25'-25'-20'-20') in order to optimize the instrumental q-space resolution.

A rod-shaped 4x4x20 mm^3 specimen, mounted in a closed-cycle refrigerator, was oriented with a (hhl) horizontal scattering zone, as represented by the shaded plane in figure 2. Satellite reflections and diffuse intensities located near the (224) fundamental Bragg reflection were monitored. Out of the eight satellite peaks at (2±η, 2±η, 4±δ), the set of four which are located in the (hhl) scattering plane are essentially extinct because the corresponding atomic displacements are along the normal to the scattering plane. The four which are active are indexed (2+η, 2-η, 4±δ) and (2-η, 2+η, 4±δ). They were brought into reflecting position by small goniometer tilt adjustments.

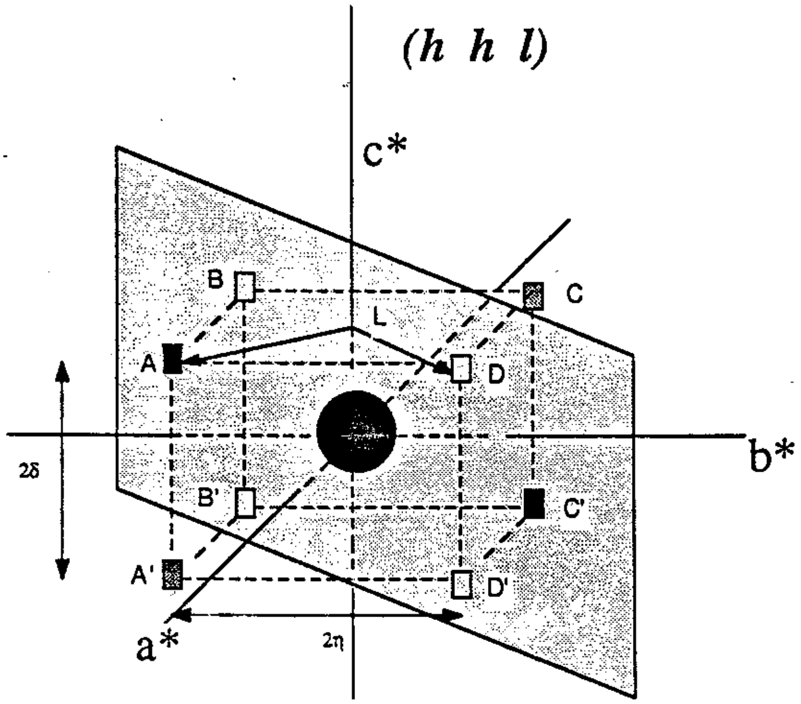

Figure 2: Reciprocal space sketch of satellite positions near the (224) Bragg peak. The shaded plane corresponds to the (hhl) scattering plane. Satellite reflections shown as closed (open) symbols are strong (nearly extinct).

All three components of the instrumental q-resolution had to be controlled simultaneously. The final trade-off between intensity and resolution yielded the following instrumental q-widths (fwhm): $\Delta q_{\parallel (110)} = 0.008$ Å^{-1}; $\Delta q_{\parallel (001)} = 0.0105$ Å^{-1}; $\Delta q_{\parallel (1\text{-}10)}$ $(=\Delta q_{\text{vertical}}) = 0.04$ Å^{-1}. The above values have been deduced from scans across the (224) reflection and therefore include the effect of sample mosaicity.

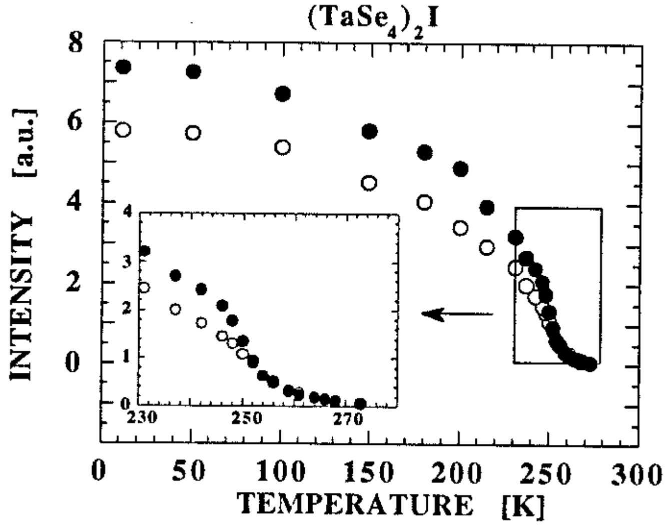

Figure 3a: Temperature variation of satellite intensity at (2-η, 2+η, 4+δ) (full circles) and (2+η, 2-η, 4+δ) (open circles). The transition temperature is located at 253 K.

In Fig. 3a we present the temperature evolution of the intensity of the satellites located at $\mathbf{G}_{224}+\mathbf{q}_1 = (2+\eta, 2-\eta, 4+\delta)$ (full circles) and $\mathbf{G}_{224}+\mathbf{q}_2 = (2-\eta, 2+\eta, 4+\delta)$ (open circles). The transition temperature, as determined from the position of the inflexion point of the curve, is found at $T_P=253\pm3$ K . The intensity tail above T_P is associated with the critical central peak.

The scattering vectors for the two satellites (A and C in Fig. 2) are related through a symmetry operation of the 422 point group:

$$2_{(x,-y)}\{\mathbf{G}_{224}+\mathbf{q}_1\} = -\{\mathbf{G}_{224}+\mathbf{q}_2\}$$

Hence, the intensity ratio of the two satellites gives information on the nature of the modulated state. In particular, the two satellite intensities are expected to be equal if the modulated structure consists in a 4-q state or a 2-q state involving a coherent superposition of $\mathbf{q}_1$ and $\mathbf{q}_2$-waves. The fact that a systematic intensity difference is observed shows that the modulated structure involves either a single-q state, or a 2-q state where $\mathbf{q}_1$ and $\mathbf{q}_2$ belong to distinct domains. The presence of domains with slowly relaxing populations gives rise to long equilibration times at low temperatures. Below 180 K, after each temperature step, the intensity of both satellites was found to fluctuate and relax on a time scale much slower than the time scale of the measurements (5 minutes for each scan).

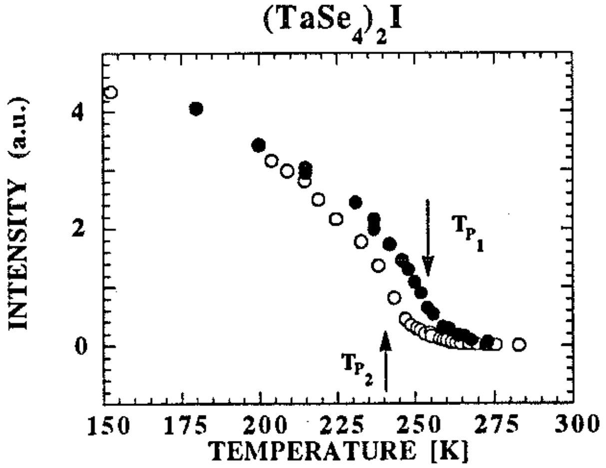

Figure 3b: Long-term drift of transition temperature: sample in virgin state (closed circles), T_{P_1} =253±3 K; same, two years later after several cooling and heating cycles (open circles) T_{P_2} =241 K. The two curves are normalised at 150 K.

The two runs shown in Fig 3b refer to the same specimen as above. They have been taken at an interval of 2 years during which the specimen was submitted to several cooling and heating cycles. The transition temperature is seen to be shifted downward by about 10 K in the later run. The temperature variation of the satellite intensity is however unchanged, as illustrated in Fig. 3c, nor is the satellite position. It has been argued that differences in T_P values could reflect small deviations from stoichiometry, as arising from iodine loss. In such a case, one would expect the change in the value of T_P to be correlated with a change in the conduction electron Fermi wavevector, and eventually in the satellite position. No such correlation is observed here.

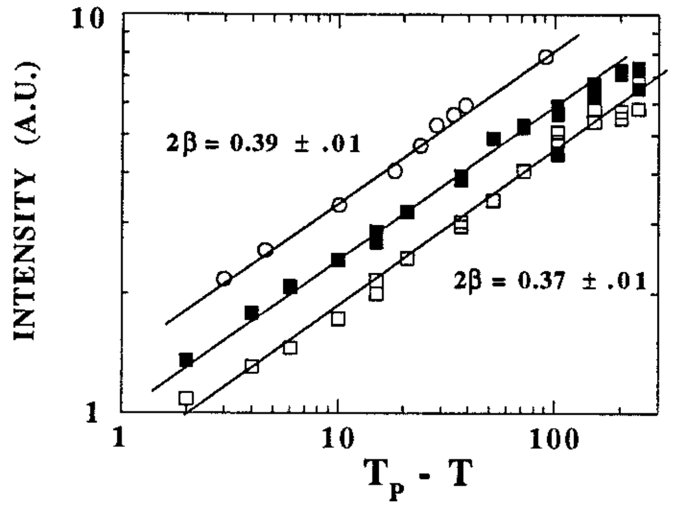

Figure 3c: Log-log plot of satellite intensities: squares refer to the same data as in Fig. 3a and circles to those of Fig. 3b. Changes in transition temperature are not correlated with changes in the critical exponent 2β ($I_{sat}(T) \approx (T_P - T)^{2\beta}$).

Above T_P we performed scans through the critical scattering distribution centered at ($2+\eta$, $2-\eta$, $4+\delta$) along three orthogonal directions a^*+b^*, a^*-b^* and c^*. The scans were corrected for resolution broadening using a standard one-dimensional deconvolution technique. In Figs 4a and 4b we show two typical scans taken at 263 K with the corresponding fits (full line) and the Gaussian resolution profile (broken line).

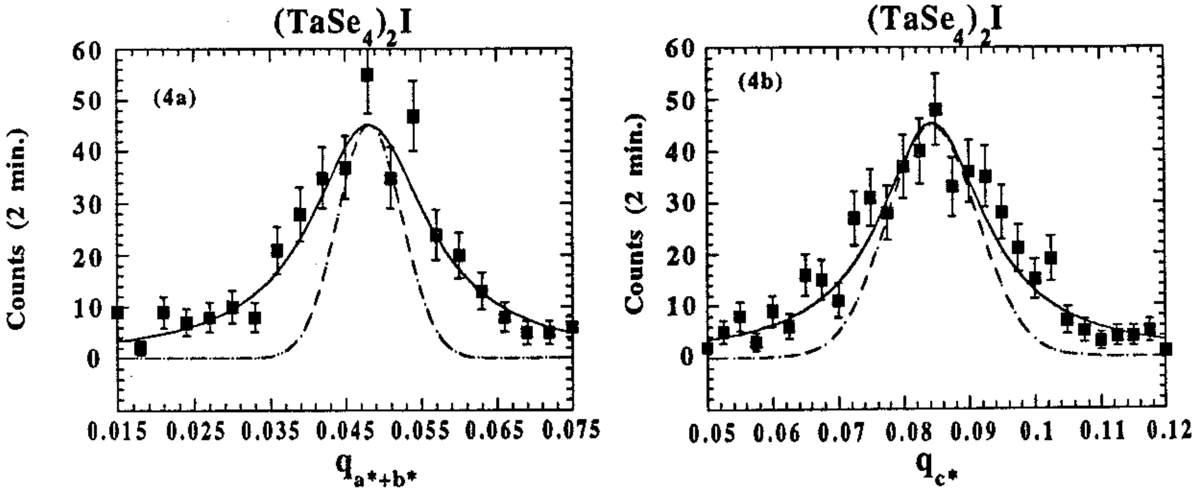

Figure 4: (**a**) Scan through the critical scattering along the **a*+b*** direction. The full line represents the result of the fit and the broken line the resolution profile along the **a*+b *** direction. (**b**) idem along the c* direction. (T=263 K; Tp=241 K).

The results for the inverse correlation lengths are plotted in Fig. 5. Within experimental accuracy, we find no anisotropy between the two basal plane correlation lengths: $\xi_{a^*+b^*} \approx \xi_{a^*-b^*}$. This result could not be foreseen on symmetry grounds as the tetragonal symmetry is broken by the fluctuating displacements which are probed in the experiment.

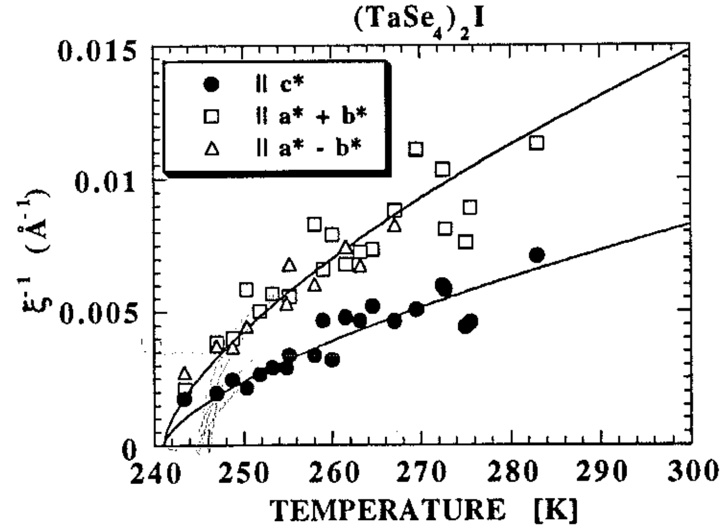

Figure 5: Temperature variation of the Lorentzian halfwidths of the critical scattering around (2+η, 2-η, 4+δ).

The anisotropy parameter, given by the ratio $\xi_{c^*}/\xi_{a^*+b^*}$, is very small: 1.8±0.2. It is consistent with the anisotropy ratio of 1.5 measured by Fujishita et al.$^{(13)}$, in the isomorphous compound $(NbSe_4)_2I$, by x-ray scattering and is at variance with that of other quasi-one dimensional conductors. In $NbSe_3$ and in $K_{0.3}MoO_3$, which have two different transverse correlation lengths, the anisotropy ratios amount to 7 and 13, and 4 and 7.5, respectively(27).

(b) $(Ta_{1-x}Nb_xSe_4)_2I$

A batch of Nb-doped samples was prepared by standard temperature-gradient furnace technique. The Nb-concentration in the ampoule was 1.2%. Chemical analysis performed on several single crystals from the same batch (typical sample size : 5x5x5 mm^3) showed the actual bulk Nb-content to be of the order of 0.4%.

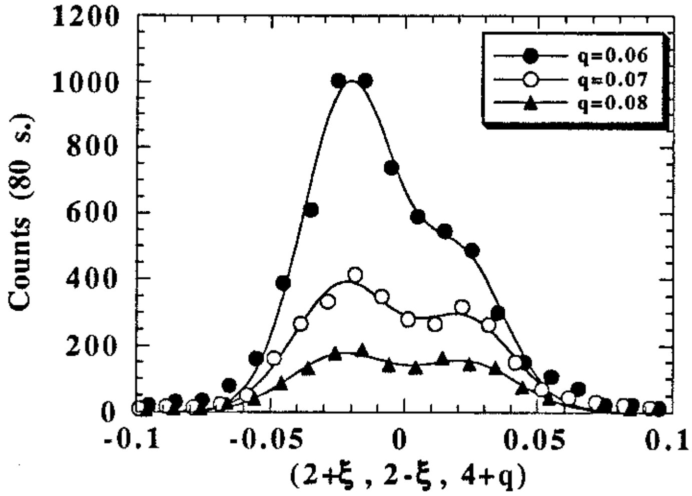

Figure 6: Diffuse scattering profile in Nb-doped $(TaSe_4)_2I$. The experimental conditions are the same as in Fig. 4 (T=12.5 K).

Doped samples studied under similar experimental conditions as above, did not produce evidence for low-temperature satellite reflections. Fig 6 shows scans along a*-b*, centered around (2, 2, 4+q), for several values of q. The remnants of the two satellite reflections at (2+η, 2-η, 4+δ) and (2-η, 2+η, 4+δ) appear as a weak double-peaked intensity distribution centered on η=±0.020. Along c*, the diffuse intensity is no longer centered on a finite value of q (= δ =0.085). Instead, it increases steadily with decreasing q-values. Scans with q-values lower than 0.05c* were not attempted because of possible contamination by the (224) Bragg reflection.

In Fig. 7, the intensity distribution for a pure and a doped sample are compared, using the 4F2 spectrometer operated at a neutron incident wavevector of $k_i = 1.97$ Å^{-1}, and under somewhat relaxed resolution conditions. The sample is oriented with a (hk0) horizontal scattering plane and measurements are performed near the (4, -2, 0) Bragg reflection. The q-resolution (fwhm) is 0.02 Å^{-1} in-plane and 0.12 Å^{-1} along the vertical [001] direction.

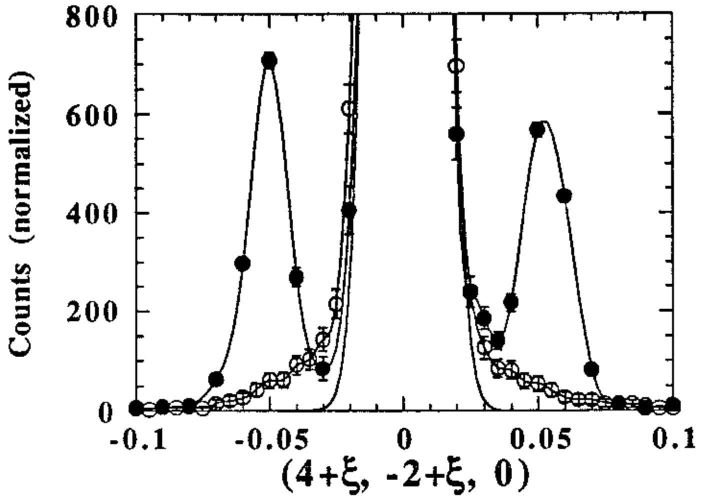

Figure 7: Transverse scan along a*+b* direction in the pure (closed circles) and doped compound (open circles) at 12.5 K. Both scans have been normalized to the peak intensity of the (4 -2 0) Bragg reflection. Experimental conditions are described in text.

With this purposely relaxed vertical resolution, the satellites at (4+η, -2+η, ±δ), symmetrically located above and below the horizontal scattering plane, are measured simultaneously in a (4+ξ, -2+ξ, 0) scan. For the undoped sample (closed circles in Fig. 7), the three peaks observed correspond to the (4-η, -2-η, ±δ) satellites, the (4, -2, 0) fundamental peak and the (4+η, -2+η, ±δ) satellites (from left to right in the figure). The same scan on a doped sample (open circles) only shows wings on both sides of the (4, -2, 0) Bragg peak. These wings correspond to diffuse intensity with a finite extension along c*, integrated by the broad vertical resolution of the instrument.

An attempt to measure the extension of the diffuse scattering along c* is shown in Fig. 8. To this end, the vertical instrumental resolution has been trimmed down to 0.055 Å^{-1} (= 0.11 c*) using vertical slits. The scan along (4+0.05, -2+0.05, ξ) shown in Fig. 8, once deconvoluted by the vertical resolution, indicates an extension of the diffuse scattering of the order of 0.10 c* (=0.05 Å^{-1}) fwhm.

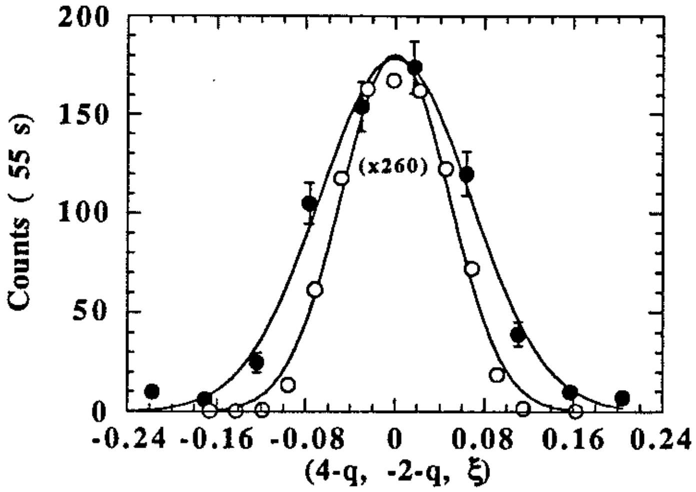

Figure 8: Extension of diffuse scattering along c* in doped sample (closed circles). The scan across the (4 -2 0) Bragg reflection (open circles) shows the instrumental resolution (T=12.5 K).

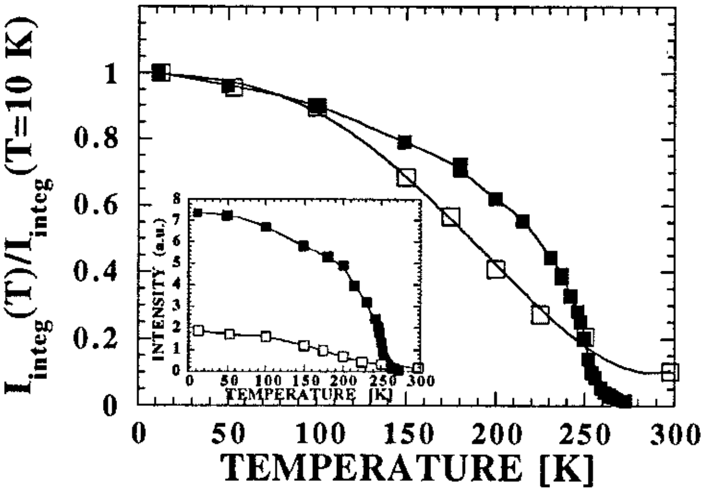

Figure 9: Temperature variation of the satellite intensity in the pure sample (closed symbol) compared with integrated diffuse intensity in the doped compound (open symbol). The data are normalized at low temperatures. Un-normalized intensities are shown in the insert.

The compounded results shown in Figs. 6-8, suggest that the diffuse intensity in the doped samples is centered around reciprocal lattice positions of the type (h±0.02, k±0.02, l), with an extension of 0.10 c* in the chain direction. The temperature dependence of this intensity, as obtained from Fig. 7 by integrating the wings of the distribution, is shown in Fig. 9 (open squares). The integrated diffuse intensity shows a much smoother behaviour than the pure-sample satellite intensity (closed squares). This behaviour appears consistent with resistivity data on similar Nb-doped samples(14), which suggest a smeared transition around 200 K.

3. Discussion and conclusions

The above measurements, together with previous structural and inelastic data, have provided additional information on the modulated structure of $(TaSe_4)_2I$. At low temperatures, we find evidence for a slowly relaxing domain structure. We suggest that just below T_P the domain walls may become sufficiently mobile to couple to ultrasonic waves. Fluctuations in the domain structure may therefore provide a plausible explanation for the recently reported(28) acoustic anomalies, observed in that temperature range.

Above T_P, strongly correlated fluctuations are observed. At 270 K (T_P + 30 K), in-plane and in-chain correlation lengths extend up to 100 Å and 180 Å, respectively. At the same relative temperature (240 K) the corresponding values for $(NbSe_4)_2I$, determined by x-ray scattering(12) are around 35 and 50 Å, respectively. Part of the difference may be due to the different technique used on the two compounds. In that respect, high resolution x-ray scattering data on the Ta compound would be highly valuable. Part of the difference may also be related to the longer wavelength of the modulation in the Ta compound, resulting in a more pronounced "modulated strain" character for the atomic displacements involved.

In any case, it seems highly unlikely that such 3-D correlated fluctuations could reduce T_P by a factor 2 or 3 with respect to its mean-field value. This, as well as the large amplitude of the modulated displacements, casts some doubt on the applicability of weak-coupling theory to the case of $(TaSe_4)_2I$.

As expected, doping has a strong influence on the nature ot the low-temperature modulated state. Unexpectedly, however, the satellite intensity becomes diffuse along the chain direction, while its wavevector component perpendicular to the chain is reduced but remains well-defined. This behaviour is quite different from what is observed in W- and Rb-doped bronzes(29) where the scattering also becomes diffuse, and assymmetric, but remains centered on the same "$2k_F$" wavevector value in the chain direction. Of course here the modulation wavevector is quite small and even a moderate amount of smearing can completely wash out the modulation periodicity. However the same argument is applicable for the wavevector components transverse to the chains and, at least from the data in Fig. 6, these components do not appear to be smeared out.

The partial smearing out of the modulation periodicity by doping has definite implications concerning the interpretation of light scattering and light absorption spectra in Nb-doped $(TaSe_4)_2I$ samples. The electromagnetic field no longer couples selectively to "$2k_F$"-modes, as in the long-range ordered modulated state, but to a continuous distribution of modes with wavevectors corresponding to the diffuse intensity distribution. For dispersive modes, such as acoustic modes, the smearing in reciprocal space is expected to induce a frequency broadening of the response. This broadening is not anharmonic in nature but is related to the coupling mechanism between the probe and the modulated system. We shall discuss this point further in the context of the inelastic neutron scattering results presented in the following paper.

We are very pleased to thank P. Boutrouille and A. Brochier for their kind assistance in the experiments, J. Chen for the resistivity measurements and M. Saint-Paul for communicating us ultrasound results prior to publication. One of us, J.E.L., also acknoledges financial support from the Spanish Ministry of Education and Science.

References

1. Recent reviews on CDW systems.

a. Low Dimensional Conductors and Superconductors, edited by D. Jerome and L.G. Caron, NATO-ASI series, vol 155 (Plenum Press, New York, 1987).

b. G. Grüner, Rev. Mod. Phys. **60**, 1129 (1988).

c. Charge Density Waves in Solids, edited by L.P. Gorkov and G. Grüner, Modern Problems in Condensed Matter Sciences vol. 25 (North-Holland, Amsterdam, 1989).

2. I. Tutto and A. Zawadowski, Phys. Rev. B **32**, 2449 (1985).

3. S. Aubry and P. Quemerais, in "Low Dimensional Electronic Properties of the Molybdenum Bronzes and Oxides", pp. 295-405; C. Schlenker ed., Kluver Academic Press (1989).

4. S. Aubry, G. Abramovici and J.L. Raimbault, J. Stat. Phys. **67**, 675 (1992).

5. J.P. Pouget and R. Comes, in " Charge Density Waves in Solids", pp. 85-136; L.P. Gor'kov and G. Gruner eds., Elsevier Science Publishers (1989).

6. D.C. Johnston, Phys. Rev. Lett. **52**, 2049 (1984).

7. G. Travaglini, P. Wachter, J. Marcus and C. Schlenker, Sol. State Comm. **37**, 599 (1981).

8. J.P. Pouget, C. Noguera, A.H. Moudden and R. Moret, J. Phys. **46**, 1731 (1985); **47** 145(E) (1986).

9. S. Girault, A.H. Moudden and J.P. Pouget, Phys. Rev. B**39**,4430 (1989).

10. C.M. Varma and A.L. Simons, Phys. Rev. Lett. **51**, 138 (1983).

11. Z.Z. Wang, M.C. Saint-Lager, P. Monceau, M. Renard, P. Gressier, A. Meerschaut, L. Guemas and J. Rouxel, Solid State Commun. **46**,325 (1983).

12. H. Fujishita, M. Sato and S. Hoshino, Solid State Commun. **49**, 313 (1984); H. Fujishita, M. Sato, S. Sato and S. Hoshino, J. Phys. C:Solid State Phys **18**, 1105 (1985).

13. J.E. Lorenzo, R. Currat, P. Monceau, B. Hennion and F. Levy, following paper.

14. T.W. Kim, S. Donovan, G. Grüner and A. Philipp, Phys. Rev. B**43**, 6315 (1991).

15. P. Gressier, L. Guemas and A. Meerschaut, Acta Cryst B**28**, 2877 (1982).

16. C. Roucau, R. Ayroles, P. Gressier and A. Meerschaut, J. Phys. C: Solid State Phys. **17**, 2993 (1984).

17. S. Kikkawa, S. Venosono and M. Koizumi, Proc. Int. Symp. of Non-Linear Transport and Related Phenomena in Inorganic Quasi One Dimensional Conductors, Sapporo 1983, pag. 245.

18. E. Sato, K. Ohtake, R. Yamamoto, M. Doyama, T. Mori, K. Soda, S. Suga and K. Endo, Solid State Commun. **55**, 1049 (1985).

19. L. Forro, J. R. Cooper, A. Janossy and M. Maki, Solid State Commun. **62**, 715 (1987).

20. C. Bansal and K. Surendranath, Solid State Commun. **76**, 209 (1990).

21. P. Gressier, M.H. Wangbo, A. Meerschaut and J. Rouxel, Inorg. Chem. **23**, 1221 (1984).

22. K.B. Lee, D. Davidov and A.J. Heeger, Solid State Commun. **54**, 673 (1985).

23. H. Fujishita, S.M. Shapiro, M. Sato and S. Hoshino, J. Phys. C: Solid State Phys **19**, 3049 (1986).

24. P. Monceau, L. Bernard, R. Currat, F. Levy and J. Rouxel, Physica **136B**, 352 (1986); Synth. Met.,**19**, 819 (1987)..

25. S. Sugai, M. Sato and S. Kurihara, Phys. Rev. B**32**, 6809 (1985).

26. J.E. Lorenzo, R. Currat, P. Monceau, B. Hennion and F. Levy, to be pub.

27. See, for instance Table III, in Ref. (5).

28. M. Saint-Paul, P. Monceau and F. Levy, Solid State Commun. **67**, 581 (1988).

29. S. Girault, A.H. Moudden, J.P. Pouget and J.M. Godard, Phys. Rev. B38, 7980 (1988).

CHAPITRE IV

Neutron scattering studies on the quasi-one dimensional compound $(TaSe_4)_2I$: II Inelastic scattering from acoustic branches

J.E. Lorenzo and R. Currat
Institut Laue-Langevin, 38042 Grenoble-Cedex, France.

P. Monceau
Centre de Recherches sur les Très Basses Températures, CNRS,
38042 Grenoble-Cedex, France.

B. Hennion
Laboratoire Léon Brillouin, Centre d'Etudes de Saclay,
91191 Gif-sur-Yvette-Cedex, France

F. Levy
Institut de Physique Appliquée, Ecole Polytechnique Fédérale de
Lausanne, CH-1015, Lausanne, Switzerland.

Abstract

We present acoustic phonon measurements in the quasi-one dimensional conductor $(TaSe_4)_2I$, by inelastic neutron scattering. The room temperature dispersion curves reflect the stiffness of the $(TaSe_4)_\infty$ chains and the comparatively weak transverse interactions. The response from the [110]-polarised TA mode, connected with the Peierls instability, is found to be weakly temperature-dependent but strongly dependent on the concentration in Nb impurities. We compare our results with ac conductivity spectra and with available theoretical predictions.

1. Introduction

(*) In the preceding paper, referred to as (I), we report on elastic neutron scattering experiments in $(TaSe_4)_2I$ above the Peierls transition T_P. The results concerning the anisotropy of the pretransitional fluctuations are at variance with the standard description of quasi-one dimensional conductors. At the same time we underline the strong acoustic component of the atomic displacements associated with the order parameter and its fluctuations. We suggest that the modulated strain character of the fluctuations is at the origin of the observed 3D correlations above T_P.

This paper is concerned with the low-frequency inelastic response (10 GHz - 2 THz) from pure and Nb-doped $(TaSe_4)_2I$ compounds. First we present room-temperature results on acoustic branches propagating along symmetry directions. These results extend previous ultrasonic measurements(1) and provide an overall picture of the acoustic response from the pure compound. Second we focus on the temperature dependence, above and below T_P of the transverse acoustic branch connected with the Peierls transition. We confirm and complement available inelastic neutron scattering results(2,3) on the acoustic branch anomaly, in the vicinity of the satellite wavevector:

$$\mathbf{q}_S = (\pm\eta, \pm\eta, \pm\delta) = (\pm 0.045, \pm 0.045, \pm 0.085)$$

The transverse acoustic phonon whose wavevector corresponds to the satellite position, lies in the frequency range where a sharp resonance is observed in ac electrical conductivity measurements(4-6), below T_P. This raises the question of whether the conductivity resonance should be interpreted as a phase-excitation of the pinned CDW (pinned phason), or simply as an acoustic mode of the average crystalline structure, which becomes optically active, below T_P , due to the static modulated distorsion.

The large oscillator strength of the mode in the $\sigma(\omega)$ data clearly points toward the former interpretation (phason-like). On the other hand, the inelastic neutron spectra described below, show little evidence for a soft-mode instability at T_P. The critical dynamics associated with the Peierls transition appears to be primarily of the slow-relaxational type (unresolved central peak). In such a situation, it is natural to expect the phase-fluctuation spectrum, below T_P, to be also relaxational in character. The sharp conductivity resonance around 30 GHz must then have a different origin. We come back to this point in more detail below.

A remarkable aspect of the data in Ref. 6, is the sensitivity of the ac response to dilute amounts of (isoelectronic) niobium impurities. For a niobium concentration of 1.2%, the authors in Ref. 6 find that the position of the resonance is shifted to 120 GHz and is considerably broadened (fwhm=110 GHz, instead of 20 GHz for the pure compound). This behaviour is consistent with the interpretation of the mode as a pinned phase-mode, for which the pinning frequency and linewidth are expected to increase with the concentration of pinning centers(7).

This prompted us to undertake neutron measurements, elastic and inelastic, on similar Nb-doped samples. We succeeded in preparing single crystals of appropriate sizes with an effective Nb concentration of 0.4%. Elastic scattering measurements, described in the preceding paper, show that doping destroys the CDW long-range order and that the modulation periodicity, in the chain direction, is no longer defined. The inelastic measurements described below, show that the TA-mode response shifts to higher frequencies, in qualitative agreement with the behaviour reported in Ref. 6. This shift, which is not accompanied by an increase in width, is observed at room temperature, i.e. at temperatures in excess of the Peierls temperature of the pure compound.

faux

The results presented below illustrate the anomalous character of the TA-mode dispersion in the neighbourhood of the satellite wavevector. They suggest that the magnitude of the anomaly is reduced in the doped samples. The stiffening of the TA-mode qualitatively accounts for the observed increase in the $\sigma(\omega)$ resonance frequency. A more detailed comparaison between the conductivity and neutron scattering results would require a complete characterisation of the doped samples used for each technique.

2. Experimental

Low-frequency measurements ($\omega < 0.5$ THz) were performed on the cold-neutron 3-axis spectrometers 4F1 and 4F2 at the Laboratoire Léon-Brillouin (Saclay, France), and IN12 and IN14 at the Institute Laue-Langevin (Grenoble, France). A number of incoming neutron wavevector values were used (k_i = 1.1, 1.4, 1.55, 1.64 and 2.0 Å^{-1}) depending on energy and momentum transfer requirements. Higher-order neutrons were removed by a beryllium filter (k_i = 1.1, 1.4, 1.55 Å^{-1}) or a graphite filter (k_i = 1.64 Å^{-1}) or by the natural cut-off of the curved neutron guide (k_i = 2 Å^{-1} on IN12).

The thermal beam 3-axis spectrometers IN3 and IN8 at ILL were used for inelastic experiments at energy transfers above $\omega > 0.5$ THz (k_i or k_f = 2.662 Å^{-1}.).

Two single crystals of $(TaSe_4)_2I$ of about 0.22 and 0.15 cm^3 as well as two smaller crystals of the Nb-doped compound $(Ta_{1-x}Nb_xSe_4)_2I$. The Nb-concentration in the ampoule was 1.2%. However chemical analysis performed on several single crystals from the same batch (typical sample size : 5x5x5 mm^3) showed the actual bulk Nb-content to be of the order of 0.4%.

As described in (I) for the elastic work, the present measurements were performed in the neighbourhood of the (2 2 4) Bragg reflection. This configuration offers a good compromise between intensity and resolution (strong satellite reflections at a moderate momentum transfer value of 3 Å^{-1}). For the (h h l)-type reflections the strongest satellites are those lying above and below the horizontal scattering plane, defined by the directions [110] and [001]. They can be brought into reflecting position by small sample-goniometer adjustements. Thus, and because of the small components of the modulation wavevector, a tight vertical resolution is required in order to integrate as little as possible of the elastic and inelastic response along the vertical $[1\ \bar{1}\ 0]$ direction.

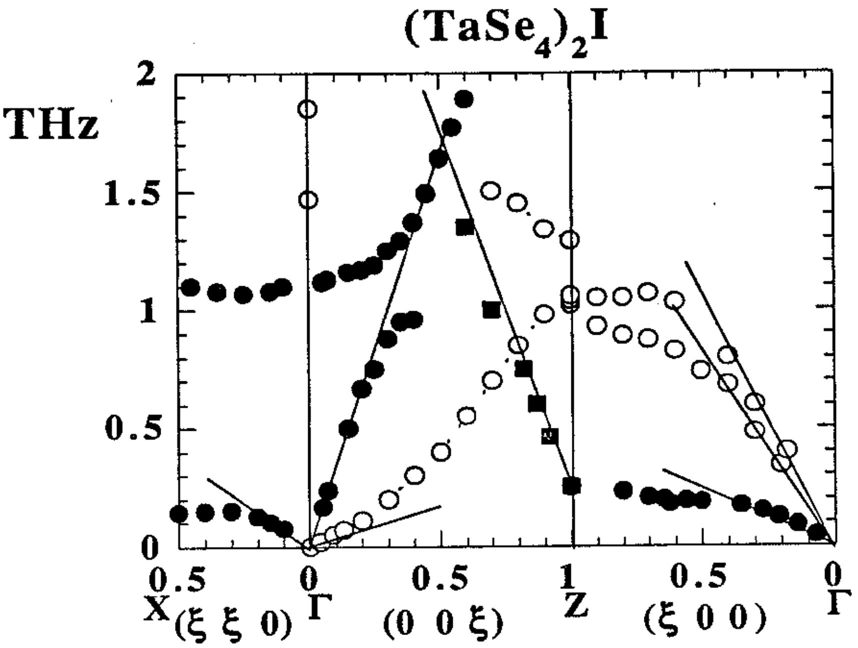

Figure 1: Phonon dispersion curves along high symmetry directions in $(TaSe_4)_2I$ at room temperature. Modes polarised along the chains (normal to the chains) are shown as closed (open) circles. The sound velocities (solid lines) are taken from ultrasonic data in Ref. (1).

3. Results and analysis.

In Fig. 1 we present the room temperature phonon dispersion curves measured along high symmetry directions. The extrapolated sound velocities are in fair agreement with ultrasonic data$^{(1)}$. In what follows we shall describe in detail the three main features characterizing the acoustic branches:

(i) the transverse acoustic branch propagating along the c* direction, whose sound velocity is given by $v_{44}=(C_{44}/\rho)^{1/2}$, follows a dispersion law of the type

$$\omega^2(q) = v_{44}^2 q^2 + C^2 q^4 \tag{1}$$

with C denoting a chain-bending force constant (v_{44} = 450 ms^{-1} = 0.71 THz Å and C = 5.24 THz Å^2). The same kind of behaviour is found in the related compound $(NbSe_4)_3I$ at room temperature$^{(8)}$ (v_{44} = 140 ms^{-1} = 0.22 THz Å and C = 8.19 THz Å^2). Below the ferrodistortive phase transition temperature (273 K), the sound velocity v_{44} in $(NbSe_4)_3I$

undergoes a strong renormalization ($v_{44} = 420$ ms^{-1} at 10 K). No such renormalization is observed in $(TaSe_4)_2I$ where the sound velocity and the TA mode dispersion is well described by eq. (1) at all temperatures.

A similar type of dispersion law is found in polymer crystals(9) and in bidimensional structures, such as graphite(10), and provides us with a measure of the dimensionality of the structure. The quasi-one dimensional character of the $(MSe_4)_nI$ structure is apparent in the elastic properties of all the compounds of the family, at least at high temperature. It is related to the rigidity of the $(MSe_4)_\infty$ backbone which in turn arises from the directionality of the covalent M-Se bonds.

(ii) The z-polarized transverse acoustic modes (TA_z), propagating in the basal plane [a*,b*], have the same v_{44} sound velocity. The peculiarity of these modes is that they are dispersionless over a wide portion of the Brillouin zone, with an extremely low frequency at the zone edge: ≈ 0.20 THz (see Figs. 1 and 6). The low-frequency plateau indicates that the $(MSe_4)_\infty$ columns are relatively free to move along the c-direction, independently of each other, due to the weak Se-I-Se interchain bonds.

The TA_z frequency is soft for all wavevectors (q_x, q_y, q_z) in the plane $q_z=0$. Its dispersion as a function of q_z, for a fixed value of (q_x, q_y), is quite steep as illustrated in Fig. 1, for the zone boundary Z-point. We find:

$$\omega^2(q_x, q_y, q_z) \approx \omega^2(q_x, q_y, 0) + v_\parallel^2 q_z^2$$

where $v_\parallel$ is very close to the longitudinal sound velocity v_{33} along the chain direction. In a following publication(11), we shall argue that the flat and low frequency TA_z dispersion sheet is at the origin of the anomalous behaviour of the specific heat(12) and thermal conductivity(13) below 5 K. Such a flat branch is also present in $(NbSe_4)_3I$ at room temperature but it disappears progressively as v_{44} increases below the 273 K transition.

(iii) The topology of the optic branches is discussed in more detail elsewhere(14). In Fig. 1, we see that the longitudinal acoustic branch along c* anticrosses a flat mode in the region of 1.1 THz and q_z = 0.25-

0.45 c*. By exploiting the symmetry compatibility relations along this direction we conclude that the flat mode has a zone center symmetry of A_1-type (totally symmetric, and thus Raman active) or A_2-type (odd with respect to both sets of two-fold axes normal to the chain axis, and infrared active in z-polarization). The peculiarity of this mode is that it is only clearly visible in the region where it anticrosses the LA mode and vanishes outside of this region. In the a*+b* direction it is hardly visible and its frequency remains constant within instrumental resolution (0.2 THz). Measurements below T_P show no detectable change in mode-frequency with temperature. In this frequency range, there are no Raman active modes whereas far-infrared experiments detect a strong resonance at 1.1 THz (36 cm^{-1}). A similar resonance has been detected in the blue bronze $K_{0.3}MoO_3$ at 40 cm^{-1} (1.2 THz) and interpreted as a bound collective mode arising from the presence of polarisable impurities. This interpretation is questioned by Creager et al.(15) who point out that in TaS_3 all lattice modes measured in far-infrared reflectivity have normal oscillator strengths.

As discussed in (I), the satellite structure factor is that of an acoustic mode of wave vector $\mathbf{q_s} = (\pm\eta, \pm\eta, \pm\delta) = (\pm0.045, \pm0.045, \pm0.085)$. The atomic displacements involved in the modulation are predominantly transverse to the chain direction and to $\mathbf{q_s}$. In Fig. 2a we illustrate the situation near a (h h l)-type Bragg reflection. The four satellites lying in the scattering plane (shaded plane) are nearly extinct (B, B', D and D'), while the two pairs located above (A,A') and below (C,C') are intense.

The L-point of coordinates (0, 0, 0.085), is located midway between the four satellites (A,B,C,D). Along ΓL the two TA branches are degenerate. Away from the ΓL direction, the two TA branches split. Fig. 2b shows the measured dispersion curves along L→D (lhs) and along L→A (rhs). In each case, only the [110]-polarised branch is visible. In the direction of the extinct satellite the phonon branch goes up in frequency rapidly. The soft polarisation for this satellite wavevector is along $[1\ \bar{1}\ 0]$ and is not visible in the experiment. In the direction of the strong satellite the phonon branch is softer and almost flat between L and A.

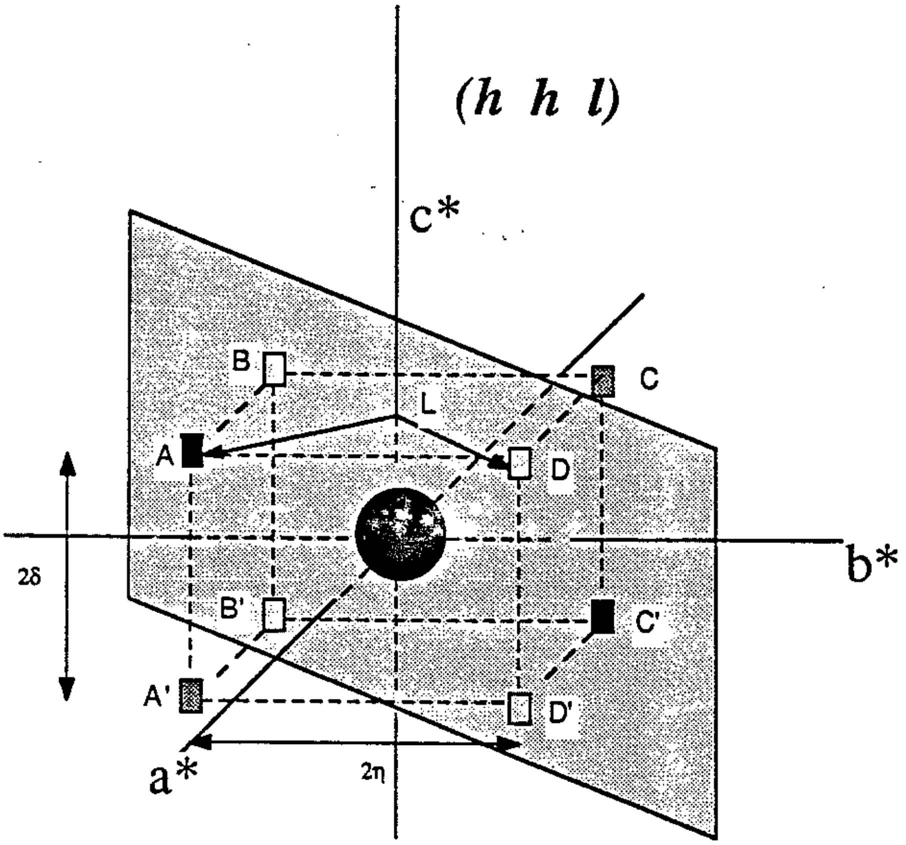

Figure 2a: Sketch showing the satellite arrangement around a (hhl) Bragg reflection. The shaded plane represents the experimental scattering plane. The strong satellites (A, A', C and C').lie outside the scattering plane. They are brought into reflecting position by tilt adjustements on the sample mount.

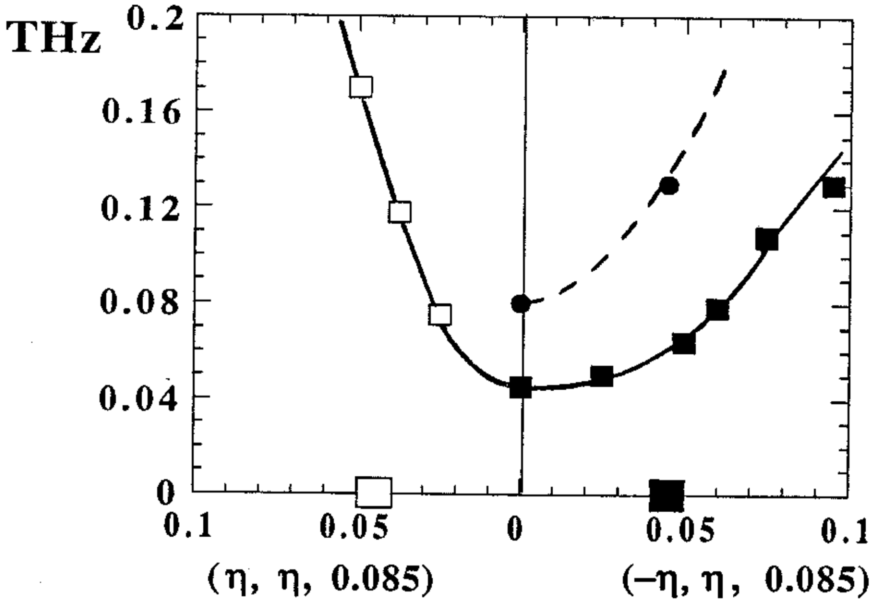

Figure 2b: TA phonon dispersion curves along the lines D→L (left hand side) and L→A (right hand side) at room temperature. Full circles correspond to the Nb-doped compound.

The difference between the two TA branches shown in Fig. 2b, illustrates the anomalous character of the mode observed near the strong satellite. Note however that no dispersion minimum is observed at the satellite position, contrary to what would be expected in a standard soft-mode picture. This is consistent with the dispersion measurements along Γ→A, reported by Fujishita et al.(3), which reveal a spoon-like anomaly but no dispersion minimum at the satellite position.

The TA anomaly may be viewed as a direct Kohn anomaly or as resulting from the interaction of the TA mode with an optic-mode Kohn anomaly(16). In Figs. 3a and 3b we study the temperature dependence of the soft TA branch, respectively, at the L-point and at the satellite position.

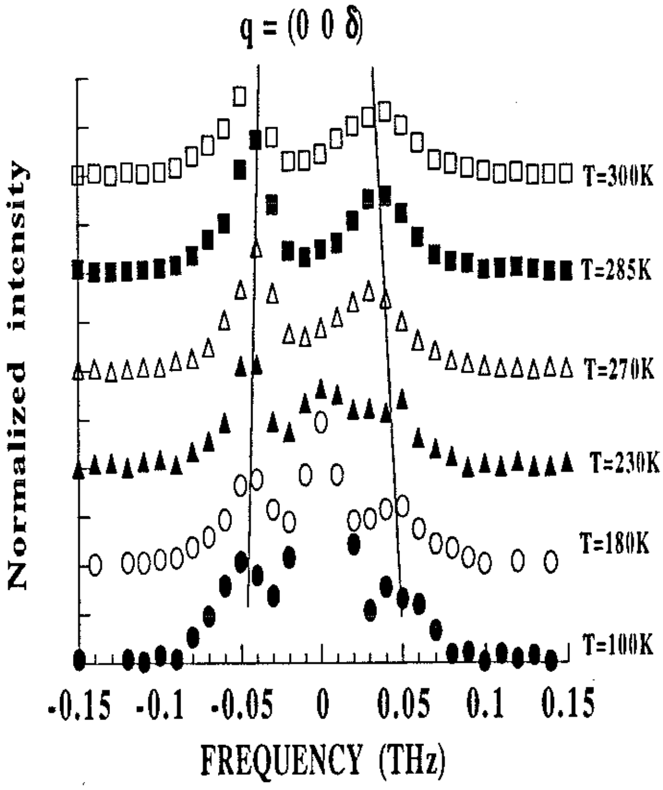

Figure 3a: Constant-Q scans at the L-point (2,2,4.085) below and above Tp. Vertical scales are normalized by a factor proportional to temperature, to account for the effect of varying thermal population factors.

At the L-point, the doubly-degenerate TA mode at 45±10 GHz shows no measurable temperature variation between 300 K and T_P = 253

K. Below T_P, the spectra in Fig. 3a show a growing elastic contamination, which arises from the A and C satellites broadened by finite vertical Q-resolution (cf. Fig. 2a). Otherwise, the inelastic lineshape is unchanged. The energy-integrated inelastic intensity varies as T, as expected from the thermal population factor and the vertical scales for the scans in Figs. 3a and 3b have been normalised accordingly.

A somewhat different behaviour is observed in Fig. 3b, for constant-Q scans at satellite position A. The elastic component corresponds to the satellite intensity at low temperatures, and to the central peak above T_P. The inelastic response shows some softening as $T \rightarrow T_P$, as well as an increase in phonon damping. Below T_P, the spectra can be fitted assuming a single oscillator response with same oscillator strength (i.e. phonon structure factor) as above T_P.

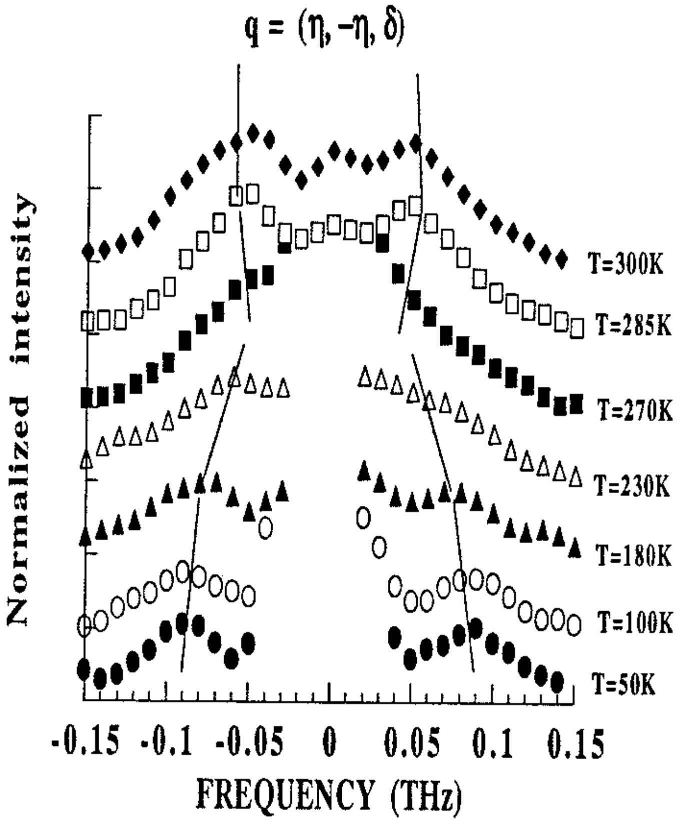

Figure 3b: Constant-Q scans at the satellite position (A-point in fig. 2a) above and below T_P.

The spectra in Fig. 3b have been analyzed using a damped harmonic oscillator response function, convoluted with the instrumental energy resolution (25 GHz fwhm). The results of the analysis are plotted in Fig. 4. The phonon energy decreases close to T_P and at the same time the damping increases. Below Tp one recovers the same response as above, keeping the same structure factor at all temperatures. We find no indication for a change in lineshape associated with a splitting of the TA response into phase and amplitude modes, as would be expected for a purely displacive transition.

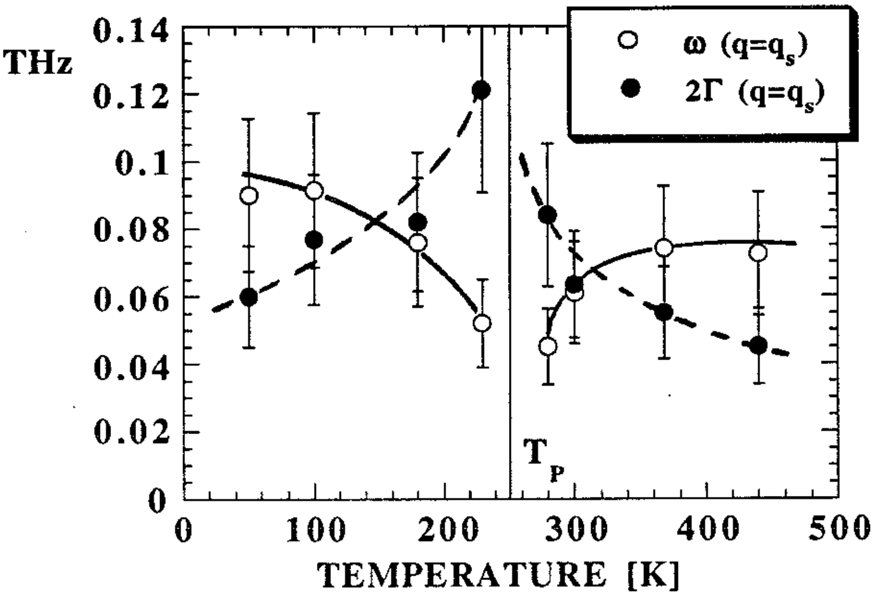

Figure 4: Temperature dependence of TA phonon frequency and damping at the satellite position.

Although the TA mode anomaly is only weakly temperature dependent, it turns out to be sensitive to doping. Some of the measurements described above were repeated on a 0.4% Nb-doped sample. As shown in (I), such a low Nb-concentration already has a dramatic influence on the Peierls transition and on the nature of the low-temperature state. In Figs. 5a and 5b we compare constant-Q scans at the L-point and at the satellite position, respectively, for the pure and doped compounds, at room temperature. The phonon frequencies are shifted from 45 GHz in the pure, to 80 GHz in the doped compound at the L-point, and from 60 GHz to 130 GHz at the A-point. No change is observed when cooling the doped sample down to 150 K.

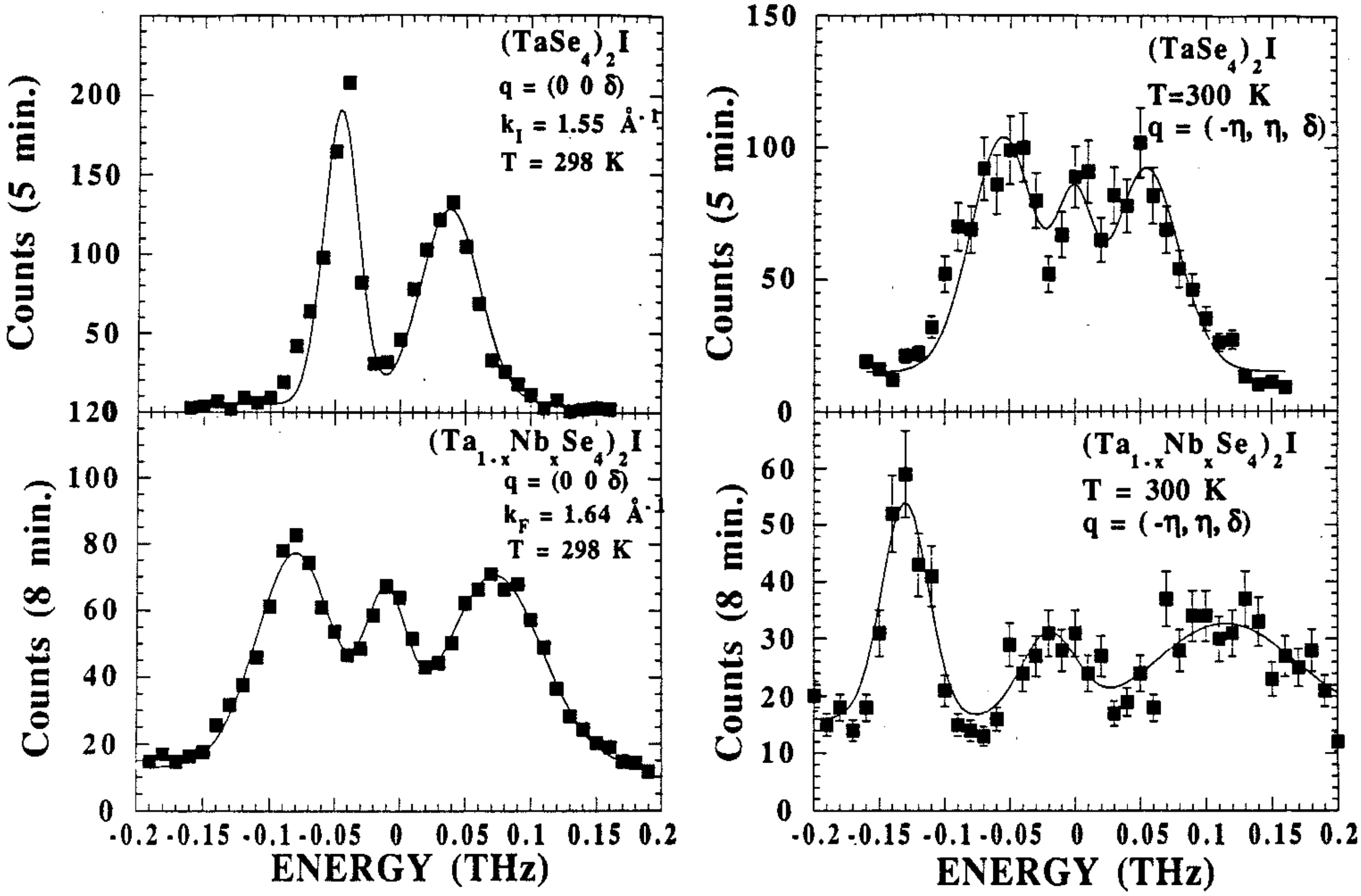

Figure 5:(a) Room temperature constant-Q scans at the L-point in the pure compound (above) and in the doped compound (below). (b) Room temperature constant-Q scans at the A-point in the pure compound (above) and in the doped compound (below).

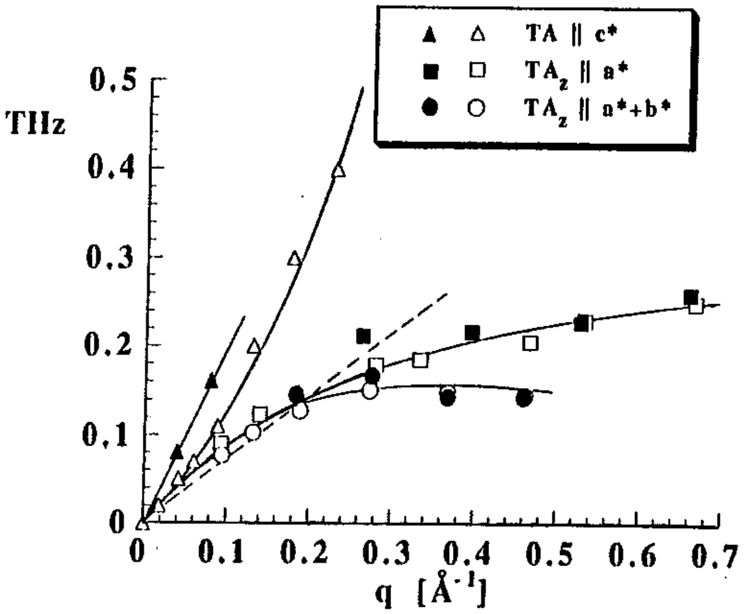

Figure 6: Phonon dispersion curves for phonon modes having v_{44} as sound velocity at room temperature. Open (closed) symbols represent measurements in the pure (doped) compound.

We have measured the flat TA_Z phonon branch in the doped compound along the a* and a*+b* directions. The results, plotted in Fig. 6, show that this sheet remains identical to that measured on the pure compound. Thus the frequency changes on doping appear to be confined to a small region around the Brillouin zone center.

4. Discussion and conclusions

In this paper we have attempted to characterize the low energy excitations at and around the wavevector of the incommensurate structure. The only hint of a phase transition as far as the dynamics is concerned lies in the limited softening of the acoustic phonon branch close to T_P. We have not observed softening of anyone of the lower frequency optic modes, in particular the TO mode of same polarisation, as initially proposed by Sugai et al.(16)

The softening of the acoustic phonon does not have a critical character. Critical behaviour is observed on the elastic (or unresolved quasielastic) central peak whose intensity and correlation lengths diverge on approaching T_P. This and the absence of decoupling between phase and amplitude modes below T_P, lead us to place the phase transition in $(TaSe_4)_2I$ in the order-disorder class.

The existence of Peierls transitions with order-disorder dynamics has been predicted by Aubry and coworkers(17,18), in the context of strong coupling theory. Beyond a critical value k_C of the electron-phonon coupling parameter k (cf. eq. 4), the ground state of the interacting electron-phonon system cannot be calculated starting from the unperturbed metallic state. This "non-analytical" regime is characterized by the existence of localised electronic states (bipolarons) strongly pinned to the lattice. The normalized electronic eigenstate of the bipolaron is given by:

$$\Psi(x) = \frac{k}{2\sqrt{2}} \frac{1}{cosh\left(\frac{k^2 x}{4}\right)} \qquad (3)$$

where the parameter k is defined as:

$$k = \lambda \sqrt{\frac{2}{t\, M\omega_0^2}} \tag{4}$$

ω_0 and M are the constant frequencies and masses of identical oscillators located at each lattice site(*), t is the electronic exchange coupling between neighbouring sites and λ is the usual dimensionless electron-phonon coupling constant.

In such a picture, the energy scale corresponding to the Peierls gap 2Δ is the bipolaron formation energy. This latter energy is closely related to the pinning energy of a single bipolaron to the lattice (Peierls-Nabarro potential E_{PN}). The activated nature of the electrical conductivity below T_P, as well as above T_P ("pseudo-gap"), is accounted for in terms of bipolaron hopping. The Peierls transition corresponds to the ordering temperature of the bipolaronic gas. The order of magnitude of k_BT_P is fixed by bipolaron interaction energies which, consistently, may be assumed to be much lower than the bipolaron formation energy, hence $k_BT_P \ll 2\Delta$ ($2\Delta = 11.4k_BT_P$ in $(TaSe_4)_2I$).

In the strong-coupling limit, the dynamics associated with the Peierls transition is of the Ising pseudo-spin type. The discrete Ising variable corresponds to the occupation of a given lattice site by the center of a bipolaron. The collective dynamics near T_P is expected to be relaxational, with a characteristic microscopic relaxation time proportional to $\exp\{E_{PN}/k_BT_P\}$ and thus quite long on a phonon time-scale. The same applies to the phase fluctuation spectrum below T_P.

The above predictions are in qualitative agreement with our experimental observations in pure $(TaSe_4)_2I$. Concerning the effect of doping, however, one finds it difficult to account for the strong influence of dilute isoelectronic impurities, within a localised-electron framework.

(*) The calculation were performed in the framework of the Holstein model (chosen for convenience) but the physical concepts are general.

The primary effect of adding 0.4% Nb impurities, should be to localise the conduction electron wavefunctions over chain segments with an average length of the order of the average distance between impurities along a given chain (≈ 800 Å). If, however, the electronic wavefunctions are *already* localized over a much smaller distance, as implied in Aubry's strong-coupling picture, one would not expect impurities to play a major role. Yet, our experimental results show that dilute isoelectronic doping renormalises the room-temperature acoustic phonon spectrum, in addition to destroying the coherence of the low-temperature CDW-state.

The effect of doping is more readily understood in the context of conventional weak-coupling theory. The difficulty in that case, lies in the large value of the Peierls gap, on the scale of $k_B T_P$. That and the existence of a "pseudo gap" above T_P, cannot be understood without assuming a regime of strong 1D fluctuations above T_P. Such a regime is not seen in our diffuse neutron scattering data (I), nor in the x-ray data of Fujishita et al.(19), on isomorphous $(NbSe_4)_2I$.

One way out of the impasse, is to postulate that different types of atomic displacements couple to the electronic CDW fluctuations in the 1D and 3D regimes. Specifically, one may postulate a high temperature regime where the CDW fluctuations involve *intrachain* optic modes. For a quarter-filled d_{z^2} conduction band, an obvious candidate would be a Ta-tetramerisation mode with Ta displacements along **c**. By analogy with the flat TA_z mode, the z-polarised intrachain optic mode may be only weakly dispersive in the directions normal to the chains, thus allowing for a regime of uncorrelated CDW fluctuations at high temperatures.

When transverse (anti-phase) correlations develop, the diffuse scattering associated with the optic-mode displacements concentrates around crystallographic Γ-points ($q_s \approx 0$). In that (3D) regime, gradient interaction terms between optic and acoustic degrees of freedom become important. They give rise to two effects:

1. the fluctuating displacements acquire a strong acoustic component, which in our case, we must assume to be dominant, at least below room temperature.

2. the critical fluctuations concentrate around positions (i.e. the satellite positions) which are close but distinct from the Γ-point.

In this model, the values of the satellite wavevector components are determined by the gradient-interaction terms. Similar phenomenological models have been developed in the context of incommensurate long-wavelength modulated dielectrics, such as quartz(20), sodium nitrite and thiourea(21). The present model, which will be formalised in a forthcoming publication, is also related to the TA-TO coupled-mode model of Sugai et al.(16), except that the modes which are coupled here have quite different polarisations and are not related via a zone folding operation.

The 1D intrachain fluctuations should give rise to detectable x-ray diffuse scattering. Fujishita et al.(22) mention the presence of a diffuse scattering component, located in reciprocal planes of integer index l, whose origin was not established experimentally. One difficulty in detecting and identifying the scattering associated with the 1D intrachain fluctuations, is that it is not expected to be intense near strong satellite positions, since the nature of the atomic displacements involved in each case is quite different. Let us illustrate this point by assuming an intrachain mode involving Ta displacements only. For a tetramerisation motion, the symmetry-related Ta ions at (0,0,0) and (0,0,1/2) move in opposite directions. The corresponding diffuse scattering will only be visible in odd reciprocal planes (l=2n+1), and will be extinct near the (224) position. Additional diffuse x-ray scattering work is clearly required.

Finally, concerning the interpretation of the 30 GHz $\sigma(\omega)$ resonance, we argue that in the context of an order-disorder phase transition at T_P, the dynamics of the phase and amplitude fluctuations below T_P, is necessarily relaxational. In view of the present neutron data, the $\sigma(\omega)$ resonance should best be referred to as an activated TA phonon, although the word phason or phase phonon is sometimes used in reference to CDW-activated optic modes(23). The results on the doped sample suggest that the mode is strongly coupled to the conduction electron states. In particular, its frequency increases on doping, in a way which is similar to the pinned phason of the displacive case. The higher frequency of the neutron mode, both for the nominally pure and for the doped samples, probably reflects the lower quality of the larger samples used in the neutron measurements.

We are pleased to thank P. Boutrouille and A. Brochier for their kind assistance in the experiments, and J.C. Lasjaunias for communicating us thermal conductivity results prior to publication. One of us, J.E.L., also acknowledges financial support from the Spanish Ministery of Education and Science.

References

1. M. Saint-Paul, P. Monceau and F. Levy, Sol. State Commun **67**, 581 (1988).

2. P. Monceau, L. Bernard, R. Currat, F. Levy and J. Rouxel, Physica **136B**, 352 (1986).

3. H. Fujishita, S.M. Shapiro, M. Sato and S. Hoshino, J. Phys. C **19**, 3049 (1986).

4. T.W. Kim, D. Reagor, G. Gruner, K. Maki and A. Virosztek, Phys. Rev. **B40**, 5372 (1989).

5. S. Donovan, Y. Kim, B. Alavi, L. Degiorgi and G. Gruner, Sol. State Commun. **75**, 721 (1990).

6. T.W. Kim, S. Donovan, G. Gruner and A. Philipp, Phys. Rev. **B43**, 6315 (1991).

7. N.I. Lebedev, A.P. Levanyuk and A.S. Sigov, Sov. Phys. JETP **65**, 140 (1987).

8. P. Monceau, L. Bernard, R. Currat and F. Levy, Physica **B156-7**, 20 (1989).

9. W.H. Stockmayer and C.E. Hecht, J. Chem. Phys. **21**, 1954 (1953); and ref. therein..

10. R. Nicklow, N. Wakabayashi and H.G. Smith, Phys. Rev. **B5**, 4951 (1972).

11. J.E. Lorenzo, R. Currat, P. Monceau, B. Hennion and F. Levy (to be published).

12. K. Biljakovic, J.C. Lasjaunias, F. Zougmore, P. Monceau, F. Levy, L. Bernard and R. Currat, Phys. Rev. Lett. **57**, 1907 (1986).

13. A. Smontara, J,C. Lasjaunias, P. Monceau and F. Levy, in press.

14. J.E. Lorenzo, R. Currat, P. Monceau, B. Hennion and F. Levy (to be published).

15. W.N. Creager, P.L. Richards and A. Zettl, Phys. Rev. **B44**, 3505 (1991).

16. S. Sugai, M. Sato and S. Kurihara, Phys. Rev. **B32**, 6809 (1985).

17. S. Aubry and P. Quemerais, in "Low Dimensional Electronic Properties of the Molybdenum Bronzes and Oxides", pp.295-405; C. Schlenker ed., Kluver Academic Press (1989).

18. S. Aubry, G. Abramovici and J.L. Raimbault, J. Stat. Phys. **67**, 675 (1992).

19. H. Fujishita, M. Sato, S. Sato and S. Hoshino, J. Phys. C **18**, 1105 (1985).

20. T.A. Aslanyan and A.P. Levanyuk, Sol. State Commun. **31**, 547 (1979); T.A. Aslanyan, A.P. Levanyuk, M. Vallade and J. Lajzerowicz, J. Phys. C **16**, 6705 (1983).

21. A.P. Levanyuk and D.G. Sannikov, Sov. Phys.: Solid State **18**, 1122 (1976).

22. H. Fujishita, M. Sato and S. Hoshino, Sol. State Commun. **49**, 313 (1984).

23. M.J. Rice, Phys. Rev. Lett. **37**, 36 (1976); Sol. State Commun. **25**, 1083 (1978).

CHAPITRE V

Neutron scattering studies on the quasi-one dimensional compounds $(TaSe_4)_2I$ and $(NbSe_4)_3I$: III Phonon density of states and low temperature specific heat.

J.E. Lorenzo R. Currat and A.J. Dianoux
Institut Laue-Langevin, 38042 Grenoble-Cedex, France.

P. Monceau
Centre de Recherches sur les Très Basses Températures, CNRS, 38042 Grenoble-Cedex, France.

F. Levy
Institut de Physique Appliquée, Ecole Polytechnique Fédérale de Lausanne, CH-1015, Lausanne, Switzerland.

Abstract

We report on neutron time-of-flight measurements of the generalised phonon density-of-states (PDOS) in two compounds, $(NbSe_4)_3I$ and $(TaSe_4)_2I$, with chain-like structure. A strongly anharmonic behaviour is observed in $(NbSe_4)_3I$, leading to a reduced anisotropy at low temperature. We assign the origin of a low-frequency step-like structure in the PDOS of both compounds to a flat transverse acoustic sheet with in-chain polarisation. We propose a simple dispersion curve model which accounts for the observed low-frequency PDOS structure and which can be adjusted to reproduce the low-temperature specific heat anomaly in $(TaSe_4)_2I$.

1. INTRODUCTION

In the preceding two papers, referred to as I and II, we have discussed elastic (I) and inelastic (II) neutron scattering results on pure and doped $(TaSe_4)_2I$ single crystals. In the present paper we describe phonon density of states (PDOS) measurements in $(TaSe_4)_2I$ and $(NbSe_4)_3I$, by neutron time-of-flight spectrometry. These two compounds are structurally similar (see Fig. 1), but have very distinct electrical transport properties(1). While $(TaSe_4)_2I$ undergoes a Peierls transition (T_P=250-260 K) to a low-temperature CDW-state(2), $(NbSe_4)_3I$ is already semiconducting at room temperature. A ferrodistortive structural instability(3,4) occurs at T_C=273 K, below which the $(NbSe_4)_3I$ conductivity is still activated, but with a *smaller* gap(3).

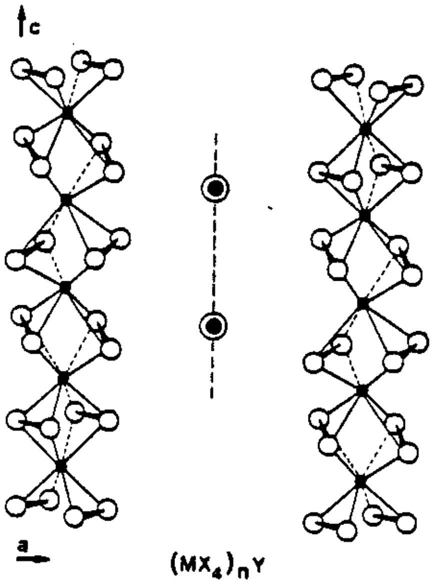

Figure. 1. General $(MX_4)_nY$ structure; M = Nb, Ta; X = S, Se; Y = halogen. The parallel $(MX_4)_\infty$ and halogen chains are arranged in a quadratic pattern.

Band calculations(5) show that the conduction band in both compounds is built from Ta (Nb) d_{z^2} orbitals, with overlapping lobes directed along the tetragonal c-axis (chain axis). The magnitude of the electronic gap can be correlated with the dispersion in the -M-M- bond lengths along the $(MSe_4)_\infty$ chains (M=Nb,Ta). In $(NbSe_4)_3I$ at room temperature, the Nb-Nb distances are strongly modulated with the periodicity of the iodine repeat unit. In the low-temperature structure(6), the Nb-Nb distances are more uniform and as a result, the electronic gap is reduced. In $(TaSe_4)_2I$ the iodine arrangement does not modulate the Ta-Ta distances at room temperature. The pseudo-metallic character of the conductivity(7) in $(TaSe_4)_2I$ above T_P ("pseudo-gap"), suggests the existence of 1D fluctuations involving a modulation of the Ta-Ta distances, as discussed in (II). The detailed analysis of the incommensurate structure below T_P, has not been yet attempted.

One purpose of this study is to explore the effect of electron-phonon interactions on the phonon spectrum of these two systems. In view of the complexity of the crystallographic structures involved (22 and 64 atoms per cell, in the Ta and Nb compounds, respectively), the study of the individual phonon dispersion branches by neutron 3-axis spectrometry is necessarily limited to the low frequency range. In (II) we report on such dispersion curve measurements for the acoustic and lowest optic branches ($\nu < 2$ THz), in $(TaSe_4)_2I$. Similar work on the Nb compound is presented in the following publication. For the higher frequency range, only the phonon density of states (PDOS) can be determined experimentally and the neutron time-of-flight (TOF) technique(8), on powdered samples, is the most practical method.

The information which can be extracted from the PDOS is of an averaged nature. It is often not as detailed as would be required for a proper analysis of the physical problem at hand. This point is well illustrated by recent literature on PDOS measurements in high-T_C superconductors(9-12). The TOF technique is nevertheless a powerful tool for exploratory and comparative studies.

An additional motivation for the present study is related to the results of specific heat measurements below 8 K on both compounds(13). Whereas in $(NbSe_4)_3I$ specific heat data show a normal Debye behaviour, in $(TaSe_4)_2I$ no Debye regime can be seen and a strong anomaly centered at 1.8 K appears in the C_P/T^3 versus temperature plot. This anomaly was initially interpreted as originating from phason-like excitations associated with the incommensurate CDW-state(13).

The phason interpretation of the C_P/T^3 anomaly in $(TaSe_4)_2I$ was based on a phason dispersion model with a lower cut-off frequency of 45 GHz, close to the frequency of the "pinned phason" resonance reported in ac conductivity measurements(14,15). The upper cut-off frequency of 270 GHz, corresponding to a normal phonon frequency at the position of the CDW-wavevector, was deduced from neutron scattering data(16).

As discussed in (II), the low-temperature neutron scattering spectra in $(TaSe_4)_2I$, do not show evidence of a dispersion minimum at the CDW wavevector $\mathbf{q}_s$. The observed resonance in ac conductivity may be ascribed to the CDW-activation of a transverse acoustic phonon of wavevector $\mathbf{q}_s$ and weakly temperature-dependent frequency. The observation of a similar specific heat anomaly on Nb-doped samples(17), casts further doubts on the validity of the phason model, as both the conductivity(18) and neutron spectra indicate a strong renormalisation of the resonance frequency with doping.

In what follows we propose a different interpretation of the specific heat anomaly, based on the existence of a sheet of low-frequency transverse acoustic modes polarised along the chain direction (TA_z) and propagating in the basal plane (cf. Fig. 1 in Ref.(II) and Fig. 8 below). In Sect. 3 we present a simple dynamical model which captures the essence of the problem and enables one to interpret the observed deviation of the TOF spectra from the Debye ω^2–law at low frequencies. Furthermore, we find that a trial PDOS distribution, consistent with the observed TOF spectra can be used to reproduce quantitatively the C_P/T^3 data in the range from 0.5 to 8 K.

The room-temperature phonon dispersion curves in $(NbSe_4)_3I$ show the same flat and low-frequency TA_z sheet. However, below the structural transition ($T<T_C=273$ K), a renormalisation of the entire dispersion sheet takes place. This is seen both in the single crystal dispersion curve data (see following paper) and in the present TOF spectra. Below 100 K, the deviation of the TOF spectra from Debye behaviour is considerably washed out, consistent with the absence of a low-temperature specific heat anomaly in $(NbSe_4)_3I$.

2. EXPERIMENTAL

Time-of-flight experiments were carried out on the IN6 spectrometer at Institute Laue-Langevin (Grenoble, France), operated in the neutron energy gain mode (up-scattering), with an incident neutron energy of 3.12 meV (λ = 5.12 Å). This instrument includes a total of 337 calibrated detectors spanning a range of scattering angles (2θ) from 10 to 115°.

The sample, in powdered form, is placed in an thin-walled aluminium cell. Empty cell runs are performed at several temperatures in the temperature range of the measurements (1.5 to 480 K). These, together with sample transmission measurements are used to correct the data from sample container contributions. The 1.5 K spectra are free from inelastic signal (due to the vanishing Bose factor) and are used for background correction purposes. Spurious "inelastic" signals arising from multiple elastic scattering processes can thus be eliminated.

The procedure to extract a phonon frequency distribution from time-of-flight data involves the following steps:

(i) Transform the TOF cross-sections into a symmetrized scattering function. For each detector (or small grouping of detectors), the scattering function is given as:

$$\tilde{S}(\theta,\omega) = \frac{\partial^2\sigma}{\partial\Omega\,\partial t}\,\frac{t^4}{2t_0^3\,E_0}\,exp\left\{-\frac{h\omega}{2k_BT}\right\} \qquad (1)$$

where t denotes the time of flight (t_0 for elastically scattered neutrons) and E_0, $E(t)$, the incident and final neutron energy. The neutron momentum transfer, Q, the energy transfer $\hbar\omega = E_0 - E(t)$ and the detector scattering angle 2θ are related through:

$$Q^2 = A\,\left(2E_0 - \hbar\omega - 2\sqrt{E_0^2 - \hbar\omega E_0}\;cos\;2\theta\right) \qquad (2)$$

with A = 0.482 meV^{-1}Å^{-2}.

(ii) Define the spectral distribution $P(\alpha,\beta)$

$$P(\alpha,\beta) = 2\beta \sinh\left(\frac{\beta}{2}\right)\frac{\widetilde{S}(\alpha,\beta)}{\alpha} \tag{3}$$

with the reduced variables:

$$\alpha = \frac{\hbar^2 Q^2}{2\, M\, k_B T}$$

$$\beta = \frac{\hbar\omega}{k_B T} \tag{4}$$

and M an average atomic mass. At this stage the Debye-Waller and multiphonon corrections are performed in a self-consistent way and lead to a corrected spectral distribution, $P'(\alpha,\beta)$.

(iii) The phonon density of states is derived from the corrected spectral distribution $P'(\alpha,\beta)$ by summing over the various detector banks:

$$G(\omega) = \sum P'(\alpha,\beta)$$

For polyatomic systems, with n atomic species, each with concentration c_i, scattering cross section σ_i and atomic mass m_i, we obtain the generalised or neutron-weighted density of states defined as:

$$G(\omega) = \frac{\sum_{i=1}^{n} \frac{c_i\, \sigma_i}{m_i}\, g_i(\omega)}{\frac{\sigma}{M}} \tag{6}$$

where $g_i(\omega)$ is the partial density of states associated with species i. M and σ are the molecular mass and scattering cross section. Tables I, II, III illustrate the weighting factor values for $(TaSe_4)_2I$ and $(NbSe_4)_3I$. The Se atoms are responsible for, respectively, 90% and 85% of the measured intensities, due to their relative abundance and favorable σ_{Se}/m_{Se} ratio. Thus, the experimental phonon density of states corresponds essentially to $g_{Se}(\omega)$, i.e. to a projection of the true PDOS, in which the contribution from each vibrational mode is weighted according to the proportion of Se displacements present in the mode eigenvector.

	σ_i (barns)	m_i (at. units)	σ_i/m_i
Se	8.31	78.9	0.105
Nb	6.255	92	0.067
Ta	6.00	180	0.0334
I	3.5	127	0.0275

Table I. Coherent scattering cross-sections, σ_i, atomic masses, m_i, and scattering weights, σ_i/m_i, of Se, Nb, Ta and I .

$(NbSe_4)_3I$ (M = 1350)

	$c_i\ \sigma_i/m_i$	%
Nb	0.201	13.5
Se	1.26	84.6
I	0.0275	1.9
	1.489	100

Table II. Relative scattering weights of elements in $(NbSe_4)_3I$

$(TaSe_4)_2I$ (M = 1118)

	$c_i\ \sigma_i/m_i$	%
Ta	0.0668	7.15
Se	0.84	89.9
I	0.0275	2.95
	0.934	100

Table III. Relative scattering weights of elements in $(TaSe_4)_2I$

The above procedure is strictly justified for incoherent scatterers only. For purely coherent scatterers, as is the case here, the validity of the method rests on the assumption that the Q-averaged coherent cross-section approximates the incoherent cross-section (so-called incoherent approximation(19)). At large energy transfers, the effective momentum transfer Q is always large (cf. eq. 2 with $|\hbar\omega| >> E_0$). The combined effect of powder averaging and detector averaging always guarantee the applicability of the incoherent approximation in that limit.

In the limit of low energy transfers, the size of the averaging Q-space volume depends on E_0 and on the detector angular range. The size of this volume must be compared to the dimensions of the sample's Brillouin zone. In the present case, with unit cell sizes of the order of 10^3 $\AA^3$ or more, one obtains an averaging volume of the order of 10^2 Brillouin zones in the elastic scattering limit, which should be sufficient to guarantee a proper statistical averaging of the coherent cross-section.

3. RESULTS AND DISCUSSION

In Fig. 2, we compare the weighted PDOS of $(TaSe_4)_2I$ and $(NbSe_4)_3I$ at a temperature of 480 K, well above their respective critical transition temperatures. Both data sets are normalised to an area of unity. A cut-off energy of about 40 meV (1 THz = 4.13 meV = 33.3 cm^{-1}= 48 K), is observed in both cases, in agreement with infrared and Raman data. The cut-off is blurred by the poor TOF resolution at large energy transfers ($\hbar\Delta\omega$=0.1 meV at $\hbar\omega$=0; =1.3 meV at 10 mev; =6 meV at 35 meV, fwhm).

The two peaks centered at 29 and 34.5 meV in $(NbSe_4)_3I$ can be attributed, respectively, to Nb-Se and Se-Se dimer-stretching modes. The peak at 33 meV in $(TaSe_4)_2I$ may be equally attributed to Se-Se stretching modes, while the analogous Ta-Se stretching mode is shifted to lower energies. An estimation of this energy can be obtained through:

$$\omega_{Ta\text{-}Se} = \omega_{Nb\text{-}Se}\sqrt{\frac{M_{Nb+Se}}{M_{Ta+Se}}} \qquad (7)$$

where M_{Nb+Se} and M_{Ta+Se} are reduced masses. This locates the mode around 25.5 meV, i.e. in the tail of the band centered around 19 meV.

External modes are observed below 20 meV, with common features in both compounds. The sharper structures observed in the Nb-compound indicate the presence of dispersionless phonon branches. This in turn reflects the pronounced 1D character of the Nb-compound at high temperatures (see below).

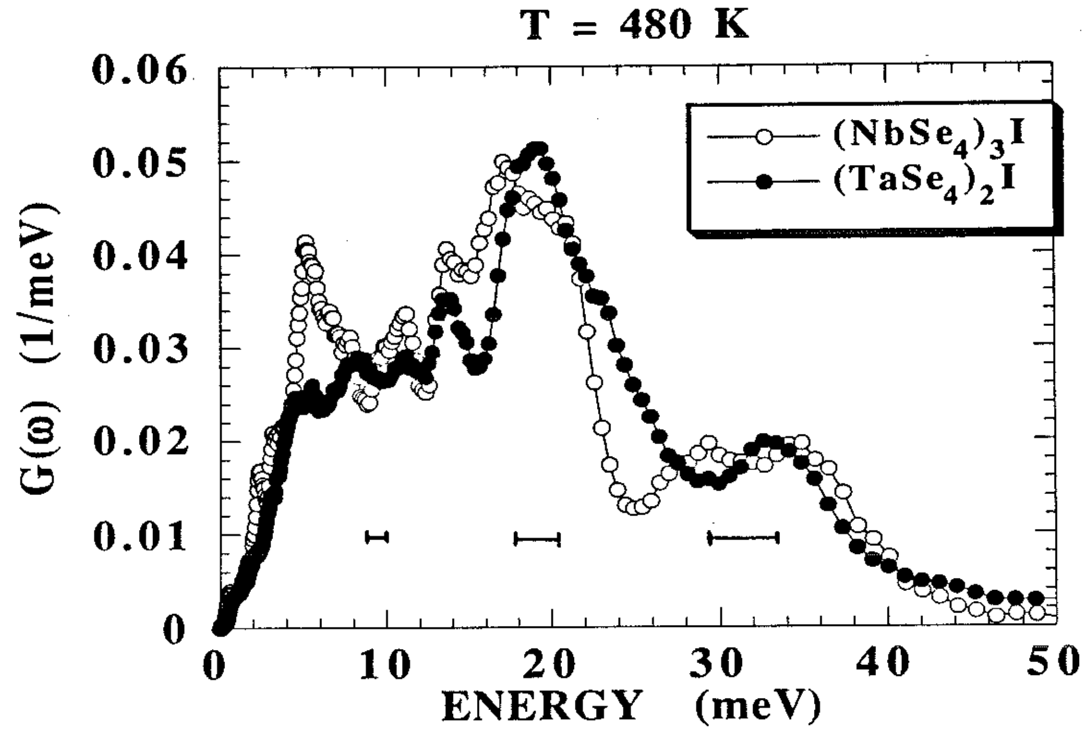

Figure. 2. Comparison of generalised phonon density-of-states in $(NbSe_4)_3I$ (open circles) and $(TaSe_4)_2I$ (closed circles). The two curves are normalised to unit area; T=480 K.

Density of states data were taken at 5 different temperatures (480, 300, 180, 100 and 50 K). However, at the lower temperatures, the statistical accuracy of the high frequency part of the spectra deteriorates, due to decreasing Bose occupation factors. As a rule of thumb, the energy transfer range which can be explored at any given temperature T, is of the order of 3-5 k_BT.

No significant changes are observed in $(TaSe_4)_2I$, between 480 K and 150 K (cf. Fig. 3). The phonon spectrum, as a whole, is insensitive to the onset of the Peierls modulated state (T_P=260 K). This picture contrasts with the picture which emerges from infrared and Raman work, where several new features are observed on cooling below T_P. Three new Raman modes are reported by Sugai et al.(20), at frequencies of 93 cm^{-1} (11.5 meV), 142 cm^{-1} (17.6 meV) and 192 cm^{-1} (23.8 meV). The first mode is assigned to a CDW-amplitude mode originating from an optic branch Kohn anomaly. However none of the observed frequencies appear to show any temperature dependence below T_P.

Similarly, far infrared measurements(21) detect four main absorption bands with A_2-symmetry at 38 cm^{-1} (4.7 meV), 78 cm^{-1} (9.6 meV), 149 cm^{-1} (18.5 meV) and 194 cm^{-1} (24 meV). Due to its large dipolar strength, the first absorption frequency was first described as an "optical phason"(21), and more recently as a "bound collective mode"(22) originating from the presence of polarisable impurities. Recent single crystal inelastic neutron experiments(23) confirm the presence of a polar branch at 36.7 cm^{-1}. However the mode frequency and oscillator strength are found to be unchanged between room temperature and 150 K. All these results suggest that the features observed in the optical spectra may correspond to the activation of existing excitations(24) as opposed to a true renormalisation of the high-temperature spectrum.

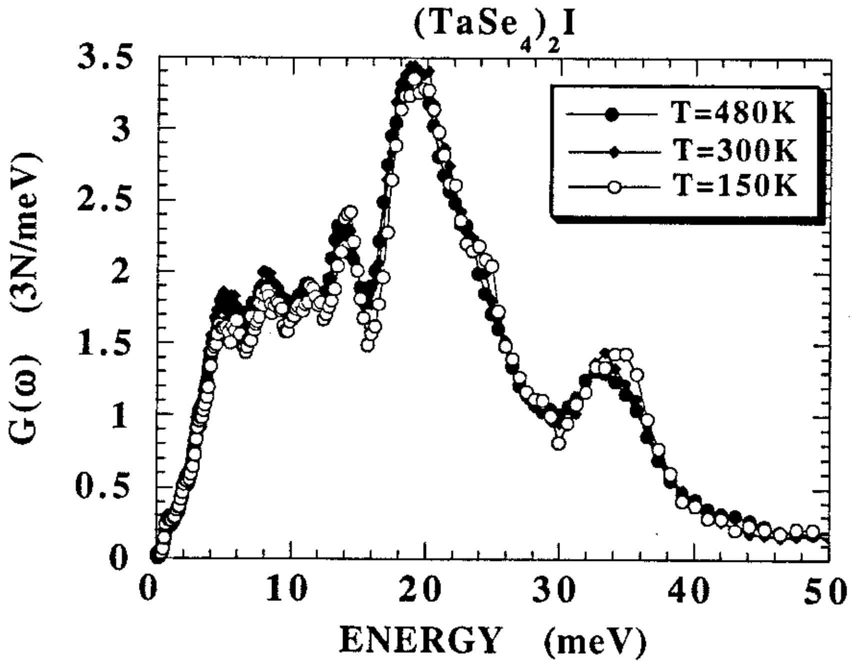

Figure 3. Temperature dependence of generalised PDOS in $(TaSe_4)_2I$.

Definite temperature effects are observed in Fig. 4 for the case of $(NbSe_4)_3I$. For example, the modes in the range 6-13 meV are enhanced on cooling while the band from 14 to 23 meV is significantly depressed. These variations appear to affect the relative strength of the various bands rather than their positions and shape. In order to quantify this, we have fitted the spectra in the interval 13-23 meV using two gaussian distributions centered at 17.4 and 21.2 meV. The temperature evolution of the spectrum can be accounted for through the variation of the height of the gaussians, their widths and positions being left constant. Peak and integrated intensities are plotted in Fig. 5. All the intensity variation is seen to occur between 100 K and room temperature.

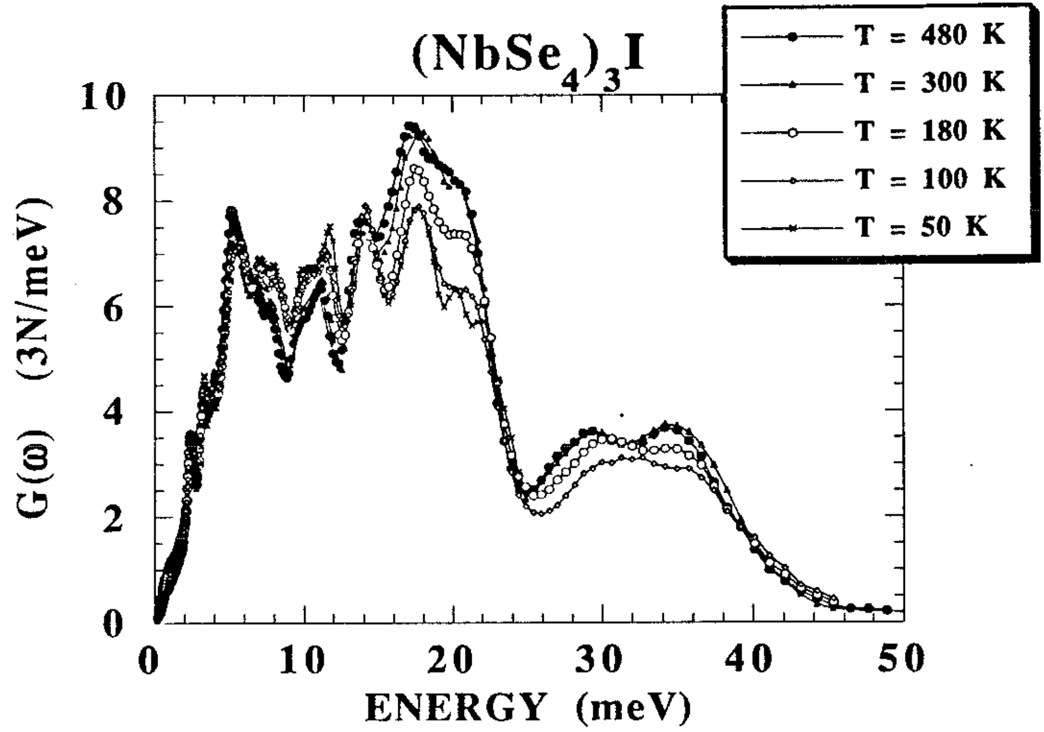

Figure 4. Temperature dependence of generalised PDOS in $(NbSe_4)_3I$.

The above intensity variations may arise from two independent sources:

(i) a change in mode eigenvectors with temperature. The neutron measured PDOS is weighted according to the proportion of Se displacements involved in each mode. This proportion may change with temperature, due to anharmonicity and to the structural transition at T_C.

(ii) a change in the anisotropy of the Debye-Waller factor. In the data analysis programme, the Debye-Waller factor is taken as isotropic, which is certainly not justified here, in view of the chain-like character of the structure. As a result some of the phonon bands are artificially enhanced, others depressed, depending on their polarisation. There is evidence from the low-frequency acoustic mode dispersion as well as from ultrasonic data (24), that the 1D character of $(NbSe_4)_3I$ is reduced in the low temperature phase, most of the change taking place between T_C and 100 K. The observed redistribution of intensity among the bands could then be associated with a reduction of the Debye-Waller anisotropy.

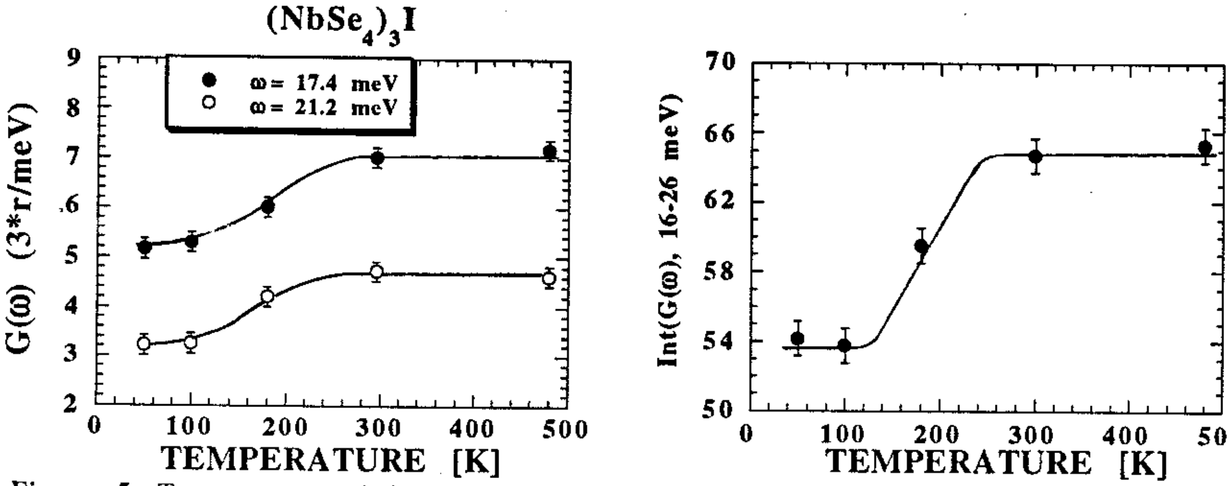

Figure 5. Temperature variation of specific features in the G(ω) curve from $(NbSe_4)_3I$: (left) intensity of structures centered on 17.4 and 21.2 meV; (right) integrated intensity between16 and 26 meV.

Both arguments imply that some of the mode frequencies must change with temperature. A change in mode eigenvectors or in the anisotropy of the Debye-Waller factors cannot take place without some change in mode eigenfrequencies. Why do these changes not give rise to observable shifts in the positions of the PDOS singularities?

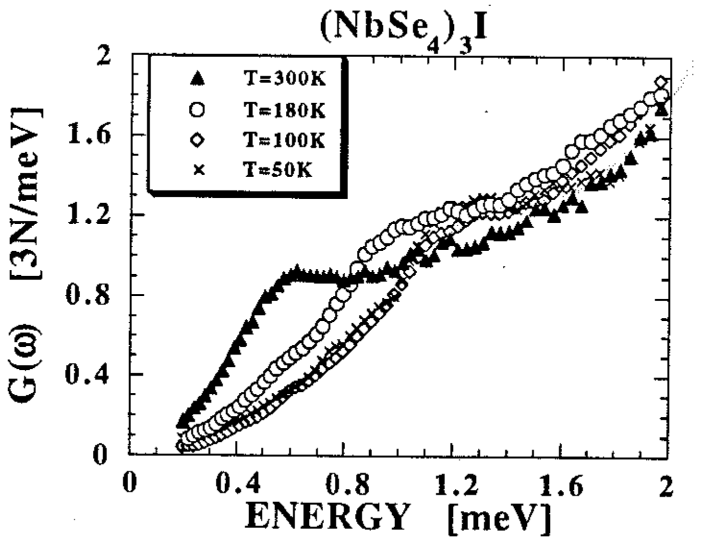

Figure 6 Temperature dependence of generalised PDOS in $(NbSe_4)_3I$ (low-frequency region).

One possible explanation is that these frequency changes are limited to the low frequency part of the spectrum. In particular, the Debye-Waller amplitudes are dominated by the contribution from the low-frequency branches. Fig. 6 shows the low-frequency part of the PDOS curves in $(NbSe_4)_3I$. Variations in the shape of the spectra are clearly observed. The structure at 0.5 meV in the room temperature data, moves to higher frequencies at low temperatures and becomes largely washed out. Such a large degree of anharmonicity, at very low frequencies, is indeed likely to affect the temperature dependence of the Debye-Waller amplitudes.

Fig. 7 shows the low-frequency PDOS from $(TaSe_4)_2I$. The same bump (or step) is observed as in the room temperature $(NbSe_4)_3I$ data. However, in the present case, no significant change in the spectrum is observed with temperature.

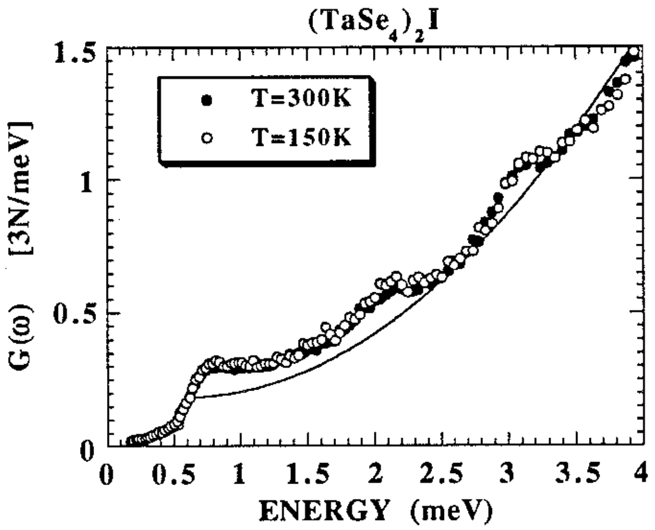

Figure 7. Generalised PDOS in $(TaSe_4)_2I$ (low-frequency region). The solid line corresponds to the g(ω) curve used in the specific heat calculation.

The interpretation of these effects is straightforward in reference to the low-frequency phonon dispersion curves deduced from single crystal work (see (II) and following paper). Fig. 8 shows the room temperature dispersion curves for both compounds. The remarkable feature, in both cases, is the very low-frequency transverse acoustic branch propagating in the (a*,b*) plane and polarised along the chain direction (TA_Z). These modes have frequencies in the range from 0.1 to

0.2 THz (0.4 to 0.8 meV), across the $(q_x,q_y,0)$ Brillouin zone plane, and a linear dispersion near the Γ-point. Away from the soft $q_z=0$ plane the TA_z dispersion can be expressed as:

$$\omega^2(q_x,q_y,q_z) = \omega^2(q_x,q_y,0) + v_{\parallel}^2 q_z^2 \tag{8}$$

where $v_{\parallel}$ is very close to the longitudinal sound velocity v_{33} along the chain direction.

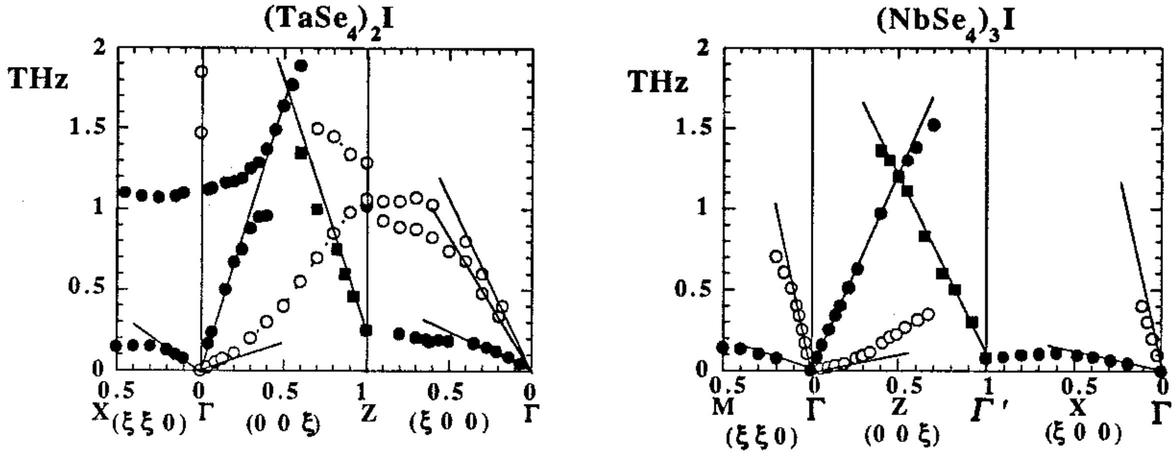

Figure 8. Low-frequency phonon dispersion curves from single crystal data: $(TaSe_4)_2I$, Ref. (II); $(NbSe_4)_3I$, following paper. Modes polarised along (normal to) the chain axis are shown as full (open) symbols. Full lines correspond to the sound velocities taken from ref. 26.

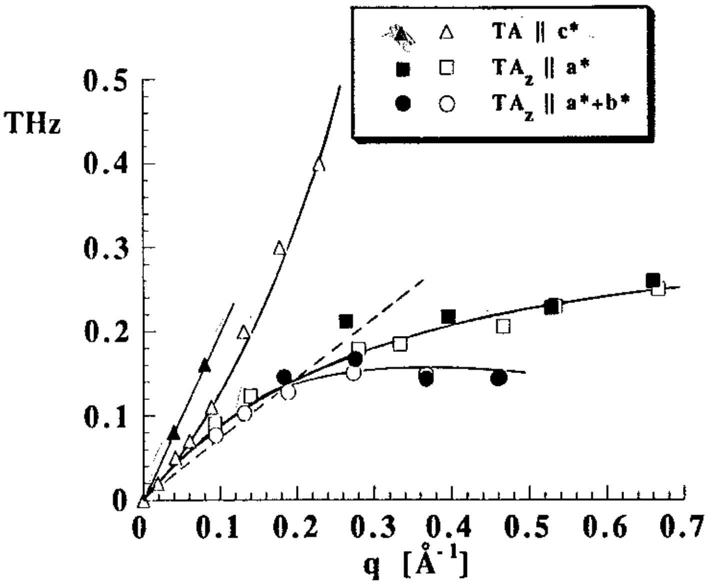

Figure 9. Comparison of phonon dispersion curves in nominally-pure (open symbols) and 0.4% Nb-doped $(TaSe_4)_2I$; T=300 K. The ultrasonic velocity$^{(26)}$ v_{44} is shown with broken line.

As discussed in (II), the dispersion of the TA_z modes in $(TaSe_4)_2I$ is unchanged from 300 K down to the lowest measured temperature (10K, for the (ξ,ξ,0) direction and 35 K for (ξ,0,0)). In contrast, the TA_z modes in $(NbSe_4)_3I$ are strongly renormalised below T_C. At low temperature, the Einstein-like character of the mode vanishes and a normal sinusoidal dispersion is observed (cf. Ref. 25 and following paper).

Fig. 9 shows the (ξ,ξ,0) and (ξ,0,0) dispersion of the soft TA_z branch in pure (open symbols) and Nb-doped (closed symbols) $(TaSe_4)_2I$ at room temperature. Measurements on the doped compound were limited to the plateau region with the aim to determine whether the plateau frequency was sensitive to doping. The data in Fig. 9 clearly show that this is not so. This result is consistent with the observation of a specific heat anomaly on the doped compound, in the same temperature range as for the pure compound(17). At the same time it shows that the soft TA_z sheet should not be viewed as an anomaly arising from electron-phonon interactions. The acoustic modes which are coupled to the conduction electrons, directly or indirectly, lie close to the Γ-point and have (x,y) polarisation. Those are the ones which are affected by doping, as seen in Fig. 9, for the doubly-degenerate TA mode propagating along c*.

To illustrate the connection between the low-frequency PDOS structure and the specific anomaly observed in $(TaSe_4)_2I$, we consider the (oversimplified) acoustic dispersion model shown in Fig. 10a.

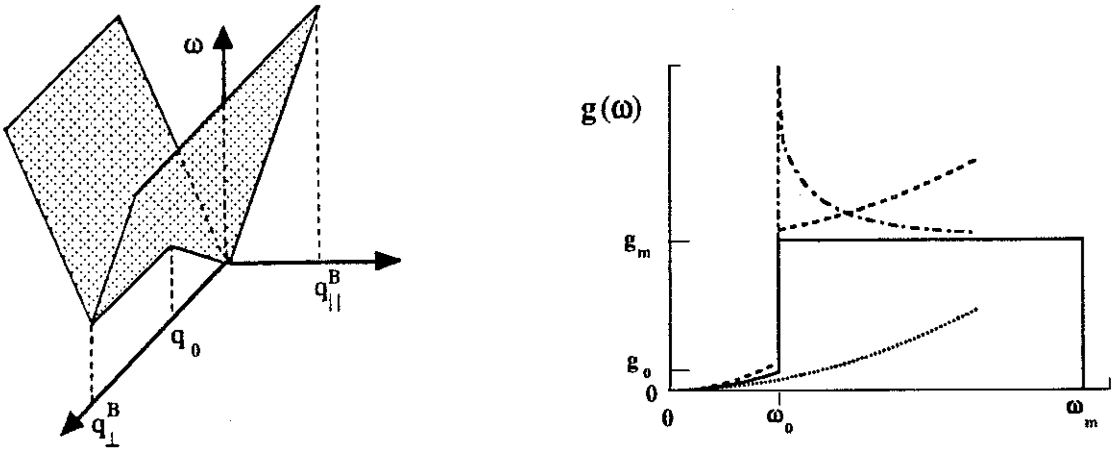

Figure 10 **(a)** Sketch of simplified dispersion curve model; **(b)** corresponding PDOS (solid line); effect of finite curvature along chain direction (dash-dotted line); contribution from other acoustic branches (dotted curve; estimate based on ultrasonic data in Ref. 26); total (broken curve). The numerical values relevant to $(TaSe_4)_2I$ are: $\omega_0 = 0.75$ meV; $\omega_m = 8$ meV; $g_m = 0.12$ meV^{-1}; $g_0 = 0.015 . meV^{-1}$.

We assume a single acoustic dispersion sheet with z-polarisation and isotropic dispersion in the basal plane:

$$\omega(\mathbf{q}) = \omega(q_{\parallel}, q_{\perp})$$

The cylindrical Brillouin zone is defined by:

$$|q_{\parallel}| < q_{\parallel}^{B} \quad ; \quad |q_{\perp}| < q_{\perp}^{B}$$

The dispersion in the basal plane is taken as linear, with velocity $v_{\perp}$ up to a cut-off wavevector q_0, and flat beyond q_0, while in the chain direction the dispersion is linear, with velocity $v_{\parallel}$, up to the zone boundary:

$$\omega(q_{\parallel}, q_{\perp}) = \begin{cases} v_{\perp} |q_{\perp}| + v_{\parallel} |q_{\parallel}| & \left(|q_{\perp}| < q_0 \ \ and \ \ |q_{\parallel}| < q_{\parallel}^{B} \right) \\ v_{\perp} q_0 + v_{\parallel} |q_{\parallel}| & \left(q_0 < |q_{\perp}| < q_{\perp}^{B} \ \ and \ \ |q_{\parallel}| < q_{\parallel}^{B} \right) \end{cases} \qquad (9)$$

The density of states $g(\omega)$ is defined as:

$$g(\omega) = C \int \frac{dS_{\omega}}{v} \qquad (10)$$

where v is the group velocity and the integral is taken over the equal frequency surface S_{ω} in q-space. The constant C is fixed by normalisation:

$$\int g(\omega)\, d\omega = 1 \qquad (11)$$

The group velocity takes on two values:

$$v = \begin{cases} \sqrt{v_{\perp}^{2} + v_{\parallel}^{2}} & \left(|q_{\perp}| < q_0 \ \ and \ \ |q_{\parallel}| < q_{\parallel}^{B} \right) \\ v_{\parallel} & \left(q_0 < |q_{\perp}| < q_{\perp}^{B} \ \ and \ \ |q_{\parallel}| < q_{\parallel}^{B} \right) \end{cases} \qquad (12)$$

The integration over S_ω is readily performed. To simplify the result even further, we make the additional assumption that the transverse velocity (of the order of v_{44}) is small compared to the longitudinal one (of the order of v_{33}). This approximation is well justified here since, for $(TaSe_4)_2I$, $v_{33} \approx 10.v_{44}$. Neglecting correction terms of the order of $(q_0 / q_\perp^B)^2$ in the normalisation constant we get:

$$g(\omega) = \begin{cases} \dfrac{1}{\omega_m} \left(\dfrac{\omega}{v_\perp q_\perp^B}\right)^2 & (\omega < \omega_0 = v_\perp q_0) \\ \dfrac{1}{\omega_m} & \left(\omega_0 < \omega < \omega_m = v_\parallel q_\parallel^B\right) \end{cases} \qquad (13)$$

Fig. 10b shows the type of PDOS which results from the above model, with values for the parameters q_0, $q_\perp^B$, $q_\parallel^B$, $v_\perp$ and $v_\parallel$ relevant to the case of $(TaSe_4)_2I$. After the initial Debye ω^2 regime for frequencies up to the plateau frequency ω_0, the PDOS jumps to a constant value up to the cut-off frequency ω_m.

The present model qualitatively accounts for the step observed in $(TaSe_4)_2I$ near 0.7 meV and in $(NbSe_4)_3I$ near 0.5 meV, at room temperature. The model can be improved in two respects:

(i) The dispersion relation in eq. 9 is not analytic at $q_\parallel=0$, and hence not realistic. A dispersion law as in eq. 8 , with a finite curvature along $q_\parallel$, for $q_\parallel \approx 0$, would be more physical. This would transform the step at ω_0 into a singularity, as sketched in Fig. 10b (dash-dotted line). When convoluted with instrumental resolution, the net result will be an enhancement of the step.

(ii) Before any comparison with experiment can be made, the contribution from the other two acoustic sheets, with basal plane polarisation, should be included in the calculated PDOS. This contribution may be assumed to be of the normal Debye-type, with an average group velocity intermediate between v_{44} and v_{33} (dotted line in Fig. 10b). The dashed line in Fig. 10b illustrates the behaviour of the total PDOS, including the estimated contribution from the normal branches.

The neutron data shown in Figs. 7 and 3, have been used to calculate the low temperature specific heat in $(TaSe_4)_2I$:

$$C_v\,(T) = \frac{R}{M} \int \left(\frac{\hbar\omega}{2k_BT}\right)^2 csch^2 \frac{\hbar\omega}{2k_BT}\; g\,(\omega)\; d\omega \tag{14}$$

with R the gas constant ($8.314\ 10^7$ erg.mole^{-1} K^{-1}) and M the primitive cell molar mass (2240 g mole^{-1}). The result is shown in Fig. 11a (dashed curve). We should stress that the neutron data are independently normalised with the help of:

$$\int g(\omega)\, d\omega = 3N \tag{15}$$

where N is the number of atoms in the primitive cell (N = 22). Hence the calculation of the specific heat involves no adjustable scale factor. The specific anomaly is indeed reproduced, although with a distorted shape and a shift in temperature (1.5 K instead of 1.8 K). The upturn of the experimental C_P/T^3 curve below 0.4 K is believed to arise from phonon activated excitations between metastable CDW states. The corresponding density of states lies below 10 μeV, i.e., outside the range of the present measurements.

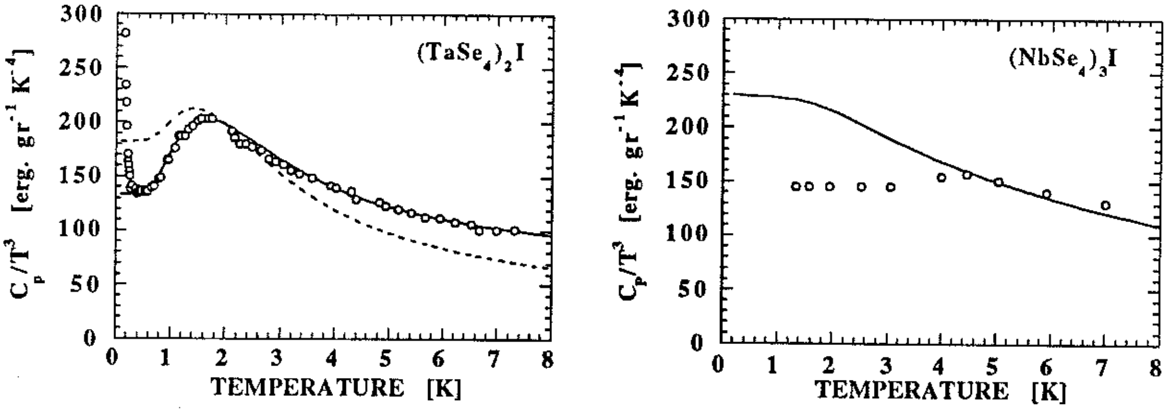

Figure 11 (a). Low-temperature specific heat in $(TaSe_4)_2I$; the data are taken from Ref. 13; the solid line is calculated using the g(ω) curve shown in Fig. 7; the dashed line is obtained from the neutron G(ω) data. **(b)** Specific heat from $(NbSe_4)_3I$; the solid line is calculated from the 50 K G(ω) data in Fig. 6; data from Ref. 13.

The specific heat values below 1 K are sensitive to the precise behaviour of the PDOS curve at low frequencies (< 0.5 meV). This is the range where the neutron curve is the least reliable due, in particular, to uncorrected multiple scattering processes. The solid line in Fig. 7 is a trial PDOS curve inspired from the model developed earlier. It includes a quadratic Debye regime at low frequencies followed by a step. The coefficient of the ω^2 law is adjusted to obtain agreement with the specific heat data near 0.5 K. Above the step the PDOS curve is fitted to the neutron curve in the frequency range from 2.5 to 4 meV. The precise shape of the PDOS curve above 4 meV has no influence on the low temperature specific heat.

The corresponding specific heat curve is shown as the solid line in Fig. 11a. The agreement with the measured C_P/T^3 curve is excellent between 0.6 K and 7 K. This test shows that the observed specific heat anomaly can be reproduced by introducing a step in a Debye-type PDOS curve. The position of the step is close to the plateau frequency of the TA_z sheet and its amplitude is consistent with the predictions of a simplified acoustic dispersion curve model.

Finally, the 50 K neutron data in Fig. 6 have been used to calculate the low temperature specific heat from $(NbSe_4)_3I$. The resulting C_P/T^3 curve is shown in Fig. 11b (solid line), and compared with the specific heat data from Ref. 13. Again, the neutron $G(\omega)$ curve appears to be too high at low frequencies.

4. CONCLUSION

In this paper we have studied the phonon density of states of two quasi-one dimensional compounds, $(NbSe_4)_3I$ and $(TaSe_4)_2I$, which both show a structural instability near room temperature.

We find that the phonon spectrum of the Ta compound is essentially unchanged above and below the Peierls instability. In particular the low frequency part of the spectrum deviates from Debye-like behaviour due to the 1D character of the transverse acoustic branches polarised along the chains. This 1D character persists down to the lowest temperatures, and is at the origin of the observed specific heat anomaly near 1.8 K.

In contrast, the Nb compound displays a very anharmonic behaviour which produces spectral changes across the entire PDOS frequency range. The changes are particularly visible in the low frequency part of the spectrum. A comparison with dispersion curve data shows that the 1D character of the TA_Z modes progressively disappears below T_C. We speculate that the renormalisation of the TA_Z frequencies reduces the anisotropy of the Debye-Waller amplitudes and is reflected across the entire spectrum due to inadequate (isotropic) Debye-Waller corrections.

A number of questions are left unanswered. One question, which we shall address in the following paper, concerns the nature of the structural instability in $(NbSe_4)_3I$ and the origin of the interchain coupling which it seems to induce.

The other question concerns the low temperature specific heat anomaly in $(TaSe_4)_2I$. In the present picture, the observed anomaly results simply from the 1D character of the low frequency phonon branches. It is therefore expected that other quasi-one dimensional compounds, CDW or not, should display similar specific heat anomalies. Indeed similar anomalies have been observed in Silicium, Germanium, Crystoballite, etc., and interpreted in terms of flat phonon dispersion curves. More extensive studies are clearly required, on both metallic and insulating quasi-1D systems. As seen from the present work, the interpretation of the low temperature specific heat behaviour generally requires a combination of dispersion curve and phonon density-of-states measurements.

We gratefully acknowledge useful discussions with J.C. Lasjaunias, K. Biljakovic and A. Smontara on their specific heat and thermal conductivity experiments. One of us, J.E.L., also acknowledges financial support from the Spanish Ministry of Education and Science.

References

1. Recent reviews on CDW systems.

a. Low Dimensional Conductors and Superconductors, edited by D. Jerome and L.G. Caron, NATO-ASI series, vol **155** (Plenum Press, New York, 1987).

b. G. Grüner, Rev. Mod. Phys. **60**, 1129 (1988).

c. Charge Density Waves in Solids, edited by L.P. Gorkov and G. Grüner, Modern Problems in Condensed Matter Sciences vol. **25** (North-Holland, Amsterdam, 1989).

2. Z.Z. Wang, M.C. Saint-Lager, P. Monceau, M. Renard, P. Gressier, A. Meerschaut, L. Guemas and J. Rouxel, Solid State Commun. **46**, 325 (1983).

3. P. Gressier, A. Meerschaut, L. Guemas, J. Rouxel and P. Monceau, J Solid State Chem. **51**, 141 (1984).

4. C. Roucau, R. Ayroles, P. Gressier and A. Meerschaut, J. Phys. C **17**, 2993 (1983).

5. P. Gressier, M.H. Whangbo, A. Meerschaut and J. Rouxel, Inorg. Chem. **23**, 1221 (1984).

6. P. Gressier, L. Guemas and A. Meerschaut, Mat. Res. Bull. 20, **539** (1985).

7. H.P. Geserich, G. Scheiber, M. Dürrler, F. Levy and P. Monceau, Physica **143B**, 198 (1986).

8. S.D. Bader, S.K. Sinha, B.P. Schweiss and B. Renker, in Topics in Current Physics, Vol. **32**; eds Ø. Fischer and M.B. Maple; pp. 223-249 (1982).

9. B. Renker, F. Gompf, E. Gering, N. Nücker, D. Ewert, W. Reichardt and H. Rietschel, Z. Phys. **B67**, 15 (1987).

10. M.J. Rosseinsky, K. Prassides, P. Day and A.J. Dianoux, Phys. Rev. **B37**, 2231 (1988).

11. R. Currat, A.J. Dianoux, P. Monceau and J.J. Capponi, Phys. Rev. **B40**, 11362 (1989)

12. M. Arai, K. Yamada, Y. Hidaka, S. Itoh, Z. A. Bowden, A.D. Taylor, and Y. Endoh, Phys. Rev. Lett. **69**, 359 (1992).

13. K. Biljakovic, J.C. Lasjaunias, F. Zougmore, P. Monceau, F. Levy, L. Bernard and R. Currat, Phys. Rev. Lett., **57**, 1907 (1986).

14. T.W. Kim, D. Reagor, G. Gruner, K. Maki and A. Virosztek, Phys. Rev. **B40**, 5372 (1989).

15. S. Donovan, Y. Kim, B. Alavi, L. Degiorgi and G. Gruner, Solid State Commun. **75**, 721 (1990).

16. P. Monceau, L. Bernard, R. Currat, F. Levy and J. Rouxel, Physica **136B**, 352 (1986).

17. S..E. Brown, J.O. Willis, B. Alavi, and G. Grüner, Phys. Rev. **B37**, 6551 (1988); J.C. Lasjaunias and K. Biljakovic, private communication.

18. T.W. Kim, S. Donovan, G. Gruner and A. Philipp, Phys. Rev. **B43**, 6315 (1991).

19. P.A. Egelstaff and P. Schofield, Nucl. Sci. Eng. **12**, 260 (1962).

20. S. Sugai, M. Sato and S. Kurihara, Phys. Rev **B32**, 6809 (1985).

21. M.S. Sherwin, A. Zettl, P.L. Richards, Phys. Rev. **B36**, 6708 (1987).

22. L. Degiorgi and G. Grüner, Phys. Rev. **B44**, 7820 (1991).

23. J.E. Lorenzo, R. Currat, P. Monceau, B. Hennion and F. Levy, in press.

24. M.J. Rice, Phys. Rev. Lett. **37**, 36 (1976); Sol. State Commun. **25**, 1083 (1978).

25. P. Monceau, L. Bernard, R. Currat and F. Levy, Physica **B156-7**, 20 (1989).

26. M. Saint-Paul, P. Monceau and F. Levy, Sol. State Commun. **67**, 581 (1988).

CHAPITRE VI

Lattice dynamics and structural instability in $(NbSe_4)_3I$.

J.E. Lorenzo and R. Currat
Institut Laue-Langevin, 38042 Grenoble-Cedex, France.

P. Monceau
Centre de Recherches sur les Très Basses Températures, CNRS, 38042
Grenoble-Cedex, France.

B. Hennion
Laboratoire Léon Brillouin, Centre d'Etudes de Saclay,
91191 Gif-sur-Yvette-Cedex, France

F. Levy
Institut de Physique Appliquée, Ecole Polytechnique Fédérale de
Lausanne, CH-1015, Lausanne, Switzerland.

Abstract

Neutron elastic and inelastic scattering experiments have been performed on the quasi-one dimensional compound $(NbSe_4)_3I$. The phase transition at $T_C=273$ K from P4/mnc to $P\bar{4}2_1c$ is driven by the condensation of a B_{1u} optic mode and is characterised by the appearance of new Bragg reflections of the type *(h 0 l)* with $h+l\neq2n$. Well above T_C, a central component is observed which diverges on approaching T_C, while the B_{1u} mode exhibits only partial softening. Below T_C the B_{1u} frequency undergoes a strong renormalization, together with a complete dispersion sheet of c-polarised, low frequency modes. The anisotropy of the correlation length of the critical fluctuations has been measured and shown to be closely related to the anisotropy in the B_{1u} dispersion.

1. Introduction

$(NbSe_4)_3I$ belongs to the family of transition metal tetraselenides(1-2) with general formula $(MSe_4)_nY$ (M = Nb or Ta; n = 3,10/3 or 4, for the known stable compounds and Y = I or Br).

The structure consists of $(MSe_4)_\infty$ chains aligned parallel to the c-axis and separated from one another by iodine atoms. Each metal atom is sandwiched between two rectangular selenium units, each consisting of two $Se_2^{(-2)}$ dimers , rotated by an angle of about 45 degrees. The role of iodine atoms is to keep the chains together by attracting and canting the selenium dimers with respect to the basal plane.

The physical properties of all the compounds are mainly determined by the metal-metal distances along the chain. So whenever the metal atoms are equally spaced, as for $(TaSe_4)_2I$(3), the compound is metallic (or pseudo-metallic), and the greater the deviation with respect to equal spacing, the lower the conductivity. This trend is illustrated by metallic $(NbSe_4)_{10/3}I$(4) with average metal-metal distance d = 3.191 Å and deviation Δd = 0.04Å , and semiconducting $(NbSe_4)_3I$ with d = 3.187 Å and Δd = 0.12Å (1).

At room temperature, $(NbSe_4)_3I$ has space group P4/mnc (Z = 4)(5) and lattice parameters: a = 9.489 Å and c = 19.13 Å. At T_C = 273 K the system undergoes a ferrodistortive phase transition to a space group $P\bar{4}2_1c$(6-7). The symmetry loss at T_C uniquely determines the irreducible representation of the order parameter, namely B_{1u} (Raman and infrared inactive) .

Above T_C, $(NbSe_4)_3I$ is semiconducting with an electronic gap of 4000 K (345 meV). Below T_C, two different types of behaviour have been observed(1): type I is characterized by a very small semiconducting gap (25 meV) whereas for type II the gap first decreases, then increases again (up to 110 meV) below 230 K. These two different behaviours are structurally indistinguishable, though type II has been tentatively associated with compositional inhomogeneities (i.e., small regions where the system is not $(NbSe_4)_3I$ but the metallic $(NbSe_4)_{10/3}I$). Recent infrared measurements(8) show that the submillimeter AC conductivity along the chain direction is higher than the DC conductivity, suggesting a hopping mechanism for the electron transport.

The structural phase transition at T_C and the properties of the low temperature phase, have been investigated by thermal conductivity(9), ultrasonic attenuation, NMR(10) and Raman spectroscopy(11). Perhaps the most striking result comes from ultrasonic measurements(12) which show that the shear constant C_{44} is renormalized below T_C and reaches, at low temperatures, a value *10 times* larger than at room temperature. Previous inelastic neutron scattering measurements(13) suggested that the renormalisation might affect a complete dispersion sheet of z-polarised acoustic modes (TA_z), all with zone-center velocity $v_{44}=\{C_{44}/\rho\}^{1/2}$. The relationship between the TA_z-branch propagating along $(\xi\ 0\ 0)$ (τ_3 in Kovalev's notation(14)) and the soft optic branch of same polarisation and τ_2 symmetry, was established.

In this paper we extend the dispersion curve measurements as a function of temperature and propagation directions and we study the critical fluctuations above and below T_C. We show that they are mostly of the elastic (or unresolved quasi-elastic) type, with a marked quasi-one dimensional character. We compare these results to x-ray scattering data(15) and to the results obtained in a similar inelastic neutron scattering study of the Peierls instability in the related compound $(TaSe_4)_2I$.

2. Experimental and data analysis

Neutron measurements were carried out on the three-axis spectrometers IN14, at the Institut Laue-Langevin (Grenoble, France), and 4F1 at the Laboratoire Leon Brillouin (Saclay, France), both installed on cold neutron beams. The critical scattering study was carried out on 4F1 operated at a neutron incident energy of E_0= 5 meV, while IN14 was used for the inelastic measurements (E_0= 5 to 14.6 meV).

The scattering plane was chosen so as to contain the **c*** direction because the phonon modes related to the phase transition are polarized along that direction. Several *(h 0 l)* Bragg positions with $h+l\neq 2n$, were explored at room temperature. These reflections are, in principle, extinct above T_C, due to the presence of the n-glide plane in the high-temperature space group. Experimentally, as shown in Fig.1 for the (3 0 6) position, a small Bragg contribution is observed due to multiple Bragg scattering. In the case of the (3 0 6) position, which was used in all the measurements, the multiple-Bragg contribution was found to be temperature independent and was subtracted off.

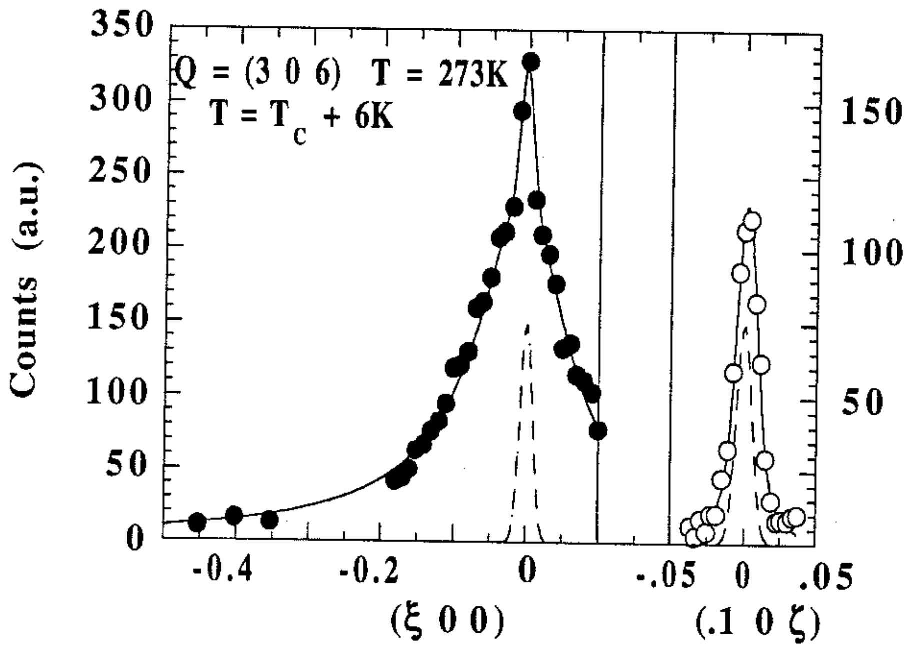

Figure 1. Elastic diffuse intensity profiles at T=273 K for $\mathbf{q} \parallel \mathbf{a}^*$ (left) and $\mathbf{q} \parallel \mathbf{c}^*$ (right). The solid lines correspond to the fit to eq. (2) after convolution with instrumental resolution. The instrumental widths along the a* (FWHM= 0.0132 Å^{-1}) and c* (0.0168 Å^{-1}) directions are shown as dotted lines. The hatched area corresponds to the multiple Bragg scattering contamination. The data between $\xi=-0.2$ and -0.35 (lhs) are contaminated by a parasitic powder reflection from the Al sample container and have been removed.

The correlation length κ_c of fluctuations along the chain axis is very large, and therefore resolution corrections are severe, as seen in Fig. 1 (rhs) for T_C + 6K. In order to avoid additional difficulties related to the multiple scattering intensity at (3 0 6), above T_C, and the growing Bragg peak below T_C, κ_c was determined from scans along (2.9 0 6+ζ) and (3.1 0 6+ζ).

The analysis was performed by fitting a resolution-convoluted response function to the data. The response function was taken as the sum of a damped harmonic oscillator

$$S(\mathbf{q},\omega)_{phon} = \frac{1}{\pi}\,|F(\mathbf{G}+\mathbf{q})|^2 \frac{\omega}{1 - exp\left(-\frac{h\omega}{k_BT}\right)}\;\frac{\Gamma_\mathbf{q}}{\left[\omega^2 - \omega_\mathbf{q}^2\right]^2 + \omega^2\Gamma_\mathbf{q}^2} \qquad (1)$$

and an elastic central component with Lorentzian q-dependence:

$$S(\mathbf{q},\omega)_{CP} = |F(\mathbf{G}+\mathbf{q})|^2\,\frac{k_BT}{\pi}\,\frac{\chi_0(T)}{1+(\kappa_a q_x)^2+(\kappa_a q_y)^2+(\kappa_c q_z)^2}\,\delta(\omega) \qquad (2)$$

This formulation is as general as possible. No functional relationship is assumed between the wavevector and temperature dependence of the central peak intensity and that of the soft phonon frequency. We only postulate that they both follow the same inelastic (or "one-phonon") structure factor F(**G**+**q**). In practice we also assumed F(**G**+**q**) to be temperature independent and to vary linearly with **q** in the neighbourhood of **G** = (3 0 6).

The first step in order to determine correlation lengths, is to integrate the inelastic response at constant-**q**. This integration is performed automatically by means of x-ray scattering and we shall compare our results to those of Iwazumi et al.(15). With neutrons, the same can be done, in principle, using high incident neutron energies on a diffractometer. In practice q-resolution requirements prevent the use of high neutron energies and the only reliable method is the energy integration of constant-**q** scans measured with a 3-axis spectrometer.

In the present case, we find that the "soft" phonon branch is only weakly temperature dependent and shows little dispersion in the temperature range and wavevector range of interest. In a first approximation, one may estimate the correlation lengths using only the central peak part of the response. Since the energy width of the central peak is always found to be resolution limited, then no energy integration is required at all.

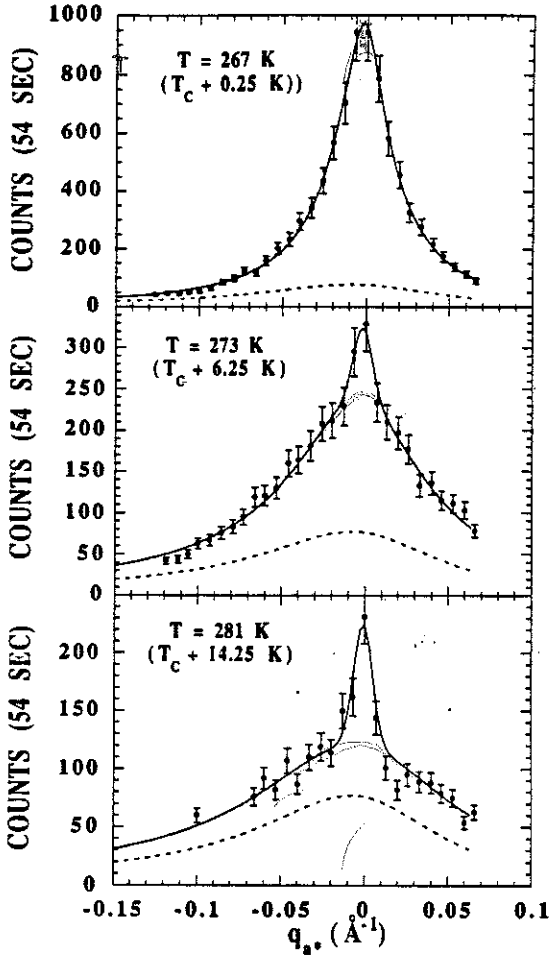

Figure 2. Elastic intensity profiles along (3+ξ 0 6) at three temperatures. The solid lines represent the fit to eq. (2) convoluted with the instrumental resolution function. The dotted lines represent the estimated $\omega = 0$ contribution of the phonon lineshape.

This procedure has been used below, i.e. the correlation lengths are deduced from the temperature and **q**-dependence of the elastically measured intensities ($\omega = 0$). In the critical regime, the $\omega \approx 0$ intensity arises from the central component and from the $\omega \approx 0$ part of the phonon response. The latter has been estimated and subtracted off (cf. Fig. 2). In Section 3.2, we come back to this point and estimate the uncertainties introduced in the final results by the use of the central component alone.

The recorded profiles were corrected for finite instrumental q-resolution using a three-dimensional convolution routine. For each temperature, scans along **a*** and **c*** were corrected simultaneously in order to obtain self-consistent values of the correlation length κ_a and κ_c.

3. Results and discussion

3.1 Inelastic measurements

The main features of the $(NbSe_4)_3I$ acoustic phonon dispersion curves have been reported in a previous paper, and can be taken as representative of all the transition metal tetrachalcogenide compounds. In Fig. 3 we have plotted the complete set of phonon dispersion curves measured at room temperature. One notices:

(i) the presence of very low-energy transverse modes polarised along c and propagating in the basal plane,

(ii) hard longitudinal modes, leading to large anisotropy ratios ($v_{33} \approx 30\ v_{44}$).

(iii) the appearance of a non negligible chain bending force which produces a characteristic upward curvature on the doubly-degenerate TA branch propagating along **c***.

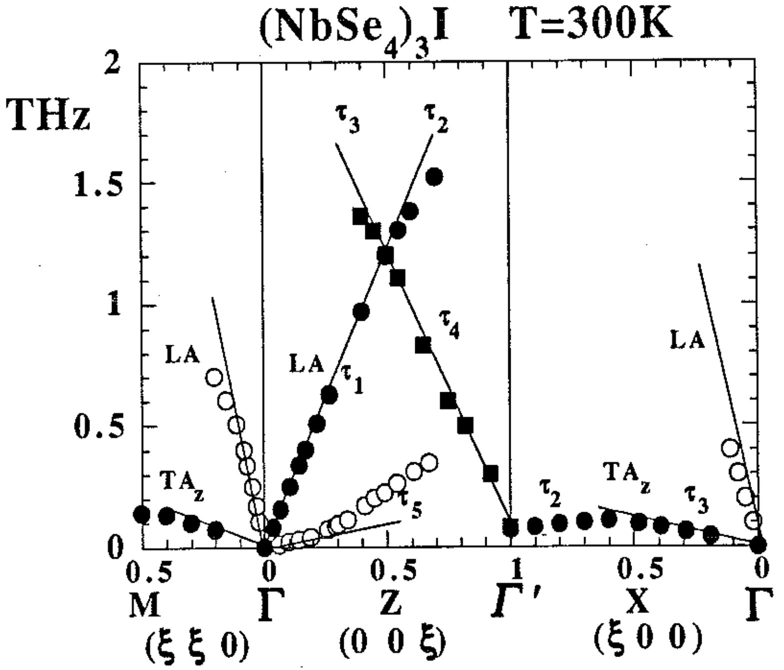

Figure 3. Low-frequency dispersion curves along principal directions in $(NbSe_4)_3I$ at room temperature. Modes polarised along (normal to) the chain axis are shown as full (open) symbols.

The point labeled Γ' in Fig. 3 corresponds to a zone center where acoustic modes are not visible. Such is the case for the (*h 0 l*) reflections with *h+l* odd or the (*h h l*) reflections with *l* odd. In this extended zone scheme, the dispersion curves cross the (0 0 1/2) and (1/2 0 0) zone boundaries in a continuous way. The curve originating from the Γ-point and labeled τ_1-τ_2, corresponds to the propagation of longitudinal sound along the $(MSe_4)_\infty$ backbone. An almost symmetric branch labeled τ_4-τ_3 originates from the soft B_{1u} frequency at Γ', and propagates along **c*** with essentially the same group velocity. This latter curve corresponds to a staggered arrangement of 1D sound waves propagating along the $(MSe_4)_\infty$ chains, neighbouring chains vibrating in anti-phase. In a reduced zone scheme the two branches would be indistinguishable except at very low frequencies. This illustrates the large degree of decoupling between chains, for motions longitudinal to the chains. The flatness of the TA_Z branches along (ξ 0 0) and (ξ ξ 0) is another manifestation of the same physical situation.

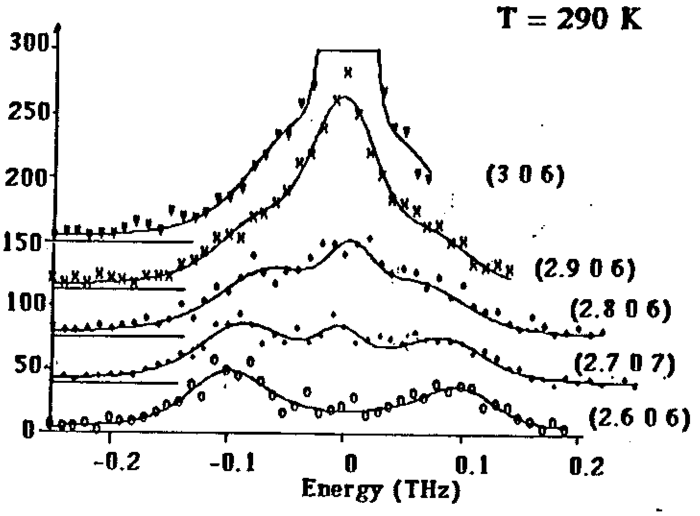

Figure 4a Soft phonon lineshape: Constant-Q scans at (3-ξ 0 6) and T=290 K with ξ=0.0, 0.1, 0.2, 0.3, 0.4.

In what follows, we study in more detail the temperature dependence of the soft B_{1u} mode and of the TA_Z branch along a* to which the B_{1u} mode is connected. Fig 4a shows the observed phonon lineshape for the TA_Z branch, at 290 K. The B_{1u} frequency is observed at the (3 0 6) position. Fig. 4b and 4c show the temperature dependence of the modes at (2.9 0 6) and (2.6 0 6), respectively.

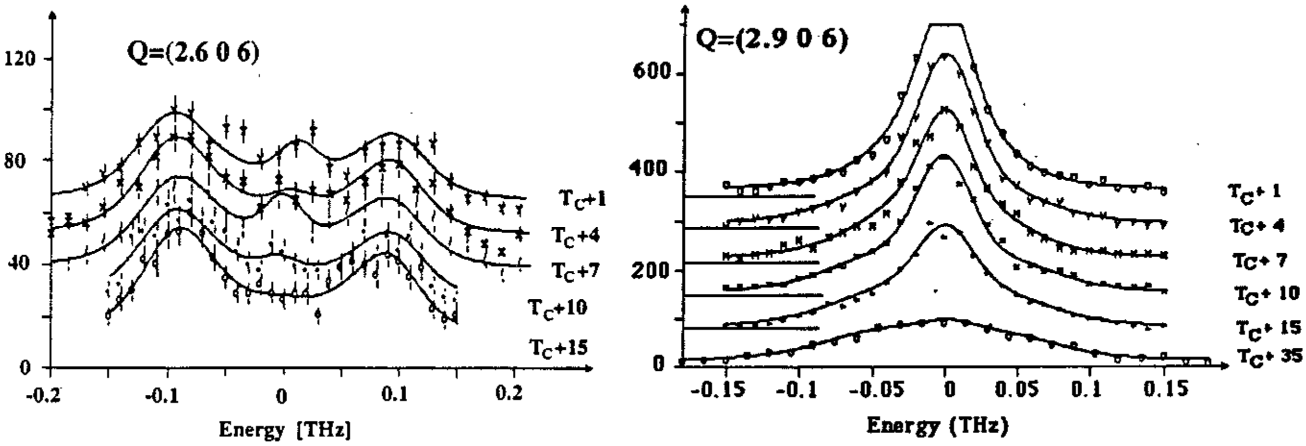

Figure 4 Soft phonon lineshape: Constant-Q scans as a function of temperature ($T>T_C$) : $\xi=0.4$ (**b**) and $\xi=0.1$ (**c**).

The whole optic branch is damped above T_C and the damping remains constant on approaching T_C. Note that at (2.6 0 6) the frequency (and the damping) remains constant at all temperatures above T_C (ω_q = 0.104 THz and Γ_q = 0.062 THz). The data analysis carried out at **Q**=(2.9 0 6) and at **Q**=(3 0 6) show that, in spite of the presence of the central peak, the frequency of this mode seems to remain constant (ω_q = 0.075 THz) until T = T_C + 18 K and decreases slightly and linearly from this temperature on down to T_C, where ω_q = 0.055 THz. The results of the analysis are shown in Fig. 5.

The very limited temperature dependence of the B_{1u} frequency above T_C contrasts with the strong renormalisation of the entire acoustic+optic $\Gamma-\Gamma'$ branch below T_C (see Fig. 6). Between T_C and the lowest measured temperature (100 K) a *seven-fold* increase of the B_{1u} frequency (Γ'-point in Fig. 6) is observed. In the same temperature interval, the acoustic slope at the Γ-point increases by a factor two. The same trend is observed by ultrasonics(12), where a eight-fold increase of the C_{44} elastic constant is observed between T_C and 100 K.

The renormalization of the TA_z branch propagating along a*+b* has also been studied, as shown in the left hand side of Fig. 6. Its acoustic slope is also controlled by the C_{44} elastic constant. The variation of its dispersion with temperature can be accounted for through the renormalization of the sound velocity.

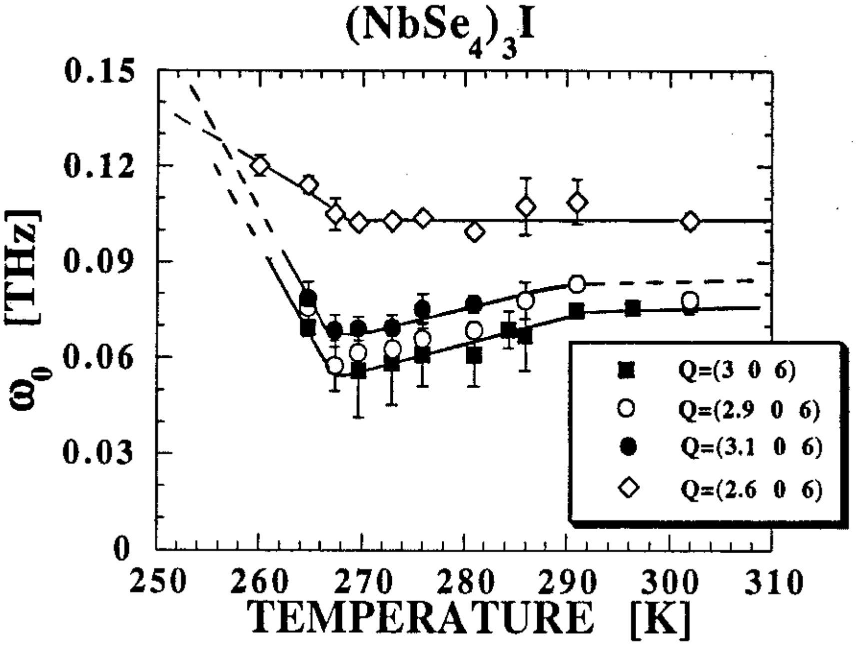

Figure 5. Temperature dependence of soft (B_{1u}) mode frequency for several Q values along (3-ξ 0 6): ξ=0 (full squares), ξ=±0.1 (open and full circles), ξ=0.4 (open squares).

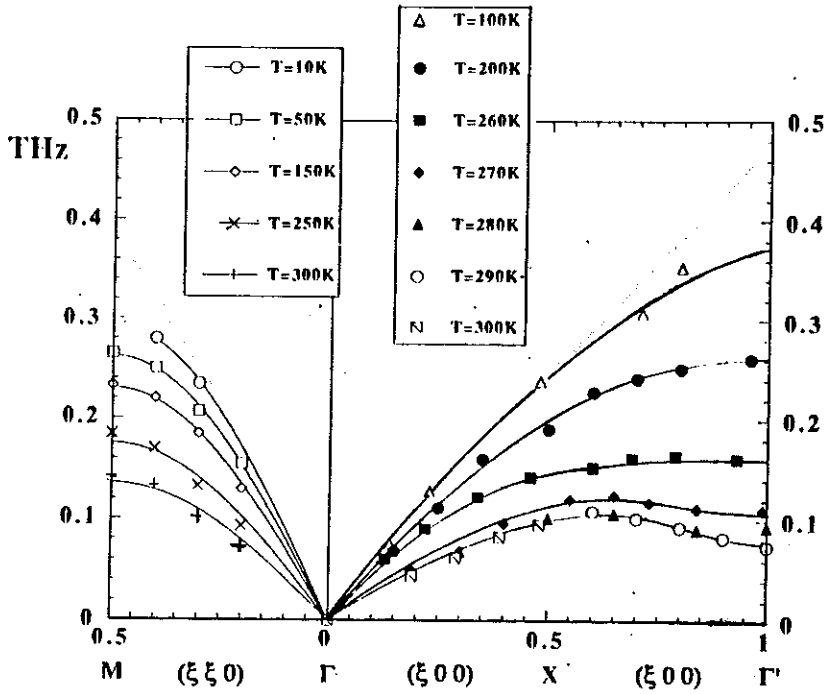

Figure 6. Temperature evolution of the c-polarised acoustic+optic dispersion branches for symmetry directions in the basal plane. The mode at Γ' corresponds to the soft B_{1u} mode.

Although no measurements have been performed for a general propagation direction in the (a*, b*) plane, one expects a strong TA_Z mode renormalisation, as in the $(\xi\ 0\ 0)$ and $(\xi\ \xi\ 0)$ directions. It is necessarily so, at least in the long wavelength limit, since all TA_Z modes propagating in the basal plane have the same acoustic slope.

The structural phase transition is characterised by the onset of a pattern of static atomic displacements. The dominant displacement component$^{(6)}$ is a staggered shift of the chain positions along z. It is not unexpected therefore that the stiffness associated with these displacements is strongly renormalised, as the static displacements develop, below T_C: this is in fact the essence of the soft mode picture. What is unusual in the present case is:

(i) the magnitude of the renormalisation below T_C, compared to the near absence of mode softening above T_C.

(ii) the extension in reciprocal space of the renormalisation which is observed across the entire Brillouin zone and not just in a neighbourhood of the critical wavevector.

3.2 Elastic measurements

Elastic scattering experiments have been performed in the temperature range 300-260 K, near the (3 0 6) Bragg position which is forbidden above T_C, due to the *n*-glide plane in the high-temperature space group, but becomes allowed below $T_C = 266$ K.

The correlation lengths along a* (in-plane or transverse) and along c* (in-chain or longitudinal), have been extracted from the measured intensity profiles, as discussed in Sect. 2. The results, shown in Fig. 7, indicate an anisotropy factor of ≈10, across the temperature range of the measurements. Both correlation lengths follow a mean field behaviour (cf. insert):

$$\kappa_{a,c}(T) \approx \left|\frac{T - T_C}{T_C}\right|^{\nu} \qquad (3)$$

with $\nu(T>T_C) = \nu'(T<T_C) \approx 0.5$. In the temperature range of our measurements the fluctuations remain three dimensional and the crossover to the one dimensional regime, defined as

$$\kappa_a(T^*) = d_\perp$$

would occur at $T^* \approx T_C + 100$ K. ($d_\perp$ is the distance between adjacent chains).

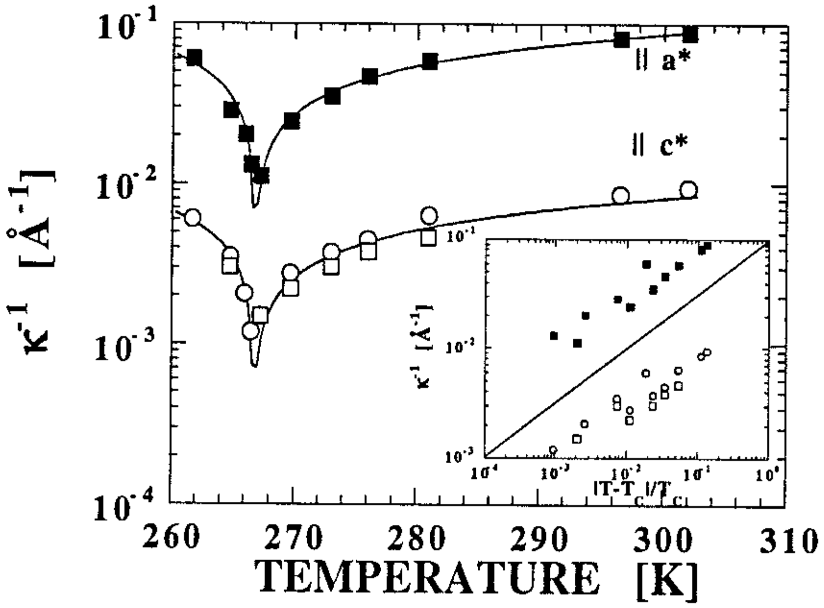

Figure 7. Inverse correlation lengths of fluctuations along **a*** (full circles) and **c*** (open squares are measured at (2.9 0 ξ) and diamonds at (3.1 0 ξ)). Solid lines correspond to $(\Delta T/T_C)^{1/2}$ fits.

The temperature variation of the critical scattering at $q = 0$ is shown in Fig 8. The values have been obtained after subtraction of the Bragg intensity and allowing for instrumental broadening, as discussed in Sect. 2. No unique critical exponent value can be deduced from the logarithmic plot (insert). The observed temperature dependence is compatible with critical exponent values in the range from 1-2. This result is in sharp contrast with the x-ray results from Iwazumi et al.(15), who report an exponent value of 0.5, lower than the mean-field value ($\gamma = \gamma' = 1$). Our correlation length values are also in poor agreement with the values given in Ref.15 for $\kappa_a(T)$, our values being shorter by a factor ≈ 4. Further x-ray measurements are planned in order to clarify this point.

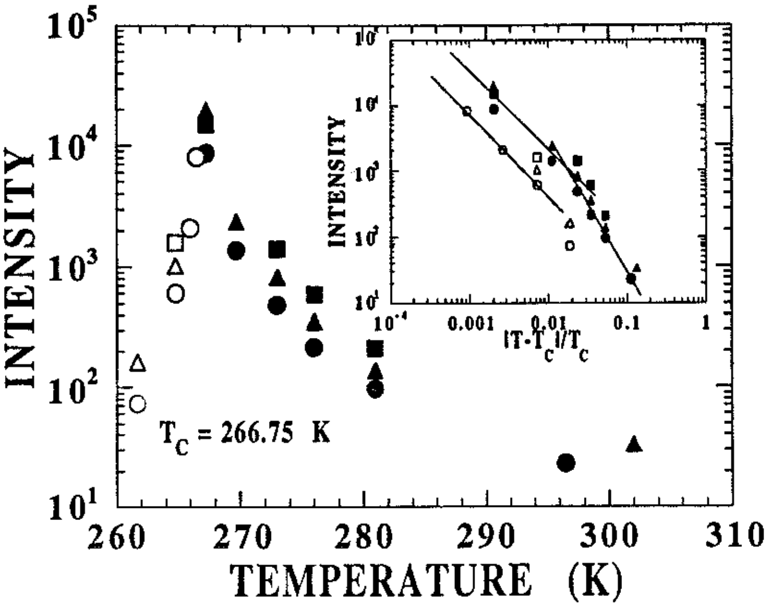

Figure 8. Temperature dependence of elastic intensity at (3 0 6), as deduced from the analysis of elastic scans along (3+ξ 0 6) (circles); (3.1 0 ζ) (squares); (2.9 0 ζ) (triangles).

It is interesting at this point to return to our initial hypothesis that a meaningful estimate for the correlation lengths can be obtained using the central component alone, as opposed to the full energy-integrated response. Specifically, one may use our knowledge of the phonon frequency at q = $q_0 = 0$, $\omega_{q0}(T)$, to derive the relationship between the correlation lengths obtained by the two techniques.

To this end, we consider the semiempirical treatment of displacive phase transitions, with appearance of a central peak, originally introduced by Shapiro et al.(16,17) Their idea is to create an additional decay channel for phonon fluctuations with frequencies less than some characteristic frequency γ. If this characteristic frequency is sufficiently small the response function can be separated into two terms: the first one given by eq. (1) and the second one that corresponds to the central peak response, given by:

$$S\,(\mathbf{q},\omega)_{cent} = \frac{k_B T}{\pi} \;\; \frac{\delta^2(T)}{\omega_0^2\;\omega_{\mathbf{q}}^2} \frac{\gamma}{\omega^2 + \gamma^2} \tag{4}$$

with $\delta^2(T)$ proportional to the coupling constant between the phonon fluctuations and the additional decay channel (For convenience, the one-phonon structure factor F(G+q) has been set to unity). ω_0^2 is defined as:

$$\omega_0^2\,(\mathbf{q},T) = \omega_{\mathbf{q}}^2\,(T) - \delta^2\,(T) = \omega_{\mathbf{q}_0}^2\,(T) - \delta^2\,(T) + \left[\Lambda\,\mathbf{q}\right]^2 \tag{5}$$

where Λ defines the phonon dispersion relation in the neighbourhood of **q** = 0. The phonon and central peak integrated intensities obey the following sum rule:

$$\int_{-\infty}^{\infty} \left[S\,(\mathbf{q},\omega\,)_{phon} + S\,(\mathbf{q},\omega\,)_{cent}\right] d\omega \;=\; \frac{k_B T}{\omega_0^2\,(\mathbf{q},T)} \tag{6}$$

To be specific, let us consider the correlation length along a* and correspondingly the soft phonon dispersion curve along this direction, $\omega_{\mathbf{q}}$. Equation (4) can be rewritten as

$$S\,(\mathbf{q},0)_{cent} = \frac{k_B T}{\pi}\;\frac{\dfrac{\delta^2(T)}{\omega_{\mathbf{q}_0}^2(T)\left[\omega_{\mathbf{q}_0}^2(T) - \delta^2(T)\right]}}{1 + \dfrac{2\,\omega_{\mathbf{q}_0}^2(T) - \delta^2(T)}{\omega_{\mathbf{q}_0}^2(T)\left[\omega_{\mathbf{q}_0}^2(T) - \delta^2(T)\right]}\,\lambda^2\,q_x^2 \,+ O\,(q_z^2, q_x^4)} \tag{7}$$

which defines the "central peak correlation length", κ_a, through:

$$\kappa_a^2 = \frac{2\,\omega_{\mathbf{q}_0}^2(T) - \delta^2(T)}{\omega_{\mathbf{q}_0}^2(T)\left[\,\omega_{\mathbf{q}_0}^2(T) - \delta^2(T)\right]}\,\lambda^2 \tag{8}$$

Our observed values for $\kappa_a(T)$ and $\omega^2_{q0}(T)$ are consistent with a temperature independent value for $\delta^2=\omega^2_{q0}(T_C)$ = 0.00291 THz². The results of the adjustment, which determines the value of λ, are plotted in Fig. 9. Finally, eq. (8) can be rewritten as:

$$\kappa_a^2(T) = \left(2 - \frac{\delta^2(T)}{\omega_{\mathbf{q}_0}^2(T)}\right)\xi_a^2(T) \tag{9}$$

where κ_a and ξ_a refer to the central peak and energy-integrated correlation lengths, respectively. In the present case, replacing $\delta^2(T)$ by $\omega^2_{q0}(T_C)$ in eq. (9), we obtain values for the ratio κ_a/ξ_a varying between 1 at T_C and 1.2 at 300 K. This is well within experimental uncertainties, as may be seen in Fig. 7, and not in the right direction to account for the discrepancy between our results and the x-ray results from Ref. 15.

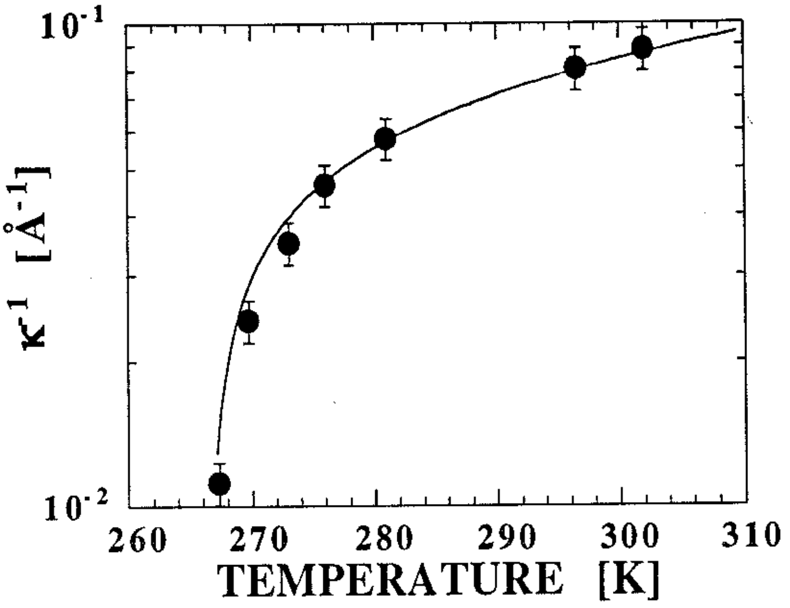

Figure 9. Correlation length κ_a vs T. The full line is computed from eq. (12) with temperature independent values for the parameters δ (= 0.054 THz) and λ (= 0.55 THz.Å).

References

1 P. Gressier, A. Meerschaut, L. Guemas, J. Rouxel and P. Monceau, J. Sol. State Chem. **51**, 141 (1984)

2. P. Monceau, Electronic Properties of Inorganic Quasi One Dimensional Compounds, (1985), Dordrecht: Reidel.

3. P. Gressier, L. Guemas and A. Meerschaut, Acta Cryst **B38**, 2877(1982).

4 A. Meerschaut, P. Gressier, L. Guemas and J. Rouxel, J. Sol. State Chem. **51**, 307 (1984)

5 A. Meerschaut, P. Palvedau and J. Rouxel, J. Sol. State Chem. **20**, 21 (1977)

6. P. Gressier, L. Guemas and A. Meerschaut, Mat. Res. Bull **20**, 539(1985).

7 M. Izumi, T. Iwazumi, K. Uchinokura, R. Yoshizaki and E. Matsuura, Sol. State Commun. **51**, 191 (1984)

8 V. Zeleny, J. Petzelt, B.P. Gorshunov, A.A. Volkov, G.V. Kozlov, P. Monceau and F. Levy, J. Phys.: Condens. Matter **1**, 10585 (1989).

9. A. Smontara, K. Biljakovic, L. Forro and F. Levy, Physica **143B**, 264 (1986).

10. P. Butaud, P. Segransan, C. Berthier and A. Meerschaut, *Springer Lecture Notes in Physics* vol 217, ed. G. Hutiray and J. Solyom (Berlin: Springer) pag. 121.

11 T. Sekine, K. Uchinokura, M. Izumi and E. Matsuura, Sol. State Commun. **52**, 379 (1984).

12 M. Saint-Paul, P. Monceau and F. Levy, Phys. Rev. **B37**, 1024 (1988).

13 P. Monceau, L. Bernard, R. Currat and F. Levy, Physica B **156-7**, 20 (1989).

14. O.V. Kovalev "Irreducible Representations of the Space Groups", Gordon and Breach Science Publishers (1965).

15. T. Iwazumi, M. Izumi, F. Sasaki, R. Yoshizaki and E. Matsuura, Physica **143B**, 261 (1986).

16. E. Pytte and J. Feder, Phys. Rev **187**, 1077 (1969).

17. S.M. Shapiro, J.D. Axe, G. Shirane and T. Riste, Phys. Rev **B6**, 4332 (1972).

CHAPITRE VII

CONCLUSION

L'objet de ce travail est l'étude des spectres de vibration de deux composés de la famille $(MX_4)_nY$, en relation avec les transitions de phase structurelles qui y sont observées. Cette étude a été effectuée à l'aide des techniques expérimentales de la diffusion des neutrons. La raison essentielle de ce choix tient à l'activité expérimentale intense dont ces composés sont l'objet. Un nombre important de résultats sont disponibles: structures cristallines, spectres optiques, transport, chaleur spécifique, ultrasons. Dans ce contexte, une étude détaillée par diffusion inélastique des neutrons se justifiait.

En principe, la diffusion neutronique permet de faire le lien entre aspects structuraux et propriétés dynamiques. Dans le cas présent, la portée de notre travail a été limitée par la complexité des systèmes étudiés et par la difficulté d'obtenir des échantillons de taille adéquate. Les principaux résultats de notre travail sont résumés ci-dessous:

En combinant les données obtenues, d'une part par spectrométrie 3-axes sur monocristaux, et d'autre part par temps-de-vol sur poudres, nous avons tenté d'établir un lien entre les spectres vibrationnels de basse fréquence et les comportements observés en chaleur spécifique, à basse température. Nous avons montré qu'il existait une interprétation plausible de ces comportements basée sur le caractère quasi-unidimensionnel du spectre vibrationnel des deux composés. Ce caractère est présent à toutes températures dans $(TaSe_4)_2I$ alors qu'il disparait dans la phase basse température de $(NbSe_4)_3I$.

La réponse électro-magnétique de l'état ODC est l'objet de nombreuses études en conductivité alternative et en absorption infra-rouge. Là encore, la diffusion inélastique des neutrons permet des recoupements utiles. Les études antérieures sur des systèmes à ODC tels que KCP et $K_{0.3}MoO_3$ l'ont montré. La technique neutronique permet d'étudier, sur un même pied, la dynamique de la phase métallique et celle de l'état condensé ODC. Elle permet donc de distinguer ce qui est caractéristique du système de ce qui est caractéristique de l'état. Dans le cas de $(TaSe_4)_2I$, nous proposons d'interpréter les résonances observées en conductivité AC comme des modes optiquement activés par l'état ODC, plutôt que comme des modes caractéristiques de cet état.

Pour les transitions de phase des deux composés nous nous sommes efforcés de préciser la nature des fluctuations critiques. Dans les deux cas, le comportement observé est très éloigné du modèle displacif. L'essentiel de la diffusion critique est de nature quasi-élastique non-résolue ("pic central"). L'anisotropie des fluctuations est cependant très différente dans les deux cas: alors que dans $(NbSe_4)_3I$ on observe une forte anisotropie, en accord avec le caractère quasi-unidimensionnel du système, dans $(TaSe_4)_2I$ nous observons un comportement pratiquement isotrope. Sur ce point, nos résultats concordent avec les résultats obtenus en diffusion des rayons X, sur le composé voisin $(NbSe_4)_2I$.

La nature isotrope des fluctuations critiques dans $(TaSe_4)_2I$, ainsi que le caractère "transverse acoustique" des déplacements atomiques en phase modulée, amènent à placer cette transition de Peierls dans une catégorie à part. En appendice (B) nous présentons un modèle phénoménologique qui prend en compte, de façon naturelle, les deux aspects ci-dessus. Ce modèle suppose l'existence de modes optiques intra-chaînes, polarisés dans la direction des chaînes, directement couplés aux variables électroniques. On montre que ces modes sont également couplés aux variables acoustiques, par l'intermédiaire de termes d'interaction bilinéaires par rapport aux variables et à leurs gradients. On montre alors que pour certaines valeurs des paramètres du modèle, une transition vers une phase modulée de vecteur d'onde $(q_1=q_2; q_3)$ sera observée. Le modèle prévoit également une composante transverse acoustique pour les déplacements modulés, polarisée $[1\,\bar{1}\,0]$, en bon accord avec l'expérience.

Bien que ce modèle permette une meilleure compréhension de la structure modulée de $(TaSe_4)_2I$, il faut reconnaître que la mise en évidence des fluctuations intra-chaînes et la caractérisation de leur réponse en fréquence, restent à faire. Ceci sera l'objet d'expériences ultérieures, par diffusion des rayons X et des neutrons.

Du point de vue du couplage électron-phonon, il ne semble pas que les résultats obtenus permettent de distinguer entre un modèle de type couplage faible conventionnel et un modèle de type bipolaronique. Le caractère non-displacif de la transition pourra sans doute apparaître comme un indice en faveur du modèle bipolaronique. Toutefois les résultats spectaculaires obtenus par dopage isoélectronique paraissent difficiles à interpréter dans le cadre d'un modèle d'électrons fortement localisés.

APPENDICE A

A1 ATOMIC STRUCTURE OF $(MSe_4)_nI$ COMPOUNDS

The transition metal tetraselenides $(MSe_4)_nI$ (M = Nb, Ta; n = 2, 3, 10/3, 4) have tetragonal symmetry and consists of MSe_4 chains running parallel to the c axis and separated by iodine atoms. In each MSe_4 infinite chain the metal atom is sandwiched by two rectangular selenium units, the dihedral angle between two adjacent rectangles (θ) being close to 45°. The interaction between metals is only through d_{z^2} overlap along the chain. The shortest interchain metal-metal distance is about 6.7 Å significantly larger than the intrachain average value of about 3.2 Å. The shorter Se-Se side of rectangles (2.35-2.4 Å) is typical of a Se_2^{2-} pair while the longer one is about 3.5-3.6 Å. Iodine atoms are well separated from one another and can be considered as I^-. The formal oxidation state of the molecule is then, $(M^{5+}(Se_2^{2-}))_nI^-$ that leads to an average number of available free electrons on each metal ion (n-1)/n. Electronic calculations have shown that the d_{z^2} band of the MSe_4 chain is rather well separated from other bands and the electronic band structures of the MSe_4 chains can be approximated by considering only their d_{z^2} bands. The band filling f of a d_{z^2} band for the $(MSe_4)_nI$ compounds is f = (n-1)/2n.. For instance, $(NbSe_4)_3I$, $(TaSe_4)_2I$ and $(NbSe_4)_{10/3}I$ would have 1/3, 1/4 and 7/20 filled bands. As n increases, f becomes closer to 1/2.

A linear chain with incomplete band filling is susceptible to a Peierls distortion which opens up a gap at the Fermi level. For f<1/2, the distortion increases the repeat distance along the chain by a factor 1/f and then a metal trimerization is expected for $(NbSe_4)_3I$ and a tetramerization for $(TaSe_4)_2I$.

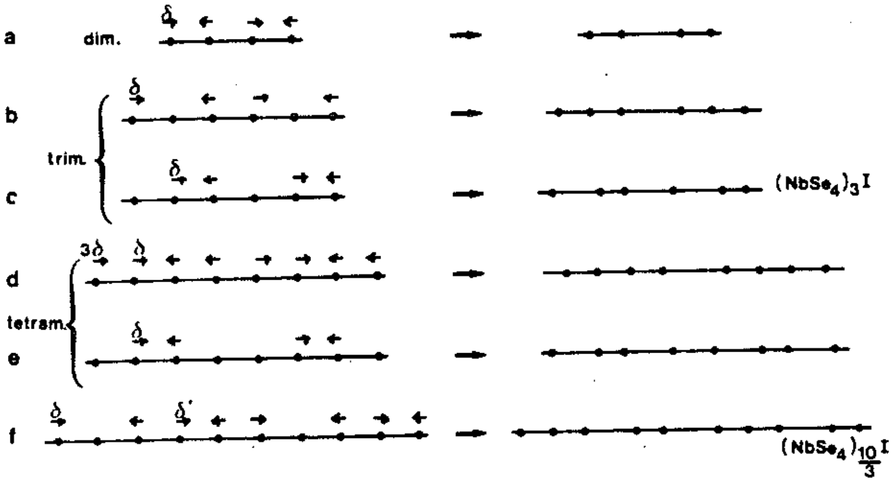

Figure A1: Expected distortions for a metal atom dimerization (a), trimerization (b and c), tetramerization (d and e) and for the compound $(NbSe_4)_{10/3}I$ (f).

A1.1 Structure of $(TaSe_4)_2I$

Space group : I422 (D_4^9)

Lattice parameters: a=9.531Å
c=12.824Å

Atomic positions (table A1):

			x	y	z	B_{eq}
Ta(1)	4(c)	222.	0	0.5	0	1.0(1)
Ta(2)	4(d)	2.22	0	0.5	0.25	1.2(1)
I	4(e)	4..	0	0	0.1553(3)	3.1(3)
Se(1)	16(k)	1	0.1212(2)	0.3120(2)	0.8809(2)	1.4(1)
Se(2)	16(k)	1	0.2160(2)	0.5449(2)	0.8693(2)	1.4(1)

Interatomic distances (table A2):

[1,3] (*)

$$\mathrm{Ta(1)} \cdots 4\mathrm{Se(1)} == 2.619(1)$$
$$\mathrm{Ta(1)} \cdots 4\mathrm{Se(2)} == 2.684(1)$$

$$\mathrm{Se(1)} \cdots \mathrm{Se(2)} == \begin{cases} 2.401(1) \\ 3.495(1) \end{cases}$$

$$\theta_1 = 46° = \theta_3$$

[2,4] (*)

$$\mathrm{Ta(2)} \cdots 4\mathrm{Se(2)} == 2.596(1)$$
$$\mathrm{Ta(2)} \cdots 4\mathrm{Se(1)} == 2.709(1)$$

$$\mathrm{Se(1)} \cdots \mathrm{Se(2)} == \begin{cases} 2.401(1) \\ 3.495(1) \end{cases}$$

$$\theta_2 = 44° = \theta_4$$

(*) 1,2,3 and 4 correspond to the Ta positions along the c-axis and the angles $\theta_1 ... \theta_4$ to the diedral angle between the Se rectangles located above and below the Ta atom.

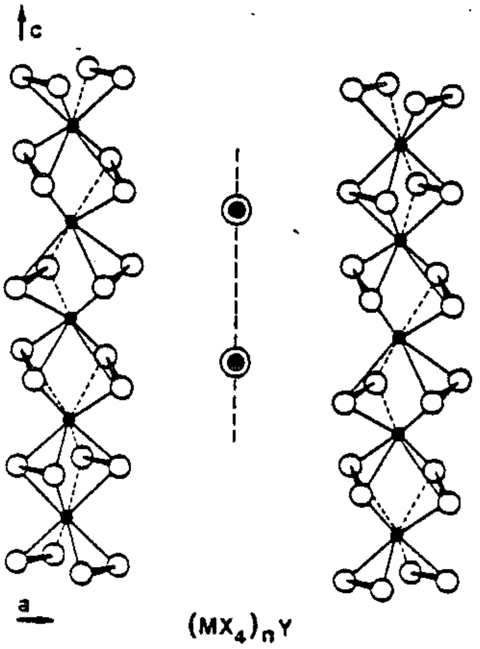

Figure A2: The structure of the $(MSe_4)_nI$ compounds.

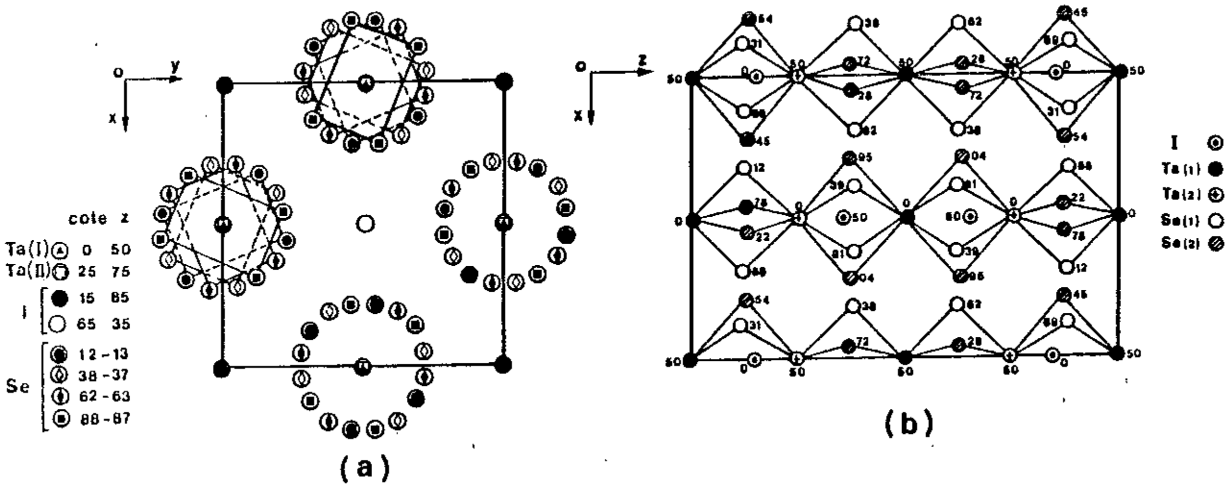

Figure A3: Proyection of the $(TaSe_4)_2I$ structure onto the x-y plane(a), onto the x-z plane (b).

A1.2 Group theory

In table A3 we show the character table for the 422 (D_4) point group. With the aid of tables A3 and A4 ($\mathbf{T}(\alpha,\mathbf{R}_i)$-matrices) we can construct the proyection operators $\underline{\mathbf{D}}(\alpha)$ for each atomic species, α (Ta(1), Ta(2), ...). $\mathbf{D}(\alpha)$ is defined as the sum of the partial contributions $\mathbf{D}_i(\alpha,\mathbf{R}_i) = \mathbf{R}_i \otimes \mathbf{T}(\alpha,\mathbf{R}_i)$ corresponding to each symmetry operation of the point group ($\mathbf{R}_i = h_1, h_2, ..h_{15}$ and h_{16}).

	$\begin{bmatrix} E(h_1) \\ (x,y,z) \end{bmatrix}$	$\begin{bmatrix} C_{2x}(h_2) \\ (x,\bar{y},\bar{z}) \end{bmatrix}$	$\begin{bmatrix} C_{2y}(h_3) \\ (\bar{x},y,\bar{z}) \end{bmatrix}$	$\begin{bmatrix} C_{2z}(h_4) \\ (\bar{x},\bar{y},z) \end{bmatrix}$	$\begin{bmatrix} C_{2\bar{x}y}(h_{13}) \\ (\bar{y},\bar{x},\bar{z}) \end{bmatrix}$	$\begin{bmatrix} C_{4z}(h_{14}) \\ (\bar{y},x,z) \end{bmatrix}$	$\begin{bmatrix} C_{4\bar{z}}(h_{15}) \\ (y,\bar{x},z) \end{bmatrix}$	$\begin{bmatrix} C_{2xy}(h_{16}) \\ (y,x,\bar{z}) \end{bmatrix}$		
A_1	1	1	1	1	1	1	1	1		$x^2 + y^2, z^2$
A_2	1	$\bar{1}$	$\bar{1}$	1	$\bar{1}$	1	1	$\bar{1}$	z, R_z	
B_1	1	1	1	1	$\bar{1}$	$\bar{1}$	$\bar{1}$	$\bar{1}$		$x^2 - y^2$
B_2	1	$\bar{1}$	$\bar{1}$	1	1	$\bar{1}$	$\bar{1}$	1		xy
E	$\begin{pmatrix} 1 & 0 \\ 0 & 1 \end{pmatrix}$	$\begin{pmatrix} 0 & 1 \\ 1 & 0 \end{pmatrix}$	$\begin{pmatrix} 0 & \bar{1} \\ \bar{1} & 0 \end{pmatrix}$	$\begin{pmatrix} \bar{1} & 0 \\ 0 & \bar{1} \end{pmatrix}$	$\begin{pmatrix} 0 & \bar{\imath} \\ i & 0 \end{pmatrix}$	$\begin{pmatrix} i & 0 \\ 0 & \bar{\imath} \end{pmatrix}$	$\begin{pmatrix} \bar{\imath} & 0 \\ 0 & i \end{pmatrix}$	$\begin{pmatrix} 0 & i \\ \bar{\imath} & 0 \end{pmatrix}$	$(x, y)(R_x, R_x)$	(xz, yz)
E'	$\begin{pmatrix} 1 & 0 \\ 0 & 1 \end{pmatrix}$	$\begin{pmatrix} 0 & 1 \\ 1 & 0 \end{pmatrix}$	$\begin{pmatrix} 0 & \bar{1} \\ \bar{1} & 0 \end{pmatrix}$	$\begin{pmatrix} \bar{1} & 0 \\ 0 & \bar{1} \end{pmatrix}$	$\begin{pmatrix} 1 & 0 \\ 0 & \bar{1} \end{pmatrix}$	$\begin{pmatrix} 0 & \bar{1} \\ 1 & 0 \end{pmatrix}$	$\begin{pmatrix} 0 & 1 \\ \bar{1} & 0 \end{pmatrix}$	$\begin{pmatrix} \bar{1} & 0 \\ 0 & 1 \end{pmatrix}$		
χ(Ta(1))	6	$\bar{2}$	$\bar{2}$	$\bar{2}$	0	0	0	0		
χ(Ta(2))	6	0	0	$\bar{2}$	$\bar{2}$	0	0	$\bar{2}$		
χ(Se(1,2))	24	0	0	0	0	0	0	0		
χ(I)	6	0	0	$\bar{2}$	0	2	2	0		

Table A3: Character table for the 422 (D_4) point group (above) and $\mathrm{Tr}(\mathbf{D}_i(\alpha,\mathbf{R}_i))$ (below).

	$\begin{bmatrix} E(h_1) \\ (x,y,z) \end{bmatrix}$	$\begin{bmatrix} C_{2x}(h_2) \\ (x,\bar{y},\bar{z}) \end{bmatrix}$	$\begin{bmatrix} C_{2y}(h_3) \\ (\bar{x},y,\bar{z}) \end{bmatrix}$	$\begin{bmatrix} C_{2z}(h_4) \\ (\bar{x},\bar{y},z) \end{bmatrix}$	$\begin{bmatrix} C_{2\bar{x}y}(h_{13}) \\ (\bar{y},\bar{x},\bar{z}) \end{bmatrix}$	$\begin{bmatrix} C_{4z}(h_{14}) \\ (\bar{y},x,z) \end{bmatrix}$	$\begin{bmatrix} C_{4\bar{z}}(h_{15}) \\ (y,\bar{x},z) \end{bmatrix}$	$\begin{bmatrix} C_{2xy}(h_{16}) \\ (y,x,\bar{z}) \end{bmatrix}$
Ta(1)	$\begin{pmatrix} 1 & 0 \\ 0 & 1 \end{pmatrix}$	$\begin{pmatrix} \rho_y & 0 \\ 0 & 1 \end{pmatrix}$	$\begin{pmatrix} 1 & 0 \\ 0 & \rho_x \end{pmatrix}$	$\begin{pmatrix} \rho_y & 0 \\ 0 & \rho_x \end{pmatrix}$	$\begin{pmatrix} 0 & \rho_x \\ \rho_y & 0 \end{pmatrix}$	$\begin{pmatrix} 0 & \rho_x \\ 1 & 0 \end{pmatrix}$	$\begin{pmatrix} 0 & 1 \\ \rho_y & 0 \end{pmatrix}$	$\begin{pmatrix} 0 & 1 \\ 1 & 0 \end{pmatrix}$
Ta(2)	$\begin{pmatrix} 1 & 0 \\ 0 & 1 \end{pmatrix}$	$\begin{pmatrix} 0 & \rho_y\rho_z \\ \rho_z & 0 \end{pmatrix}$	$\begin{pmatrix} 0 & \rho_z \\ \rho_x\rho_z & 0 \end{pmatrix}$	$\begin{pmatrix} \rho_y & 0 \\ 0 & \rho_x \end{pmatrix}$	$\begin{pmatrix} \rho_z\rho_y & 0 \\ 0 & \rho_z\rho_x \end{pmatrix}$	$\begin{pmatrix} 0 & \rho_x \\ 1 & 0 \end{pmatrix}$	$\begin{pmatrix} 0 & 1 \\ \rho_y & 0 \end{pmatrix}$	$\begin{pmatrix} \rho_z & 0 \\ 0 & \rho_z \end{pmatrix}$

Table A4: T-matrices for the metal atoms and $\rho_{x,y,z} = \exp(2\pi i q_{x,y,z})$. There are 8 Ta atoms in the unit cell (4Ta(1)+4Ta(2)), but related by a (1/2,1/2,1/2) translation vector. The atomic coordinates are: Ta(1):: (0 1/2 0) and (1/2 0 0); Ta(2):: (0 1/2 1/4) and (1/2 0 1/4).

The displacement vectors, calculated from the proyection operators $\underline{\mathbf{D}}(\alpha)$, for each one of the zone center irreducible representations are given in figure A4. For simplicity, we have only represented the metal atoms.

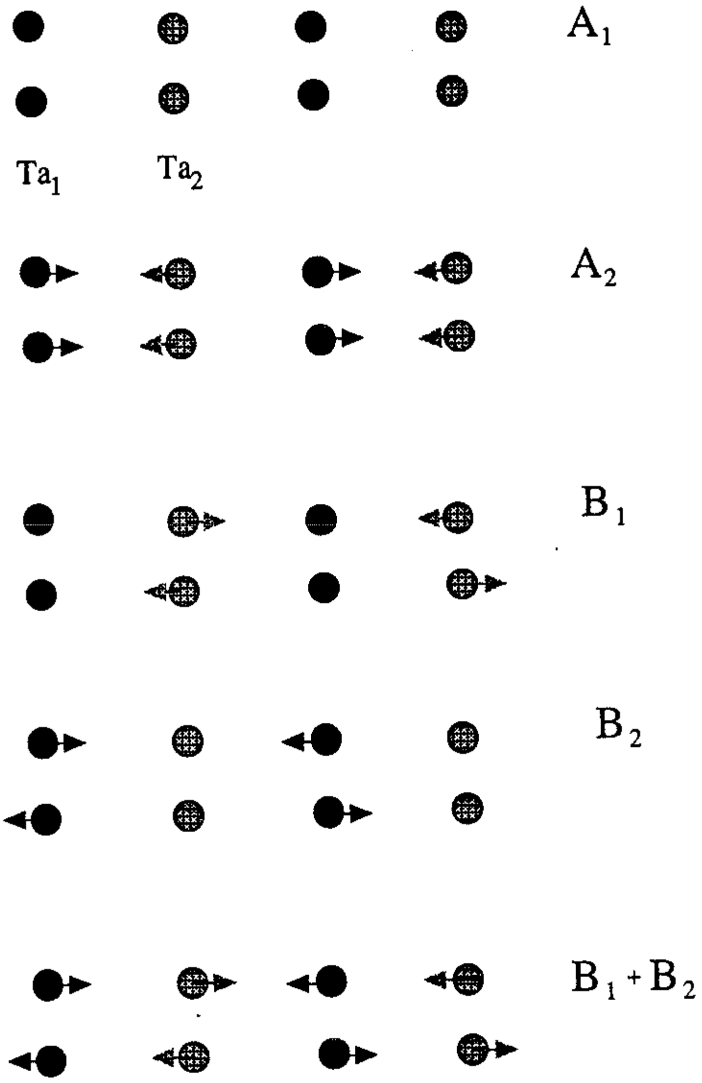

Figure A4: Metal atom displacements in each of the zone center irreducible representations. Note that the combination of B_1 and B_2 type displacements yield the expected tetramerization, as shown in figure A1.

	η_1	η_2	e_4	e_5	x	y	$\frac{\partial\eta_1}{\partial z}$	$\frac{\partial\eta_2}{\partial z}$	$\frac{\partial\eta_1}{\partial x}$	$\frac{\partial\eta_2}{\partial x}$	$\frac{\partial\eta_1}{\partial y}$	$\frac{\partial\eta_2}{\partial y}$
C_{4z}	$-\eta_1$	$-\eta_2$	e_5	$-e_4$	$-y$	x	$-\frac{\partial\eta_1}{\partial z}$	$-\frac{\partial\eta_2}{\partial z}$	$\frac{\partial\eta_1}{\partial y}$	$\frac{\partial\eta_2}{\partial y}$	$-\frac{\partial\eta_1}{\partial x}$	$-\frac{\partial\eta_2}{\partial x}$
C_{2z}	η_1	η_2	$-e_4$	$-e_5$	$-x$	$-y$	$\frac{\partial\eta_1}{\partial z}$	$\frac{\partial\eta_2}{\partial z}$	$-\frac{\partial\eta_1}{\partial x}$	$-\frac{\partial\eta_2}{\partial x}$	$-\frac{\partial\eta_1}{\partial y}$	$-\frac{\partial\eta_2}{\partial y}$
C_{2x}	η_1	$-\eta_2$	e_4	$-e_5$	x	$-y$	$-\frac{\partial\eta_1}{\partial z}$	$\frac{\partial\eta_2}{\partial z}$	$\frac{\partial\eta_1}{\partial x}$	$-\frac{\partial\eta_2}{\partial x}$	$-\frac{\partial\eta_1}{\partial y}$	$\frac{\partial\eta_2}{\partial y}$
C_{2xy}	$-\eta_1$	η_2	$-e_5$	$-e_4$	y	x	$\frac{\partial\eta_1}{\partial z}$	$-\frac{\partial\eta_2}{\partial z}$	$-\frac{\partial\eta_1}{\partial y}$	$\frac{\partial\eta_2}{\partial y}$	$-\frac{\partial\eta_1}{\partial x}$	$\frac{\partial\eta_2}{\partial x}$

Table A5: Transformation table for the order parameters, η_1 and η_2 and their gradients, and the shear elastic strains (e_4, e_5 and e_6). Note, from table A3, that e_6 transfoms as η_2 and e_1-e_2 as η_1.

A2.1 High temperature structure of $(NbSe_4)_3I$

Space group	:	P4/mnc (D_{4h}^{6})
Lattice parameters:		a=9.489Å
		c=19.13Å

Atomic positions (table A6):

			x	y	z	B_{eq}
Nb(1)	8(f)	2..	0	0.5	0.4200(3)	1.88
Nb(2)	4(d)	2.22	0	0.5	0.25	2.07
I	4(e)	4..	0	0	0.6297(4)	4.69
Se(1)	8(h)	m..	0.2754(6)	0.0180(7)	0	1.95
Se(2)	8(h)	m..	0.3910(6)	0.8000(2)	0	1.92
Se(3)	16(i)	1..	0.1265(3)	0.6851(4)	0.3394(2)	1.78
Se(4)	16(i)	1..	0.7844(4)	0.5476(4)	0.3283(2)	1.78

Interatomic distances (table A7):

[1,3,4,6] (*)	[2,5] (*)
Nb(1)···2Se(1) == 2.63(1)	
Nb(1)···2Se(2) == 2.65(1)	Nb(2)···4Se(3) == 2.730(8)
Nb(1)···2Se(3) == 2.627(9)	Nb(2)···4Se(4) == 2.576(9)
Nb(1)···2Se(4) == 2.73(1)	
Se(1)···Se(2) == $\left\{\begin{array}{l}2.43(2)\\3.60(2)\end{array}\right.$	Se(3)···Se(4) == $\left\{\begin{array}{l}2.37(1)\\3.50(1)\end{array}\right.$
Se(3)···Se(4) == $\left\{\begin{array}{l}2.37(1)\\3.50(1)\end{array}\right.$	
$\theta_1 = \theta_3 = 50.5° = -\theta_4 = -\theta_6$	$\theta_2 = 46.2° = -\theta_5$

(*) As in table A2

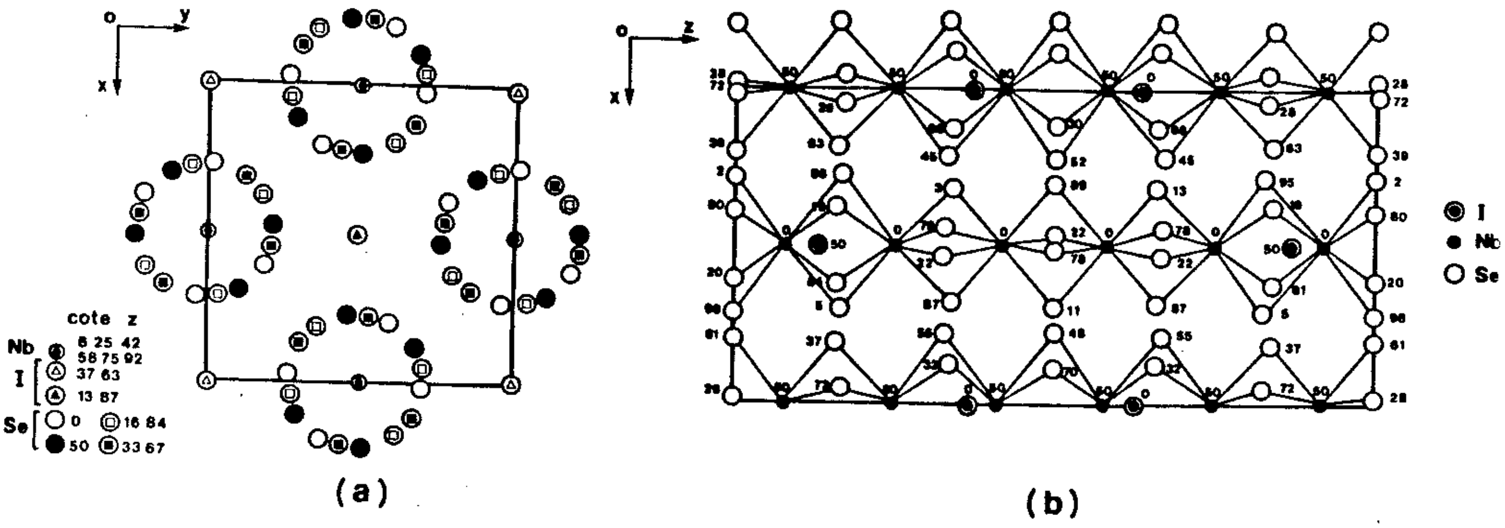

Figure A5. Proyection of the $(NbSe_4)_3I$ high temperature structure onto the x-y plane (a), onto the x-z plane (b).

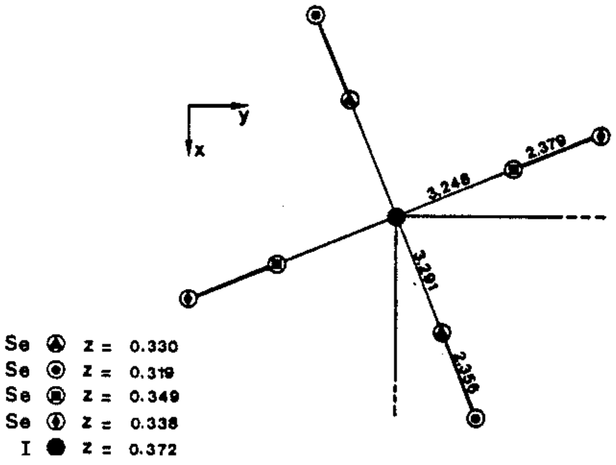

Figure A6. Proyection of I-4Se bonds corresponding to the low temperature $(NbSe_4)_3I$ structure onto the x-y plane. The I-4Se bond lengths are no longer equivalent: I-4Se(5) = 3.248Å and I-4Se(3) = 3.291Å. These I-4Se bond lengths are equivalent in the high temperature structure: 3.27Å.

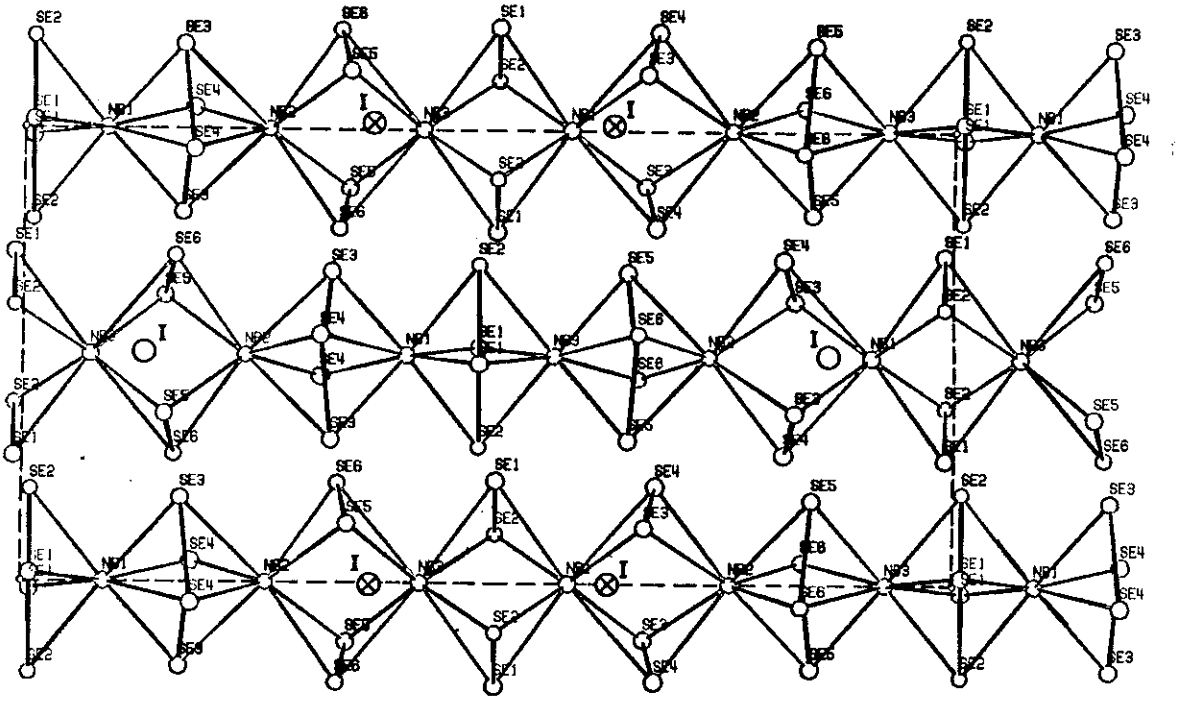

Figure A7 Proyection of the $(NbSe_4)_3I$ low temperature structure onto the x-y plane.

A2.2 Low temperature structure of $(NbSe_4)_3I$

Space group :	$P\bar{4}2_1c$ (D_{2d}^4)
Lattice parameters:	a=9.450(7)Å
(T=128K)	c=19.08(6)Å

Atomic positions (table A8):

			x	y	z	B_{eq}
Nb(1)	4(d)	2..	0	0.5	0.0882(5)	0.9(2)
Nb(2)	4(d)	2..	0	0.5	0.2617(5)	0.7(1)
Nb(3)	4(d)	2..	0	0.5	0.4278(6)	0.9(2)
I	4(c)	2..	0	0	0.3719(4)	2.1(1)
Se(1)	8(e)	1..	0.0176(7)	0.7249(8)	0.0093(4)	0.9(1)
Se(2)	8(e)	1..	-0.2016(7)	0.6081(7)	0.0093(4)	0.7(1)
Se(3)	8(e)	1..	0.1852(9)	0.6230(9)	0.1697(4)	0.9(1)
Se(4)	8(e)	1..	-0.0455(9)	0.7145(9)	0.1815(4)	1.0(1)
Se(5)	8(e)	1..	0.1298(9)	0.6852(9)	0.3485(4)	0.9(1)
Se(6)	8(e)	1..	-0.2189(9)	0.5493(9)	0.3378(4)	0.7(1)

Interatomic distances (table A9):

[1,4] (*)	[3,6] (*)	[2,5] (*)
Nb(1)··· 2Se(1) = 2.610(2)	Nb(3)··· 2Se(1) = 2.639(3)	Nb(2)··· 2Se(3) = 2.739(3)
Nb(1)··· 2Se(2) = 2.635(2)	Nb(3)··· 2Se(2) = 2.664(3)	Nb(2)··· 2Se(4) = 2.5763)
Nb(1)··· 2Se(3) = 2.614(3)	Nb(3)··· 2Se(5) = 2.619(3)	Nb(2)··· 2Se(5) = 2.704(3)
Nb(1)··· 2Se(4) = 2.732(3)	Nb(3)··· 2Se(6) = 2.729(3)	Nb(2)··· 2Se(6) = 2.569(3)
$\mathrm{Se(1)}\cdots\mathrm{Se(2)} = \begin{cases} 2.347(2) \\ 3.596(3) \end{cases}$	$\mathrm{Se(1)}\cdots\mathrm{Se(2)} = \begin{cases} 2.347(2) \\ 3.596(3) \end{cases}$	$\mathrm{Se(3)}\cdots\mathrm{Se(4)} = \begin{cases} 2.356(3) \\ 3.460(4) \end{cases}$
$\mathrm{Se(3)}\cdots\mathrm{Se(4)} = \begin{cases} 2.356(3) \\ 3.460(4) \end{cases}$	$\mathrm{Se(5)}\cdots\mathrm{Se(6)} = \begin{cases} 2.379(4) \\ 3.543(4) \end{cases}$	$\mathrm{Se(5)}\cdots\mathrm{Se(6)} = \begin{cases} 2.379(4) \\ 3.543(4) \end{cases}$
$\theta_1 = 51.4° = -\theta_4$	$\theta_3 = 50.2° = -\theta_6$	$\theta_2 = 46.2° = -\theta_5$

(*) As in table A2

APPENDICE B

B. Modèle Phénoménologique

Dans le Chapitre IV, nous avons postulé l'existence d'un ou de plusieurs modes optiques directement couplés aux électrons de conductions. La nature des orbitales électroniques de conduction, permet de supposer que les modes de vibrations concernés impliquent des déplacements des ions Ta le long de l'axe des chaines. De plus, le taux de remplissage de la bande de conduction (bande 1/4-pleine), conduit à considérer des modes de type "tétramérisation", correspondant à une surstructure d'ordre 4 pour les positions des ions Ta (cf. Appendix A).

La condensation d'une telle distorsion ne modifie pas nécessairement la maille cristallographique. En effet, bien que les distances Ta-Ta soient uniformes (d=3.205 Å) dans $(TaSe_4)_2I$ au-dessus de T_P, le paramètre de maille, c, correspond à 4 distances Ta-Ta: c=4d. En particulier, si les distorsions se couplent en antiphase sur les chaines premières voisines, la maille cristallographique ne sera pas modifiée.

Les déplacements des Ta sont alors décrits par une combinaison linéaire de deux modes optiques *de centre de zone*, de symétrie B_1 et B_2. Le mode B_1 (cf. Fig. A4), correspond à un déplacement alterné des ions Ta(2) sur une même chaîne, les ions Ta(1) restant au repos. Les déplacements associés au mode B_2 s'obtiennent par permutation des ions Ta(1) et Ta(2).

Les sites des ions Ta(1) et Ta(2) étant cristallographiquement très voisins, on s'attend à ce que les fréquences propres des modes B_1 et B_2 soient très proches. Il convient donc, a priori, de considérer les deux types de déplacements comme deux paramètres d'ordre possibles, η_1 et η_2. De plus, la présence d'un pseudo-invariant de Lifshitz entre ces deux variables (voir ci-dessous), implique que les déplacements statiques dans la phase condensée, contiendront une combinaison linéaire des deux modes.

Nous sommes donc amenés à écrire un potentiel thermodynamique contenant les invariants associés aux variables η_1 et η_2 et à leurs gradients. De plus, la forte composante de type "acoustique" des déplacements observés conduit à inclure les termes de couplages avec les variables élastiques.

Les propriétés de transformation des variables η_1 (x^2-y^2) et η_2 (xy) et de leurs gradients sont montrées au Tableau A5. La densité de potentiel thermodynamique, développée à l'ordre le plus bas, s'écrit sous forme de trois termes:

$$F = F_\eta + F_E + F_C \tag{1}$$

avec:

$$F_\eta = \alpha_1\eta_1^2 + \alpha_2\eta_2^2 + \beta_1\eta_1^4 + \beta_2\eta_2^4 + \beta_3\eta_1^2\eta_2^2 + f\left(\eta_2\frac{\partial\eta_1}{\partial z} - \eta_1\frac{\partial\eta_2}{\partial z}\right) + \tau_1'\left(\left[\frac{\partial\eta_1}{\partial x}\right]^2 + \left[\frac{\partial\eta_1}{\partial y}\right]^2\right) + \tau_2'\left(\left[\frac{\partial\eta_2}{\partial x}\right]^2 + \left[\frac{\partial\eta_2}{\partial y}\right]^2\right) + \tau_1\left[\frac{\partial\eta_1}{\partial z}\right]^2 + \tau_2\left[\frac{\partial\eta_2}{\partial z}\right]^2 \tag{2a}$$

$$F_E = \frac{1}{2}C_{11}\left(e_1^2 + e_2^2\right) + \frac{1}{2}C_{33}e_3^2 + C_{12}e_1e_2 + C_{13}(e_1 + e_2)e_3 + \frac{1}{2}C_{44}\left(e_4^2 + e_5^2\right) + \frac{1}{2}C_{66}e_6^2 \tag{2b}$$

$$F_C = \delta_1\eta_1(e_1 - e_2) + \delta_2\eta_2e_6 + \gamma_1\left(e_5\frac{\partial\eta_1}{\partial y} + e_4\frac{\partial\eta_1}{\partial x}\right) + \gamma_2\left(e_5\frac{\partial\eta_2}{\partial x} - e_4\frac{\partial\eta_2}{\partial y}\right) \tag{2c}$$

Pour discuter de la stabilité d'une phase condensée modulée, il est utile d'introduire le vecteur de déplacement acoustique $\boldsymbol{u}(\boldsymbol{r}) = (u_1(\boldsymbol{r}), u_2(\boldsymbol{r}), u_3(\boldsymbol{r}))$ associé aux déformations élastiques:

$$\begin{aligned} e_1 &= u_{11} = \frac{\partial u_1}{\partial x} & \qquad e_4 &= u_{23} = \frac{1}{2}\left(\frac{\partial u_2}{\partial z} + \frac{\partial u_3}{\partial y}\right) \\ e_2 &= u_{22} = \frac{\partial u_2}{\partial y} & \qquad e_5 &= u_{13} = \frac{1}{2}\left(\frac{\partial u_1}{\partial z} + \frac{\partial u_3}{\partial x}\right) \\ e_3 &= u_{33} = \frac{\partial u_3}{\partial z} & \qquad e_6 &= u_{12} = \frac{1}{2}\left(\frac{\partial u_1}{\partial y} + \frac{\partial u_2}{\partial x}\right) \end{aligned} \tag{4}$$

On introduit les composantes de Fourier des variables $\eta_1(\boldsymbol{r})$, $\eta_2(\boldsymbol{r})$ et $\boldsymbol{u}(\boldsymbol{r})$:

$$\begin{aligned} \eta_j(\mathbf{r}) &= \sum_{\mathbf{q}} \eta_{j\mathbf{q}}\, e^{i\,\mathbf{q}\,\mathbf{r}} \quad , \ j = 1,2 \ \ and \ \ \eta_{j\text{-}\mathbf{q}} = \eta_{j\mathbf{q}}^* \\ u_{ij}(\mathbf{r}) &= \varepsilon_{ij} + \frac{i}{2}\sum_{\mathbf{q}\neq 0}\left(q_i\,u_{j\mathbf{q}} + q_j\,u_{i\mathbf{q}}\right)e^{i\,\mathbf{q}\,\mathbf{r}} \end{aligned} \tag{5}$$

Le potentiel thermodynamique s'écrit alors:

$$\Phi = \int \mathrm{F\ dr} = \mathrm{V} \sum_{\mathrm{q}} \Phi_{\mathrm{q}} \tag{6}$$

Afin de simplifier l'expression du potentiel Φ_q, il convient de préciser les valeurs des phases relatives des variables complexes η_{1q}, η_{2q} et u_q. Ces phases sont déterminées, au première ordre, par les trois termes de couplage suivants:

$$f\left(\eta_2 \frac{\partial \eta_1}{\partial z} - \eta_1 \frac{\partial \eta_2}{\partial z}\right) \rightarrow -i\, q_3 f \left(\eta^*_{1q}\eta_{2q} - \eta_{1q}\eta^*_{2q}\right) \tag{7}$$

$$\eta_1(e_1 - e_2) \rightarrow \frac{i}{2}\eta^*_{1q}(q_1 u_{1q} - q_2 u_{2q}) - \frac{i}{2}\eta_{1q}\left(q_1 u^*_{1q} - q_2 u^*_{2q}\right) \tag{8}$$

$$\eta_2 e_6 \rightarrow \frac{i}{4} q_1\left(\eta^*_{2q} u_{2q} - \eta_{2q} u^*_{2q}\right) + \frac{i}{4} q_2\left(\eta^*_{2q} u_{1q} - \eta_{2q} u^*_{1q}\right) \tag{9}$$

Le premier terme induit un déphasage de $\pi/2$ entre les variables η_{1q} et η_{2q} Dans ce qui suit, on choisit l'origine de telle sorte que η_{1q} soit réel:

$$\eta_{1q} = \eta^*_{1q} = \overline{\eta}_1 \tag{10}$$

L'équation (7) entraine alors que la variables η_{2q} est imaginaire. Si on choisit des valeurs réelles pour les variables u_{1q} et u_{2q}, on voit que l'expression (8) s'annule: une valeur non nulle de η_{2q} entrainera alors (cf. éq.(9)) un cisaillement modulé de type e_6. Si par contre on choisit des valeurs imaginaires pour les variables u_{1q} et u_{2q}, l'expression (9) s'annule et l'expression (8) induira un cisaillement modulé de type $e_1 - e_2$.

C'est cette dernière solution qui est observée expérimentalement: en effet les déplacements atomiques dans la phase condensée ont une forte composante du type transverse acoustic $q(110)\, u\left(1\,\overline{1}\,0\right)$ c.à.d. $q_1 = q_2$, $u_{1q} = -\, u_{2q}$. On choisira donc des valeurs imaginaires pour les variables u_{1q} et u_{2q}. Toutefois, ce choix n'est pas rigoureux car, en réalité, les phases des variables η_{2q}, u_{1q} et u_{2q} doivent être obtenues par minimisation simultanée des trois termes de couplage (7), (8) et (9). Les phases et les déplacements correspondants prendront alors des valeurs générales. Toutefois l'étude des intensités des raies satellites permet de supposer que les déplacements atomiques réels sont voisins des déplacements simplifiés que nous considérons ici.

Dans le cadre de l'approximation ci-dessus:

$$\eta_{2\mathrm{q}}^{*} = -\eta_{2\mathrm{q}} = i\overline{\eta}_2 \qquad u_{1\mathrm{q}}^{*} = -u_{1\mathrm{q}} = i\overline{u}_1 \qquad u_{2\mathrm{q}}^{*} = -u_{2\mathrm{q}} = i\overline{u}_2 \tag{11}$$

les termes de l'éq. (2c) s'écrivent:

$$\eta_1(e_1 - e_2) \rightarrow \overline{\eta}_1(q_1\overline{u}_1 - q_2\overline{u}_2) \tag{12}$$

$$e_5\frac{\partial\eta_1}{\partial y} + e_4\frac{\partial\eta_1}{\partial x} \rightarrow \frac{1}{2}\overline{\eta}_1 q_1 q_2\left(u_{3\mathrm{q}} + u_{3\mathrm{q}}^{*}\right) \tag{13}$$

$$e_5\frac{\partial\eta_2}{\partial x} - e_4\frac{\partial\eta_2}{\partial y} \rightarrow \frac{i}{4}\overline{\eta}_2\left(q_1^2 - q_2^2\right)\left(u_{3\mathrm{q}} - u_{3\mathrm{q}}^{*}\right) + \frac{1}{2}\overline{\eta}_2 q_3(q_1\overline{u}_1 - q_2\overline{u}_2) \tag{14}$$

La symétrie des expressions ci-dessus impose de prendre $|q_1| = |q_2|$ et $|\overline{u}_1| = |\overline{u}_2|$. En accord avec l'expérience nous choisissons: $q_1 = q_2 = q$ et $\overline{u}_1 = -\overline{u}_2 = u$. La phase de la variable u_{3q} est alors déterminée par l'éq. (13):

$$u_{3q} = u^{*}_{3q} = u_3. \tag{15}$$

Le potential thermodynamique Φ_q se décompose en trois termes:

$$\Phi_{\mathrm{q}}^{\eta} = \alpha_1\overline{\eta}_1^2 + \alpha_2\overline{\eta}_2^2 + 2q_3 f\,\overline{\eta}_1\overline{\eta}_2 + q_3^2\left(\tau_1\overline{\eta}_1^2 + \tau_2\overline{\eta}_2^2\right) + 2q^2\left(\tau_1'\overline{\eta}_1^2 + \tau_2'\overline{\eta}_2^2\right) + O\left(\eta^4\right) \tag{16}$$

$$\Phi_{\mathrm{q}}^{E} = C_{11}q^2u^2 + \frac{1}{2}C_{33}q_3^2u_3^2 - C_{12}q^2u^2 + \frac{1}{4}C_{44}\left(q^2u_3^2 + q_3^2u^2\right) + \frac{1}{8}C_{66}q^2u^2 \tag{17}$$

$$\Phi_{\mathrm{q}}^{C} = 2\delta_1\overline{\eta}_1 qu + \gamma_1\overline{\eta}_1 q^2u_3 + \gamma_2\overline{\eta}_2 q_3 qu \tag{18}$$

En minimisant $\Phi_q{}^E + \Phi_q{}^C$ par rapport à u et u_3, on obtient les valeurs d'équilibre des déplacements acoustiques:

$$u = -\frac{4\delta_1\overline{\eta}_1 q + 2\gamma_2\overline{\eta}_2 q q_3}{4Cq^2 + C_{44}q_3^2} \qquad u_3 = -\frac{2\gamma_1\overline{\eta}_1 q^2}{2C_{33}q_3^2 + C_{44}q^2}$$

$$\text{with } C = C_{11} - C_{12} + \frac{1}{8}C_{66} \tag{19}$$

La contribution du terme en γ_2 est d'ordre plus élevé que celle du terme en δ_1: elle peut donc être négligée en première approximation. D'où:

$$u\,q = -\frac{4\delta_1\bar{\eta}_1}{4C + C_{44}\rho^2} \qquad and \quad \rho = \frac{q_3}{q}$$
$$u_3 = -\frac{2\gamma_1\bar{\eta}_1}{2C_{33}\rho^2 + C_{44}} \tag{20}$$

En reportant les valeurs (20) dans l'expression du potentiel on obtient:

$$\Phi_{\mathbf{q}} = \bar{\alpha}_1\bar{\eta}_1^2 + \bar{\alpha}_2\bar{\eta}_2^2 + 2q_3\bar{f}\bar{\eta}_1\bar{\eta}_2 + O(\eta^4)$$

$$\bar{\alpha}_1 = \alpha_1 + \tau_1 q_3^2 + 2\tau_1' q^2 - \frac{4\delta_1^2}{4C + C_{44}\rho^2} - \frac{\gamma_1^2 q^2}{C_{44} + 2C_{33}\rho^2}$$

$$\bar{\alpha}_2 = \alpha_2 + \tau_2 q_3^2 + 2\tau_2' q^2$$

$$\bar{f} = f - \frac{2\delta_1\gamma_2}{4C + C_{44}\rho^2} \tag{21}$$

Par minimisation par rapport à $\bar{\eta}_1$ *et* $\bar{\eta}_2$ on obtient la solution triviale $\bar{\eta}_1 = \bar{\eta}_2 = 0$ sauf si $\bar{\alpha}_1\bar{\alpha}_2 = q_3^2\bar{f}^2$. A l'ordre le plus bas, par rapport aux variables q et q_3, cette condition s'écrit:

$$\alpha_1'\alpha_2 + q^2\left\{2\alpha_1'\tau_2' + 2\alpha_2\tau_1' - \frac{\alpha_2\gamma_1^2}{C_{44} + 2C_{33}\rho^2}\right\} + q_3^2\left\{\alpha_1'\tau_2 + \alpha_2\tau_1 - \left(f - \frac{2\delta_1\gamma_2}{4C + C_{44}\rho^2}\right)^2\right\} + O(q^4, q_3^4) = 0 \tag{22}$$

où α_1' est le module renormalisé de la variable η_1:

$$\alpha_1' = \alpha_1 - \frac{4\delta_1^2}{4C + C_{44}\rho^2} \tag{23}$$

Du fait du couplage avec les déformations ce module acquiert un caractère non-analytique dans la limite des petits vecteurs d'onde. Au vu de la très faible valeur de la constante élastique C$_{44}$, cet effet n'est sans doute pas observable.

L'expression (22) montre que pour des valeurs suffisamment faibles des coefficients τ_1, τ_2, τ'_1, et τ'_2, les coefficients des termes en q^2 et q_3^2 peuvent prendre des valeurs négatives alors que les modules α_1' et α_2 sont toujours positifs. On observera alors une transition vers un état modulé de vecteur d'onde $q_1 = q_2 \neq q_3 \neq 0$. Les déplacements modulés auront une composante de type transverse acoustique polarisée dans la direction $\left(1\ \bar{1}\ 0\right)$ ainsi qu'une composante acoustique polarisée le long des chaînes. Ceci est en bon accord avec l'expérience dans le cas de $(TaSe_4)_2I$. Les composantes optiques de type η_1 et η_2 n'ont pas été mise en évidence pour l'instant.

APPENDICE C

SPANISH SCIENTIFIC RESEARCH USING NEUTRON SCATTERING TECHNIQUES
Servicio de Publicaciones. Universidad de Cantabria. 1991

SOME DIFFRACTION ASPECTS IN $NbTe_4$: A NEUTRON STUDY

J.E. Lorenzo

Institut Laue-Langevin, 38042 Grenoble Cedex, France.

In collaboration with R. Currat *, P. Monceau ** and F. Levy ***
* Institut Laue-Langevin, 38042 Grenoble Cedex, France.
** Centre de Recherches sur les Tres Basses Temperatures, CNRS, 38042 Grenoble Cedex, France.
*** Institut de Physique Appliquée, Ecole Polytechnique Fédérale de Lausanne, CH-1015, Lausanne, Switzerland.

ABSTRACT

A single crystal diffraction study has been carried out on $NbTe_4$. Critical scattering measurement in the high temperature non modulated phase has been performed. The fine structure of the low temperature incommensurate satellites have been resolved. A comparison with present models is also performed.

I. INTRODUCTION

Transition metal chalcogenides are a wide family of compounds with general formula $(MX_n)_mY$ with[1]

- M: Nb, Ta, V
- X: Se, Te, S
- Y: I, Br, Cl
- n: 2, 3, 4, 5
- m: 1, 2, 3, 10/3,...

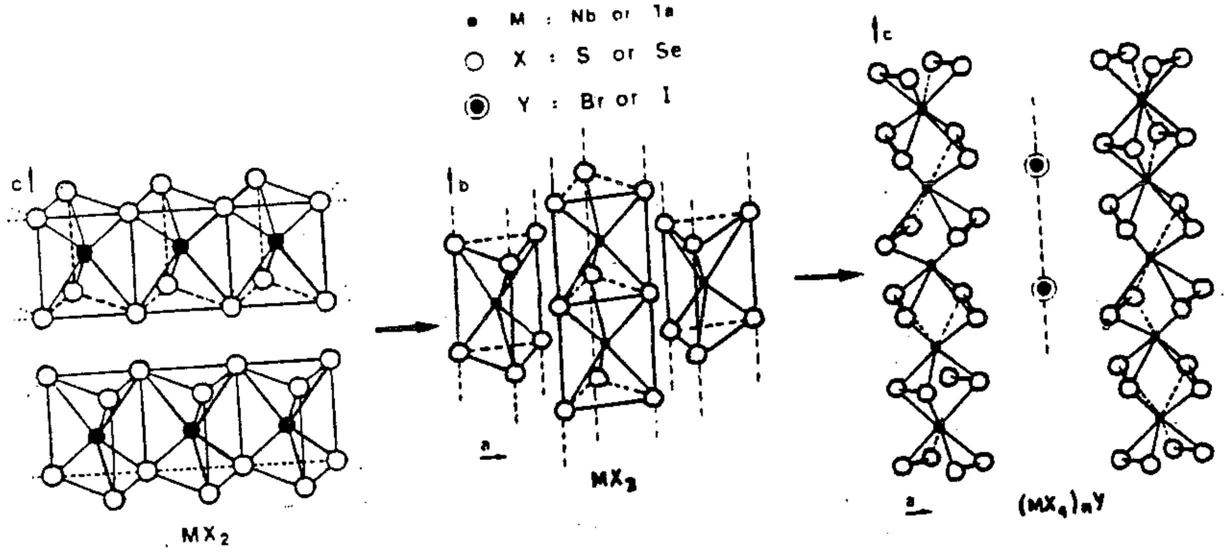

FIG. 1: MX_2, MX_3 and MX_4 schematic models.

This family is usually divided into 3 different subfamilies, namely, transition metal dichalcogenides, trichalcogenides and tetrachalcogenides (see fig. 1). The first two have been currently studied for nearly twenty years and still nowadays. The reason is twofold: first they are low dimensional compounds and second they exhibit non linear transport properties related to the formation of so called charge density waves (CDW)[1-2].. Representative compounds of these two subfamilies are $TaSe_2$ and $NbSe_3$.

The CDW appears as the consequence of a Peierls distortion: the 1D (or 2D) free electron gas is unstable under fluctuations that open a gap (or several minigaps) at the Fermi level the system becoming an insulator or semiconductor below a critical temperature called the Peierls temperature, T_P. The screening of the atom-atom interaction by the electron gas induces an anomaly in the phonon spectra: one or several modes soften at a certain $\mathbf{q}_I$ value giving rise to a modulated structure. In terms of electronic band structure the Peierls transition can be viewed as the nesting of the Fermi surface between positions $+\mathbf{k}_F$ and $-\mathbf{k}_F$ by means of suitable phonons with wave vector $2\mathbf{k}_F= \mathbf{q}_I$.

Transition metal tetrachalcogenides[3-4] are a series of quasi-one dimensional compounds, with $(TaSe_4)_2I$ and $(NbSe_4)_3I$ as the most studied and representative examples but with different characteristics. The first one undergoes a metal-insulator phase transition at $T_P=263$ K with the formation of a modulated structure below T_P and modulation vector $\mathbf{q}_I = (0.045, 0.045, 0.085)$. The second one exhibits a semiconductor-semiconductor transition accompanied by a ferrodistortive phase transition at $T_C=274$ K, going from P4/mnc to $P\overline{4}2_1c$ below T_C. These compounds are made of chains of (MX_4) groups separated by strands of iodine. The transition metal is sandwiched between two layers of Se arranged in a tilted rectangular way and each rectangle is made of 2 Se_2^{2-} dimers.

Among the transition metal tetrachalcogenides, $NbTe_4$ and $TaTe_4$ form a completely different class of compounds (fig. 2). As before, the transition metal is sandwiched between two square layers of four Te atoms forming a set of parallel chains. Now Te atoms from neighbour chains form a strong covalent bond and can be considered as dimers. Due to this bonding between Te from adjacent chains it is very much unlikely that these two compounds can be considered as quasi one dimensional, at least in their structural properties. Firstly characterized by Selte and Kjekshus[5]. in 1964, they have been widely studied in the last seven years due mainly to their fascinating variety of modulated phases and phase transitions, and the simplicity of their normal non-modulated structure. Parallel to the structural stu-

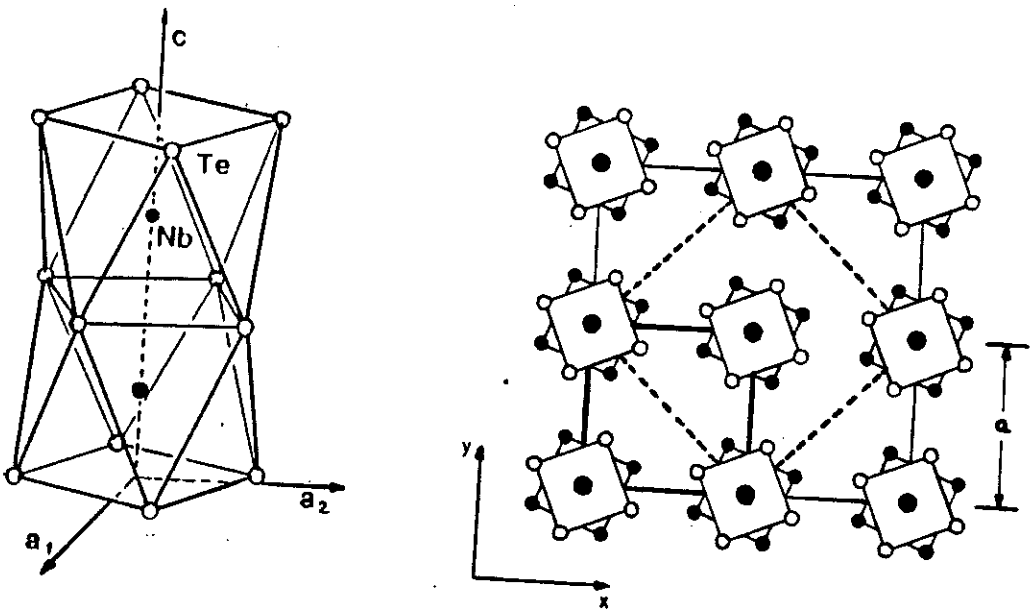

FIG. 2: The basic structure of $NbTe_4$ (left) and the basal plane modifications in the different superstructures (right).

dies, theories explaining the different transitions have been developed by Walker and collaborators[6]. Despite all these efforts, very little is known about their macroscopic properties and the mechanisms driving the different phase transitions are still being investigated.

In this paper we report some recent neutron scattering work on single crystals and it is organized as follows: in part (ii), the experimental conditions are described. In part (iii), we present the results of our experiments and the discussion under the framework of present theories and previous experiments . Finally some concluding remarks are presented in part (iv).

II. EXPERIMENTAL

Diffraction experiments were performed on several three axis spectrometers: 1T at CEN-Saclay and IN3, IN14 and IN12 at ILL (Grenoble). The incident wave vector was k_I=2.662 Å^{-1} for the three first spectrometers and 2 Å^{-1} for the last one. Smaller wave vectors could not be used because of the small size of the unit cell, $a^* \approx c^* \approx$ 1Å^{-1}. Tight horizontal collimations (20^3) insured a good transverse q-resolution, as needed for the study of the low temperature satellites.

The low temperature data were taken using a closed cycle refrigerator. Two different samples were used mounted inside aluminium containers: one with the directions *(hh0)* and *(00l)* lying in the instrument scattering plane and the other with directions *(h00)* and *(00l)*. However, some measurements required tilting the sample around one of the above mentiones directions in order to reach different superstructure reflections (such as (2.5, 0.5, 1.688)).

For the high temperature measurements, a furnace was used. In this case the sample holder was, first, a niobium cylinder, which is very suitable for neutron experiments due to its high melting temperature (2500°C) and low neutron absorption. The container was sealed by electron beam welding in vacuum. After several days at elevated temperatures the sample progressively decomposed by a chemical reaction involving Te transport to the Nb walls of the container. A second attempt was performed using a silica tube with a few milligrams of excess Te to create a Te vapor pressure at high temperatures. The results look satisfactory and no sample deterioration has been detected. However a large background coming from the silica ampoule is the price to pay.

III. STRUCTURE ANALYSIS

In 1964, Selte and Kjekhus first determined the structure of $NbTe_4$. They fitted their data in a tetragonal unit cell P4/mcc with lattice parameters a=6.499 Å and c=6.837 Å and atomic positions

$$\text{Nb (a)} \pm (0, 0, \tfrac{1}{4})$$

$$\text{Te (m)} \pm (x, y, 0; \bar{y}, x, 0: \bar{x}, y, \tfrac{1}{2}; y, x, \tfrac{1}{2})$$

though they mentioned the presence of a superstructure of the form 2a x 2a x 3c.

In 1983, Boswell, Prodan and Brandon[7] pointed out the formation of another incommensurate structure below 150 K, characterized by weak diffuse and streaked satellites running at positions along the c* axis. They proposed to explain both the room temperature modulated structure and the low temperature streaked structure the formation of three charge density waves on three different chains, as an analogy to the 3q-state observed in $NbSe_3$ (Wilson[8] 1979). The wave vectors are

$$\mathbf{q}_1=(0, 0, 0.311) \qquad \mathbf{q}_2=(1/2, 1/2, 0.344)$$
$$\mathbf{q}_3=(1/2, 0, 1/3)$$

In 1985, Eaglesham, Bird, Withers and Steeds[9], and Mahy, Van Landuyt, Amelincx, Uchida, Bronsema and Van Smaalen[10] reported, independently, the existence of a third phase below 50 K. This is a commensurate phase which results from the destruction of discommensurations walls at dislocations (or sharp interfaces). These last authors proposed a model[11] (1986) based on discommensuration to explain all the structures of $NbTe_4$. It was in late 1986 that Van Smaalen, Bronsema and Mahy[12] achieved to fully analyze the incommensurate room temperature structure of $NbTe_4$. They showed that the superstructure can be explained in terms of a 4-dimensional space group given by the vectors,

$$h\mathbf{a}^* + k\mathbf{b}^* + l\mathbf{c}^* + m\mathbf{q}'$$

with

$$\mathbf{q}' = 1/2\,\mathbf{a}^* + 1/2\,\mathbf{b}^* + 0.688\mathbf{c}^*$$

Analogous work on $TaTe_4$ appeared in 1987 yielding a commensurate wave vector

$$\mathbf{q}' = 1/2\,\mathbf{a}^* + 1/2\,\mathbf{b}^* + 2/3\mathbf{c}^*$$

Also in 1987 the high temperature non-modulated structure of $NbTe_4$ was characterized by

Böhm[13] proposing P4cc as space group (see note). The satellite integrated intensity temperature variation gives evidence of a second order phase transition located at 793 K.

From 1985 on, Walker and collaborators published a series of theoretical analyses based on a Landau free energy expansion explaining the formation of the different superstructures in terms of single column distortions. To determine the phase relation (ϕ_n) between the distortions($\Psi^{(m)}$) of different chains they assume an interaction of the form,

$$F_{nm} = \frac{1}{4} G \int \mathrm{Re}\left[\Psi^{(m)}(z)\Psi^{(n)*}(z)\right] dz$$

where n and m label the columns. Nearest-neighbour (G_1), next-nearest-neighbour (G_2) and third nearest-neighbour (G_3) interactions are taken into account. Depending on the values of these parameters several solutions are possible.

To obtain the correct low temperature commensurate and incommensurate structure for $NbTe_4$ and $TaTe_4$ (2a x 2a basal plane) the first two interactions must assumed to be repulsive (both G_1 and G_2 positive, with G_1 larger than G_2) and the third could be attractive (G_3 negative, but much smaller that the other two) or repulsive, depending on how the high temperature modulated phase becomes unstable.

The high temperature commensurate and incommensurate structures for $NbTe_4$ and $TaTe_4$ ($\sqrt{2}a$ x $\sqrt{2}a$ basal plane) are stabilized for G_1 positive and G_2 negative.

Besides, assuming that $\Psi^{(n)}(z)$ has a constant amplitude and a constant phase, the phase relations among chains in the different phases are

- For the 2a x 2a basal plane,

$$\phi_A = \phi_B = 0 \qquad \phi_C = \phi \qquad \phi_D = -\phi$$

and for small values of G_1 and G_2, $\phi = 2/3\pi$.

- For the $\sqrt{2}a$ x $\sqrt{2}a$ basal plane,

$$\phi_A = \phi_C = \phi \qquad \phi_B = \phi_D = -\phi$$

IIIa. High temperature structure

This high temperature normal structure appears at temperatures above 520 °C, as it was reported by Böhm. The space group seems to be P4cc. The difference with the average structure at room temperature consists in positional shifts of the Nb atoms along the z-direction, leading to the disappearance of the mirror plane perpendicular to the fourfold axis. The atomic positions for both Nb and Te are

$$\mathrm{Nb(a)}(0,0,z;\ 0,0,z+\tfrac{1}{2})$$
$$\mathrm{Te(d)}(x,y,z;\ \bar{x},\bar{y},z;\ \bar{y},x,z;\ y,\bar{x},z;$$
$$x,y,z+\tfrac{1}{2};\ \bar{x},y,z+\tfrac{1}{2};\ \bar{y},\bar{x},z+\tfrac{1}{2};\ y,x,z+\tfrac{1}{2})$$

with z(Nb)=0.242(1) and x(Te)=0.1440(6), y (Te)=0.3276(6) and z(Te)=0.

In this phase we have performed measurements of the correlation lengths of the incommensurate structure fluctuations with the aim of checking for the possibility that the phase transition could be driven by one dimensional charge density waves developing on each chain. The results are plotted in fig. 3 and show that these fluctuations are clearly 3D with a ratio between longitudinal and transverse correlation lenghts of

$$\frac{\xi_{\parallel}}{\xi_{\perp}} = 1.3$$

and $\xi_{\parallel}$ =.0823c* (12 unit cells) at $T=T_C + 20$. Note that the same ratio amounts to 7.5 in $K_{0.3}MoO_3$ and 13 in $NbSe_3$[14], where a clear CDW behaviour have been observed. So, two different interpretations can be proposed:

- The 3D fluctuations regime extends above T_C+20 and measurements at higher temperatures have to be performed to attain the 1D fluctuations regime or,
- This phase transition is not driven by 1D CDW fluctuations.

Due to the fact that this system remains metallic at all temperatures , it is the second possibility the most likeably.

IIIb. Incommensurate I structure

Van Smaalen et al. have analyzed this incommensurate I structure at room temperature in terms of a long period commensurate structure. The enlarged unit cell is defined as **A=a+b**, **B=a-b** and **C=16c**. The original average positions 2(a) for Nb and 8(m) for Te in the P4/mcc space group are transform into 64 Nb and 256 Te positions. In this enlarged unit cell the position of each atom is written as

$$u^{\mu}_{\alpha}(x^{\mu}_{4}) = \sum_{n=1}^{\infty}\left[P^{\mu}_{n\alpha}\cos(2\pi n x^{\mu}_{4}) + Q^{\mu}_{n\alpha}\sin(2\pi n x^{\mu}_{4})\right]$$

with α=x,y,z, μ=Nb, Te, $x_4^{\mu} = \mathbf{q}\cdot\mathbf{r}^{\mu}$, and the value of coefficients P and Q as given in the original paper. Physically this modulation shows a trimeriza-

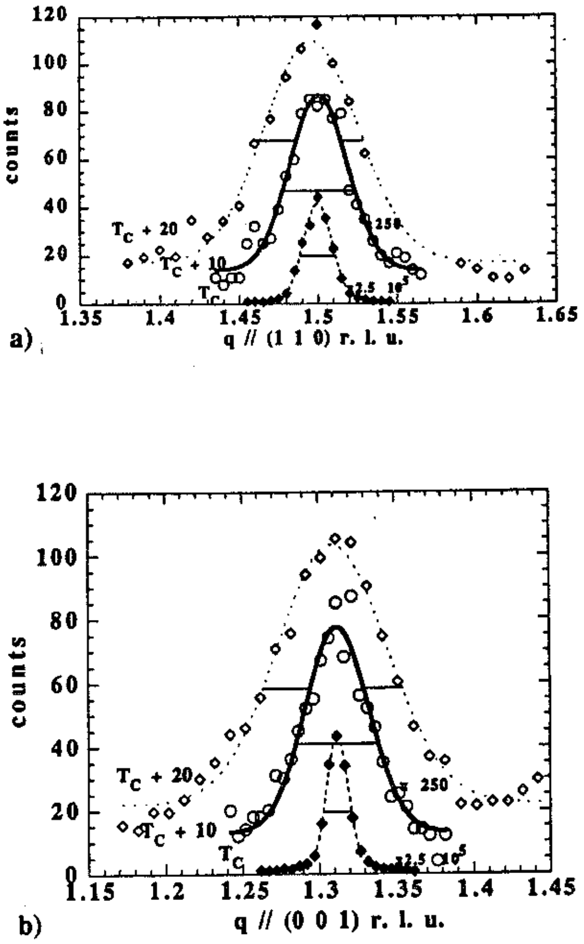

FIG. 3: (a) Critical scattering along (110)-direction. (b) Critical scattering along (001)-direction. The lines corresponds to the fits. Note that the instrumental resolution is given by the width at T_C.

tion of Nb atoms whose phase displacement is π from column to column coupled to a slight displacement of Te atoms along the c axis and a shrinking-expansion combined with the rotations of Te cages around the c axis.

This structure develops below 520°C at positions q=(1/2, 1/2, 1/3(1-δ)) (δ=0.064) which does not change with temperature. On cooling the sample down to room temperature the intensity of these superlattice reflections grows and appears, systematically, as large as the fundamental whereas previous X-ray analyses carried out by Van Smaalen et al. showed a difference of, approximately, three orders of magnitude between fundamental and satellite intensities. Neutron powder diffraction and electron microscopy experiments confirm Van Smaalen results. The high quality of our samples and their relative large thickness (5*5*10 mm^3) provide us with a large extinction for the fundamental reflections.

IIIc. Incommensurate II structure

This low temperature spots (LT) arise at positions

$$q = \left(\frac{1}{2}, 0, \frac{2}{3}(1+\Delta)\right)$$

with Δ = (3n+1)δ for the set labelled LT1 and Δ=(3n-1/2)δ for the set labelled LT2. δ=0.033 and n=0,±1,±2,±3,.... Electron microscopy experiments distinguished these two sets separately or simultaneously in different regions of the crystal. Mahy et al showed that the LT1 set together with the room temperature incommensurate reflections can be explained by the theory of shear structures[15] (Van Landuyt et al., 1970), where the periodicity and the R-vector of planar defects was determined from the fractional shifts of the satellites from their commensurate positions. This model gives account of the first set but not of the LT2-type. Walker and collaborators described the LT1 structure in terms of phason and amplitudon symmetry mode distortion of the (3+1) dimensional room temperature supercrystal. Only Nb atoms were taken into account and the calculations were carried out for the single q-state.

In fact the real LT1 and LT2 structures are still unknown. X-ray conventional diffraction methods doesn't have enough resolution so as to clearly separate the satellites. Lately Prodan[16] et al. have started to perform computer simulations of electron diffraction patterns in order to account for both sets of satellites. To do this they first presuppose a high temperature unit cell enlargement A=2a, B=2b and C_{LT1}=16c, yielding four different columns (see fig. 2) instead of two. LT1 satellites are reproduced from the incommensurate I structure by shifting oppositely the complete columns III and IV by an amount d along the c-axis while columns I and II remain unshifted. Different values of d varies the LT1-type satellites intensities with no significant effects on the incommensurate I and fundamental structure. In order to reproduce the LT2 type of structure, a further doubling of the unit cell along c (C_{LT2} = 32c) is needed because the positions of these reflections lie exactly half-way between those of LT1. The displacements corresponding to this structure contain alternate

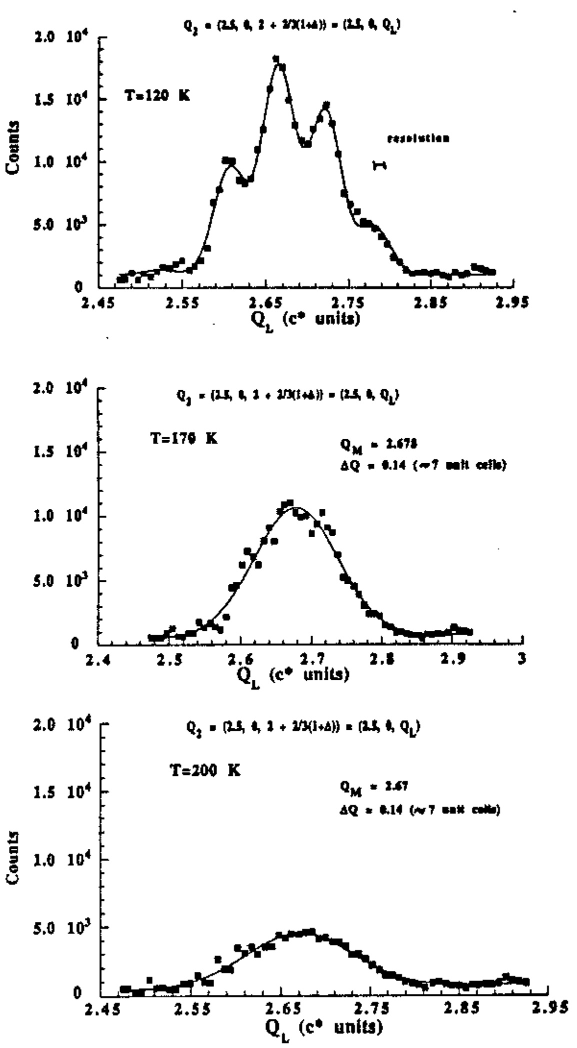

FIG. 4: The streaked structure at 120, 170 and 200 K. At 120 K 5 different peaks can be distinguished at positions corresponding to LT2-type satellites:2.523 (n=-2), 2.589 (n=-1), 2.655 (n=0), 2.721 (n=1) and 2.787 (n=2).The width of each peak amounts 0.045c* (22 unit cells) whereas the envelope structure width is 0.141c* (7 units cells). The same envelope width is found at 170 and 200 K. The continuous line corresponds to the fit of experimental data.

clockwise and anticlockwise rotations of the Te cages around the c axis superimposed to the room temperature modulation. As for the LT1, the amplitude of these rotations can be varied resulting in stronger or weaker LT2 satellites intensities without affecting those of room temperature.

The calculated LT1 and LT2 phases resemble the $TaTe_4$ room temperature modulation structure, although the phase shifts are different

Two sets of strong satellites were examined at positions

$$Q_1=\left(2, \frac{1}{2}, 2+\frac{2}{3}\left(1+\Delta\right)\right)$$

$$Q_2=\left(2.5, 0, \frac{2}{3}\left(1+\Delta\right)\right)$$

Their typical intensities at 100K are 320 and 1300 times smaller than that of (002) Bragg reflections, respectively. The streaked structure developed below 170K is of LT2-type in all sets of measured satellites and no clear evidence of LT1-type is present. Contrary, Prodan simulations yield for the Q_1 satellite an equal contribution for both LT1 and LT2 sets whereas for Q_2 the LT2 set contributes stronger than LT1. These discrepancies force to reexamine the above mentioned model.

As shown in fig. 4, these satellites exhibit an intrinsic width of about 0.042c* (23 unit cells approximately) and no significant broadening is observed (at least in the limits of our resolution) along perpendicular directions (a*, b*-plane).

The temperature variation of the integrated intensity is shown in fig. 5. Below 200 K a diffuse structure centered at Q_M=2.67c* starts to develop, its width amounting 7 unit cells, approximately (see also fig. 4). At around 170K the streaked structure starts to form from this diffuse intensity, the envelope structure keeping this 7 unit cells. Contrary to expected the streaks don't disappear on cooling below 50K, as it was reported previously, and no

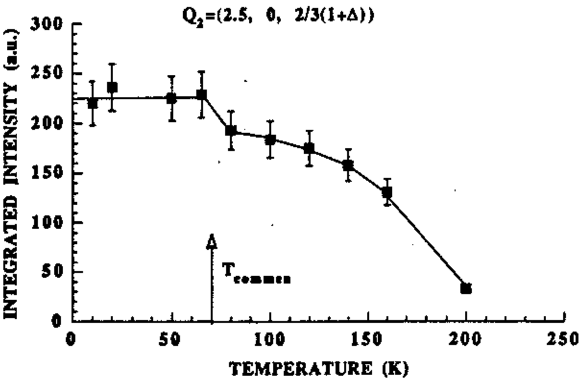

FIG. 5: Variation of satellite integrated intensity with temperature. The jump at 70 K is associated to the appearance of a locking-phase.

extra pealr appears at commensurate position 2/3 [7]. The only trace of a further commensurate structure is the discontinuously increase of the integrated intensity below 70K. This is a first order phase transition and consequently sample dependent.

IV. CONCLUSIONS

NbTe$_4$ can not be consider as a one dimensional compound. Its metallic character at all temperatures makes a charge density formation along the c-axis suspicious. The fluctuations correlation length measured above 520 °C indicates clearly the presence of a three dimensional ordering.

No trace of LT1-type structure has been found in our samples and the locking phase transition at lower temperatures doesn't carry out the disappearance of the streaked structure.

We wish to thank the technical support provided by the Laboratoire de Cristallographie and Centre de Recherches sur les Tres Basses Temperatures, CNRS-Grenoble and the aid of M.T. Fernandez-Diaz and J. Rodriguez-Carvajal on analyzing powder neutron diffraction data.

Note: There is a discrepancy between the determined space groups in the high temperature normal phase (P4cc) and in the incommensurate phase (P4/mcc). The diffraction data are unable to fully discern between both because the mirror plane perpendicular to the four fold axis doesn't give any extra limiting reflections conditions. As it was shown by Walker[6a.], both space groups are valid, yielding identical results in the above mentioned discussions.

REFERENCES

[1] P. Monceau (ed.), "Electronic Properties of Inorganic Quasi-One-Dimensional Materials", II, 139-268 (1985) by D. Reidel Publishing Company.

[2] (For a review see), G. Grüner, Rev Mod. Phys. **60**, 1129 (1988) (and references therein)

[3] P. Gressier, A. Meerschaut, L. Guemas, J. Rouxel and P. Monceau, *J. Solid State Chemistry* **51**, 141 (1984).

[4] A. Meerschaut, P. Palvadeu, and J. Rouxel, *J Solid State Chem.* **20**, 21(1977).

[5] K. Selte and A. Kjekshus, *Act. Chem. Scandinava* **18,** 690 (1964)

[6] M.B. Walker, *Can. J. Phys.* **63**, 46 (1985). M.B. Walker and Rose Morelli, *Phys. Rev. B* **38**, 4836.(1988). Rose Morelli and M.B. Walker, *Phys. Rev. Lett.* **62**, 1520 (1989). Z.Y. Chen M.B. Walker and R Morelli , *Phys. Rev. B* **39**, 11742 (1989). Rose Morelli and M.B. Walker, *Phys. Rev. B* **40**, 7542 (1989). Z.Y. Chen and M.B. Walker, *Phys. Rev. B* **40**, 8983 (1989). W.E. Goff, M.B. Walker and Z.Y. Chen, *Phys. Rev. B* **43**, 655(1991).

[7] F. W. Boswell, A. Prodan and J.K. Brandon, *J. Phys. C: Solid State Phys* **16** 1067(1983).

[8] J.A. Wilson, *Phys. Rev. B***19** 6456 (1979)

[9] D.J. Eaglesham, D. Bird, R.L. Withers and J.W. Steeds, *J. Phys. C.: Solid State Phys* **18** 1 (1985).

[10] J. Mahy, J. van Landuyt, S. Amelinckx, K.D. Bronsema and S. Van Smaalen, *J. Phys. C.: Solid State Phys* **19** 5049 (1986).

[11] S. Van Smaalen, K.D. Bronsema.and J. Mahy, *Act. Crystallogr.* **B42,** 43 (1986).

[12] K.D. Bronsema, S. Van Smaalen, J.L. de Boer, G.A. Wiegers, F. Jellineck, and J. Mahy, *Acta Cryst.* **B43**, 305 (1987).

[13] H. Böhm, *Z. für Kristallog.* **180,** 113 (1987).

[14] see for instance, J.P. Pouget and R. Comes in "Charge density waves in solids" pag.104, ed. L. P. Gor'kov and G. Grüner, ElsevierScience Publishers B.V., (1989).

[15] J. Van Landuyt, R. De Ridder, R. Gevers and S. Amelinckx, *Mater. Res. Bull.* **5**, 353 (1970)

[16] A. Prodan, F.W. Boswell, J.C. Bennett, J.M. Corbett, T. Vidmar, K. Marinkovic and A. Budkowski, *Acta Cryst.* **B46**, 587 (1990).

SPANISH SCIENTIFIC RESEARCH USING NEUTRON SCATTERING TECHNIQUES
Servicio de Publicaciones. Universidad de Cantabria, 1991

PHONONS IN TRANSITION METAL TETRACHALCOGENIDES: $NbTe_4$ AND $TaTe_4$

J.E. Lorenzo

Institut Laue-Langevin, 38042 Grenoble Cedex, France.

In collaboration with R. Currat+, P. Monceau++ and F. Levy+++
+Institut Laue-Langevin, 38042 Grenoble Cedex, France.
++Centre de Recherches sur les Tres Basses Temperatures, CNRS, 38042 Grenoble Cedex, France.
+++Institut de Physique Appliquée, Ecole Polytechnique Fédérale de Lausanne, CH-1015, Lausanne, Switzerland.

ABSTRACT

Phonon dispersion curves measurements have been carried out on $NbTe_4$ and $TaTe_4$ along selected and high symmetry directions.

$NbTe_4$ and $TaTe_4$ belong to the structure family of $CuAl_2$ which is characterized by a tetragonal antiprismatic coordination of the metal atom. $NbTe_4$ is a tetragonal compound[1] with average space group P4/mcc. It undergoes a series of incommensurate and commensurate phase transitions, at 550K, 200K and 50K, as has been described in a previous paper in this volume and in references therein. These instabilities have been currently associated to the formation of charge density waves as in others transition metal tetrachalcogenide compounds (like $(TaSe_4)_2I$ and $(NbSe_4)_{10/3}I$). However and unlike the other tetrachalcogenides, they exhibit 3D-metallic properties at all temperatures. Electronic structure calculations reveal that interchain interactions are much stronger than in the related halogenated compounds of S and Se. Mixing of the Te_2 $p\sigma^*$ orbitals with metal d_{xy} induces a deep electron pocket in the lowest conduction band at the (110) zone corner, stabilizing the structure against cell doubling into a metal-metal paired semiconducting state. It is then appealing to measure the phonon dispersion curves and try to develop an atom-atom model potential which can be used in analyzing the mechanisms responsible for the observed structural instabilities. At the same time it is worth studying the lattice-dynamical effects associated with the 550K normal-to-incommensurate phase transition, with modulation wave vector $\mathbf{q}_I = (0.5, 0.5, 0.688)$, and check the possibility of an electron-phonon coupling mechanism as responsible for this phase transition.

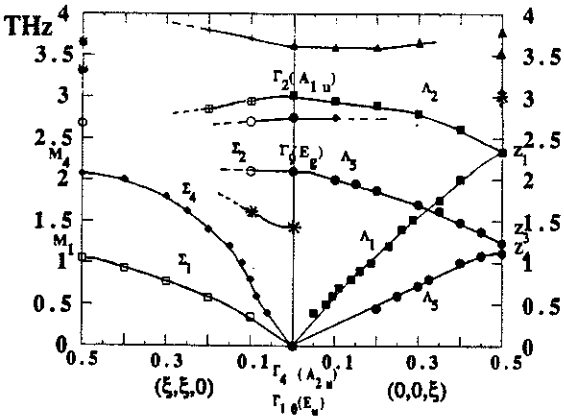

FIG. 1: Phonon dispersion curves in $NbTe_4$ along high symmetry directions (0 0 ξ) and (ξ ξ 0). The acoustic phonons exhibit the same behaviour as in $TaTe_4$ (see fig. 4).

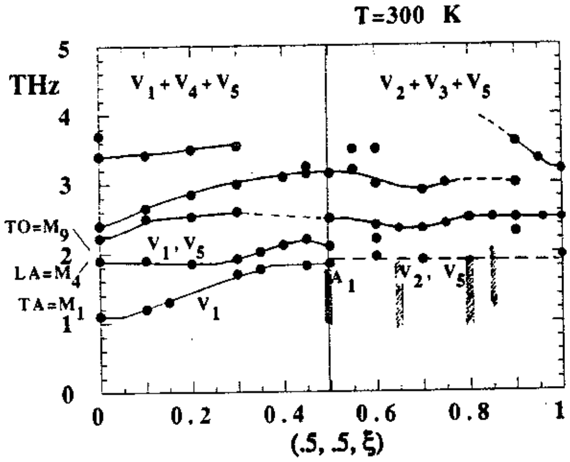

FIG. 2: Phonon dispersion curves in NbTe$_4$ along (0.5 0.5 ξ). On top of the figure the symmetry of modes visible in each Brillouin zone as due to the presence of c glide planes in the space group. ξ=0 corresponds to (hkl) Bragg reflections with l even whereas ξ=1 corresponds to those Bragg reflections with l odd. The satellite reflections are located at positions q_I = (0.5 0.5 0.688). Note the presence of diffuse intensity between 1-2 THz around q_I.

Measurements were carried out on several three-axis spectrometers at Institute Laue-Langevin (Grenoble-France) (IN3, IN8 and IN14) and at Laboratoire Leon Brillouin (1T) working at both constant incident or final energy (14.7 meV), depending on the specific instrument characteristics. A graphite filter was used to remove λ/2 contamination and collimations were, mainly, 25-40-40-40 and 25-60-40-60. Slits were located as close as possible to the sample so as to minimize background. High temperature measurements were performed in a furnace. In order to prevent sample decomposition the sample was located, firstly, in a Nb container sealed in vacuum. After two days at high temperatures the sample starts to decompose because of Te transport from the sample to the container wall. In a late experiment the sample was kept in a quartz ampoule with a small amount of Te to create a vapor pressure. Under this conditions the sample seems to remain stable at temperatures well above the incommensurate-normal phase transition temperature. Nevertheless a high inelastic background appears in all the scans.

From Raman scattering and phonon density of states measurements in analogous chalcogenated compounds it is possible to deduce the energy range of vibrations in NbTe$_4$ and TaTe$_4$. For the former

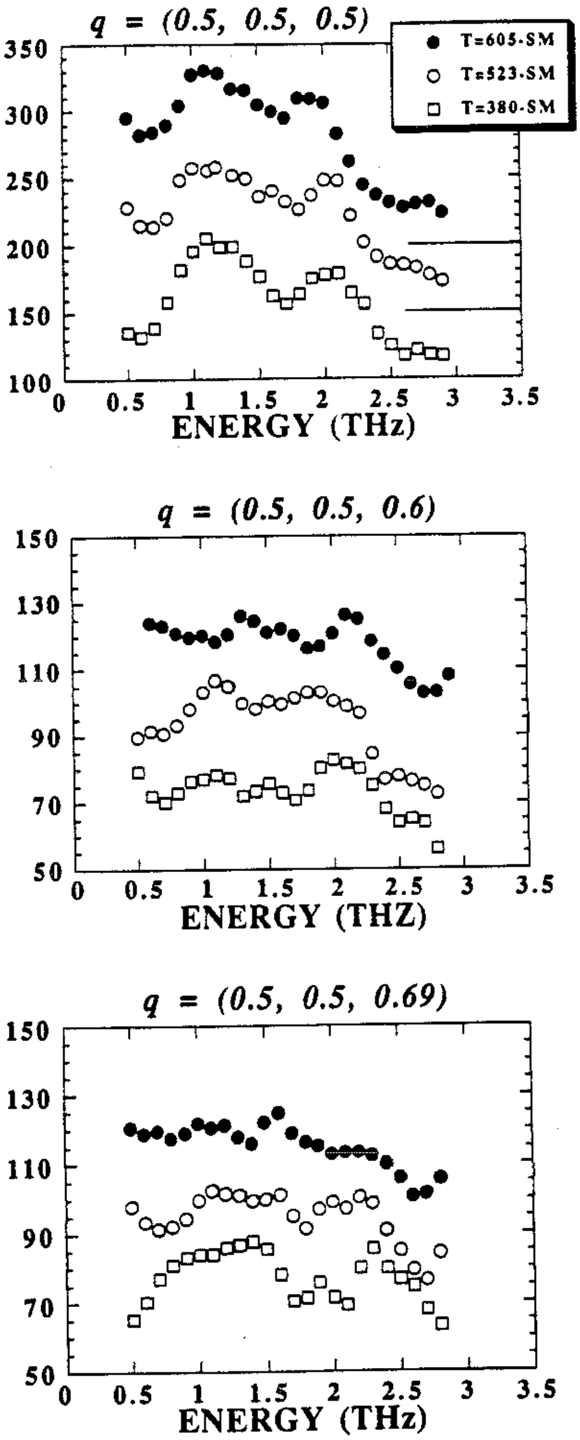

FIG. 3: Inelastic scans in NbTe$_4$ at three q-values near q_I and three temperatures. Inelastic background coming from the quartz ampoule have been already substracted. Some differences can be appreciated though we can not presently interprete them.

the range is 0-5 THz whereas for the latter is 0-3.5 THz. Fig. 1-2 show the measured phonon dispersion curves at room temperature in $NbTe_4$. Phonon dispersion curves show a typical 3D, metallic behaviour. Satellite structure factor analysis seems to indicate that the symmetry of the modes involved in the normal-incommensurate phase transition are V_2-type, along (0.5, 0.5, ξ) direction. At the present we have not observed any anomaly in these modes, though it is difficult to assert because there are many V_5-type symmetry modes with non-vanishing structure factor in the neighbourhood. Fig. 3 shows inelastic scans at three different q-positions and three temperatures below and above T_C. Some differences appear among the scans taken near $\mathbf{q_I}$ and new measurements are needed to better characterize the observed temperature effect.

For the sake of comparison, we have begun to characterize the acoustic mode dispersions in $TaTe_4$, as shown in fig. 4. This compound exhibits two commensurate modulated phases, analogous to the incommensurate phases observed in $NbTe_4$ though their transition temperatures are shifted towards upper values, i.e., at room temperature it is observed a commensurate structure equivalent to that of $NbTe_4$ below 200K. Acoustic modes in $TaTe_4$ resembles that of $NbTe_4$ and an anomalous behaviour in the transverse mode propagating along (001) has been detected. Elastic constants have been computed (except c_{13}) on the basis of our neutron measurements and the results are shown in the table. The precision of these results is estimated as within 10-15% of the proposed values.

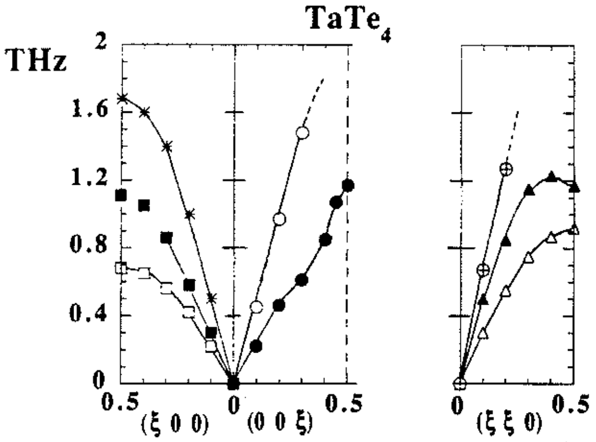

FIG. 4: Acoustic phonon dispersion curves in $TaTe_4$ along the three principal directions.

TABLE

Values of the elastic stiffness constants in $TaTe_4$ and $NbTe_4$ calculated from the acoustic slopes of the phonon dispersion curves.

	TaTe4 *	NbTe4*
c_{11}	$8.48\ 10^{11}$	
c_{33}	$7.18\ 10^{11}$	$8.52\ 10^{11}$
c_{44}	$1.68\ 10^{11}$	$1.59\ 10^{11}$
c_{66}	$2.85\ 10^{11}$	
c_{12}	$1.05\ 10^{11}$	
c_{13}		
$c_{11+2c66+c12}$	$15.23\ 10^{11}$	$12.9\ 10^{11}$

* units are dyn/cm2

REFERENCES

[1] see the paper *"Some diffraction aspects in $NbTe_4$: a neutron study"* by the same authors, in this volume, and references therein.